DETERMINATION OF BIOMECHANICAL AND ARCHITECTURAL MUSCLE PROPERTIES

— From single muscle fibre to whole muscle mechanics —

Von der Fakultät für Wirtschafts- und Sozialwissenschaften der Universität Stuttgart
zur Erlangung der Würde eines Doktors
der Philosophie (Dr. phil.) genehmigte Abhandlung

vorgelegt von

André Tomalka

aus Leinefelde

Hauptberichter: Prof. Dr. Tobias Siebert
Mitberichter: Prof. Oliver Röhrle, Ph.D.

Tag der mündlichen Prüfung: 04.06.2018

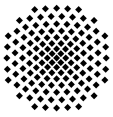

Universität Stuttgart

Institut für Sport- und Bewegungswissenschaft
Abteilung für Bewegungs- und Trainingswissenschaft

2018

Abstract

The work presented in this thesis aims to provide a more detailed insight in the complex physiology of certain muscle tissue types. This thesis builds upon the results of *in vitro* contractile and *ex vivo* architectural experiments with muscle tissue preparations from rats (*Rattus norvegicus*), rabbits (*Oryctolagus cuniculus*) and pigs (*Sus scrofa domesticus*) — investigated by experimental and modelling approaches. During the course of this work the chapters are intended to determine, describe and interprete the distinct properties of muscle tissue samples of *striated skeletal* and *smooth* musculature. These species-specific properties have not been observed before, but are needed for modelling approaches and a better understanding of contractile mechanics and muscle growth. Despite the numerous studies on skeletal and smooth muscle tissue, there are still fundamental questions about the physiology and force generation of the muscle. Hence, the determination of specific biomechanical and architectural muscle properties allows a quantitative understanding of the mechanisms involved in force development. Moreover, this is a crucial step towards reliable, realistic muscle models and thus also to increased predictive quality of muscle-driven multi-body models.

The *'General Introduction'* in **Chapter 1** outlines the basis for this thesis by building an overall introductory frame for the following **Chapters 2–6**. The *'Physiological background'* section 1.1 is intended to facilitate the access to this work by enabling insights in the structure and function, mechanisms underlying

active force production, and architectural determinants of muscle tissue. Thereby, distinct differences of contractile properties between striated skeletal and smooth musculature will be reported. Specific questions and hypotheses, based on cutting edge molecular, biomechanical, and morphological discoveries — presented within this theoretical framework — will be addressed in the following chapters.

Chapter 2 outlines the experimental setups used within this thesis to determine species-specific properties of distinct muscle tissue types. The biomechanical and architectural muscle properties have been studied extensively using a wide variety of experimental methods. Briefly, calcium-dependent force- and length measurements of single muscle fibres, digital high-speed videography for sarcomere length tracking, electric field stimulation of smooth muscle tissue, and manual digitisation (MicroScribe MLX) to investigate complex 3D fascicle architectures, have been used. Histological examinations have been realised on cryosections of gastric tissue strips, using standard immunohistochemistry protocols.

The study presented in **Chapter 3** is intended to investigate biomechanical muscle properties as force – length and force – velocity relations of gastric smooth muscle strips from pigs, extended by the analysis of 'history-effects' on smooth muscle force, which are unknown so far. History-effects include residual force depression (RFD: muscle force is reduced after muscle shortening compared to the isometric force at the same length) and residual force enhancement (RFE: muscle force is enhanced after muscle lengthening compared to the isometric force at the same length).

Hence, different isometric, isotonic, and isokinetic contraction protocols were performed during electrical muscle stimulation on $n = 54$ tissue strips in longitudinal direction from the ventral fundus of porcine stomachs. To determine the microstructure in more detail, cross-sectional areas of smooth muscles were determined from stained cryo-histological sections. Results revealed that maximum smooth muscle tension

was 10.4 ± 2.6 N/cm^2. Maximum shortening velocity and curvature factor of the force – velocity relation were 0.04 ± 0.01 [optimum muscle length/s] and 0.36 ± 0.15, respectively. The findings presented within this work demonstrated significant ($P < 0.05$) force depression (up to 32% maximum muscle force) and force enhancement (up to 16% maximum muscle force) of gastric muscle tissue, respectively. The force enhancement and force depression values increased with increasing ramp amplitude. For the first time a comprehensive set of stomach smooth muscle parameters, including classic biomechanical muscle properties and history-dependent effects, is provided by this work. This dataset facilitates novel insights in gastric motility and contraction behaviour based on the re-evaluation of existing contractile mechanisms. More specifically, experimentally observed history-effects of smooth muscle tissue affect the force-generating capacity of the stomach and subsequently support gastric emptying. This potentially explains the functional relevance of RFE in stomachs.

In **Chapter 4**, the active force – length relationship during extensive eccentric contractions in skinned skeletal muscle fibres — obtained from the *musculus extensor digitorum longus* of the rat — is investigated.

In contrast to experimentally observed progressive forces in eccentric contractions, cross-bridge and sliding filament theories of muscle contraction predict that varying myofilament overlap will lead to increases and decreases in active force during eccentric contractions. Non-cross-bridge contributions potentially explain the progressive total forces. However, it is not clear whether underlying abrupt changes in the slope of the nonlinear force – length relationship are visible in long isokinetic stretches, and in which proportion cross-bridges and non-cross-bridges contribute to muscle force. In this chapter will be demonstrated, that maximally activated single skinned muscle fibres from rats behave (almost across the entire working range) like linear springs. Cross-bridge and non-cross-bridge contributions to muscle force were investigated using an actomyosin inhibitor. The experiments revealed a nonlinear progressive contribution

of non-cross-bridge forces and suggest a nonlinear cross-bridge contribution similar to the active force – length relationship. The observed slight increase in slope with initial length is in accordance with current models attributing the non-cross-bridge force to titin. This distinct muscle behaviour might offer high impact shock absorption during braking movements such as downhill walking or landing after a jump.

In **Chapter 5**, a theoretical study — proposing a structurally consistent model of sarcomere contraction — is presented.

The active isometric force – length relationship can be directly explained with actin and myosin filament overlap, whereas qualitative changes in overlap lead to slope changes of the force – length relation. The plateau region and the descending limb of the force – length relationship are well explained by the sliding filament and cross-bridge theories of muscle contraction. However, it is not clear which mechanism(s) are responsible for the decrease in force in the shallow and the steep slope regions of the ascending limb of the force – length relation. Until now, this slope-change is explained, for example, with the folding or compression of the myosin filaments on the Z-disc. Anyway, this is in strong conflict with experimental observations. The model presented in **Chapter 5** enables myosin filament sliding through the Z-disc by the transition from hexagonal to tetragonal actin filament arrangement near the Z-disc, together with a thoughtful titin arrangement. With no fitting of parameters required, the model predicts straightforwardly the fibre's entire force – length behaviour and the dependence of the maximum contraction velocity on sarcomere length. The model enables new perspectives on the relation between striated fibre structure and its mechanical function. For example, muscle diseases like Duchenne muscular dystrophy are accompanied by a loss of structural integrity of the Z-disc contributing to the observed muscle weakness.

The underlying theoretical considerations are supported by experiments with single permeabilised fibres from the *musculus extensor digitorum longus* of the rat.

The study in **Chapter 6** is aimed to analyse growth-related changes in the muscle structure of rabbit *gastrocnemius lateralis*, *gastrocnemius medialis*, *flexor digitorum longus*, and *tibialis anterior*.

Much is known about active muscle force generation and the muscle architecture at a particular age, but less is known about changes in muscle structure during growth. Changes in tendon length, muscle belly- and aponeurosis dimensions were determined using $n = 55$ rabbits between 18 and 108 days. Additionally, the three-dimensional muscle fascicle architecture of five rabbits of different ages (21, 37, 50, 70, 100 days) was determined using a manual digitiser.

Most of the geometrical parameters observed exhibited an almost linear increase over time. In contrast to the pronounced increase in muscle belly length of *gastrocnemius lateralis* and *gastrocnemius medialis*, *flexor digitorum longus* and *tibialis anterior* exhibited more uniform muscle belly growth. In general, the aponeuroses of the muscles exhibited lower growth rates in width than in length, and aponeurosis areas were larger than physiological cross-sectional areas. There were almost no changes in fascicle lengths with increasing age for *gastrocnemius lateralis*, *gastrocnemius medialis* and *flexor digitorum longus*, except for *tibialis anterior*. Pennation angles of *tibialis anterior* and *flexor digitorum longus* remained almost unchanged but increased for *gastrocnemius lateralis* from the youngest to the oldest animal. For all muscles observed, the tendon-muscle fascicle length ratio changed during growth. Therefore, the results of this study facilitate new insights regarding changes in three-dimensional muscle architecture and aponeurosis shape during growth.

Chapter 7 provides general conclusions from the results presented in the **Chapters 3–6**. Based on these studies, the underlying thesis enables a substantial contribution to a much more detailed understanding of overall muscle behaviour and muscle growth. Furthermore, this work contributes to the answering of so far unresolved questions in terms of muscular contraction dynamics on the molecular and cellular level

by the re-evaluation of existing models or proposed contractile mechanisms. These unique insights facilitate an holistic view of the impact of force generation and muscle architecture on biological locomotion and motility, respectively.

Zusammenfassung

Die in dieser Thesis vorgestellte Arbeit ist dahingehend ausgerichtet, einen detaillierten Einblick in die komplexe Physiologie bestimmter Muskelgewebearten zu geben. Die Arbeit baut auf den Ergebnissen von kontraktilen *in vitro* und architektonischen *ex vivo* Experimenten mit Muskelgewebepräparaten von Ratten (*Rattus norvegicus*), Kaninchen (*Oryctolagus cuniculus*) und Schweinen (*Sus scrofa domesticus*) auf. Im Laufe dieser Arbeit werden die charakteristischen Eigenschaften von Muskelgewebeproben, sowohl von *quergestreifter skelettaler* als auch *glatter* Muskulatur, untersucht. Die erstmalige Erfassung dieser artspezifischen Eigenschaften wird sowohl für Modellierungsansätze als auch für ein besseres Verständnis der kontraktilen Mechanik und des Muskelwachstums benötigt. Trotz der zahlreichen Studien an quergestreifter Skelett- und glatter Muskulatur gibt es noch grundlegende Fragen zur Physiologie und Krafterzeugung des Muskels. Die Bestimmung spezifischer biomechanischer- und architektonischer Muskeleigenschaften erlaubt mitunter ein quantitatives Verständnis der an der Kraftentwicklung beteiligten Mechanismen. Des Weiteren stellt dies einen entscheidenden Schritt auf dem Weg zu verlässlichen, realistischen Muskelmodellen und damit auch zu einer verbesserten Vorhersagekraft von muskelgetriebenen Mehrkörpermodellen dar.

Die *Allgemeine Einleitung* in **Kapitel 1** repräsentiert die Grundlage für diese Thesis und bildet die Eckpfeiler für die folgenden **Kapitel 2–6**. Der Abschnitt 1.1

(Physiologischer Hintergrund) soll den Zugang zu dieser Arbeit erleichtern, indem er Einblicke in die Struktur und Funktion, zugrundeliegende Mechanismen der aktiven Kraftproduktion, und die architektonischen Determinanten von Muskelgewebe ermöglicht. Diesbezüglich werden distinkte Unterschiede kontraktiler Eigenschaften zwischen quergestreifter Skelett- und glatter Muskulatur dargestellt. Spezifische Fragestellungen und Hypothesen, die auf aktuellen molekularen, biomechanischen und morphologischen Entdeckungen beruhen, werden in den folgenden Kapiteln behandelt.

Kapitel 2 beschreibt die Versuchsaufbauten, welche innerhalb dieser Arbeit Verwendung fanden, um die artspezifischen Eigenschaften entsprechender Muskelgewebetypen zu bestimmen. Die biomechanischen- und architektonischen Muskeleigenschaften wurden ausgiebig unter Verwendung einer Vielzahl von experimentellen Methoden untersucht. Zu diesen zählen u.a. kalziumabhängige Kraft- und Längenmessungen an Einzelmuskelfasern, digitale Hochgeschwindigkeits-Videografie zur Sarkomerlängenverfolgung, elektrische Feldstimulation glatter Muskulatur, und manuelle Digitalisierung (MicroScribe MLX) zur Untersuchung komplexer 3D-Faszikelarchitekturen. Histologische Untersuchungen wurden an Kryoschnitten von Magengewebestreifen — mit Hilfe immunhistochemischer Standardprotokolle — durchgeführt.

Die in **Kapitel 3** vorgestellte Studie befasst sich mit der Untersuchung biomechanischer Muskeleigenschaften anhand von glatten Muskelstreifen des Schweins entnommen aus dem ventralen Fundus des Magens. Diese klassischen Parameter werden zusätzlich durch die Analyse von ‘Geschichtseffekten’ (‘history-effects’: Muskelkräfte sind größer / kleiner als mit klassischen Theorien erwartet) auf die Muskelkraft erweitert, welche bislang unbekannt sind.

Unterschiedliche isometrische, isotonische und isokinetische Kontraktionsprotokolle wurden während elektrischer Muskelstimulation an $n = 54$ Gewebestreifen in

Längsrichtung durchgeführt. Um die Mikrostruktur ausführlich zu bestimmen, wurden die Querschnittsflächen der glatten Muskulatur aus kryo-histologischen Schnitten bestimmt. Die maximale Muskelspannung betrug $10.4 \pm 2.6\,\mathrm{N/cm^2}$. Die maximale Verkürzungsgeschwindigkeit und der Krümmungsfaktor (curvature factor) der Kraft – Geschwindigkeitsrelation war jeweils 0.04 ± 0.01 [optimale Muskellänge/s], und 0.36 ± 0.15. Die Ergebnisse, die in dieser Arbeit vorgestellt werden, zeigen eine signifikante ($P < 0.05$) Kraftverringerung (bis zu 32% der maximalen Muskelkraft) und Kraftüberhöhung (bis zu 16% der maximalen Muskelkraft) des Magengewebes. Die Werte der Kraftüberhöhung und Kraftverringerung erhöhten sich jeweils mit zunehmender Rampenamplitude. Erstmalig wird ein umfangreicher Datensatz von glatten Muskelparametern des Schweinemagens, einschließlich klassischer, biomechanischer Muskeleigenschaften und geschichtsabhängiger Effekte, bereitgestellt. Dieser Datensatz ermöglicht neue Einblicke in die Magenmotilität und das Kontraktionsverhalten auf Grundlage der Neubewertung bestehender kontraktiler Mechanismen. Insbesondere experimentell beobachtete Geschichtseffekte an glattem Muskelgewebe beeinflussen die Krafterzeugung des Magens und unterstützen folglich die Magenentleerung. Dies erklärt möglicherweise die funktionelle Relevanz von signifikant erhöhten Kräften während und nach Muskellängung (RFE) für den Magen-Darm-Trakt.

In **Kapitel 4** wird die aktive Kraft – Längenbeziehung während extensiver, exzentrischer Kontraktionen anhand von gehäuteten Skelettmuskelfasern — entnommen vom *musculus extensor digitorum longus* der Ratte — untersucht.

Während die Gleitfilament- und Querbrückentheorie nahezu fehlerfreie Voraussagen für isometrische und konzentrische Kontraktionen gewährleisten, so versagen diese jedoch z.B. bei der Vorhersage von isometrischen Kräften nach exzentrischen Kontraktionen. Noch immer sind kraftgenerierende Mechanismen während exzentrischer Kontraktionen, vor allem auf molekularer Ebene, nicht vollständig verstanden. Ungeachtet dessen hängt die aktive Kraft eines Muskels von der Myofilamentüberlappung ab, welche

zu klar sichtbaren Anstiegswechseln der aktiven Kraft – Längenbeziehung führt. Daraus resultiert die Fragestellung, respektive Hypothese, ob sich diese ausgeprägten Anstiegswechsel in ausreichend langen, exzentrischen Kontraktionen widerspiegeln und in welchem Maß Querbrücken- und Nicht-Querbrückenstrukturen (primär Titin) zur Muskelkraft beitragen. Es wird gezeigt, dass sich maximal aktivierte, gehäutete Einzelmuskelfasern der Ratte annähernd wie lineare Federn verhalten. Die Querbrücken- und Nicht-Querbrückenbeiträge zur Muskelkraft wurden mit einem Actomyosin-Inhibitor untersucht. Die Experimente zeigten einen nichtlinearen, progressiven Beitrag von Nicht-Querbrückenkräften und suggerieren einen nichtlinearen Querbrückenbeitrag ähnlich zur aktiven Kraft – Längenbeziehung. Darüber hinaus entspricht die beobachtete leichte Erhöhung des Anstiegs der Kraft – Längenverläufe den aktuellen Modellen, welche die Nicht-Querbrückenkraft auf das Protein Titin zurückführen. Dieses charakteristische Muskelverhalten unterstützt potentiell die Stoßdämpfung bei Bremsbewegungen wie bergab gehen oder während der Landung nach einem Sprung.

In **Kapitel 5** wird eine theoretische Studie vorgestellt, welche ein strukturell-konsistentes Modell der Sarkomerkontraktion vorschlägt.

Die aktive isometrische Kraft – Längenbeziehung kann direkt mit der Aktin- und Myosinfilamentüberlappung erklärt werden, während qualitative Veränderungen der Überlappung zu Anstiegswechseln der Kraft – Längenrelation führen. Die Plateau-Region und der absteigende Ast der Kraft – Längenbeziehung werden durch die Gleitfilament- und Querbrückentheorie der Muskelkontraktion präzise erklärt. Es ist jedoch nicht klar, welche Mechanismen für die Abnahme der Kraft in den flachen und steilen Abschnitten des aufsteigenden Astes der Kraft – Längenkurve verantwortlich sind. Bisher wird dieser Anstiegswechsel z.B. mit der Faltung oder Kompression der Myosinfilamente an der Z-Scheibe erklärt, welches jedoch in starkem Konflikt zu experimentellen Beobachtungen steht. Aufgrund einer tetragonalen

Aktinfilament- und durchdachten Titinanordnung ermöglicht das in **Kapitel 5** dargestellte Modell ein Gleiten des Myosinfilaments durch die Z-Scheibe. Das Modell ermöglicht direkte Vorhersagen des gesamten Kraft – Längenverhaltens der Faser in Abhängigkeit von der maximalen Kontraktionsgeschwindigkeit — ohne Anpassung der benötigten Parameter. Des Weiteren ermöglicht es neue Perspektiven im Hinblick auf die Beziehung zwischen quergestreifter Faserstruktur und ihrer mechanischen Funktion. Beispielsweise gehen Muskelerkrankungen wie die Duchenne-Muskeldystrophie mit einem Verlust der strukturellen Integrität der Z-Scheibe einher, was zur beobachteten Muskelschwäche beiträgt.

Die zugrundeliegenden theoretischen Überlegungen werden durch Experimente an permeabilisierten Einzelfasern vom *musculus extensor digitorum longus* der Ratte untermauert.

Die Studie in **Kapitel 6** forciert die Analyse wachstumsbedingter Veränderungen in der Muskelstruktur des *gastrocnemius lateralis*, *gastrocnemius medialis*, *flexor digitorum longus* und *tibialis anterior* des Kaninchens.

Es besteht ein relativ detailliertes Wissen hinsichtlich der aktiven Krafterzeugung und Muskelarchitektur in einem bestimmten Alter. Das Verständnis im Hinblick auf die Veränderungen der Muskelstruktur während des Wachstums ist jedoch weniger ausgeprägt. Änderungen der Sehnenlänge, Muskelbauch- sowie Aponeurosendimensionen wurden anhand von $n = 55$ Kaninchen, zwischen 18 und 108 Tagen, bestimmt. Darüber hinaus wurde die dreidimensionale Muskelfaszikel-Architektur von fünf Kaninchen unterschiedlichen Alters (21, 37, 50, 70, 100 Tage), mit einem manuellen Digitiser, bestimmt.

Es wurde eine nahezu lineare Zunahme über die Zeit in den meisten der untersuchten geometrischen Parametern gefunden. Im Gegensatz zu der ausgeprägten Zunahme der Muskelbauchlänge des *gastrocnemius lateralis* und *gastrocnemius medialis*, zeigten *flexor digitorum longus* und *tibialis anterior* ein gleichmäßiges Muskelbauchwachstum.

Im Allgemeinen zeigten die Aponeurosen der Muskeln niedrigere Wachstumsraten in der Breite als in der Länge, und die Aponeurosenflächen waren größer als die physiologischen Querschnittsflächen. Im Gegensatz zum *tibialis anterior* gab es nahezu keine Veränderungen in den Faszikellängen mit zunehmendem Alter für *gastrocnemius lateralis*, *gastrocnemius medialis* und *flexor digitorum longus*. Die Fiederungswinkel des *tibialis anterior* und *flexor digitorum longus* blieben nahezu unverändert, wohingegen der Fiederungswinkel des *gastrocnemius lateralis*, vom jüngsten zum ältesten Tier, zunahm. Für alle beobachteten Muskeln änderte sich das Sehnen-Muskelfaszikel-Längenverhältnis während des Wachstums. Die zugrundeliegenden Ergebnisse erlauben neue Erkenntnisse im Hinblick auf die Veränderungen der dreidimensionalen Muskelarchitektur und -Aponeurose während des Wachstums.

Kapitel 7 liefert allgemeine Schlussfolgerungen aus den Ergebnissen, welche in den **Kapiteln 3–6** dargestellt werden. Diese Arbeit ermöglicht auf Grundlage dieser Studien einen erheblichen Beitrag zu einem verbesserten Verständnis des Gesamtmuskelverhaltens und Muskelwachstums. Darüber hinaus trägt diese Thesis zu der Beantwortung offener Fragen bezüglich muskulärer Kontraktionsdynamik auf molekularer und zellulärer Ebene durch die Neubewertung bestehender Modelle oder vorgeschlagener kontraktiler Mechanismen bei. Diese Erkenntnisse erlauben eine ganzheitliche Sicht bezüglich des Einflusses der Kraftgenerierung und Muskelarchitektur auf biologische Fortbewegung und Motilität.

Contents

List of Figures

List of Tables

List of Symbols and Abbreviations

Chapter 1

Symbol	*Definition*
3D	Three-dimensional
Ca^{2+}	Calcium ion
CSA	Cross-sectional area
curv	Curvature factor
EDL	Musculus extensor digitorum longus
F_{im}	Maximum isometric force
FLR	Active isometric force – length relationship
FVR	Force – velocity relationship
L	Muscle (fibre) length
L_0	Optimum muscle (fibre) length associated with F_{im}
L_S	Sarcomere length
L_{S0}	Optimum sarcomere length
PEVK	Titin I-band region composed of repetitions of amino acids proline (P), glutamate (E), valine (V), and lysine (K)
RFD	Residual force depression
RFE	Residual force enhancement
SSC	Stretch-shortening cycle
v_{max}	Maximum shortening velocity

Chapter 2

Symbol	*Definition*
ELWD	Extra long working distance
G	Gauge — unit of measurement for the size of the nominal outer diameter of e.g. cannulas, hypodermic needles and tubes
h	Height
L_{slack}	Slack length
NA	Numerical aperture
v/v	Volume/volume
w/v	Weight/volume
w	Width

Chapter 3

Symbol	*Definition*
p	Percentage of longitudinal muscle layer from total CSA
P_{im}	Maximum smooth muscle tension

Chapter 4

Symbol	*Definition*
ATP	Adenosine 5'-triphosphate disodium salt hydrate
BDM	2,3-Butanedione monoxime
CK	Creatine phosphokinase
CP	Creatine phosphate
E-64	Trans-Epoxysuccinyl-L-leucylamido(4-guanidino)butane
EGTA	Ethylene glycol-bis(2-aminoethylether)- N,N,N',N'-tetraacetic acid
f_{XB}	Fraction of cross-bridges suppressed by BDM
f_v	Scaling factor for constant eccentric velocity
GLH	Glutathione
HDTA	1,6-Diaminohexane-N,N,N',N'-tetraacetic acid

IMID	Imidazole
KOH	Potassium hydroxide
KP	Potassium propionate
L_e	Length at the end of eccentric ramp
L_i	Initial length
PMSF	Phenylmethanesulfonyl fluoride
TES	N-[Tris(hydroxymethyl)methyl]-2-aminoethanesulfonic acid

Chapter 5

Symbol	*Definition*
half-sarcomere lengths l:	
l_1	No actin–myosin overlap
l_2	Start of plateau
l_3	Start of shallow slope
l_4	Start of steep slope
l_5	Actin–actin–myosin overlap meets myosin–myosin–actin overlap
l_6	Actin filaments of adjacent half-sarcomere meet Z-disc
l_7	Myosin filaments of adjacent half-sarcomeres meet bare zone
l_8	Myosin filaments of adjacent half-sarcomeres meet M-line

Chapter 6

Symbol	*Definition*
ρ	Density of skeletal muscle (≈ 1.054 g/cm^3)
α	Mean pennation angle of the muscle
R^2	Coefficient of determination
APO	Aponeurosis
A_{APO_mean}	Average of distal and proximal aponeurosis areas
area APO_{dist}	Distal aponeurosis area
area APO_{prox}	Proximal aponeurosis area

FDL	Musculus flexor digitorum longus
GL	Musculus gastrocnemius lateralis
GM	Musculus gastrocnemius medialis
length APO_{dist}	Distal aponeurosis length
length APO_{prox}	Proximal aponeurosis length
A_{APO}	Aponeurosis area
l_{APO}	Aponeurosis length
l_{fasc}	Muscle fascicle length
l_m	Muscle belly length
l_{SEC}	Series elastic component length (including tendon and aponeurosis)
l_t	Tendon length
m_{muscle}	Muscle mass
PLA	Musculus plantaris
r_{ACSA}	Aponeurosis-CSA ratio
r_{TFL}	Tendon-muscle fascicle length ratio
SEC	Series elastic component
SOL	Musculus soleus
TA	Musculus tibialis anterior
t_m	Muscle belly thickness
t_{fg}	Normalised growth data to the ages when skeletal growth is almost complete
width APO_{dist}	Distal aponeurosis width
width APO_{prox}	Proximal aponeurosis width
w_{APO}	Aponeurosis width
w_m	Muscle belly width

Chapter 1

General Introduction

Muscular tissue represents a fascinating, elegant and complex machinery, enabling active force production, movement and stability of the skeleton, storage and transport of substances within the body and generation of heat. These multiple physiological processes are based on the mode of operation of muscles. The variety of highly specialised and diverse muscle functions requires a comprehensive understanding of the biomechanical, ultrastructural, architectural and functional properties of certain muscle tissues in order to enhance our knowlegde of **how muscles work** and **how they cover prevailing complex mechanical conditions**.

Hence, the aims of the present research are both: *first*, the experimental determination, interpretation and modelling of biomechanical- (**Chapters 3–5**) and histological properties (**Chapter 3**) on the microstructural level. *Second*, the characterisation of morphological- (**Chapter 3**) and the investigation of architectural properties (**Chapter 6**) on the macrostructural level of skeletal and smooth muscle tissue (see Figure 1.1). Whereby the term *'microstructure'* is related to the ultrastructural, celluar and molecular level and the *'macrostructure'* is related to the gross anatomy (Gans & Bock, 1965; Lieber & Frieden, 2000). The goals of this approach are the extension of existing knowledge and the presentation of possible answers for so far unresolved questions in terms of muscle dynamics and structure, and their functional

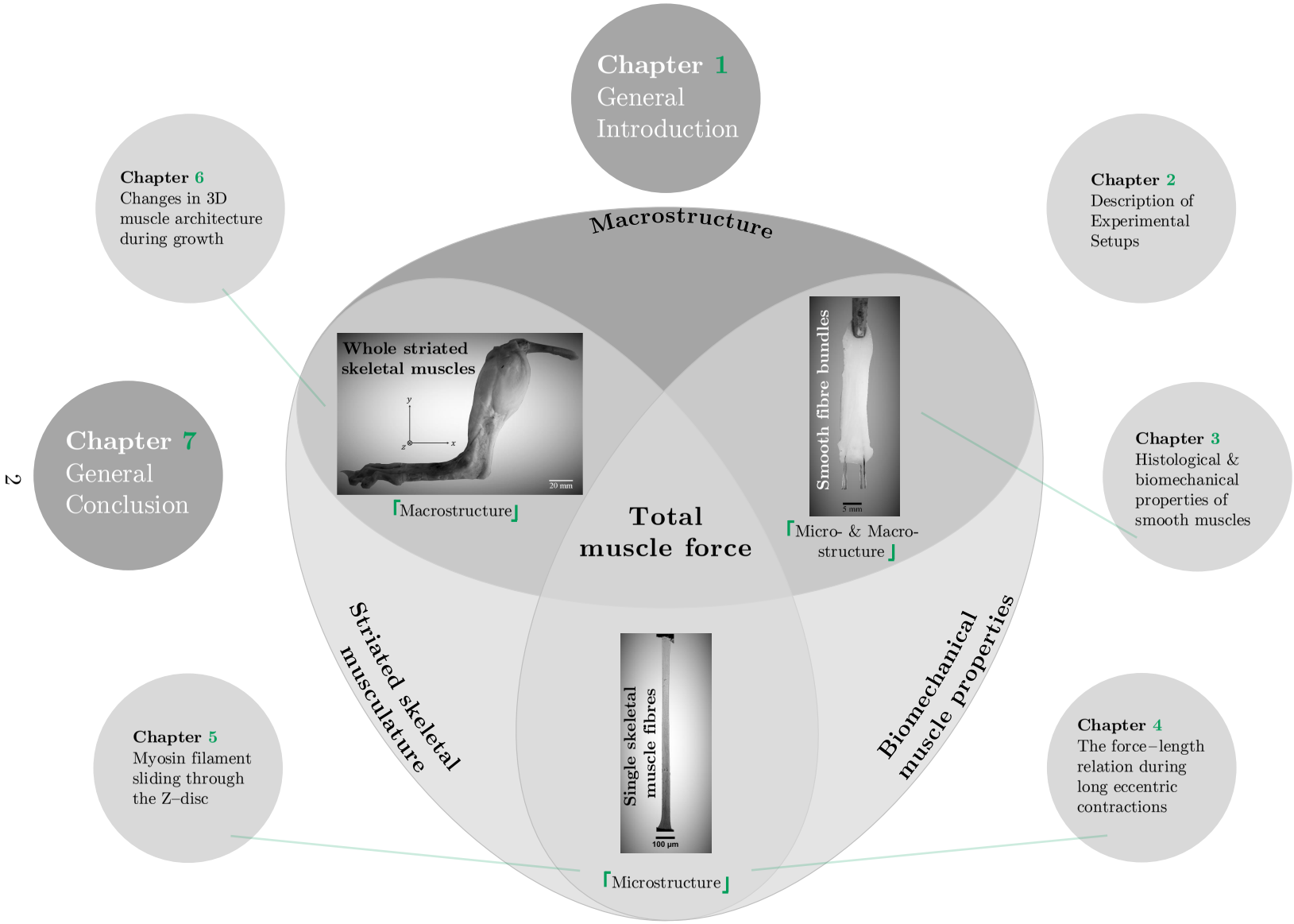

Figure 1.1: Structure of this thesis.

relevance of e.g. gastrointestinal motility and architectural changes during growth. In Figure 1.1 the structure of this thesis is shown. The *'General Introduction'* (**Chapter 1**) is intended to give a physiological background and presents research questions addressed in this thesis. **Chapter 2** illustrates the *'Experimental Setups'* used within this work. **Chapters 3, 4** and **6** report three experimentally based studies. In **Chapter 5**, a theroretical approach — supported by fibre experiments — is presented. In the *'General Conclusion'* (**Chapter 7**) the results are discussed and integrated in a research context.

1.1 Physiological background

In order to ensure a gentle access to this work, muscle morphology and contractile mechanisms underlying active force production of muscle tissue are introduced. General explanations and pioneering observations of the last century, that provide the fundamentals for this thesis, will follow.

1.1.1 Muscle structure and function

Generally, muscles can be distingusihed between *striated* (skeletal and cardiac) and *smooth* muscle tissue with regard to their functional, chemical, morphological and mechanical properties. For the research presented here, the main subjects for the determination of contractile muscle properties are *(1)* permeabilised (skinned) single fibres of skeletal muscle tissue from rats (*Rattus norvegicus*) and *(2)* smooth gastric muscle fibre bundles from pigs (*Sus scrofa domesticus*). For the investigation of architectural properties *(3)* whole skeletal muscle preparations from rabbits (*Oryctolagus cuniculus*) have been used (Figure 1.1). Hence, the following work is focussing on these two distinct (*striated skeletal* and *smooth*) types of muscular tissue.

For the following sections of **Chapter 1**, background information of skeletal muscle tissue is emphasised to ensure a rigorous and comprehensible description of biomechanical (force – length [FLR] and force – velocity relations [FVR], history-effects;

see List of Symbols and Abbreviations) and morphological properties. A basic comparison of these muscle properties between skeletal and smooth musculature is made in subsequent paragraphs, respectively. A more detailed differentiation between these two distinct muscular tiusse types is given in **Chapter 3**, section 3.4.1 *'Smooth gastric muscle properties'*).

Smooth muscle tissue serves as motor for the system of internal organs of vertebrates. It is located i.a. in the walls of hollow viscera, airways and blood vessels, and transports material by muscle contraction. Thus, smooth muscles have a central role along the respiratory-, the cardio-vascular- and the digestive system (Tortora & Nielsen, 2013). Skeletal musculature, however, serves together with the skeleton as locomotor system, often performing diverse roles, acting as motor, shock absorber, strut, spring and break or combinations thereof (Dickinson *et al.*, 2000; Azizi, 2014).

Morphologically, a skeletal muscle has a strictly hierarchical and well organised structure (Figure 1.2). Beginning with the entire muscle level, the force — generated by the active muscle — is transmitted via the aponeurosis, which provides the attachment area for the muscle fibres, and the tendon, which connects the muscle appropriately to the bone; commonly known as the muscle–tendon unit. The entire muscle, again, is surrounded by a fascia and further connective tissue called the epimysium, which binds several fibre bundles (fascicles) together. The fascicles, formed by numerous single muscle fibres, are wrapped in the perimysium. The fibre bundles are strongly embedded in an continuous intermeshing network of connective tissue, the extra-cellular matrix. The next smaller structure, the muscle fibre (diameter 10–100 μm), is surrounded by the endomysium. The muscle fibres, in turn, are composed of hundreds of contractile subunits, the myofibrils. Myofibrils lying parallel to each other along their longitudinal axis and are mainly composed of the contractile proteins actin (thin filament) and myosin (thick filament), the regulatory proteins tropomyosin and troponin and the structural protein titin. The length of the thick contractile protein myosin is approximately 1.6 μm

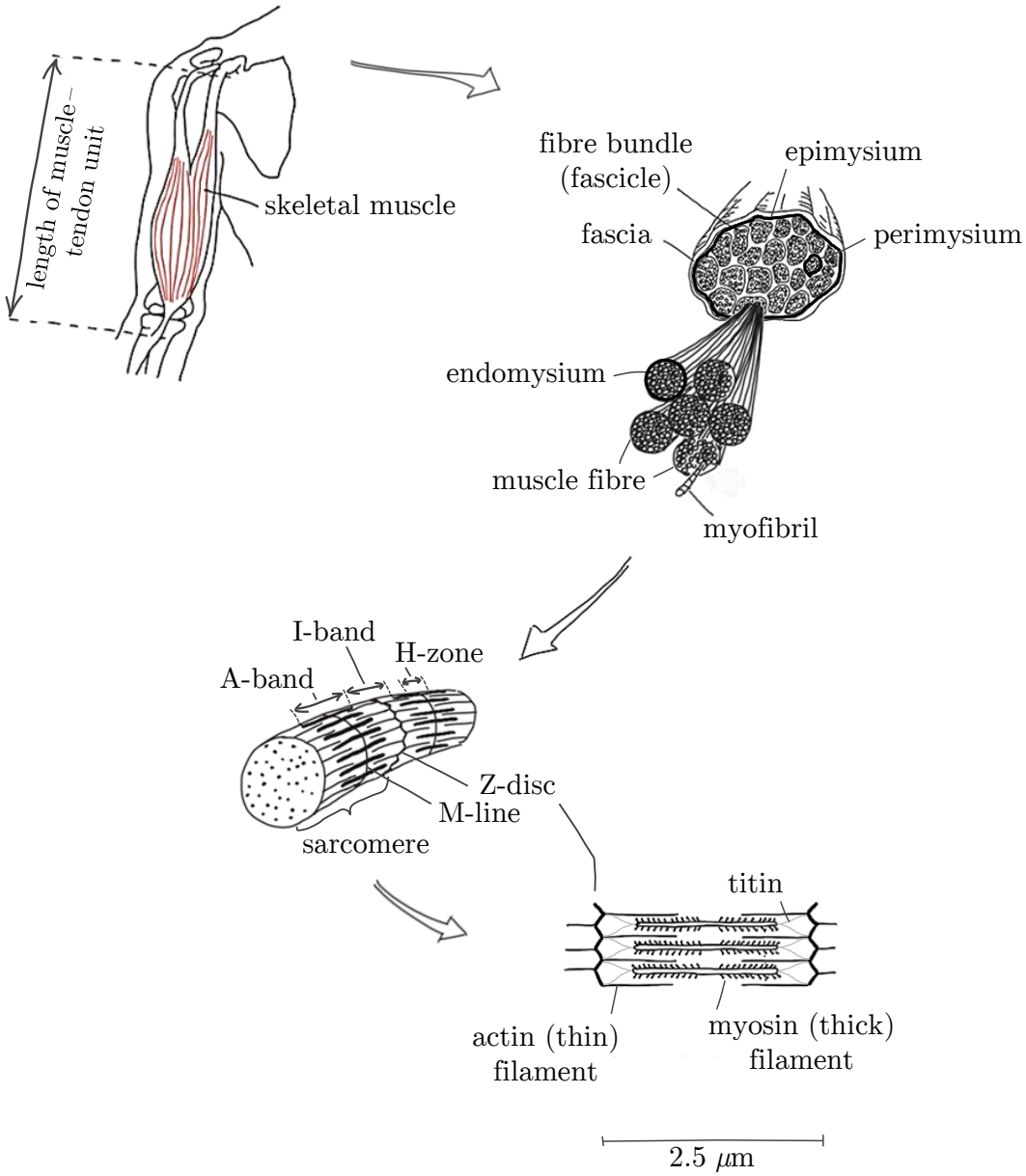

Figure 1.2: Schematic illustration of skeletal muscle structure with decreasing scale starting from entire (top) to molecular (bottom) level. Defining the sarcomere as the smallest contractile unit of striated muscle tissue. Note that the optimal sarcomere length (L_{S0}) varies among species due to variations in thin filament length (for details see text). The illustrated length of 2.5 μm of the sarcomere schematic (bottom) represents L_{S0} for maximal isometric force (F_{im}) development in rat muscles (Stephenson & Williams, 1982). Schematic adaptated from Toigo (2015).

in the skeletal muscles of both mammalians and anurans, while the thin filament length is more varible (0.9–1.3 μm) (Walker & Schrodt, 1974). These proteins are organised in compartments called sarcomeres. The regular organisation of these sarcomeres gives skeletal (and cardiac) muscles their distinctive striated pattern on the level of muscle fibres and myofibrils, visible under a light microscope (Figure 1.3). A sarcomere within a myofibril can be divided into 5 sections: the Z-discs, appearing as fine dense lines, forming the lateral boundaries of sarcomeric units in striated muscles (Luther, 2009). The A-band (A = anisotropic), contains only the myosin filaments, the I-band (I = isotropic), contains only the actin filaments. In the centre of the H-zone, an overlap zone of thick and thin filaments, a dark M-line (M = middle) is visible. This M-line is a meshwork consisting of structural proteins, similar to the Z-disc (cf. Figure 1.2; myofibril schematic at the bottom).

In addition to the contractile and regulatory proteins, muscle fibres consist of several structural proteins (e.g. titin, nebulin, desmin), which contribute to stability, elasticity, alignment and even to active force production, although in a supportive manner (Linke, 2017; Herzog *et al.*, 2016). Concerning this matter, titin — acting as a molecular spring — is the third most abundant protein in skeletal muscles (and in a similar form in smooth muscles), that spans half a sarcomere from the Z-disc to the M-line and anchors the thick and thin myofilaments to the Z-disc (Prado *et al.*, 2005; Li *et al.*, 2016). In skeletal musculature it consists of a proximal and distal immunoglobulin domain, the PEVK region (abundant in the amino acids proline (P), glutamate (E), valine (V) and lysine (K)), and a N2A region (Labeit & Kolmerer, 1995).

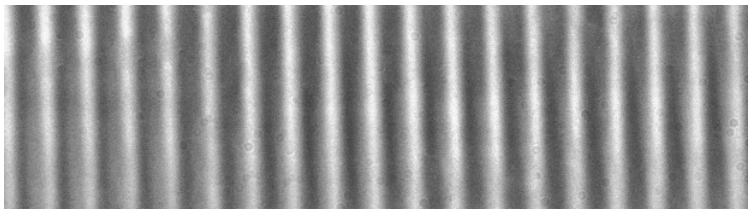

Figure 1.3: Characteristic striation pattern illustrated by a relaxed skeletal muscle fibre segment from a rats extensor digitorum longus (EDL) muscle at $L_{S0} = 2.5\,\mu$m at $1000\times$ magnification.

Comparision with smooth musculature — Structure and function

To enable a better understanding of the structure and function of smooth compared to striated skeletal musculature, the following sections provide a brief overview of distinct differences.

There are characteristic differences in the underlying microstructure of smooth muscle tissue. The smooth muscle is called 'smooth' because the various filaments have no regular pattern of overlap, thus, no striation pattern can be observed under a light microscope. Smooth muscle fibres are considerably smaller than skeletal muscle fibres. A single fusiform smooth muscle fibre in a relaxed state is 30–400 μm long and 2–10 μm thick — with a single, oval, centrally located nucleus within the fibre (Tortora & Nielsen, 2013). In addition to the contractile filaments actin and myosin, the smooth muscle fibre also contains intermediate filaments (diameter of 10 nm). The actin filaments are attached to the numerous intracellular dense bodies, which are functionally similar to Z-discs in striated musculature. The side-polar arrangement of cross-bridges in smooth muscle tissue compared to the typical bipolar structure of myosin filaments in striated musculature (Figure 1.4) represents a further distinction (Xu *et al.*, 1996).

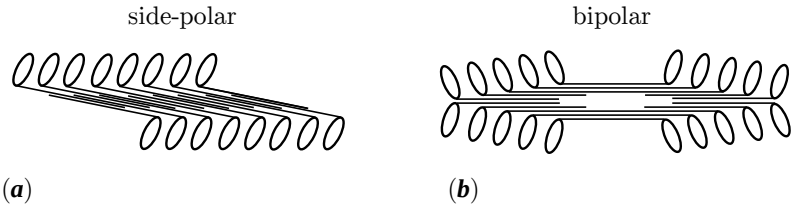

Figure 1.4: Schematic comparison of (***a***) side-polar myosin filaments of smooth muscles and (***b***) bipolar myosin filaments of striated muscles. Schematic adapted from Xu *et al.* (1996).

1.1.2 Muscle contraction and force production

Based on the pioneering investigations of the two research groups of Huxley & Niedergerke (1954) and Huxley & Hanson (1954), the generally accepted mechanisms of

active force production in sarcomeres are the sliding filament- (Huxley & Niedergerke, 1954; Huxley & Hanson, 1954) and the later proposed cross-bridge theory (Huxley, 1957a). Briefly, while actin and myosin filaments slide past each other during muscle length changes (sliding filament theory), active muscle force is generated by cross-bridges, which are formed by myosin heads that attach cyclically to the actin filaments and pull the filaments relative to each other (cross-bridge theory).

Comparision with smooth musculature — Force production

Irrespective of distinct differences in structural and functional determinants of smooth compared to skeletal muscles, the underlying force-producing mechanisms (cross-bridge and sliding filament theory) have proved to be similar, although they are much more thoroughly understood in smooth muscles (Arner & Malmqvist, 1998; Gordon & Siegman, 1971; Siegman *et al.*, 2013). Anyway, smooth muscle tissue exhibits some distinct differences in its contractile behaviour. Observations by Warshaw *et al.* (1987) of isolated fibres revealed marked cellular twisting (corkscrew-like) during active shortening, suggesting a helically oriented alignment of the contractile apparatus. During relaxation, smooth muscle fibres rotate in the opposite direction.

Moreover, during the last years a major development in the field of smooth muscle physiology took place. It has been recognised that certain smooth muscles (e.g. airway and bladder) undergo plastic adaptations to chronic shortening or lengthening (Wang *et al.*, 2001; Martinez-Lemus *et al.*, 2004; Seow, 2005). These length adaptations result in a shift of passive and active force – length relationships (or the optimum muscle length (L_0)) in dependence of the length at which the muscle has been adpated (Wang *et al.*, 2001). Hence, the ability of smooth musculature to generate the same maximum isometric force (F_{im}) over a wide range of lengths differs significantly from the ability of force production in striated muscles (cf. section 1.1.2.1 *'Force – length relationship'*). This distinct behaviour of smooth muscle-specific length adaptations is attributed to a plastic rearrangement of contractile and other cytoskeletal filaments (Kuo *et al.*, 2003;

Seow, 2005; Herrera *et al.*, 2005; Van Den Akker *et al.*, 2010; Stålhand & Holzapfel, 2016) — resulting in an extension of the working range of smooth musculature (Seow, 2005) (cf. section 1.1.2.1 *'Comparision with smooth musculature — FLR'*).

1.1.2.1 Force – length relationship

Nearly a century ago, based on investigations on striated skeletal muscles by Blix (1891) and Ramsey & Street (1940), (*i*) the length dependency of muscle force — one of the main determinants of active muscle force production — could be described for the first time (Figure 1.5). Briefly, up to a certain extent the active isometric muscle force firstly rises linearly with muscle length, and decreases linearly again above the optimum length.

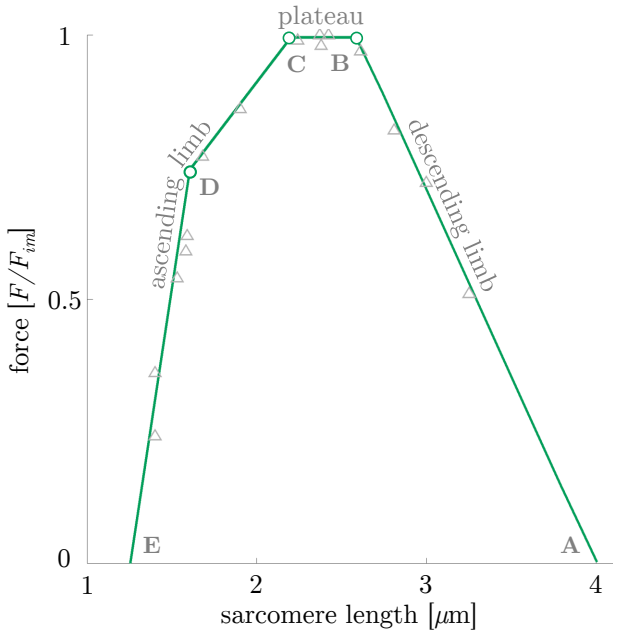

Figure 1.5: Representative sarcomere length dependence of active isometric force in maximally Ca^{2+}-activated mammalian skeletal muscle fibres — illustrated by a fast single skinned fibre of a rat EDL muscle ($n = 1$). The active isometric FLR can be directly explained with actin and myosin filament overlap. Qualitative changes in myofilament overlap lead to slope changes of the FLR (indicated with open circles at lengths B, C, D). Specifically, the linear ascending limb consists of a characteristic slope change with a shallow and steep part; the plateau region corresponds to the optimum fibre length at which the maximum number of cross-bridges can be formed; and the linear descending limb is characterised by the number of effective cross-bridges that decrease with a reduction in filament overlap. Triangles indicate active isometric fibre forces.

However, the functioning of skeletal musculature remained unclear at this time. Gordon *et al.* (1966) validated an entire isometric force – length relationship (FLR) by careful investigation of frog muscle fibre force at different lengths. Furthermore, he suggested a geometrical model explaining the experimental FLR partly by actin and myosin overlap. Specifically, the FLR exhibits a linear ascending limb, a plateau region, and a linear descending limb (cf. Figure 1.5).

These findings provided an insight into force-generating mechanisms yielding to a generally accepted understanding of muscle structure and functioning. However, the geometrical model approach by Gordon *et al.* (1966) does not fully explain the FLR. To describe the ascending limb of the FLR, further, as yet unverified assumptions (as e.g. myosin compression at lengths $< 1.6\,\mu$m; cf. Figure 1.5 (range below D)), are required. Additionally, there is considerable experimental evidence which demonstrate significant muscle forces at short fibre lengths (cf. Figure 1.5 (range left of E)) (Ramsey & Street, 1940; Schoenberg & Podolsky, 1972; Sugi & Ohta, 1983; Lopez *et al.*, 1981; Rüdel & Taylor, 1970, 1971). Even though without any explanatory approaches so far, these findings are in strong contrast to classic assumptions of force generation at muscle lengths $< 1.6\,\mu$m (Gordon *et al.*, 1966; Trombitas & Tigyi-Sebes, 1985; MacIntosh *et al.*, 2006). **Thus, a structurally based understanding of the FLR — in particular of the steep part of the ascending limb — is pending.** Hence, this specific issue will be addressed in the study presented in **Chapter 5** (Figure 1.1).

Comparision with smooth musculature — FLR

The shape of the isometric force – length relationship of smooth muscles is generally similar to that of striated skeletal muscles (Gordon *et al.*, 1966; Herlihy & Murphy, 1973). In contrast to the typical change in slope at the ascending limb of skeletal muscles (Figure 1.5), the ascending limb of smooth musculature is astonishing linear. The absence of this typical slope change might be partially explained by the side-polar myosin filaments in smooth muscles (Herrera *et al.*, 2005) compared to bipolar myosin

filaments in striated muscles (cf. Figure 1.4) (Craig & Megerman, 1977). The side-polar filaments have myosin heads with single polarity along the entire filament length and the opposite polarity along the other side (Craig & Megerman, 1977). These myosin filaments are assumed to be as long as the distance between the dense bodies in a contractile unit of smooth muscles and they are supposed to overlap the actin filaments completely. Therefore, upon shortening of the contractile unit the filament overlap will decrease in a linear manner in dependence of contractile unit length (Herrera *et al.*, 2005). In addition, smooth muscles can both, shorten and stretch, to a greater extent than striated skeletal muscles, which allows hollow organs to operate properly (Tortora & Nielsen, 2013; Siegman *et al.*, 2013) (cf. section 1.1.2 *'Comparision with smooth musculature — Force production'*). **However, there is a limited knowledge about the shape and the microstructural understanding of the entire FLR of stomach smooth muscles, as well as of specific, biomechanical parameters required for modelling, so far** (Siegman *et al.*, 2013). Therefore, these specific issues will be addressed in the study presented in **Chapter 3** (Figure 1.1).

1.1.2.2 Force – velocity relationship

In addition to (*i*) the force – length dependency — describing the overlap of actin and myosin filaments — (*ii*) the contraction velocity is the second main determinant of active force production in muscles (Figure 1.6). The concentric (shortening contractions) part of the force – velocity relation (FVR) has been first observed and described mathematically by Hill (1938). The FVR describes the relation between the maximum muscle force and its instantaneous rate of change in length (Nigg & Herzog, 2007). Briefly, if a muscle shortens during contraction, the shortening velocity depends on the load, while the contraction velocity decreases with increasing load in a hyperbolic manner (Hill, 1938). To the contrary, the ability to exert force is much less at fast velocities compared to slow shortening velocities. Moreover, while the concentric FVR describes how the maximum force produced by a single muscle (fibre) during muscle shortening is

inversely proportional to the contraction velocity, the FVR during muscle lengthening is the reverse process. The ability to exert high forces during lengthening contractions is much less at slow velocities compared to fast eccentric velocities (cf. Figure 1.6).

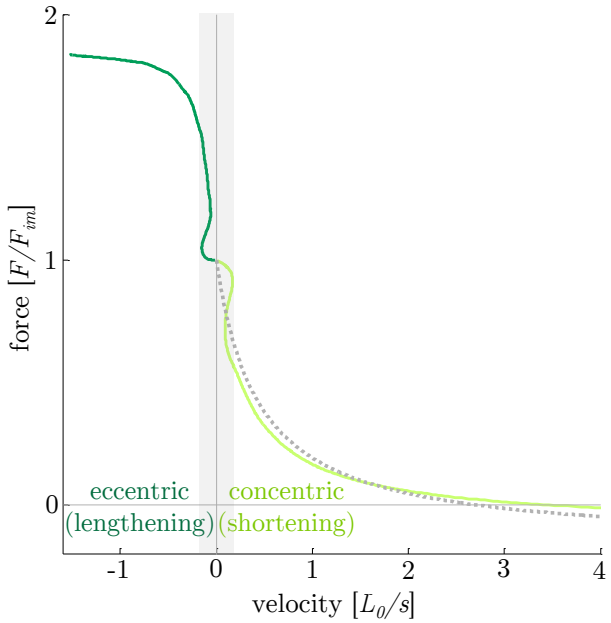

Figure 1.6: Representative sarcomere force – velocity relationship (FVR) — illustrated by a maximally Ca^{2+}-activated fast single skinned fibre (L = 0.54 mm) of a rat EDL muscle ($n = 1$). The experiments are conducted at a constant temperature of 12 °C. The force – velocity properties are determined by means of force ramp pertubations (FR method; a constant change in force over time) at $\pm 2.5\, F_{im}$/s in accordance to Iwamoto *et al.* (1990) and Lin & Nichols (2003). The initial fibre lengths and the length change limits for concentric and eccentric trials are chosen to limit sarcomere length (L_S) between 2.4 and 2.8 μm, which is near or on the plateau region of the FLR (at which the maximum isometric force (F_{im}) remained high and essentially constant) in skinned EDL muscle fibres from rats (Stephenson & Williams, 1982). The FR method allows to measure both, the concentric (bright green line) and eccentric (dark green line) FVRs within the same fibre in only two activations. The FVR is constructed by deriving velocities from lengths and plotting them against the imposed forces. The gray dotted curve shows the typical hyperbolic shape of the concentric FVR observed by Hill (1938). Note, that the FR approach differs from those measured with isotonic methods (cf. section 3.2.1) in two respects: 1.) a velocity offset in the FVR (see shaded rectangle) occurs due to short-range stiffness (Morgan, 1977) or in-series elastic-like response (Iwamoto *et al.*, 1990; Lin & Nichols, 2003; Gollapudi & Lin, 2013); 2.) the force – velocity properties as maximum shortening velocity (v_{max}) and curvature factor ($curv$) might slighty differ from those obtained using the isotonic method (Ranatunga, 1984; Iwamoto *et al.*, 1990; Lin & Nichols, 2003). However, for robustly estimation of model parameters over the entire range of physiological forces and velocities, the advantages of the FR method outweigh this disadvantages (Lin & Nichols, 2003; Roots *et al.*, 2007).

Hence, to produce high levels of force the muscle is required to lengthen quickly. In case of eccentric contractions, Katz (1939) found that the force produced by an active muscle during rapid lengthening was about $1.8 \times F_{im}$. Based on classic Hill-type model approaches (Hill, 1938; Haeufle *et al.*, 2014), it has been assumed that cross-bridges (formed by actomyosin interaction) are the only force-generating components in muscles. However, recent studies show that there is an additional parallel 'non-cross-bridge' component (as e.g. titin) contributing to the total force response (Pinniger *et al.*, 2006; Till *et al.*, 2008; Rode *et al.*, 2009; Schappacher-Tilp *et al.*, 2015). Consequently, both cross-bridge and non-cross-bridge components are involved in eccentric contractions. **Anyhow, the proportion of their contributions is not yet clear.** Hence, this specific issue will be addressed in the study presented in **Chapter 4** (Figure 1.1).

Comparision with smooth musculature — FVR

The concentric force – velocity relationship of smooth muscle tissue features the typical hyperbolic shape similar to skeletal muscles (cf. Figure 1.6, grey dotted curve). Anyway, the contraction behaviour in smooth muscles is more slowly and lasts much longer (Warshaw, 1987). Maximum shortening velocities of smooth musculature are one to two orders of magnitude smaller compared to skeletal muscles (Barany, 1967). Active, species-specific muscle properies are required for the development and evaluation of realistic whole organ computer models. These models can be used in biomechanics and medicine to simulate and to evaluate the mechanical and contractile behaviour of whole internal organs. Hence, 3D computer models are essential to understand the overall function of hollow organs in health and disease (e.g. bladder: Seydewitz *et al.* (2017) and arteries: Böl *et al.* (2012); Böl & Schmitz (2013); Schmitz & Böl (2011)). Therefore, the need for realistic, experimental input data with regards to electrical-, chemical- and biomechanical properties becomes more and more important (Röhrle *et al.*, 2016; Heidlauf *et al.*, 2016, 2017; Böl *et al.*, 2011b,a, 2015).

In particular the stomach — as a central musculomembranous hollow organ and part of the gastrointestinal tract of vertebrates — is of special interest. It has multiple sophisticated and autonomous functions including digestion, storage, mixing, absorption, excretion, protection, and subsequently, the controlled delivery of ingested food to the small intestine (Cheng *et al.*, 2010; Zhao *et al.*, 2008). Hence, the stomach is functionally subjected to a larger degree, compared to other parts of the gastrointestinal tract, to considerable mechanical deformations (Schulze-Delrieu *et al.*, 1998). Although a variety of gastrointestinal dysfunctions and diseases such as pyloric stenosis (Hernanz-Schulman, 2003) and tachygastria (Telander *et al.*, 1978), pathophysiological abnormalities as e.g. vomiting (emesis) and pylorospasm (Horn, 2008) or chronic tissue alterations in response to gastrointestinal obstruction or strain (Zhao *et al.*, 2010), are recognised, most of there etiologies remain unknown. A basic prerequisite in order to identify the causes of disease is the specific understanding of how the healthy stomach works. This requires the determination of characteristic biomechanical and physiological properties, which in turn are difficult to determine for humans — as studies on intact human gastric muscle tissue are hardly possible. Therefore, the examination of stomachs from the pig is of special importance due to the structural and mechanical similarity to the human stomach (Jia *et al.*, 2015; Zhao *et al.*, 2008). Although, **mechanical and contractile investigations of the stomach — especially of the FVR of porcine stomachs — are scarce compared to those of other organs**. Therefore, the study in **Chapter 3** addresses these distinct issues and aims to resolve open questions (Figure 1.1).

1.1.2.3 History-dependence of muscle force production

Since more than 60 years it has been known that skeletal muscle force depends on so-called history-effects, namely residual force depression (RFD) following active muscle shortening and residual force enhancement (RFE) following active muscle stretch, compared with the corresponding isometric reference contraction (Abbott & Aubert, 1952) (Figure 1.7). RFE and RFD have been investigated in whole muscle

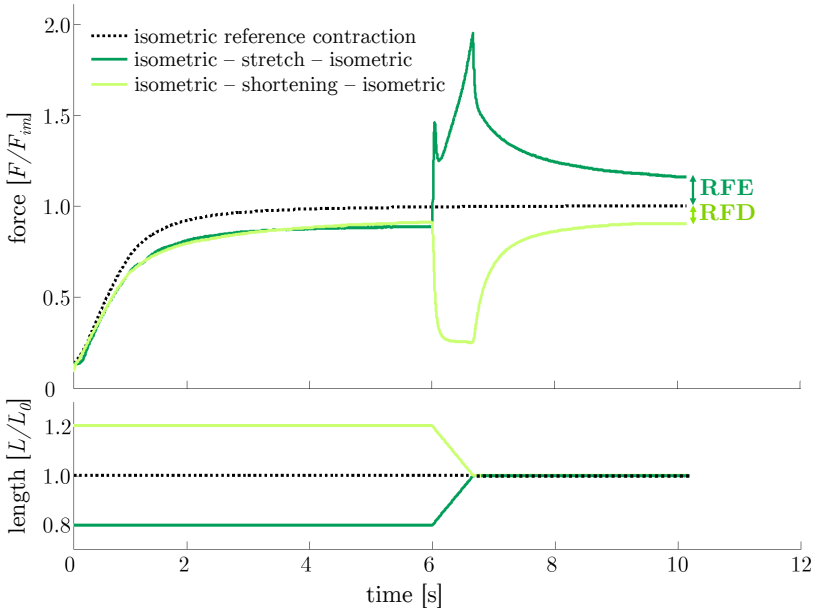

Figure 1.7: Representative force – time (upper graph) and length – time trace (lower graph) gathered by length controlled contractions of a single skinned EDL muscle fibre ($n = 1$). The fibre is maximally Ca^{2+}-activated (pCa = 4.5) at t = 0 s for 10 s. The black dotted line is the isometric reference contraction at optimum fibre length (1.0 L_0). To investigate history-dependent effects a concentric (bright green line), and an eccentric (dark green line) contraction from 1.2 and 0.8 L_0, respectively, back to 1.0 L_0, are applied. The force is enhanced after active stretch (RFE), and depressed after active shortening (RFD), compared to the isometric force, respectively. The contraction velocity in both experimental conditions is 0.3 L_0/s.

preparations (Abbott & Aubert, 1952; Siebert *et al.*, 2015), muscle fibres (RFD: Edman (1975); RFE: Edman & Tsuchiya (1996); Edman *et al.* (1982)) and in myofibrils (RFD: Joumaa & Herzog (2010); RFE: Joumaa *et al.* (2008)). RFE-effects (max. 200% F_{im} (Leonard & Herzog, 2010)) are about one order of magnitude larger than RFD-effects (5–20% F_{im} (Abbott & Aubert, 1952; Herzog & Leonard, 1997)). Although maximum RFE measured under physiological conditions (Rassier, 2017; Herzog *et al.*, 2016) as well as underlying mechanisms and functions of investigated history-dependence remain a matter of intense scientific debate, (*iii*) history-effects are a well acknowledged and generally accepted property — and the third main determinant of active force

production — of skeletal muscles (Rassier, 2017; Herzog *et al.*, 2016; Siebert *et al.*, 2015; Campbell & Campbell, 2011; Edman, 2010; Rode *et al.*, 2009).

Comparision with smooth musculature — History-dependence

Irrespective of the intense investigation of history-dependent effects in skeletal musculature for decades, **history-effects are nearly unconsidered in smooth musculature so far**. This is remarkable, as smooth muscles often perform huge length changes as e.g. bladder smooth muscle during micturition, which might be associated with history-effects. However, only a couple of studies reported RFD and RFE in smooth muscles tissue (urinary bladder: Menzel *et al.* (2017); Minekus & van Mastrigt (2001); van Asselt *et al.* (2007), and trachea: Gunst (1986)). These findings suggest an distinctive muscle behaviour during the concentric and eccentric working phase of gastric musculature, which is not accounted for in existing smooth muscle models so far. RFE-effects (around 12% F_{im} (Menzel *et al.*, 2017)) are in the range of RFD-effects in smooth- (12–18% F_{im} (Menzel *et al.*, 2017; Gunst, 1986)) and skeletal muscles (5–20% F_{im} (Abbott & Aubert, 1952; Herzog & Leonard, 1997)), respectively. Additionally, RFE-effects in smooth muscles are about one order of magnitude smaller than RFE-effects in skeletal musculature (max. 200% F_{im} (Leonard & Herzog, 2010)). **Anyway, there is no research investigating RFE and RFD in the porcine stomach so far. Therefore, a structurally and physiologically based understanding of the influence of history-effects on gastric smooth muscle force in pigs — including accurate input data required for realistic stomach modelling — is pending.** Hence, these open issues will be addressed in the study presented in **Chapter 3** (Figure 1.1).

1.1.3 Considerations about sliding filament and cross-bridge theories

Although extensive experimental research has been done on isolated skeletal muscles since over 100 years (Blix, 1891), underlying force-generating mechanisms are not

fully understood at this time. Even the generally accepted and groundbreaking Hill-type (Hill, 1938) or Huxley-type (Huxley, 1957b) models are not capable to describe history-dependent effects. Especially since the causes of RFE and RFD lie in the phase of length change (movement phase) (Siebert *et al.*, 2008; Kosterina *et al.*, 2013; Siebert *et al.*, 2015). Although RFE and RFD experiments have no everyday significance, the sequence of eccentric- followed by concentric muscle actions — combined in stretch-shortening cycles (SSC) — plays a major role in natural locomotion and represents an essential part of fundamental movement patterns such as walking, running or jumping (Komi, 2000). SSCs are thought to provoke a performance enhancement of the whole musculoskeletal system and even on the muscle fibre level in isolated muscle preparations (without a series elastic component such as the tendon and aponeurosis). A key feature is that the muscular strength, work and performance during the concentric phase of an SSC can be increased by up to 50% compared to purely concentric muscle actions without previous eccentric stretching. Furthermore, this performance enhancement is associated with increased efficiency (Cavagna *et al.*, 1968; Seiberl *et al.*, 2015). However, mechanisms of this enhanced performance remain a matter of debate. So far, there is no computational model capable to explain such phenomenon. **Thus, there is a huge significance of the implementation of RFE and RFD experiments in movement simulations — requireing a structural understanding and precise model parameters (under reduced boundary conditions) of underlying mechanisms. Hence, the need for experimental input data of activated muscle fibres in extensive stretch/shortening contractions becomes increasingly important and derives from the magnitude of such effects** (**Chapter 4**) (Figure 1.1).

To account for history-dependence in skeletal muscles (and even in smooth musculature), modifications of existing cross-bridge models are required (Rode *et al.*, 2009; Nishikawa *et al.*, 2012; Schappacher-Tilp *et al.*, 2015; Heidlauf *et al.*, 2016, 2017). Despite a number of explanatory approaches for RFD and RFE, there is still a scientific

debate about the causes of these history-effects and no generally accepted model existing (Nigg & Herzog, 2007; Edman, 2010; Campbell & Campbell, 2011; Siebert *et al.*, 2014b). Discussed mechanisms are e.g. modified cross-bridge kinetics (Maréchal & Plaghki, 1979; Walcott & Herzog, 2008), the contribution of sarcomere chain dynamics (Edman *et al.*, 1982; Edman, 2010; Morgan *et al.*, 1982; Telley *et al.*, 2006; Campbell & Campbell, 2011), or non-cross-bridge contributions to muscle force (Rode *et al.*, 2009; Leonard & Herzog, 2010; Till *et al.*, 2010). The proposed modifications of the cross-bridge cycle have not yet been confirmed experimentally (Mehta & Herzog, 2008). Moreover, only a fraction of the experimentally observed dynamics ($0.05\,F_{im}$ Morgan *et al.* (2000); Campbell & Campbell (2011)) can be described by sarcomere length inhomogeneities. Other authors prefer explanatory approaches in which titin — a semi-active, non-cross-bridge structure in striated muscles — has a crucial role in the generation of RFE and RFD (Noble, 1992; Pinniger *et al.*, 2006; Roots *et al.*, 2007; Rode *et al.*, 2009; Nishikawa *et al.*, 2012; Schappacher-Tilp *et al.*, 2015; DuVall *et al.*, 2017). This three filament model of skeletal muscle force production is supposed to overcome significant deviations between experimental observations and predictions by the sliding filament and cross-bridge theories (Rode *et al.*, 2009; Nishikawa *et al.*, 2012; Schappacher-Tilp *et al.*, 2015; Herzog *et al.*, 2016; Heidlauf *et al.*, 2017).

1.1.3.1 Force production in concentric and eccentric contractions

Albeit history-dependent effects are typically investigated under isometric conditions (following active muscle lengthening / shortening), it is plausible to investigate such effects under dynamic conditions (Siebert *et al.*, 2008; Kosterina *et al.*, 2013; Siebert *et al.*, 2015) — due to the physiological non-steady state behaviour of muscles. Despite the wide variety of applications of muscle models in life sciences such as medicine, physiology and biomechanics, **many experimental findings are conflicting with the predictions based on the classic sliding filament and cross-bridge theories.** This leads to substantial uncertainties regarding the validity of the conclusions derived

from these models. Specifically, compared to experimentally observed progressive forces in eccentric contractions, classic muscle models predict that varying myofilament overlap will lead to increases and decreases in active force during eccentric contractions. Non-cross-bridge contributions (such as titin) potentially explain the progressive total forces.

The study presented in **Chapter 4** addresses these issues and attempts to clarify **whether underlying abrupt changes in the slope of the nonlinear force – length relationship are visible in long isokinetic stretches** — applied to single skinned skeletal muscle fibres — **and in which proportion cross-bridges and non-cross-bridges contribute to total muscle force** (Figure 1.1)**.**

Comparision with smooth musculature — Limitations of Force production in isokinetic contractions

Despite distinct differences in the ultrastructure and functioning of smooth compared to skeletal muscle tissue (refer to section 1.1.2 *'Muscle contraction and force production'*), the underlying force-producing mechanisms are similar, although much less understood in smooth musculature. Therefore, a transfer of currently discussed various mechanisms, that provide some possible explanations with regards to history-dependent effects in skeletal muscles, is appropriate (Heidlauf *et al.*, 2016, 2017; Nishikawa *et al.*, 2012; Rode *et al.*, 2009). While the structural protein titin does only exist in striated muscles, the molecule smitin — with similar functional and structural characteristics as titin — occurs in smooth muscles (Kim & Keller, 2002). **Anyhow, a conclusive understanding of underlying titin-actin mechanisms in striated muscles (or of potential smitin-actin interactions in smooth muscles), is still lacking and remains highly speculative** (Menzel *et al.*, 2017; Shalabi *et al.*, 2017; Siebert *et al.*, 2014b). Alternatively, it has been hypothesised that classic cross-bridge dynamics may be modified during eccentric contractions in skeletal muscles (Walcott & Herzog, 2008). Similar behaviour has been experimentally described for smooth muscles by Dillon *et al.*

(1981) and Arner & Malmqvist (1998), whereby cross-bridges enter the so-called 'latch state'. The rate of detachment in this state might depend on the strain of cross-bridges. Thus, to cover prevailing mechanical conditions, high loads lead to prolonged binding of cross-bridges, and low loads accelerate cross-bridge release (Huxley & Simmons, 1971; Veigel *et al.*, 2003). This dynamic modification of contractile properties in smooth muscle tissue might lead to shifts of contractile phenotypes ('slow' to 'fast' and vice versa) following small length-changes or hormonal adaptations (Arner & Malmqvist, 1998). However, the dynamic shifts of the contractile properties seem to require several days (Arner & Malmqvist, 1998), and the 'stuck cross-bridge' idea could not be validated in experiments, neither on skeletal muscles (Mehta & Herzog, 2008) nor on smooth muscles (Butler *et al.*, 1983).

Hence, the study presented in **Chapter 3** is intended to investigate the **force-dependence on history-effects in smooth gastric muscle tissue, which remained almost unnoticed so far**. To address the issues previously described we **re-evaluated existing contractile mechanisms to facilitate novel insights into gastric motility and contraction behaviour** (Figure 1.1).

1.1.3.2 Force production at short sarcomere lengths

In this section, past and recent experimental evidence is reported which raised serious doubts about the classic sliding filament and cross-bridge theories of muscle contraction. The active isometric force – length relationship can be directly explained with actin and myosin filament overlap, while qualitative changes in overlap lead to distinct slope changes of the FLR — experimentally observed on the isolated muscle fibre- (Gordon *et al.*, 1966) as well as on the whole muscle level (Rode & Siebert, 2009; Winters *et al.*, 2011; Siebert *et al.*, 2015). The slope change on the ascending limb of the FLR is explained with the compression or folding of the myosin filament on the Z-disc during striated muscle fibre contraction — accompanied with a potentially reduced number of available cross-bridges (Gordon *et al.*, 1966; Trombitas & Tigyi-Sebes,

1985; MacIntosh *et al.*, 2006). **However, there are numerous contradictory experimental evidence of muscle force development at short fibre lengths with prolonged stimulus duration that conflicts with the classic explanatory approaches** (Ramsey & Street, 1940; Schoenberg & Podolsky, 1972; Sugi & Ohta, 1983; Lopez *et al.*, 1981; Rüdel & Taylor, 1970, 1971)**.**

Hence, the theoretical study presented in **Chapter 5** aims to re-evaluate classic textbook assumptions by presenting a **structurally consistent model of sarcomere contraction, that reconciles these findings with the well-accepted sliding filament and cross-bridge theories.** These theoretical considerations are supported by experiments with permeabilised fibres of the rat EDL muscle (Figure 1.1).

1.1.4 Three-dimensional muscle architecture

Finally, to obtain a more complete picture of muscular contraction dynamics and functioning, a brief introduction to the relation between three-dimensional muscle architecture (Figure 1.8) and total muscle force production is given. Additionally to the

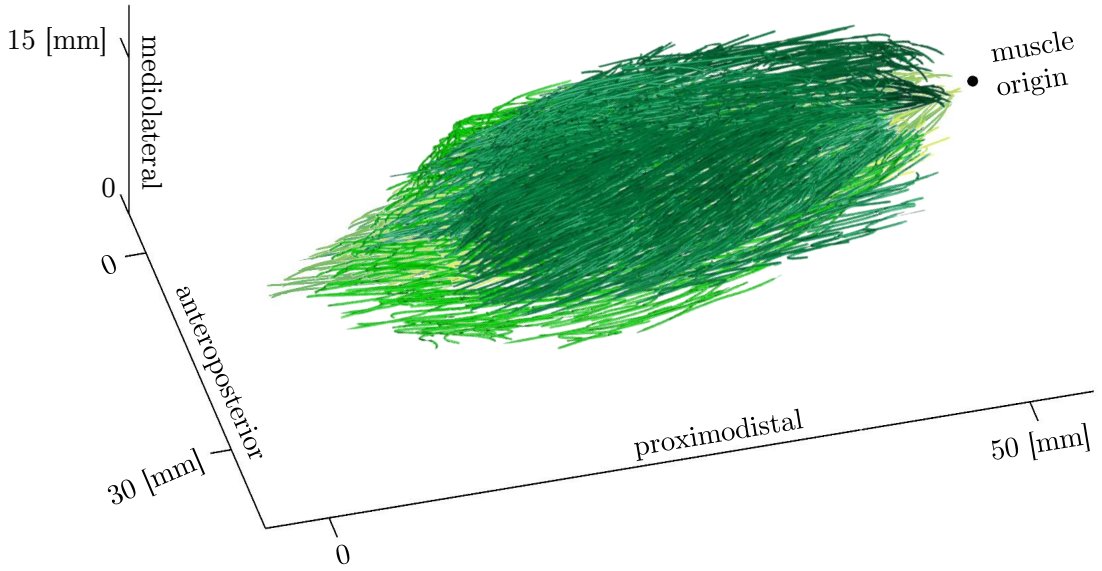

Figure 1.8: Representative picture of 3D fascicle architecture of *M. gastrocnemius medials* (bright green) and *M. gastrocnemius lateralis* (dark green) of rabbit left hind leg.

the contractile properties of active muscle force production on the microstructural level — as (*i*) FLR, (*ii*) FVR and (*iii*) history-dependent effects — (*iv*) the three-dimensional muscle architecture is a further crucial property influencing the total muscle force (cf. Figure 1.1). Skeletal muscles can differ considerably in architectural design such as fibre length and -type, pennation angle, and connective tissue organisation (Biewener, 2016). They appear in a diversity of sizes and shapes to cover prevailing conditions for realising a wide variety of complex tasks — including noisemaking, posture, endurance, ballistic movements, isometric 'lock' and thermogenesis (Lieber & Ward, 2011; Schaeffer & Lindstedt, 2013). These muscular functions must be covered over the entire lifespan. Therefore, the functionality of the muscles must be ensured despite changing boundary conditions (e.g. human being: increase in body size by a factor of 3–4 from birth, increase in body weight by a factor of 10–20). It is known that e.g. the muscle belly length of the *gastrocnemius medials* muscle in children changes from 5 years to 12 years by 47%, while body mass and tibia length increases by 3.5 kg and 1.8 cm per year, respectively, within this period (Bénard *et al.*, 2011).

While much is known about the muscle architecture at a particular age, **there is a limited knowledge about changes in muscle structure during growth (e.g. the muscle fascicle architecture and aponeurosis dimensions)**. The 3D muscle fibre architecture, on the one hand, is an important determinant of a muscle's mechanical function. Whereby changes in muscle shape represent a muscle gearing system to modulate muscle performance over a wide range of mechanical demands (Azizi *et al.*, 2008). The aponeurosis, on the other hand, is a crucial, functional component in terms of load transmission and energy storage in skeletal muscles (Böl *et al.*, 2016; Azizi & Roberts, 2009; Epstein *et al.*, 2006).

Hence, the study in **Chapter 6** is aimed to analyse **growth-related changes in the muscle structure** of rabbit *gastrocnemius lateralis*, *gastrocnemius medialis*, *flexor digitorum longus*, and *tibialis anterior*, **to facilitate new insights regarding changes in three-dimensional muscle architecture and aponeurosis shape** (Figure 1.1).

Chapter 2

Description of Experimental Setups

2.1 Determination of *smooth* muscle tissue properties

2.1.1 Preparation and handling

For the biomechanical characterisation of smooth muscle tissue — as illustrated in **Chapter 3** — stomachs from 41 freshly killed female pigs (age: ∼ 6 months, weight: ∼ 100 kg) from a local slaughterhouse were used. Porcine stomachs were chosen for this study due to their structural and mechanical similarity to the human stomach (Jia *et al.*, 2015; Zhao *et al.*, 2008).

Immediately after death a predefined piece of smooth gastric tissue (30 × 20 mm) was dissected from the ventral fundus of the proximal stomach (Figure 2.1). Care was taken to prevent contact of the tissue sample with gastric acid to avoid smooth muscle degeneration. Afterwards, the preparation was preserved in an icebox in aerated (95% O_2 and 5% CO_2) Krebs solution (refer to section 2.1.2 *'Experimental setup'* for details) at a constant temperature of 4 °C for transportation. Subsequently, within 60–90 min postmortem, small tissue strips (0.66 ± 0.2 g) of

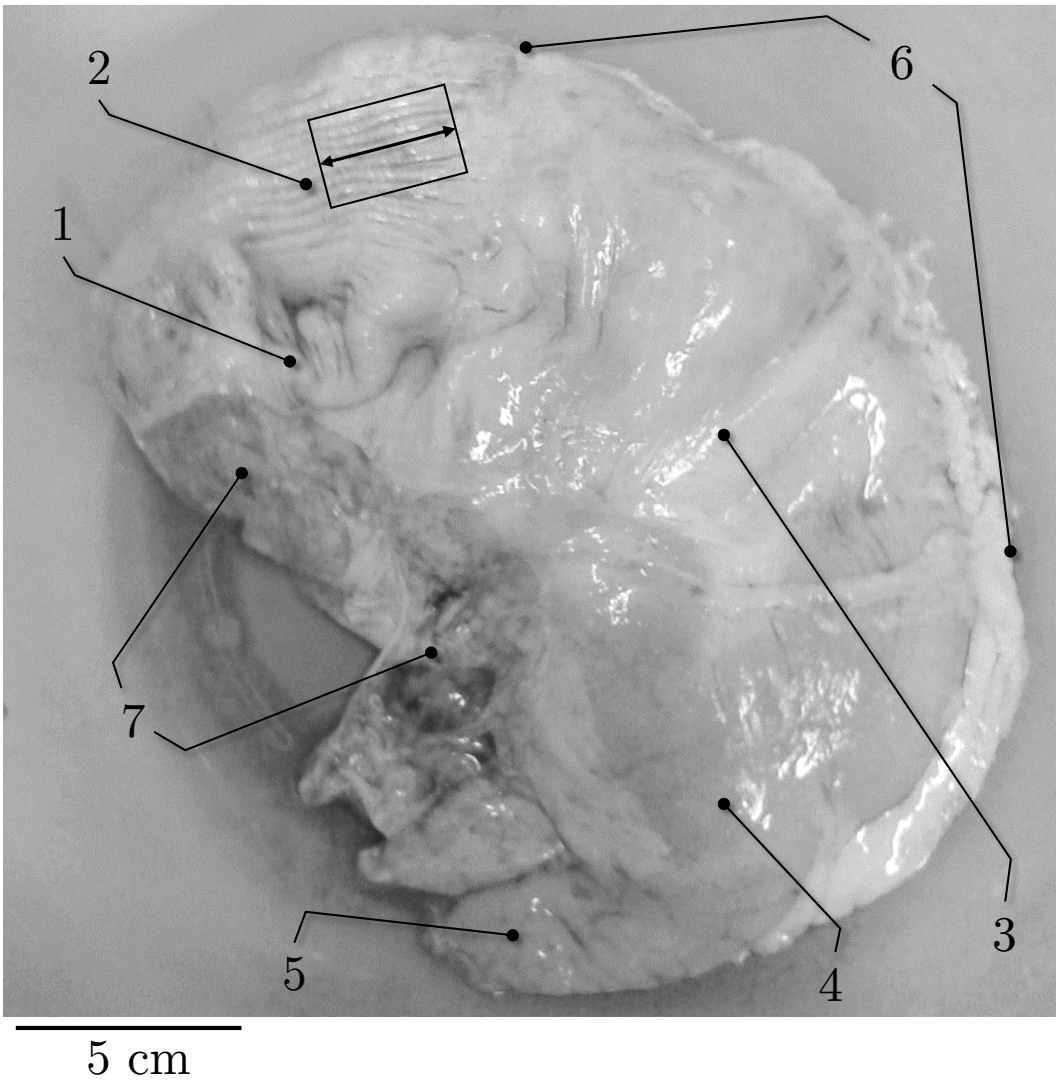

Figure 2.1: Representative picture of porcine stomach. Ventral view of external anatomy of a porcine stomach. (1) cardia, (2) fundus, (3) corpus, (4) antrum, (5) pylorus, (6) greater curvature, (7) smaller curvature. Black rectangle indicates longitudinal muscle strip dissected from the fundus. Longitudinal direction is marked by the black arrow.

16 × 8 mm in longitudinal orientation (i.e. parallel to the direction of the gastric serosal fold, parallel with the greater curvature; cf. Figure 2.1) were prepared in the laboratory from the predefined tissue sample of the fundus. The preparation and handling of smooth muscle tissue samples was carried out in a petridish filled with ice-cooled Krebs solution positioned on a customised, temperature-controlled stage, that kept the temperature constant at 4–6 °C (Figure 2.2). The dissected tissue strips were pinned (slightly

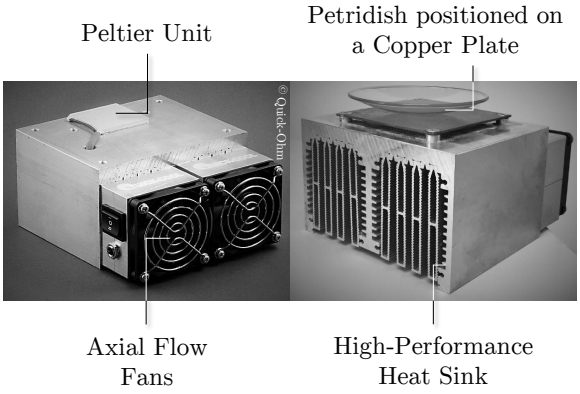

Figure 2.2: Temperature-controlled stage. A thermo-electric Peltier unit (Quick-Ohm, Wuppertal, Germany) mounted on a high-performance heat-sink — machined from a block of aluminum — is used to control the temperature of a petridish filled with certain solutions (i.e. Krebs or storage solution). The temperature of the stage is adjustable from -20 °C up to +120 °C via a stepless regulated 12V power supply unit.

stretched) at both ends — retaining the approximately *in vivo* length — down to a silicone elastomer surface (Adisil® glasklar 1 : 1, SILADENT Dr. Böhme & Schöps GmbH, Germany) of a petridish. Finally, the tissue strips were removed from the tunica mucosa by means of sharp scissors.

2.1.2 Experimental setup

The Aurora Scientific 1205A *in vitro* test apparatus (Figure 2.3) enables to study intact muscle tissue under physiological conditions — thereby quantifying biomechanical and contractile properties of isolated muscle tissue. The test system consists of a vertical

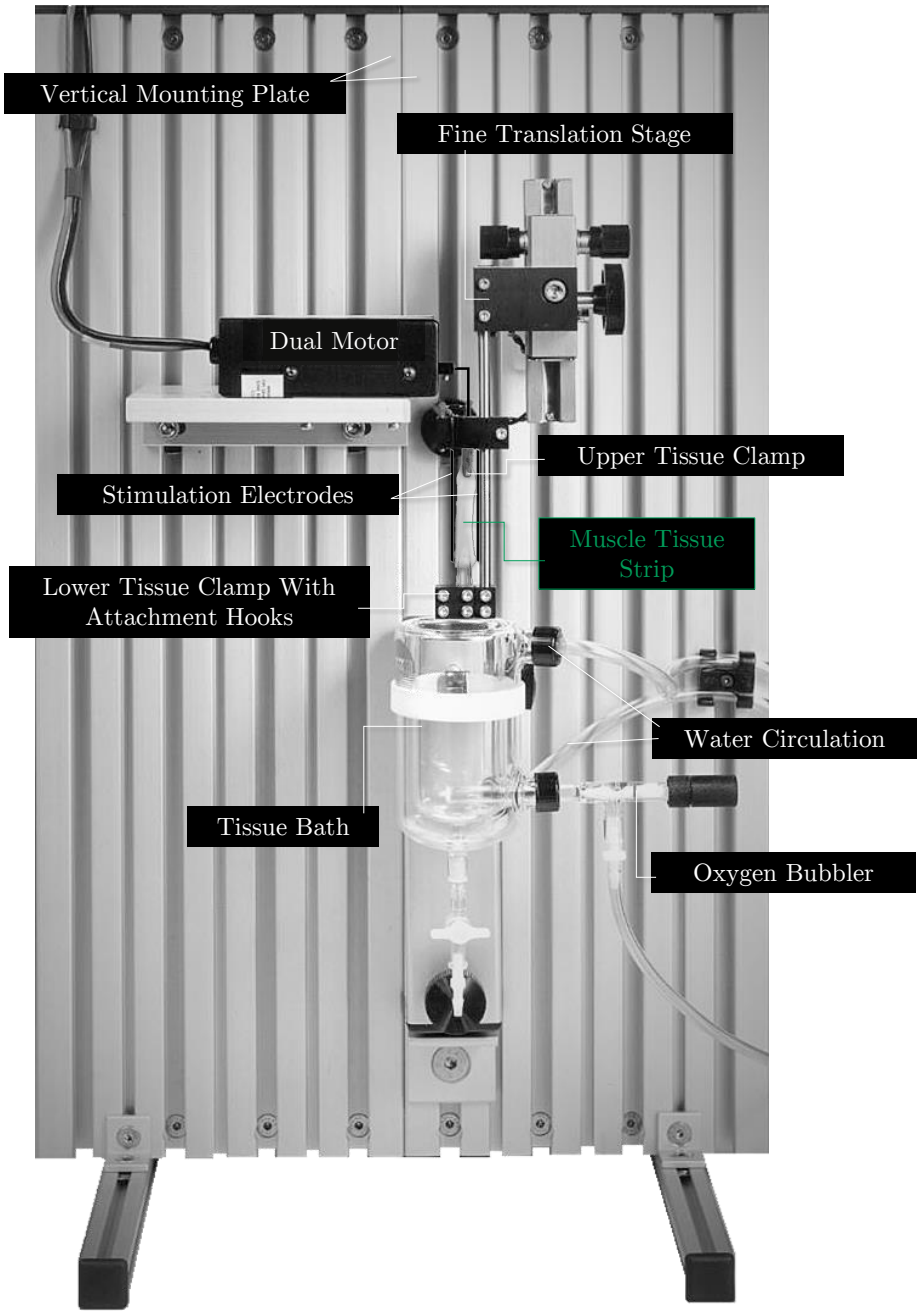

Figure 2.3: Annotated photo of an *in vitro* test apparatus for determination of smooth muscle properties. When attaching the muscle tissue strip (labeled by the green line), the tissue bath is in down position. Note, high-power field stimulator, data acquisition hardware and water circulating pump are not shown. Photo adaptated from ©Aurora Scientific Inc., Aurora, ON, Canada.

mounting plate, a dual motor, a tissue bath, an oxygen bubbler, a high-power field stimulator in conjunction with two platinum electrodes, an attachment unit for the tissue preparation, and a fine translation stage to adjust the position of the muscle tissue. The muscle test system is adjustable and allows to lower and raise the tissue bath to attach and manipulate the tissue sample. The isolated muscles tissue strip is vertically attached to two customised hooks (made from 29 G stainless steel hypodermic needles) at the bottom and an alligator clamp at the top (cf. Figure 2.3, the muscle tissue strip is labeled by the green line). The alligator clamp is connected to a motor/force transducer (Aurora Scientific 305C-LR dual-mode muscle lever system) using a surgical suture (Maprolen 2 × DRE 13, 5/0, Catgut GmbH, Germany). The position of the lever arm and the applied force are recorded by a signal interface (Aurora Scientific 604A) linked to a National Instruments PC-based A/D card. The stimulation and mechanical setup is software-controlled (Aurora Scientific 605A). The muscle tissue strip is stimulated transversally by alternating pulses (1 A, 100 Hz frequency, and 5 ms pulse width) via two parallel platinum electrodes (65 × 2 mm) (Menzel *et al.*, 2017; van Mastrigt & Glerum, 1985). Alternating voltage pulse patterns are generated by a high-power, bi-polar pulse stimulator (Aurora Scientific 701C). The tissue strip is surrounded by a cylindrical water-jacketed tissue bath (100 ml), filled with Krebs solution, which is continuously aerated by an oxygen bubbler. All mechanical experiments are conducted at a constant temperature of 32 °C ± 0.1 °C in aerated Krebs solution (124 mM NaCl, 5 mM KCl, 2.5 mM $CaCl_2$, 15 mM $NaHCO_3$, 1.2 mM KH_2PO_4, 1.2 mM $MgSO_4$, 10 mM $C_6H_{12}O_6$; pH 7.3 at 32 °C) (Moriya & Miyazaki, 1982). At this temperature, the tissue samples proved very stable and able to withstand active protocols over an extended period of time (Essig *et al.*, 1985). The temperature is kept constant by means of a water circulation system in combination with a circulating pump. The length of the suspended strip is 'set-up' in a relaxed state until a passive baseline force of 5–10 mN is reached. Afterwards, the length of the strip between clamp and attachment hooks is determined with a digital sliding caliper and is defined as slack length (L_{slack}). After an equilibration period of

30 min at L_{slack}, the strips are stimulated isometrically for about 15 s every 5 min until a steady state force (deviation $< 5\%$ of maximum isometric force (F_{im})) is reached (Herrera *et al.*, 2005).

Finally, the experimental setup is ready to **examine biomechanical characteristics of *smooth* muscle tissue** — as presented in **Chapter 3** — **illustrated by porcine stomachs** (Figure 1.1).

2.2 Determination of *skeletal* muscle fibre properties

2.2.1 Preparation and handling

The muscle fibres used for the studies illustrated in **Chapters 4** and **5** were obtained from EDL muscles from both hind limbs (in total 12 muscles from six rats) of freshly killed female Wistar rats (8–10 months, 300–350 g, cage-sedentary, 12 h : 12 h light : dark cycle, housing-temperature: 22 °C). The EDL is a predominantly fast skeletal muscle with a fibre type distribution of approximately 75% of type 2B fibres (Soukup *et al.*, 2002).

Four to six small fibre bundles (length: 10–20 mm, width: 2–4 mm) were immediately dissected from the medial region of each EDL muscle after animal sacrifice (Figure 2.4) under a stereomicroscope (Leica A60 F). For the mechanical experiments, the skinned muscle fibres were prepared according to the protocol of Goldmann & Simmons (1984).

Briefly, fibre bundles are permeabilised at 4 °C in a skinning solution (refer to Table 4.1 of **Chapter 4**, section 4.2.3 *'Solutions'*). Afterwards, the demembranated fibre bundles are pinned at both ends — at approximately *in vivo* sarcomere length — to a silicone elastomer surface (cf. Figure 2.4 (3)). Subsequently, the fibre bundles are stored at -20 °C in a storage solution (skinning solution made up in 50% glycerol) (Table 4.1) and used within six weeks. On the day of the experiments, small segments of the skinned fibre bundles are dissected and used to prepare several single muscle fibres (1.5–2 mm long) in a petridish filled with storage solution positioned on a customised temperature-controlled

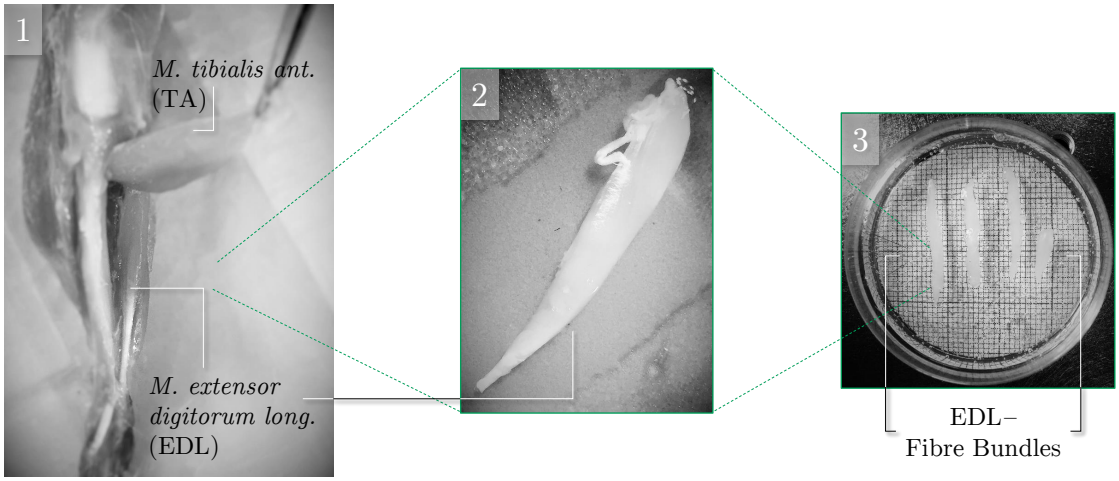

Figure 2.4: Skeletal muscle preparation. (1) Dissection and (2) subsequent isolation of *Musclus extensor digitorum longus* (EDL) of rat hind limbs. (3) Preparation of several muscle fibre bundles from the EDL in relaxing solution (refer to Table 4.1) at 4 °C on a temperature-controlled stage (Figure 2.2).

stage (Figure 2.2) at 4–6 °C. Thereafter, the fibre extremities are loosely clamped by aluminum foil 'T-clips' (Figure 2.5 (4); Institute of Applied Physics, Ultrafast Optics, Jena, Germany; Appendix A), in accordance to Ford *et al.* (1977). Afterwards, the fibres are treated with relaxing solution (Table 4.1) containing Triton X-100 (1% v/v) for 1–2 min at 4 °C to ensure complete removal of internal membranes without affecting the contractile apparatus (Linari *et al.*, 2007; Fryer *et al.*, 1995). The fibres are either used immediately or stored overnight at -20 °C in a storage solution.

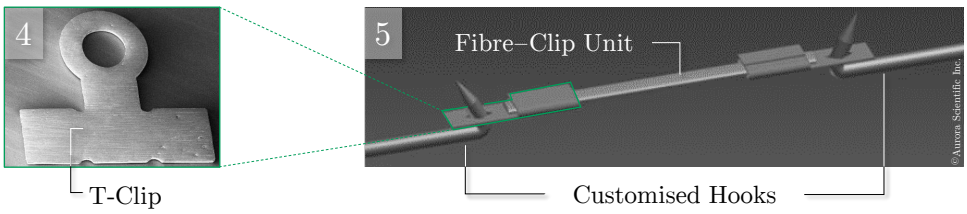

Figure 2.5: (4) The fibre ends are clamped by custom-made 'T-clips' (Institute of Applied Physics, Ultrafast Optics, Jena, Germany) — made from 2.5 μm thin aluminum foil. (5) Schematic of fibre – clip unit attached to the hooks of the force- and length transducer, respectively.

2.2.2 Experimental setup

For determination of single skeletal muscle fibre properties — as illustrated in **Chapters 4** and **5** — a permeabilised test system (Aurora Scientific 1400A) (Figure 2.6) is utilised.

Briefly, the transfer of the previously prepared fibre–clip unit to the experimental chamber is carried out in a small custom-made glass spoon or modified pipette tip. Thereupon, the fibre–clip unit (cf. Figure 2.5 (5)) is mounted in the test apparatus — positioned on the x-y moving stage of an inverted microscope (Nikon Eclipse Ti-S). The test apparatus consists of a temperature-controlled stage with seven wells (160 μl) and a single large chamber (200 μl) for multiple solutions, which are moved horizontally by a stepper motor. This large chamber is filled with a relaxing

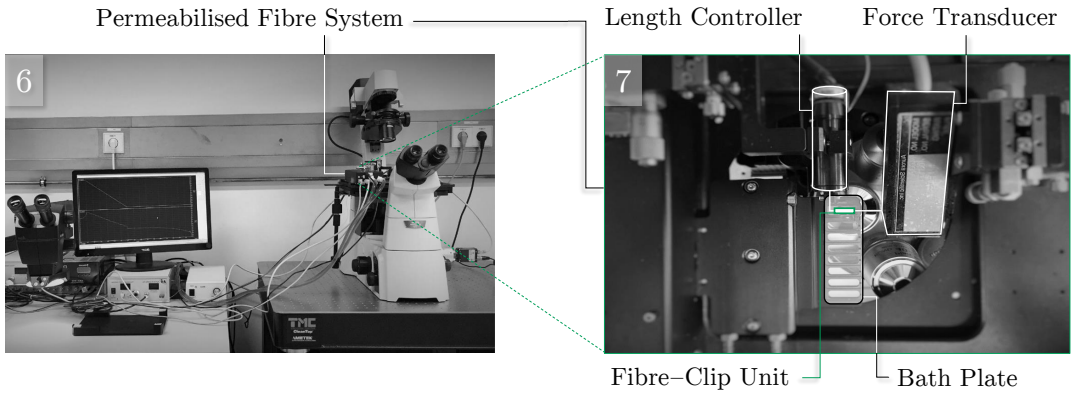

Figure 2.6: (6) Overview of experimental setup mounted on a vibration-isolated lab table (TMC-63-534). (7) Close-up of the permeabilised fibre test apparatus. The fibre–clip unit (marked by the green rectangle) is attached to a length/force transducer via two customised hooks made from 29 G hypodermic needle tubings.

solution (Table 4.1), and the clips are attached via customised hooks (made from 29 G hypodermic needle tubings) to a force transducer (Aurora Scientific 403a, force range: 5 mN, force resolution: 0.1 μN) and a high-speed length controller (Aurora Scientific 322 C-I, max. force: 100 mN, length signal resolution: 0.5 μm) (cf. Figure 2.6 (7)). The attachment unit of the hook and clip is free of clearance and rigid. This ensures optimal

horizontal alignment between the fibre and transducer lever. It also minimises movement of the fibre on the hook during transfer between solutions and during large, rapid length changes (Burton *et al.*, 2006) used in some of the experiments as represented in **Chapter 4**. The fibre ends are cross-linked (Figure 2.7) with a drop of 'fixative' solution

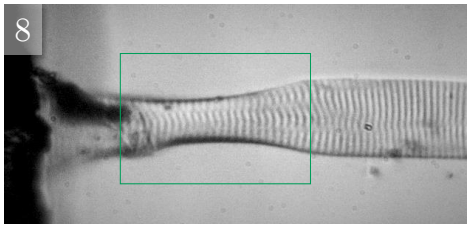

Figure 2.7: (8) Representative picture of a cross-linked muscle fibre end. Note the distinct shrinkage of the fixed fibre-part after successful fixation procedure (marked by the green rectangle). The photomicrograph is captured with a 10 × objective under bright-field illumination.

(rigor solution containing 8% (v/v) glutaraldehyde and 5% (w/v) toluidine blue) (Hilber & Galler, 1998). This minimises sarcomere length inhomogeneity and improves stability and mechanical performance by reducing fibre end compliance (Chase & Kushmerick, 1988). The fixation of the fibre extremities — under a stereomicroscope — is carried out by a silicon tube with an internal diameter of about 300 μm. Subsequently, the tip of the tube is submerged in the 'fixative' solution while the solution is sucked inside the tube by capillarity. Afterwards, the extremities of the fibre (just over the clip) are touched gently by the tip and become fixed. The fixation procedure is carried out while the fibre – clip unit is in air. The fixed fibre-part is determined by visualising the toluidine blue and the slight shrinkage thereof (Thirlwell *et al.*, 1994) (cf. Figure 2.7).

Afterwards, the fibre width (w) and height (h) are measured in approximately 0.1 mm intervals over the entire length with a 40 × ELWD dry-objective (NA 0.60, Nikon) and a 10 × eyepiece. For visualisation of the striation pattern and for accurate, dynamic tracking of L_S changes, a high-speed video system (Aurora Scientific, 901B) is used in combination with a 20 × ELWD dry-objective (NA 0.40, Nikon) and an accessory lens (2.5 ×, Nikon). Thereafter, the sarcomere

length L_S, measured in the central segment of the fibre (Figure 4.1*b*), was set to 2.5 ± 0.05 μm, which is the optimal sarcomere length (L_{S0}) for maximal isometric force (F_{im}) development in EDL muscle fibres (Stephenson & Williams, 1982). The corresponding fibre length was defined as the individual optimal fibre length (L_0).

Proper preparation of skeletal muscle tissue and setting-up individual single muscle fibres for activation are essential in order to address the specific issues illustrated in **Chapters 4** and **5** (Figure 1.1).

2.3 Determination of 3D muscle structure

2.3.1 Preparation and handling

For the architectural characterisation of 3D fascicles from skeletal muscles — as presented in **Chapter 6** — the *M. gastrocnemius (medialis & lateralis)*, *M. flexor digitorum longus* and *M. tibialis anterior* from freshly killed female rabbits (age: between 18 and 108 days) are used. Preparation techniques of rabbit muscles are in accordance to Böl *et al.* (2013). Briefly, immediately after animal sacrifice the hind legs are amputated above the knee. The skin is removed and the preparation is fixed in Bouin solution (an aqueous solution of picric acid, acetic acid and formaldehyde that minimises tissue shrinkage (Mulisch & Welsch, 2010; Schenk *et al.*, 2013)) for 72 h (Gorb & Fischer, 2000). The preparations are fixed at knee angles of about 88° and ankle angles of about 96° (refer to Table 6.1 of **Chapter 6** for details). Subsequently, the bone–muscle preparation is embedded in wax to provide additional mechanical stability during the digitising process (Figure 2.8 (2)).

2.3.2 Experimental setup

For the investigation of the complex 3D fascicle architecture from distinct skeletal muscles a manual digitiser (MicroScribe MLX, solution technologies, USA) — with a sampling frequency of 5 Hz and an accuracy of 0.07 mm — is used (Figure 2.9 (3)). For the digitisation of the whole muscle architecture of each muscle, small fascicle bundles

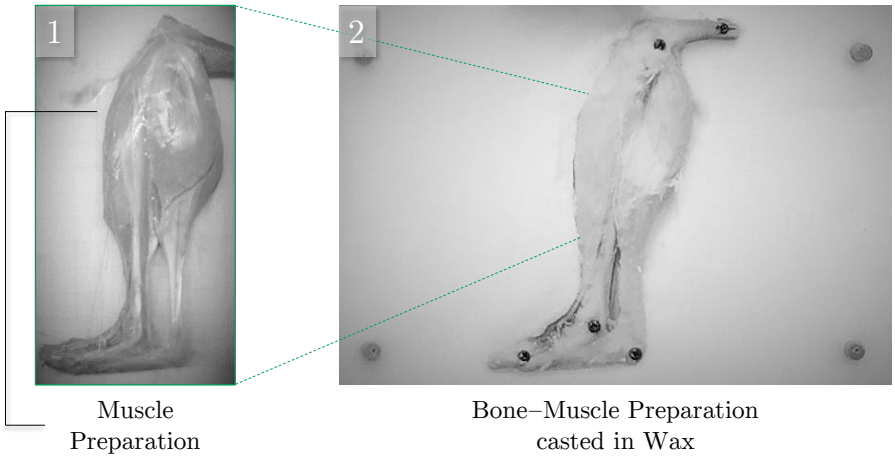

Figure 2.8: (1) Anatomical preparation of bone – muscle complex of rabbit left hind leg. (2) Histologically fixed bone – muscle preparation embedded in wax.

(termed fascicles in the following) are successively dissected with a micro forceps. Their original position is then recorded using the manual 3D digitiser. This process is repeated until all fascicles of the individual muscle are recorded. Each fascicle is approximated using 20 points in space (cf. Figure 2.9). During the dissection and digitisation, the palm of the hand — holding the digitiser handpiece — is placed on the preparation table to minimise movement of the digitiser tip ($< 0.1\,\mathrm{mm}$). The fascicle lengths and pennation angles are calculated in accordance to Schenk *et al.* (2013). Subsequently, the visualisation of individual fascicle traces is based on a custom-made Matlab script (MATLAB R2014a, The MathWorks, Inc., Natick, MA, USA) (cf. Figure 1.8).

In the following, open questions regarding **growth related changes in the muscle structure of rabbit hind legs** are illustrated in **Chapter 6** (Figure 1.1).

2.4 Ethical approval

The studies represented in **Chapters 3** and **6** were exempted from ethical committee review according to national regulations (German Animal Welfare Act), as the pigs and rabbits, respectively, were obtained from a slaughterhouse immediately after animal

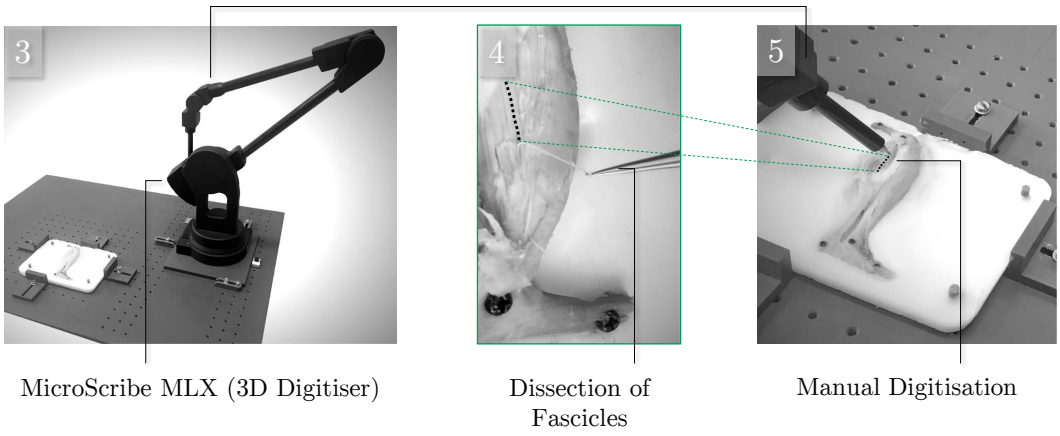

Figure 2.9: (3) MicroScribe digitiser enables 3D inspection and digitisation of skeletal muscle architecture. (4) A fascicle is dissected using a micro forceps. (5) The original position of the fascicle (black dashed line) is manually digitised by tracking the dashed line using the MicroScribe.

sacrifice. The skeletal muscle fibres from rats used for the studies illustrated in **Chapters 4** and **5** have been provided by another animal study that was approved according to the regulations of the German animal protection law (Tierschutzgesetz, § 4 (3)). The applicants of the approved animal study had no objection against the extraction of muscle fibres from dead rats. Their results were not impaired by the extraction of muscle fibres. Rabbits utilised in the study demonstrated in **Chapter 6** were pathogen-free and experiments were performed following standard operating procedures (Böl *et al.*, 2016). The rabbits were kept according to the German guidelines for rabbit breeding (§ 34 TierSchNutztV, 2014). Infants remained with their mother until they were weaned at 4–6 weeks of age. Following this period, the animals were separated into groups of four and, subsequently, housed in stainless steel cages. Water as well as food (hay and rabbit pellets, Deukanin®, Deutsche Tiernahrung Cremer GmbH & Co. KG, Düsseldorf, Germany) was provided ad libitum every morning and evening. The cages had a 14-hour controlled light-dark cycle (lights on from 6 a.m. to 8 p.m.). All investigations have been carried out in accordance to the regulations of the German animal protection law (Tierschutzgesetz, § 4 (3)). Since no experiments were carried out on living animals, the underlying studies are neither subjected to authorisation nor notifiable.

Chapter 3

Porcine stomach smooth muscle force depends on history-effects[1]

3.1 Introduction

Smooth musculature is located in the walls of various hollow organs, like the urinary bladder, the intestine, and the stomach; transporting several substances (e.g. fluids, bolus and nutrients) by muscle contraction. The stomach is part of the gastrointestinal tract, connecting the gullet (esophagus) to the duodenum, while mainly serving as a mixing area and holding reservoir. Furthermore, to accommodate a large amount of food, the position and size of the stomach varies continually — yielding the digestive organ to the most distensible portion of the gastrointestinal tract (Tortora & Nielsen, 2013). Hence, it's biomechanical properties are of great functional importance (Zhao *et al.*, 2005).

To enable the variability of functions of smooth gastric muscle, an elegant adjustment of varying contraction-types (e.g. concentric [active shortening], isometric [under constant length] and eccentric contractions [active lengthening]) — ensuring tonic and

[1] Tomalka A., Borsdorf M., Böl M., Siebert T. *Front. Physiol.* 2017 Oct 18;8:802.

peristaltic contraction-behaviour — is necessary (Pal *et al.*, 2004, 2007; Schulze-Delrieu *et al.*, 1998). To better understand stomach motility and function, knowledge about the influence of muscle length, velocity, activation level, and history-dependent effects (Abbott & Aubert, 1952; Ebashi & Endo, 1968; Gordon *et al.*, 1966; Hill, 1938; Huxley & Hanson, 1954; Rode *et al.*, 2009) on smooth muscle force, is required. Due to the structural and mechanical similarity of the porcine to the human stomach (Jia *et al.*, 2015; Zhao *et al.*, 2008), the examination of stomachs from pigs is of particular importance. However, appropriate studies examining active and passive muscle properties are rare. While only a handful of studies have been observed force – velocity relations on guinea pigs (Moriya & Miyazaki, 1985) and toads (Warshaw, 1987), intense research has been done on the relationship between muscle length and force production in a variety of vertebrate and invertebrate smooth muscles (Gordon & Siegman, 1971; Herlihy & Murphy, 1973). Nevertheless, there is a limited knowledge about the shape and the microstructural understanding of the entire force – length relation of stomach smooth muscles (Siegman *et al.*, 2013). Consequently, almost nothing is known about the classic biomechanical properties as force – length and force – velocity relations in the porcine stomach (Gunst, 1986; Minekus & van Mastrigt, 2001).

The influence of history-dependent effects on stomach smooth muscle force is of particular interest for developing a functional understanding of the peristaltic mode of operation. Since more than six decades it has been known that skeletal muscle force depends on history-effects (Abbott & Aubert, 1952). For example, force is enhanced in the isometric phase following active stretching (residual force enhancement, RFE) by up to 100% (Edman *et al.*, 1982; Leonard & Herzog, 2010) and depressed following active shortening (residual force depression, RFD) by up to 20% (Herzog & Leonard, 1997; Siebert *et al.*, 2015) compared with the corresponding isometric muscle force. Force generation during gastric distension as well as during and after gastric emptying is accompanied by large muscle length changes and, consequently, might be associated with RFE and RFD, respectively. Although there are a couple of studies reporting RFD and

RFE for urinary bladder smooth muscle (Menzel *et al.*, 2017; Minekus & van Mastrigt, 2001; van Asselt *et al.*, 2007), to the best of our knowledge, there are no studies of history-effects in the porcine stomach.

Hence, the aims of this study were the determination and analysis of biomechanical muscle properties (force – length and force – velocity relations) of intact, activated smooth muscle tissue from porcine stomach. Furthermore, this study represents the first *in vitro* approach to examine the influence of history-dependent effects on gastric smooth muscle force and the functional interpretation thereof.

3.2 Materials and Methods

The experimental setup, handling and preparation of smooth muscle tissue has been described earlier (Menzel *et al.*, 2017). Moreover, these techniques have been illustrated in great detail in **Chapter 2**, section 2.1 *'Determination of smooth muscle tissue properties'*.

3.2.1 Determination of gastric muscle properties

To determine the specific biomechanical muscle properties (force – length relation [FLR], force – velocity relation [FVR] and history-dependent effects), isometric, isotonic and isokinetic contractions have been performed in accordance with previous studies for smooth muscle tissue (Menzel *et al.*, 2017; Seydewitz *et al.*, 2017) and skeletal muscles (Böl & Schmitz, 2013; Siebert *et al.*, 2015). Fifty-four ($n = 54$) tissue strips were used in total for the *in vitro* dynamic parameter determination (Table 3.1). To investigate the active and passive force – length relationships, a series of 18–19 isometric contractions (with length increments of 0.1 L_{slack} in ascending order), starting from an initial sample length of 0.8 L_{slack}, have been conducted. The tissue strips were stretched up to passive forces of about 50% F_{im} to avoid muscle damage induced by excessive lengthening. At each length, the maximum

Strip number	S1–S14	S15–S37	S38–S42	S43	S44–S53	S54	n
Force – length relation	x		x			x	20
Force – velocity relation		x		x		x	25
History-dependent effects			x	x	x	x	17

Table 3.1: Categorisation of observed muscle properties from smooth porcine tissue strips. n is the number of samples.

active and passive muscle force were determined as the maximum force value and the passive force at the instant before muscle activation, respectively. Linear regression models following the equation:

$$f(x) = mx + b, \text{with } x = L/L_{slack}, \tag{3.1}$$

were used to fit the ascending- and descending limb of the FLR. The muscle length at F_{im} was defined as the optimal muscle length (L_0).

The force – velocity relation was identified by a series of about six isotonic contractions starting from L_0 against forces in the range of 0.10 to 0.90 F_{im} (Till *et al.*, 2008) in ascending order. The force – velocity relation followed the typical hyperbolic Hill equation (Hill, 1938):

$$f(v) = \frac{v_{max} - v}{v_{max} + v/curv}, v < 0 \tag{3.2}$$

for concentric contractions, with v_{max} defined as maximum shortening velocity and $curv = a/F_{im}$ (where a is the asymptote of force (Hill, 1938)). A recovery phase of 7 min between the experiments has been conducted over the entire experimental protocol for determination of force – length and force – velocity relations.

In order to investigate the impact of ramp length and velocity on history-dependent

effects, isokinetic contractions (Herzog & Leonard, 1997; Menzel *et al.*, 2017) have been applied to $n = 17$ tissue strips in dependence of varying ramp amplitudes at a given velocity (40% v_{max}) and in dependence of different velocities at a constant length amplitude (7% L_0), respectively. The isokinetic ramps started after a period of pre-stimulation (around 14 s) under full activation until steady-state maximum isometric force, characterised by the development of a plateau, was reached. The stimulation continued for at least 14 s after the end of the ramp. Shortening and lengthening ramps for the determination of residual force depression (RFD) and residual force enhancement (RFE) in dependence of ramp length started at $L_0 \pm 5\%$, $\pm 7\%$, and $\pm 10\%$ L_0, respectively, and were finished at 1.0 L_0. To examine the dependency of history-effects on speed, concentric and eccentric ramps from 1.0 $L_0 \pm 7\%$ to 1.0 L_0 with different ramp velocities (20, 40, 70% v_{max}) were applied to the tissue strips. All ramp experiments have been carried out in randomised order (Figure 3.1). To calculate RFE and RFD, the difference between the redeveloped and the corresponding purely isometric force at the same length has been identified 10 s after the end of each ramp. The relaxation period during the entire history-block was 12 min to ensure an optimal recovery phase of force-generating processes (Gunst, 1986). The 'cycling-protocol' by Brenner (1983) was utilised to conserve the structural and mechanical properties in maximally activated smooth gastric strips over an extended period of time as well as to reduce length-inhomogeneities of overlapping myofilaments.

To calculate force degradation, isometric reference contractions at L_0 were performed before and after each of the ramp experiments. Plastic length adaptations of smooth muscle strips by dissolution and reformation of myosin filaments (Seow, 2005), occurring at periods of hours (Martinez-Lemus *et al.*, 2004; Wang & Kernell, 2001) or days (Arner *et al.*, 1984; Naghshin *et al.*, 2003; Zeidan *et al.*, 2000), were not considered within this study, as the time period between the reference contractions was much shorter and muscle strips were held at a constant length (L_0) during the experiments. During isokinetic ramp experiments, the isometric force in successive activations decreased at an

average rate of 1.1% per activation. Data from preparations that produced an isometric force less than 6 N/cm^2 have been rejected.

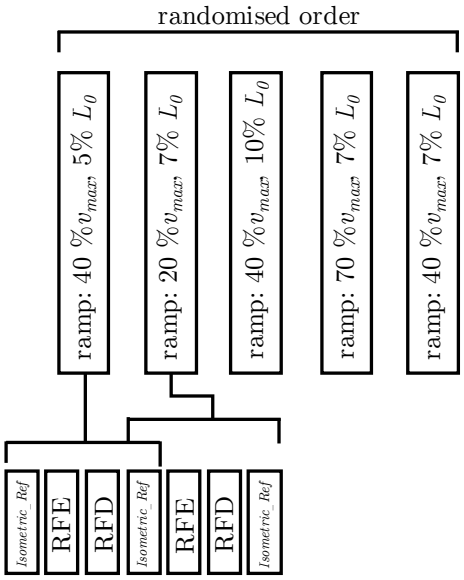

Figure 3.1: Experimental protocol. Examination of varying ramp parameters followed a pseudorandomised block design (upper trace). The applied ramp – velocity and ramp – length are normalised to the maximum shortening velocity (v_{max}) and optimum muscle length (L_0), respectively. The lower trace illustrates the fixed protocol of muscle contractions consisting of isokinetic ramp experiments (RFE: residual force enhancement, RFD: residual force depression), and isometric reference contractions (*Isometric_Ref*).

3.2.2 Histological observations

The histological examination was carried out in accordance with the procedure previously described by Menzel *et al.* (2017) and has been realised on samples of the same tissue-region that were used for the determination of dynamic parameters in the present study. Briefly, the cryo-histological sections of smooth gastric tissue strips were stained with Picrosirius Red staining protocol (Junqueira *et al.*, 1979) at 200% L_{slack}, and photographed using a digital microscope (Zeiss Smartzoom 5). To examine the muscle cross-sectional areas (CSA) in the longitudinal direction (refer to **Chapter 2**, Figure

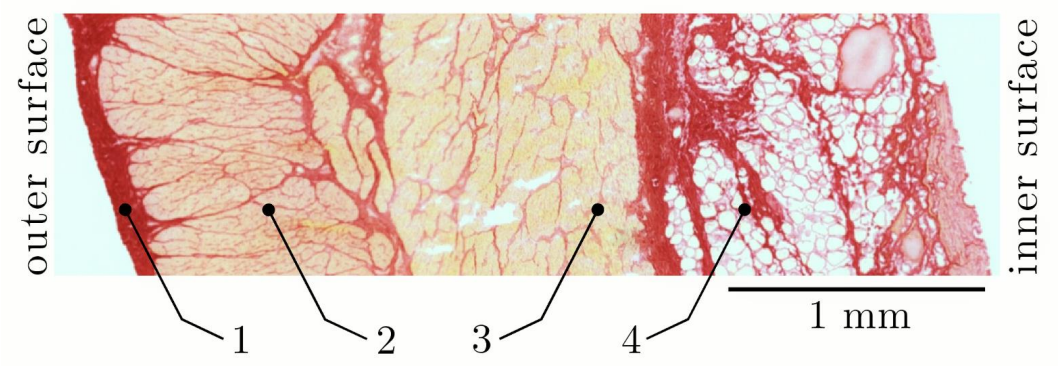

Figure 3.2: Section of a characteristic smooth tissue sample from porcine stomach. Representative picture from histological staining of samples from the proximal stomach (fundus) at 200% slack length (L_{slack}) in longitudinal direction. Four distinct layers can be identified: (1) tunica serosa, (2) longitudinal muscle layer (tunica muscularis), (3) transversal (circumferential) muscle layer (tunica muscularis) and (4) tela submucosa.

2.1), the average length and width of the individual sample strips (Figure 3.2) was determined with an image editing software (ImageJ 1.49v, National Institutes of Health, USA). The CSA was calculated by assuming a rectangular cross-section. The muscle tension (P_{im}) of a smooth gastric tissue sample was determined with:

$$P_{im} = \frac{F_{im}/CSA}{p}, \tag{3.3}$$

where p describes the percentage of the longitudinal muscle layer from the total CSA.

3.2.3 Data processing and statistics

The length and force signals from the dual-mode muscle lever were recorded at 100 Hz with an A/D interface (604A, Aurora Scientific, Canada). A real-time software package (610A Dynamic Muscle Analysis, Aurora Scientific) was used for data acquisition. A program written in MATLAB (version R2014a (8.3.0), The MathWorks, Inc., Natick, MA, USA) was used for data analysis. Data were expressed as mean ± standard deviation (s.d.). For statistical analyses, normalised data were used. Force values were

divided by individual F_{im}. Length data were divided by L_{slack} and L_0 and velocity data were expressed in absolute values [mm/s] and normalised to optimum muscle length [L_0/s], respectively. A Kolmogorov-Smirnov Test with $P > 0.05$ indicated no deviation from normality. To test significant differences of history-effects in dependence of ramp amplitude and velocity, a one-way ANOVA with repeated measures was used. For homogeneous variances, post-hoc analyses were performed using the Tukey-HSD test. A significance level of $P < 0.05$ was used for all analyses. Statistical analyses were carried out using SPSS 23 (IBM Corp, Armonk, NY, USA).

3.3 Results

3.3.1 Histological characterisation

The results of the structural observations of histologically stained tissue samples (ventral fundus of the stomach) at 200% slack length are illustrated in Figure 3.2. Based on the photographs of the histological sections different tissue types can be distinguished. Following Figure 3.2, the stomach wall can be divided into four distinct layers: 1) tunica serosa, 2) tunica muscularis in longitudinal- and 3) transversal (circumferential) orientation and 4) tunica submucosa. Note that the tunica mucosa is dissected from the tissue samples. All structures that stained yellow-orange correspond to muscle tissue, while the stained red structures correspond to collagen. In agreement with Zhao *et al.* (2010), the highest collagen content was found in the submucosal layer (in between the fat tissue). The collagen content likely determines the gastric wall stiffness since collagen is supposed to be the stress-bearing structure in most tissues (Fung, 1993; Zhao *et al.*, 2010). Picrosirius staining also revealed a continuous intermeshing network of collagen throughout the entire stomach wall. The CSA of the longitudinal tissue strip is 30.01 $\pm$ 5.66 mm^2 ($n = 53$), whereas the percentage of the longitudinal muscle layer from the total CSA is 36.6% $\pm$ 2.6%.

3.3.2 Gastric muscle properties

The smooth gastric tissue samples exhibited a characteristic force – length relation (FLR) — similar to skeletal muscles. The active isometric FLR showed clearly visible pronounced slope changes, characterised by a linear ascending and descending limb, and a bell-shaped plateau region (Figure 3.3). The plateau region (> 95% F_{im}) ranged from

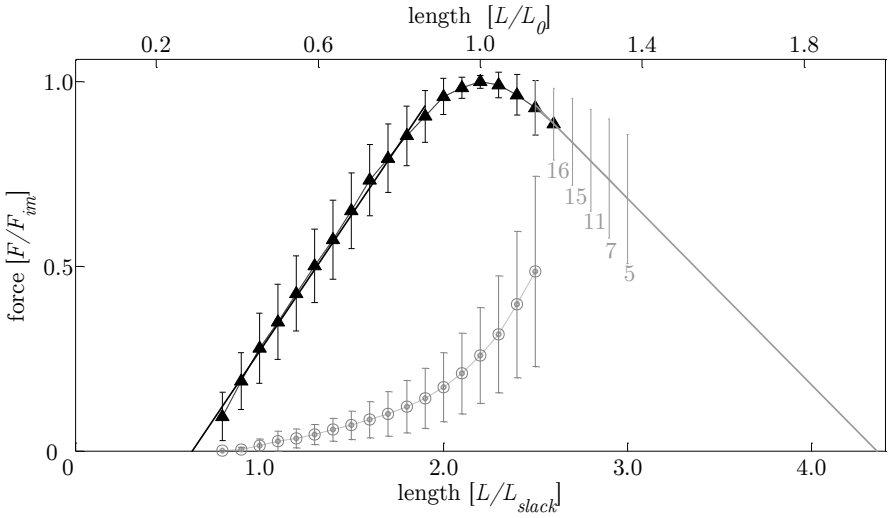

Figure 3.3: Force – length relationship. The length is normalised to optimum muscle length (L_0, upper abscissa) and slack length (L_{slack}, lower abscissa), respectively. The force is normalised to maximum isometric force (F_{im}). Filled triangles and open circles indicate mean values of active and passive isometric smooth muscle forces, respectively. Bars indicate corresponding standard deviations. The ascending limb ($f_1(x)$; indicated by the solid black line) and descending limb ($f_2(x)$; indicated by the solid grey line) of the force – length relation (FLR) were fitted by linear regression models following the equations: $f_1(x) = 0.74x$ - 0.47 and $f_2(x) = -0.51x + 2.2$, with $x = L_{slack}$. Isometric force – length measurements comprise $n = 20$ tissue samples up to lengths of 2.5 L/L_{slack} (corresponding to around 50% F_{im}). For determining the descending limb of the FLR for lengths longer than 2.5 L_{slack}, varying sample sizes were investigated (labelled with grey numbers below standard deviation- (s.d.) bars on the descending limb of the FLR).

0.9 to 1.1 L_0 or 2.0 to 2.4 L_{slack}, with a mean slack length of 13.42 ± 1.42 mm. Extrapolation of the ascending and descending limb of the FLR (cf. section 3.2.1) yielded zero force at 0.65 ± 0.14 L_{slack} or 0.29 ± 0.06 L_0 and 4.37 ± 1.00 L_{slack} or 1.99 ± 0.45 L_0, respectively (Figure 3.3). The maximum isometric force (F_{im}) at L_0 was 1 141.2 ± 295.8 mN ($n = 20$). Longitudinal muscle strips of porcine stomach, stimulated by

supramaximal AC field stimulation, attained their F_{im} after 13.6 ± 1.5 s (n = 20) at 32 °C.

Based on histological observations in Section 3.3.1, the mean maximum muscle tension (P_{im}) of gastric tissue samples was 10.4 ± 2.6 N/cm^2 in longitudinal orientation. The passive FLR of the unstimulated muscle strip was characterised by an exponential increase of force with sample length, accompanied by passive forces of 25.8 ± 13% F_{im} at L_0. The gastric muscle strips' ability to shorten under various loads was studied by means of a series of isotonic releases. The maximum shortening velocity was 1.08 ± 0.32 mm/s (corresponding to 0.04 ± 0.01 L_0/s) with a *curv*-factor of 0.36 ± 0.15 (n = 25). The investigated force – velocity relationships (FVR) of the tested stomach samples featured the typical hyperbolic shape (Figure 3.4).

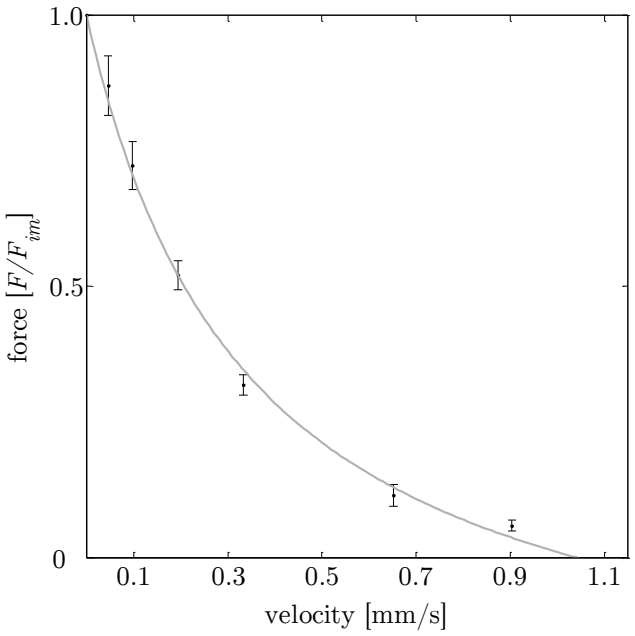

Figure 3.4: Force – velocity relationship. Based on a series of isotonic contractions, the normalised force (means ± standard deviations are indicated by black bars) was determined as function of the velocity. The grey curve shows the typical hyperbolic shape observed by Hill (1938), with a/F_{im} = *curv* = 0.36 (a describes the force asymptote) and v_{max} = 1.08 mm/s (the intersection of the fitted hyperbolic curve with the velocity-axis). Isotonic force – velocity measurements comprise n = 25 tissue samples. The force is normalised to maximum isometric force (F_{im}) and the velocity is expressed in absolute values [mm/s].

The investigation of history-dependent effects yielded significantly ($P < 0.05$) enhanced forces following stretching and depressed forces following shortening compared with the corresponding isometric forces. A summary of all history-dependent effects investigated in this study is shown in Table 3.2.

	(% F_{im})	n	P
Residual Force Enhancement (RFE)			
Ramp length (% L_0)			
5	12.45 ± 4.39	10	0.05 (#†)
7	15.68 ± 5.43	10	
10	16.38 ± 5.21	10	
Ramp velocity (% v_{max})			
20	10.28 ± 5.81	13	0.01 (△)
40	15.83 ± 5.20	13	
70	14.37 ± 5.12	13	
Residual Force Depression (RFD)			
Ramp length (% L_0)			
5	15.52 ± 3.01	10	0.001 (#)
7	21.23 ± 4.65	10	0.00 (†⁎)
10	31.78 ± 6.81	10	
Ramp velocity (% v_{max})			
20	25.16 ± 6.78	13	
40	23.35 ± 5.33	13	*ns*
70	23.00 ± 4.53	13	

Table 3.2: Mean and standard deviation of enhanced forces (RFE) and depressed forces (RFD) determined 10 s after the end of the ramp. History-effects were determined for three different ramp amplitudes (5, 7, 10% L_0) and three varying velocities (20, 40, 70% v_{max}). Significant differences ($P < 0.05$) are marked as follows: # between 5% and 7% L_0, † between 5% and 10% L_0, ⁎ between 7% and 10% L_0, △ between 20% and 40% v_{max}. *ns* means 'not significant' and n is the number of samples.

Statistical analyses yielded significant influence of ramp length on isometric muscle force after length change. RFD and RFE increased almost linearly with ramp length (cf. Figures 3.5 and 3.6 A).

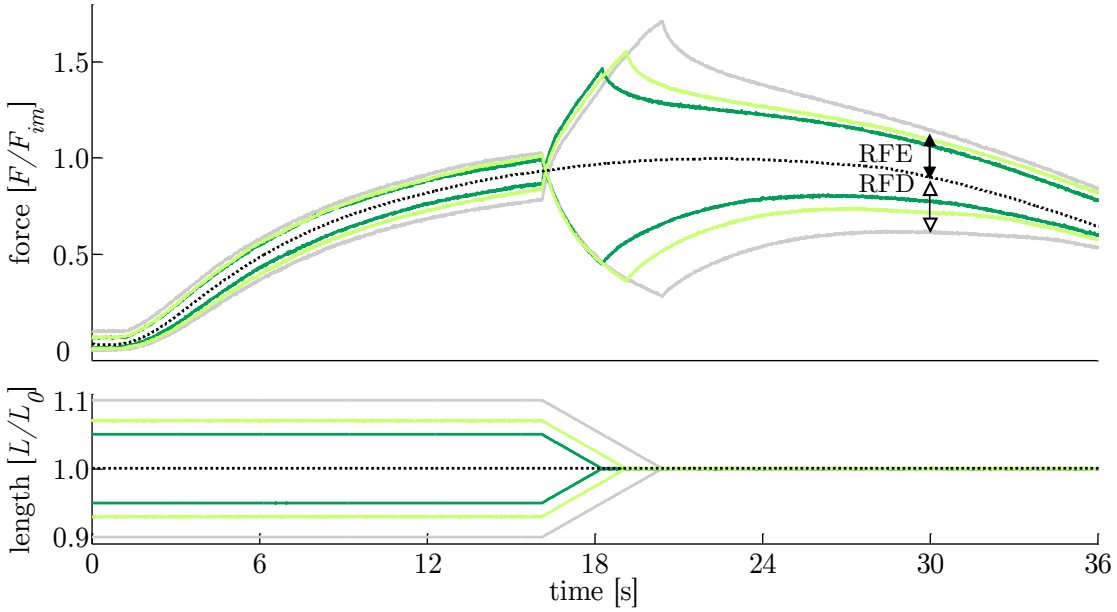

Figure 3.5: History-effects with varying ramp amplitudes. Representative force — time (upper graph) and length — time traces (lower graph) with isokinetic length changes comprising three different ramp amplitudes (5, 7, 10% L_0) at constant velocity of 40% v_{max} (strip number S40). The force is normalised to maximum isometric force (F_{im}) and length to optimum muscle length (L_0). Residual force enhancement (RFE, difference between black arrows) and residual force depression (RFD, difference between white arrows) are the force difference between ramp experiments (solid lines) and isometric reference contraction (dotted line) determined 10 s after the end of the ramp, shown exemplarily for the longest (10% L_0) ramp.

RFD is about twice as much (31.78% F_{im}) for the longest ramp length (10% L_0) compared to the shortest ramp length (15.52% F_{im} for 5% L_0; $P < 0.001$) (cf. Figure 3.6 A). For varying ramp velocities at constant ramp length (7% L_0; $n = 13$) statistics yielded a significant increase in RFE between slow (20% v_{max}) and moderate (40% v_{max}) stretch velocities ($P < 0.05$; cf. left columns of Figure 3.6 B).

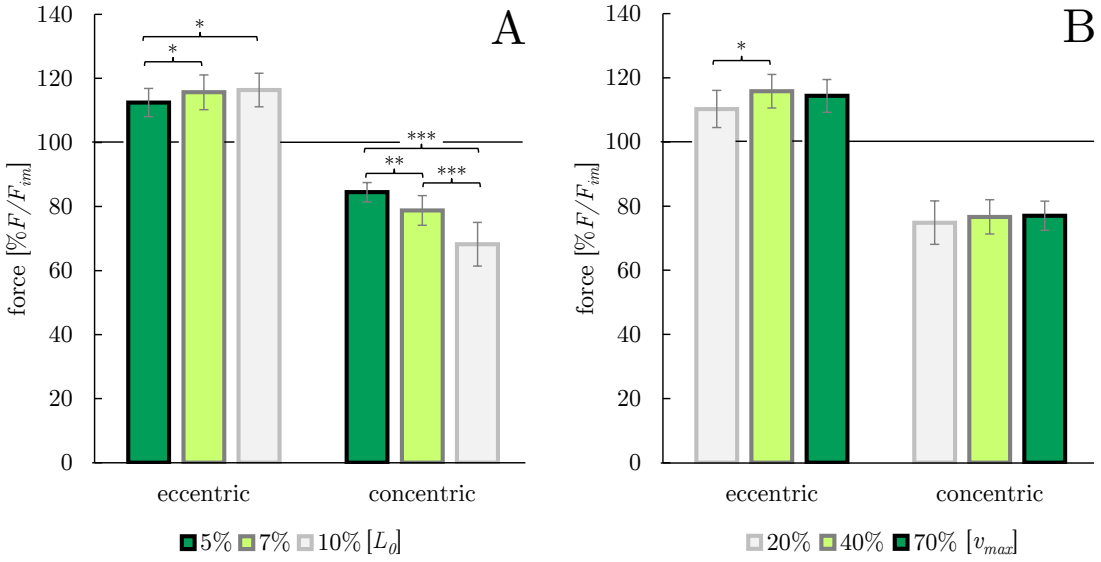

Figure 3.6: Dependency of history-effects (RFE and RFD) on ramp length (**A**) and on ramp velocity (**B**). Mean forces ± standard deviations are given. Forces are normalised to the forces obtained during purely isometric reference contraction (in percent of maximum isometric force [% F/F_{im}]) at optimum muscle length [L_0] (indicated by horizontal black solid lines). (**A**) Ramp length was varied (dark green: 5% L_0, bright green: 7% L_0, grey: 10% L_0) at constant ramp velocity (40% v_{max}). (**B**) Ramp velocity was varied (grey: 20% v_{max}, bright green: 40% v_{max}, dark green: 70% v_{max}) at constant ramp length (7% L_0). Brackets and asterisks (*) mark differences in forces after stretch (eccentric) and shortening (concentric) in the intergroup comparison. Significance levels are marked as follows: * $P < 0.05$, ** $P < 0.01$, and *** $P < 0.001$.

Further increases in eccentric velocity up to 70% v_{max} yielded no further change in RFE. RFD decreased by trend (from 25 to 23% F_{im}) but not significantly with increasing ramp velocities (cf. right columns of Figure 3.6 B; see Figure 3.7).

3.4 Discussion

A comprehensive dataset consisting of histological as well as specific biomechanical muscle properties (such as force – length and force – velocity relations) has been investigated within this study. Furthermore, this study represents the first *in vitro* approach that examined the influence of history-dependent effects induced by ramps with various lengths and velocities on stomach smooth muscle force.

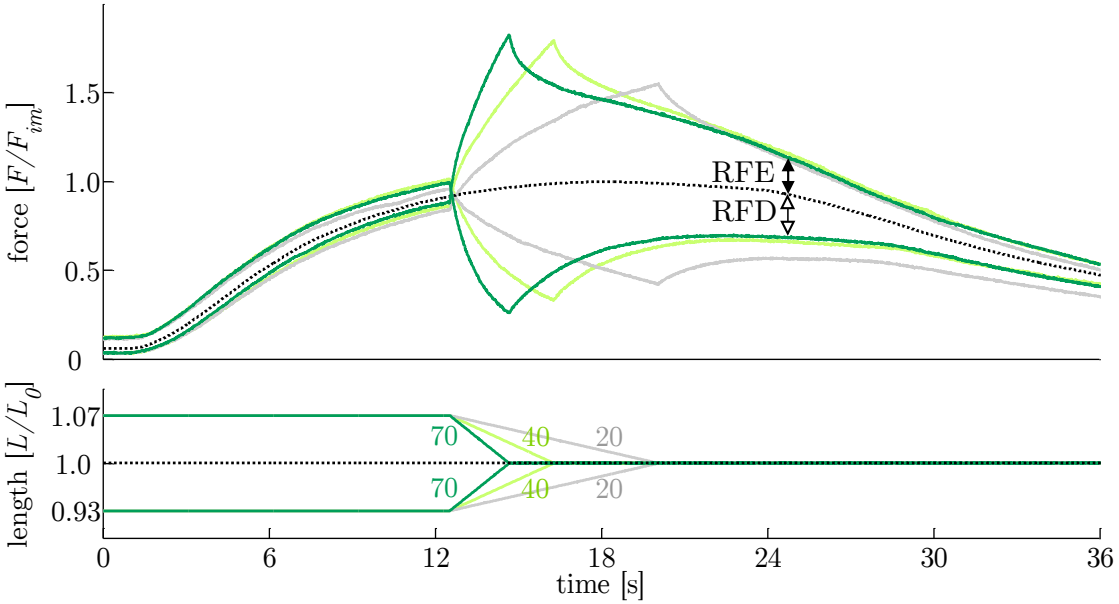

Figure 3.7: History-effects with varying ramp velocities. Representative force — time (upper graph) and length — time traces (lower graph) with isokinetic length changes comprising three different ramp velocities (20, 40, 70% v_{max}) at constant ramp amplitude of 7% L_0 (strip number S38); numbers without units indicate velocity in percent of maximum shortening velocity [% v_{max}]. The force is normalised to maximum isometric force (F_{im}) and length to optimum muscle length (L_0). Residual force enhancement (RFE, difference between black arrows) and residual force depression (RFD, difference between white arrows) are the force difference between ramp experiments (solid lines) and isometric reference contraction (dotted line) determined 10 s after the end of the ramp, shown exemplarily for the fastest (70% v_{max}) ramp.

3.4.1 Smooth gastric muscle properties — comparison with the literature

Mean maximum tension of active smooth muscle from porcine stomach is $10.92 \pm 2.85\,\mathrm{N/cm^2}$. This value is about 2–3 times higher compared to muscle tension values of porcine bladder (2.5–6.0 $\mathrm{N/cm^2}$ (Menzel *et al.*, 2017; van Mastrigt & Glerum, 1985)), but about half as much when compared to smooth muscle tissue of stomachs from small mammals such as guinea pigs (19.2 $\mathrm{N/cm^2}$ (Moriya & Miyazaki, 1982)). The mean passive forces of about 26% F_{im} at L_0 are in accordance with previous findings on smooth muscles (Gordon & Siegman, 1971; Menzel *et al.*, 2017; Siegman *et al.*, 2013).

In agreement with the FLR from porcine urinary bladder (Menzel *et al.*, 2017), rabbit taenia coli (Gordon & Siegman, 1971), and rat arterial vessel (Mulvany & Warshaw, 1979), the force–length dependency determined in the present study exhibited an obvious linearity of the ascending and the descending limb (Figure 3.3). Furthermore, the shape of the active FLR of smooth muscles is generally similar to that of striated skeletal muscles (Gordon *et al.*, 1966; Herlihy & Murphy, 1973) — implicating a dependence of muscle force with regards to myofilament overlap and muscle length. Considering this, active force production in smooth muscles is roughly based on the mechanisms described by the sliding filament and cross-bridge theories (Gordon *et al.*, 1966; Huxley & Hanson, 1954; Huxley & Niedergerke, 1954) for skeletal muscles, although this is much more thoroughly understood in smooth muscles (Arner *et al.*, 1984; Gordon & Siegman, 1971; Siegman *et al.*, 2013). However, there are distinct differences in the underlying microstructure of smooth muscles. Actin filaments are connected to dense bodies (Somlyo *et al.*, 1973) and thus there is no Z-disc as in striated muscles. In contrast to the perfect straight alignment of actin and myosin filaments in skeletal muscles, ultrastructural studies of smooth muscles demonstrate a quite randomly orientated arrangement of myofilaments under activation, accompanied by cellular twisting (corkscrew-like) during active shortening (Bond & Somlyo, 1982; Fay & Delise, 1973; Warshaw *et al.*, 1987). These structural characteristics might explain specific differences in the muscle properties between smooth and striated muscles. Smooth muscles exhibit no slope change at the ascending limb of the FLR (Herrera *et al.*, 2005), which is typical for striated muscles (Rode & Siebert, 2009; Winters *et al.*, 2011) and muscle fibres (Stephenson, 2003) at sarcomere lengths of about 1.6 μm (see **Chapter 4**). In striated muscles this slope change is attributed to the myosin filament sliding through the Z-disc (see **Chapter 5**). The absence of this slope change in smooth muscles (Figure 3.3) might be partially explained by the side-polar myosin filaments in smooth muscles (Herrera *et al.*, 2005) compared to bipolar myosin filaments in striated muscles (Craig & Megerman, 1977) (cf. section 1.1.1; Figure 1.4). However, the structural understanding

of the entire force – length relationship in smooth muscles is incomplete so far (Siegman *et al.*, 2013).

The maximal shortening length of smooth gastric muscle tissue from pigs investigated in this study is 0.65 ± 0.14 L_{slack} (corresponding to 0.29 ± 0.06 L_0), which is in accordance with findings of other smooth muscle studies (Gordon & Siegman, 1971; Mulvany & Warshaw, 1979; Warshaw, 1987; Siegman *et al.*, 2013). The descending limb is characterised by a linear force decrease in proportion to increasing length. This yielded zero forces at $4.37 \pm 1.0\ L_{slack}$ or $1.99 \pm 0.45\ L_0$, accompanied by non-myofilament overlap. These values are slightly higher than those for such smooth muscles as rat arterial vessel (1.82 L_0) (Mulvany & Warshaw, 1979) or rabbit taenia coli muscles ($\sim 1.9\ L_0$) (Siegman *et al.*, 2013). For lengthening skeletal muscles, active force production is limited to about 1.6 L_0 (Gordon *et al.*, 1966; Stephenson, 2003). Differences might be due to the functional necessity of gastric tissue to withstand high distension (Jia *et al.*, 2015; Korossis *et al.*, 2009). The complex microstructure of smooth muscles comprises a loose, irregular myofilament arrangement held in a mesh, whereas intermediate filaments appear to link the dense bodies in a cytoskeletal network (Bond & Somlyo, 1982; Fay & Delise, 1973; Mulvany & Warshaw, 1979; Somlyo *et al.*, 1973). These filaments, which have a more structural rather than a contractile function, are assumed to have a role in force transmission and mechanical stability (Arner & Malmqvist, 1998; Tortora & Nielsen, 2013). Additionally, smooth muscles are able to actively contract in response to stretching, followed by a reduction in tension within a short period of time (Gordon & Siegman, 1971; Hill, 1926; Tortora & Nielsen, 2013). This stress-relaxation response allows smooth muscles to undergo great length changes while still preserving the ability to contract efficiently (Siegman *et al.*, 1976; Tortora & Nielsen, 2013). Furthermore, side-polar myosin filaments could help to explain the ability of smooth muscles to shorten by large amounts (Xu *et al.*, 1996).

The *curv*-factor (0.36 ± 0.15) observed in this study is within the range (0.1 – 0.5) reported for smooth- (Menzel *et al.*, 2017; Moriya & Miyazaki, 1985; van Mastrigt, 2002)

and skeletal muscles (Siebert *et al.*, 2015), respectively. Maximum shortening velocity (0.04 ± 0.01 L_0/s) is in the lower range of values from $0.03-0.6$ L_0/s reported for other mammalian smooth muscles (Gordon & Siegman, 1971; Kong & Stephens, 1983; Menzel *et al.*, 2017; Moriya & Miyazaki, 1985; van Mastrigt, 2002). Compared to values reported for skeletal muscles (v_{max}: $3-7$ L_0/s, (Gollapudi & Lin, 2013; Ranatunga, 1984; Siebert *et al.*, 2008)), maximum shortening velocities of smooth muscles were one to two orders of magnitude smaller (Barany, 1967).

The behaviour of the smooth gastric tissue strips investigated in this study is generally in agreement with history-effects reported for other smooth (Gunst, 1986; Menzel *et al.*, 2017; van Asselt *et al.*, 2007) and skeletal muscles (Rassier & Herzog, 2004; Siebert *et al.*, 2015). Whereas the evidence of force depression and force enhancement has been shown for other canine and porcine smooth muscles in previous studies (Gunst (1986) trachea; Menzel *et al.* (2017); van Asselt *et al.* (2007) urinary bladder), this study represents the first approach investigating smooth gastric muscle tissue. Findings reveal a linear dependency of history-effects (RFE and RFD) with regards to their ramp amplitude (Table 3.2, Figure 3.5) similar to findings on skeletal muscles (Abbott & Aubert, 1952; Edman *et al.*, 1982). Maximum values of RFE (up to 16% F_{im}) and RFD (up to 32% F_{im}) exceed previous findings on smooth muscles (12% and 18% F_{im} for RFE and RFD, respectively (Menzel *et al.*, 2017)).

In accordance with previous investigations (Menzel *et al.*, 2017), ramp velocity was found to have no significant influence on RFD and RFE, except for differences between lengthening contractions with 20% and 40% v_{max} ($P < 0.05$; Table 3.2). The investigated influence of ramp velocity on RFE (at low ramp velocities) might be influenced by the experimental protocol and the contractile properties of smooth gastric muscle tissue. Low ramp velocities require long stimulus durations resulting in a decrease in muscle force induced by fatigue — accompanied by an additional flattening of the force trace — yielding to significantly reduced RFE for slow eccentric ramps (Table 3.2, Figure 3.6 B). Thus, results of RFE for low velocities should be considered with caution. In

accordance with findings by Menzel *et al.* (2017) on smooth muscle tissue as well as on skeletal muscles (Abbott & Aubert, 1952), force depression decreased by trend (but not significantly) with increasing ramp velocity.

3.4.2 Underlying mechanisms of history-dependence of muscle force

To date, there is an intensive debate about mechanisms and functions of history-dependent effects in skeletal muscles (Campbell & Campbell, 2011; Herzog *et al.*, 2008; Hessel *et al.*, 2017; Siebert *et al.*, 2014b). Titin, a non-cross-bridge, semi-active structure, is increasingly recognised as an important protein that contributes to active force production during and following eccentric contractions (Herzog *et al.*, 2016). While titin does only exist in striated muscles, a molecule having similar functional and structural titin-like characteristics, named smitin, occurs in smooth muscles (Kim & Keller, 2002). Therefore, a transfer of currently discussed various mechanisms, that provide some possible explanations with regards to history-dependent effects in skeletal muscles, is likely (Heidlauf & Röhrle, 2014; Nishikawa *et al.*, 2012; Rode *et al.*, 2009; Schappacher-Tilp *et al.*, 2015). However, further experimental and modelling evidence is required to demonstrate conclusive explanatory approaches of underlying mechanisms of history-dependent effects of force production in smooth muscle tissue (cf. section 1.1.3 for details).

3.4.3 Functional and physiological relevance

The investigated tissue samples were dissected out of a predefined section of the fundus (Figure 2.1, black rectangle), which is mainly serving as food reservoir. Hence, when the proximal stomach is filled due to ingestion, accompanied by a large expansion of surrounding tissue, history-dependent effects, observed experimentally in this study, might have physiological relevance in order to suit gastric motility. The motility of the fundus (proximal stomach) is characterised by almost tonic contractions induced by permanent but irregular muscle activity (Azpiroz & Malagelada, 1984; de Wever

et al., 1978; Notivol *et al.*, 1995). More specifically, in between meals (interdigestive phase) the fundus maintains a high basal muscle tone (a state of continuous partial contraction) (Notivol *et al.*, 1995). Upon food intake, the muscle tone of the proximal stomach suppresses, but will never be switched off completely (Janssen *et al.*, 2011; Notivol *et al.*, 1995; Schwizer *et al.*, 2002; Tack *et al.*, 2002). This enables gastric accommodation and enhances the storage capacity of the stomach by increasing the compliance of the fundic stomach muscle (Kindt & Tack, 2006; Villanova *et al.*, 1997). These findings suggest an eccentric contraction behaviour of the fundus during ingestion, even though at suppressed gastric tone (Azpiroz & Malagelada, 1984; Janssen *et al.*, 2011). Accordingly, we expect enhanced forces following active muscle stretch which might subsequently support gastric emptying. This potentially explains the functional relevance of significantly enhanced forces during and after lengthening as observed in this study. Hence, a protective and supportive function of RFE prior to gastric emptying to avoid excessive distension of the stomach might represent specific adaptations to gastric functionality. Furthermore, RFE might counteract rapid extension of gastric tissue due to acceleration of gastric contents in impact situations e.g. at ground contact during jumping or tumbling. Additionally, the large working range of about 3.7 L_{slack}, high muscle tension of smooth gastric tissue, as well as the ability to withstand large eccentric forces, enables the fundus to operate suitably during filling.

RFD might occur following food consumption (postprandial phase), when the fundus propels the gastric content distally by a tonic concentric contraction, going along with considerably dimensional changes accompanied by slow muscle shortening (Farré & Tack, 2013; Schulze-Delrieu *et al.*, 1998). Anyway, high RFD values seem to be functionally counterproductive for this region and could be seen as an unwanted by-product of RFE (Rode *et al.*, 2009). Consequently, the observed muscle properties of the fundus muscle tissue might represent functional adaptations to cover prevailing conditions. However, to verify the hypothesised relation between contractile properties and stomach function, structural reasons for history-dependent effects in smooth muscles as well as potential mechanisms of adaptation have to be analysed in prospective studies.

3.5 Conclusion

The findings provided by the current research support the idea of a holistic reflection of stomach structure and function, extending well-known mechanisms and processes (such as distinct signal pathways, various triggered mechanoreceptors) by history-dependent effects. A key role in explaining the enhanced and depressed total force responses during active stretching and shortening, respectively, might represent the titin-like structure smitin. This semi-active element might behave like a spring during fundic distension and emptying, thus, energy may be stored and recoiled as reported for skeletal muscles in stretch-shortening cycles (Roberts & Azizi, 2011), respectively. Consequently, an elegant, energy saving, elastic mechanism similar to the bouncing gait in vertebrate locomotion (Cavagna *et al.*, 1977; Roberts, 2016; Roberts & Azizi, 2011) might enable, or at least enhance, efficient stomach function. The results presented here provide new insights into stomach function and might facilitate development and validation of realistic three-dimensional muscle models of hollow organs like the stomach.

Chapter 4

The active force – length relationship is invisible during extensive eccentric contractions in skinned skeletal muscle fibres[2]

4.1 Introduction

Muscle force production depends on the arrangement of fibres within the muscle, the contraction velocity, the fibre length, the activation, and the muscle contraction history (Hill, 1938; Abbott & Aubert, 1952; Ebashi & Endo, 1968; Gordon *et al.*, 1966). The variability in the function of skeletal muscles during movements (Dickinson *et al.*, 2000; Mörl *et al.*, 2016) requires concentric (active and shortening), isometric (active and at constant length), and eccentric (active and lengthening) contractions as well as combinations thereof. Muscles activated during eccentric movements can serve as shock

[2]Tomalka A., Rode C., Schumacher J., Siebert T. *Proc Biol Sci.* 2017 May 17;284(1854).

absorbers, energy stores, and struts, e.g. to stabilise posture, decelerate, or prepare reutilisation of stored energy for power enhancement (Dickinson *et al.*, 2000; Roberts & Azizi, 2011). However, processes underlying lengthening contractions on the molecular level remain unclear. A novel, physiological model of fibre contraction (see **Chapter 5**) extends the well-accepted mechanisms of active force production in sarcomeres — the sliding filament (Huxley & Niedergerke, 1954; Huxley & Hanson, 1954) and cross-bridge theories (Huxley, 1957a) — to short sarcomere lengths (Figure 4.1*a*, range left of D).

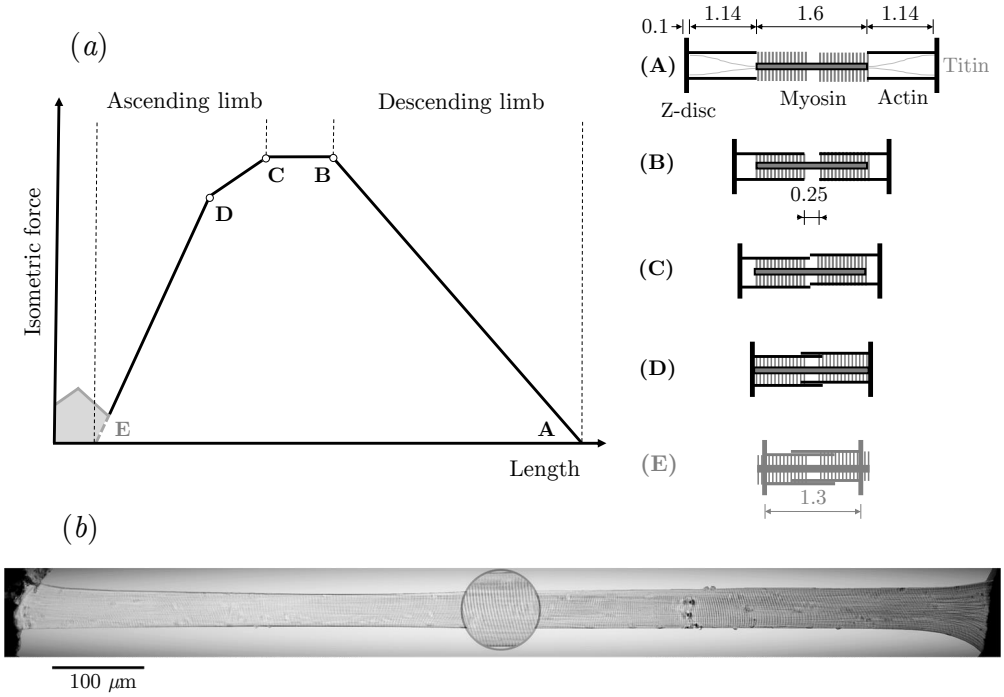

Figure 4.1: Force – length relationship (FLR) and EDL muscle fibre. (*a*) The active isometric FLR can be directly explained with actin and myosin filament overlap (Gordon *et al.*, 1966). Qualitative changes in overlap (see corresponding sarcomere configuration schematics (*A*) – (*E*) to the right) lead to slope changes of the FLR (indicated with open circles at lengths *B, C, D*). Forces in the range below *D* (including the force hump (Ramsey & Street, 1940) left of *E* for very short sarcomere lengths, illustrated by the grey area) can be explained with myosin filament sliding through the Z-disc (refer to **Chapter 5**). (*b*) Representative picture of a permeabilised single muscle fibre of a rat EDL muscle at optimal sarcomere length $L_{S0} = 2.5\,\mu$m in relaxed state. Only fibres with a homogeneous sarcomere pattern, without any lesions or damage were analysed. The photomicrograph was captured with a 20 × objective under bright-field illumination. The spot (500 × magnification) shows the striation pattern.

Application of these well-accepted theories of muscle contraction fails spectacularly when predicting the isometric muscle force after an active eccentric contraction, for example (Leonard & Herzog, 2010). While titin, a non-cross-bridge structure connecting the myosin filaments to the Z-disc (Figure 4.1*a*, top right schematic), is suggested to be a key player in explaining the differences between predictions and experiments (Heidlauf *et al.*, 2017, 2016; Noble, 1992; Nishikawa *et al.*, 2012; Rode *et al.*, 2009; Schappacher-Tilp *et al.*, 2015), there is still debate and an incomplete understanding with regard to the underlying force-producing mechanisms (Schappacher-Tilp *et al.*, 2015; Colombini *et al.*, 2007; Herzog *et al.*, 2008; Till *et al.*, 2010; Siebert & Rode, 2014). Many studies have reported a linear rise in tension for moderate muscle lengthening that is independent of contraction speed for whole muscles (Edman, 1979; Till *et al.*, 2008; Siebert *et al.*, 2015), across muscle fibre bundles (Pinniger *et al.*, 2006; Roots *et al.*, 2007), down to intact single fibres (Colombini *et al.*, 2007). These findings agree with the idea of a passive, spring-like contribution of, for example, titin to total muscle force. However, because a muscle's active force depends on myofilament overlap that leads to clearly visible pronounced slope changes of the active isometric force–length relationship (FLR) — especially at the fibre level (Figure 4.1*a*, (Gordon *et al.*, 1966)) — these different slopes and particularly the slope changes (marked with open circles in Figure 4.1*a*) should be reflected in sufficiently long isokinetic lengthening contractions. The currently reported linear force rise in lengthening contractions might have resulted from performing experiments on limited FLR regions of constant slope. Only one very long eccentric ramp comprising different slope regions of the FLR showing an unexpected linear force rise during the complete stretch has been reported (Till *et al.*, 2008). This group stretched a degraded whole muscle–tendon complex from 30% below to 40% above optimum fibre length. Such a linear behaviour deviates from the behaviour of classic muscle models, and it could simplify the control of muscles during locomotion. Some doubts remain as to whether this behaviour is a genuine

property of the contractile machinery of the muscle or is a result of degradation, three-dimensional muscle deformation, or interaction with elasticities outside of the fibre. Therefore, measurements at the muscle fibre level with extensive magnitudes of stretch seem suitable to clarify this. To better understand the underlying mechanisms of force production in lengthening contractions, it is useful to characterise the cross-bridge and non-cross-bridge contributions. A systematic limitation of cross-bridge force has been achieved by applying various amounts of the strong actomyosin-inhibitor 2,3-butanedione monoxime (BDM) to the activation solution (Herrmann *et al.*, 1992; Bagni *et al.*, 1992; Rassier & Herzog, 2004). BDM acts at the myofibrillar level directly and reversibly on the myosin heads (Higuchi & Takemori, 1989). A reduction in myosin ATPase slows the phosphate release and suppresses cross-bridge attachment even at low BDM concentrations (less than 1mM, mM represents mmol/l) (Bagni *et al.*, 1992; Higuchi & Takemori, 1989; McKillop *et al.*, 1994). Accompanied with reduced shortening speed and suppressed isometric tension, the entire contractile apparatus is inhibited (Herrmann *et al.*, 1992; Bagni *et al.*, 1992). This presumably allows a study of force effects that is nearly independent of cross-bridges when comparing forces obtained with and without BDM. The aim of this study was to investigate whether slope changes in the FLR (Figure 4.1*a*) would be visible in force traces of lengthening contractions of activated fibres as expected considering the sliding filament and cross-bridge theories (Gordon *et al.*, 1966; Zajac, 1989). A second goal was to separate cross-bridge and non-cross-bridge contributions to total muscle fibre force. To achieve these goals, *in vitro* isokinetic stretch experiments of maximally activated single skinned fibres from rat extensor digitorum longus (EDL) muscles were performed with extensive magnitudes of stretch comprising different characteristic ranges of the FLR. To separate forces, cross-bridge contributions were increasingly suppressed using BDM. We tested the hypothesis that the superposition of cross-bridge forces — in accordance with classic theories of contraction — and non-cross-bridge forces yield total fibre forces in eccentric contractions.

4.2 Methods

Muscle preparation, storage and activation techniques for permeabilised single muscle fibres are in accordance to Goldmann & Simmons (1984). These techniques have been illustrated in great detail in **Chapter 2**, section 2.2 *'Determination of skeletal muscle fibre properties'*.

4.2.1 Experimental protocol

All skinned fibre experiments were conducted at a constant temperature of 12 °C ± 0.1 °C. At 12 °C, the fibres proved very stable and able to withstand active lengthening protocols over an extended period of time as well as prolonged activations (Bottinelli *et al.*, 1996; Ranatunga, 1982, 1984). Each fibre was activated by calcium diffusion in the presence of ATP. The fibre was immersed in preactivating solution for 60 s for equilibration and afterwards in an activating solution (pCa = 4.5, free Ca^{2+} is sufficient to produce maximum force (Millar & Homsher, 1990)). This offered maximal activation that was characterised by a rapid rise in force until a plateau (defined as a change in force of less than 1% over a period of 1 s, achieved approx. 5 s after activation) was reached. Then, the fibre was stretched. Subsequently, fibres were immersed in relaxing solution for at least 450 s. Eccentric ramps comprised three blocks of repeated experiments. First, fibres (five rats, six fibres each) were actively stretched in randomised order from three different initial fibre lengths L_i (0.7, 0.85, and 1.0 L_0) with constant stretch amplitudes of 0.45 L_0 to corresponding end lengths L_e (1.15, 1.3, and 1.45 L_0), respectively. Second, fibres (six fibres of one rat, four fibres of two other rats each) were stretched in activating solution with varying concentrations (0, 2, 5, and 10 mM) of BDM in randomised order from L_i of 0.85 and 1.0 L_0 to corresponding L_e of 1.3 and 1.45 L_0, respectively. Third, a subset of the fibres from the first and second blocks of experiments as well as additional fibres were stretched in prolonged ramps from 0.7 L_0 to 1.45 L_0. To ensure structural and mechanical integrity of fibres in the experiments, the following criteria were applied

to discard fibres: *(i)* isometric force in reference contractions was decreased by more than 10%, *(ii)* abnormal behaviour of force traces, evidenced by artefacts, oscillations, or abrupt flattening was noted, and *(iii)* lesions, ruptures, or fibre contortion were identified visually. This procedure resulted in at least two valid experiments per rat in eccentric ramps of the first block starting at 0.7 L_0 and at least three valid experiments per rat in all other experimental conditions. All stretches were performed at a velocity of 11% maximum shortening velocity (v_{max}). The v_{max} was defined as 2.25 L_0/s, an average value of maximum unloaded shortening velocity of EDL muscles from young (three to six months, $v_{max} = 2.47 \pm 0.90$ L_0/s) and old (22-24 months, $v_{max} = 2.00 \pm 0.66$ L_0/s) female Wistar rats determined at 12 °C in a previous study by Degens *et al.* (1998). The 'cycling-protocol' by Brenner (1983) was used to conserve the structural and mechanical properties in maximally activated fibres over an extended period of time as well as to reduce sarcomere inhomogeneities. For calculating force degradation, isometric reference contractions at L_0 were performed before and after the ramp experiments. In eccentric contraction experiments, the isometric force in successive activations decreased at an average rate of 1.80% per activation.

4.2.2 Data processing and statistics

The length and force signals from the transducers were recorded at 1 000 Hz with an A/D interface (604A, Aurora Scientific, Canada). Real-time software (600A, Aurora Scientific) was used for data acquisition. Force values were divided by individual F_{im} and fibre length data divided by L_0. The mean L_0 was 0.73 ± 0.24 mm, the fibre cross-sectional area (CSA) was determined assuming an elliptical cross-section:

$$CSA = \frac{\pi hw}{4}, \tag{4.1}$$

with w defined as fibre width and h as fibre height. The CSA was $5\,017 \pm 1\,400\,\mu m^2$. The force – length traces were cut after the bump (100 ms after beginning the eccentric

ramps). For the first block of experiments, a linear regression model was used to estimate the slope of the force–length trace and the corresponding coefficient of determination of each eccentric ramp. Each rat's force–length slope (first block of experiments) and the force–length data using BDM (second block of experiments) were analysed using Gaussian linear mixed effect models accounting for repeated measurements per rat and per fibre. In addition, rat-specific variances of data were allowed (using the nlme package of the statistics software system R (Pinheiro *et al.*, 2014)).

To assess the effect of initial length on the slope of the force–length traces, an intercept-only model was compared with a model accounting for starting length as a factor using a likelihood-ratio test. To assess the nonlinearity of the force–length traces during eccentric ramps for different BDM concentrations, a hierarchical series of models incorporating linear and quadratic length effects, BDM concentration as a factor and their interactions was compared with likelihood-ratio tests. In both cases, assumptions were checked by plotting standardised residuals. For graphical display, all data are expressed as mean ± standard deviation (s.d.) across all valid experiments.

4.2.3 Solutions

Table 4.1 describes the solutions. The concentrations of components were calculated with the computer program of Millar & Homsher (1990). Cysteine and cysteine/serine protease inhibitors (*trans*-epoxysuccinil-L-leucylamido-(4-guanidino) butane, E-64, 10 μM; leupeptin, 20 μg/ml) were added to all solutions to preserve lattice proteins and thus sarcomere homogeneity (Linari *et al.*, 2007).

Solution compositions									
	TES	**$MgCl_2$**	**Na_2ATP**	**EGTA**	**Na_2CP**	**GLH**	**HDTA**	**CaEGTA**	**CK (U/ml)**
Relaxing	100	7.7	5.44	25	19.11	10	–	–	400 – 500
Preactivating	100	6.93	5.45	0.1	19.49	10	24.9	–	400 – 500
Activating	100	6.76	5.46	–	19.49	10	–	25	400 – 500
	KP	**$MgCl_2$**	**Na_2ATP**	**EGTA**	**IMID**	**GLH**	**PMSF**	**Glycerol**	**CK (U/ml)**
Skinning	170	2.5	2.5	5	10	–	0.2		–
Storage	170	2.5	2.5	5	10	10	0.2	50%	–

Table 4.1: Solution compositions. All concentrations are in mmol l^{-1}, except glycerol (v/v) and creatine phosphokinase. TES, *N*-tris[hydroxymethyl]methyl-2-aminoethanesulphonic acid; ATP, adenosine 5'-triphosphate disodium salt hydrate; EGTA, ethylene glycol-bis(2-aminoethylether)-N,N,N',N'-tetraacetic acid; CP, *N*-[Imino(phosphonoamino) methyl]-N-methylglycine; GLH, glutathione; HDTA, 1,6 diaminohexane-N,N,N',N'-tetraacetic acid; KP, potassium propionate; IMID, imidazole; PMSF, phenylmethanesulfonyl fluoride; 10 μM transepoxysuccinyl-L-leucylamido-(4-guanidino)butane (E-64) and 20 μg ml^{-1} leupeptin. pH (adjusted with KOH) was 7.1 at 12 °C. The ionic strength was 190 mM. CK was obtained from Roche (Mannheim, Germany); all other chemicals from Sigma (St Louis, MO, USA).

4.2.4 Calculations of cross-bridge and non-cross-bridge forces

Two methods (A and B) were used to separate cross-bridge and non-cross-bridge forces during lengthening contractions from the experimental data. Both assume that cross-bridges produce a constant average force during isokinetic stretch after an initial equilibration of cross-bridge distributions (Huxley, 1957a; Huxley & Simmons, 1971). The factor f_v corresponding to the applied constant stretch velocity was estimated to be 1.1 from Figure 4.2*a* by drawing a line through the linear part of the eccentric force of the ramp starting at the plateau of the FLR and taking the intercept value similar to Roots *et al.* (2007). Because the contribution of all cross-bridges depends on filament overlap only, this contribution should resemble the FLR scaled by f_v during stretch.

Moreover, BDM suppresses only a fraction f_{XB} of cross-bridges (this was assessed by comparing the initial isometric force with and without BDM); it reached 94% in the case of 10 mM BDM. Method A assumes that the active force during stretching is suppressed by BDM percentagewise like the isometric force. Furthermore, in methods A and B, we assumed that BDM does not affect the passive force and that the FLR is valid

during stretching, respectively. Hence, for method A, the difference between control force (Figure 4.3, black solid line) and BDM-suppressed force (Figure 4.3, solid coloured lines) was divided by f_v and f_{XB} to obtain the normalised, isometric force (Figure 4.3, coloured dashed lines). This can be compared with the FLR. In method B, the difference between control force and FLR multiplied with f_v (Figure 4.4, blue dashed line) was calculated to obtain the expected non-cross-bridge force that can be compared with the measured 10 mM BDM suppressed force.

4.3 Results

Neither the force–length traces of the isokinetic eccentric ramps starting from different initial lengths (Figure 4.2*a*) nor those of the long isokinetic eccentric ramps (Figure 4.2*b*) reflected the slope changes of the underlying FLR. In contrast, linear regression models fitted the linear force–length traces remarkably well (mean coefficient of determination of 0.99). This is in stark contrast to classic theories of muscle contraction. According to these theories, forces during isokinetic eccentric stretching resemble a scaled version of the FLR (ignoring the passive forces, which only start at long lengths, cf. Figure 4.2).

4.3.1 Slope increases slightly with initial length in isokinetic eccentric ramp experiments

A slight increase in stiffness for longer initial lengths is seen (Figure 4.2 *a*, black versus green line). Statistical analyses yielded significantly different estimated slopes (Table 4.2, model 1c) of 2.82, 3.02, and 3.15 F_{im}/L_0 for initial lengths of 0.70, 0.85, and 1.0 L_0, respectively. Stretching the fibre by 0.45 L_0 from each initial length resulted in a force increase by about 1.5 F_{im}. Thus, for eccentric contractions starting at L_0 (Figure 4.2 *a*, green line), eccentric forces of 2.5 F_{im} were observed in the descending limb of the FLR. This clearly exceeded the maximum active forces produced by cross-bridges at these lengths according to the sliding filament and cross-bridge theories.

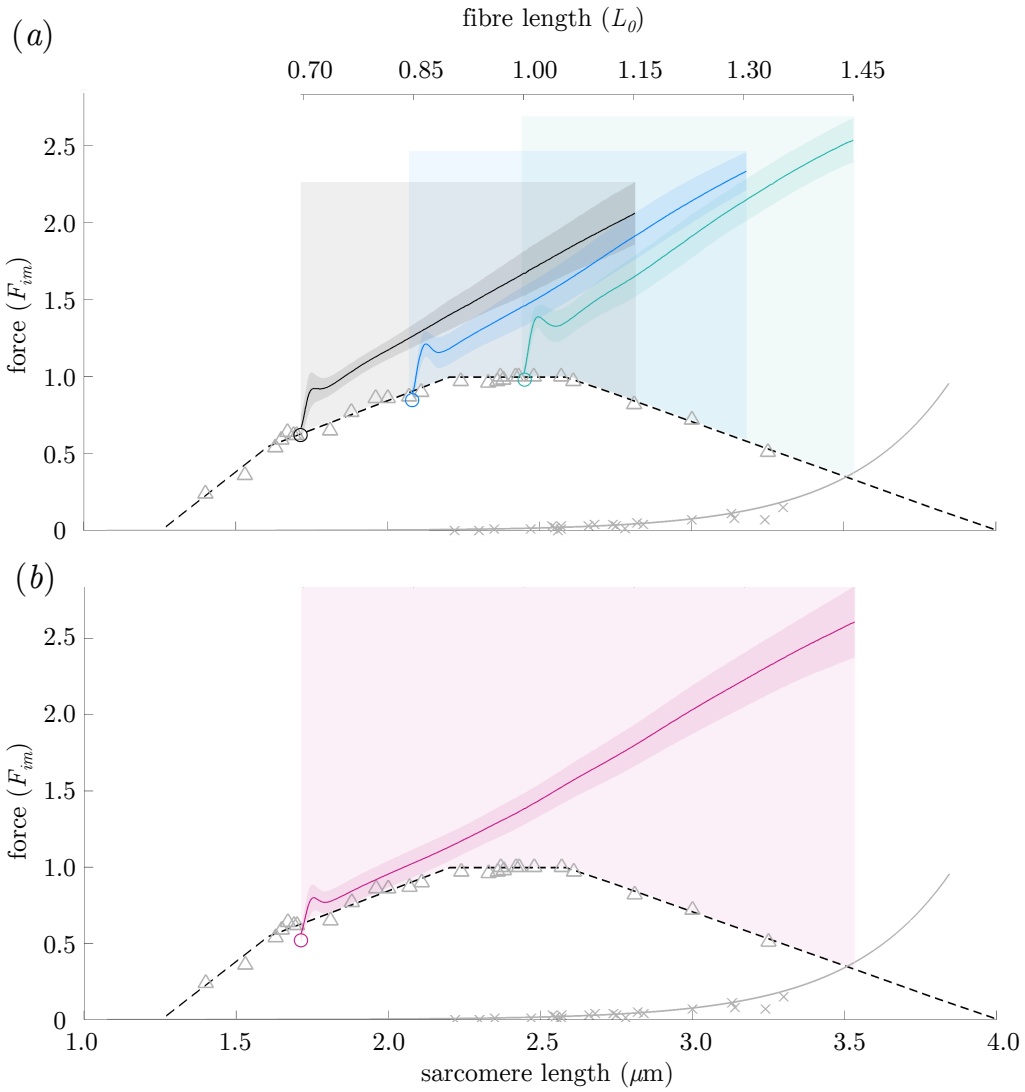

Figure 4.2: The mean ± s.d. of force–length traces of eccentric isokinetic contractions. Solid black, blue, and green lines indicate the means. The shaded regions around the solid lines indicate the corresponding s.d. during active stretching. (*a*) Eccentric ramps show a small bump followed by a linear force increase. The small bump after initiation of the stretch could be due to short range stiffness (Morgan, 1977) and passive properties of the fibre such as inertia or viscosity (Ford *et al.*, 1977). Eccentric ramps starting from 0.7, 0.85, and 1.0 L_0 comprise 17, 24, and 24 experiments, respectively. (*b*) Extensive ramps with stretch amplitude of 0.75 L_0 also show a linear force increase. Extensive ramps comprise 18 valid experiments. The stretch velocity is 11% v_{max} in all ramps. The force is normalised to F_{im} and length to L_0. Isometric pre-stimulation is not shown. Crosses and triangles indicate measurements of passive and active isometric fibre forces, respectively. For comparison, the active isometric sarcomere FLR (dashed line) and passive sarcomere force–length data (solid grey line) of fast single skinned fibres from EDL muscles, reported by Stephenson & Williams (1982) and Stephenson (2003), are shown. Comparison of statistical linear mixed effect models accounting for repeated measurements (refer to Table 4.2) revealed a significant increase in slope with initial length.

4.3.2 Determination of the effects of cross-bridge kinetics on eccentric force generation

Increasing BDM concentrations (2, 5, and 10 mM) decreased the maximum isometric forces to 0.33, 0.13, and 0.06 F_{im} at L_0, respectively (Figure 4.3 *b*). A similar suppression of cross-bridge forces was observed for 0.85 L_0 (Figure 4.3 *a*). Accordingly, forces during and at the end of the stretch decreased with increasing BDM concentrations (Figure 4.3, solid coloured lines). Interestingly, in contrast to the linear behaviour in the control experiments (Figure 4.3, coloured solid lines), increasing BDM increased the nonlinearity of the force response (Figure 4.3, coloured solid lines). In accordance with this, the estimated quadratic coefficients in model 2d (Table 4.2) describing the progressive nonlinear effect of force increased from 1.05 to 1.17 to 1.74 to 2.79 for ramps starting at 0.85 L_0 and from -1.2 to 2.6 to 4.1 to 5.5 for ramps starting at 1.0 L_0, respectively, for 0 to 2 to 5 to 10 mM BDM concentration.

Experiments	Model	Model name	d.f.	Likelihood-ratio	p-value
	slope ~ -1	1a	6		
block 1 (slopes)	slope ~ 1	1b	7	32.2	<0.0001
	slope ~ 1 + as.factor(init length)	1c	9	6.9	.0311
block 2	force ~ 1 + length	2a	7		
$L_i = 0.85\ L_0$	force ~ 1 + length × BDM	2b	13	350 806.2	<0.0001
(BDM)	force ~ 1 + length × BDM + (length^2)	2c	14	23 514.6	<0.0001
	force ~ 1 + (length + (length^2)) × BDM	2d	17	4 609.5	<0.0001
block 2	force ~ 1 + length	2a	7		
$L_i = 1\ L_0$	force ~ 1 + length × BDM	2b	13	290 509.6	<0.0001
(BDM)	force ~ 1 + length × BDM+(length^2)	2c	14	6 832.7	<0.0001
	force ~ 1 + (length + (length^2)) × BDM	2d	17	9 219.8	<0.0001

Table 4.2: Hierarchical statistical model comparisons. The likelihood-ratio statistics and p-values for subsequent model comparisons. To determine the effect of starting length on the slope of eccentric ramps (cf. Figure 4.2*a*), we tested if the slope differs from 0 (models 1a versus 1b) and if the slope changes with starting length by considering initial length as a factor (models 1b versus 1c). To check for a nonlinear effect of BDM on force in eccentric ramps (cf. Figure 4.3), data were tested for a nonlinear effect in force by adding a quadratic length effect to the model (models 2a versus 2b). It was then tested for improvement by adding BDM levels (model 2b versus 2c) and finally for interactions between BDM and length effects (models 2c versus 2d).

To investigate the cross-bridge contributions (method A), BDM-suppressed forces (Figure 4.3, coloured solid lines) were subtracted from the total forces of control ramps (Figure 4.3, black lines) and then divided by f_v and f_{XB}. The resulting normalised isometric forces (Figure 4.3, coloured dashed lines) reach about 1.2 F_{im} in their plateau region (Figure 4.3, indicated by blue vertical bars). Assuming that this plateau results from the underlying FLR, one of the most intriguing results of this investigation is the remarkable rightward-shift by approximately 15% (to between 2.85 and 3.05 μm sarcomere length) during active stretching versus the plateau region of the classic FLR.

Finally, our BDM results indicate that both the cross-bridge and non-cross-bridge components contribute nonlinearly to force production, and their forces sum up to a linear force response of activated muscle in extensive stretch contractions.

4.4 Discussion

The most surprising result of this study is the absence of changes in the eccentric force slope, while the underlying FLR does have slope changes. In contrast, in classic muscle models, i. e. models that incorporate the sliding filament and cross-bridge theories, the corresponding slope changes are clearly visible during stretch simulations because their predicted force represents a scaled FLR in isokinetic eccentric contractions. Experimental observations of linear force responses during stretching in the muscle fibres imply the following: *(i)* the physiology of eccentric muscle contraction is not completely understood, *(ii)* muscle models must be adapted and/or changed to represent muscle behaviour, and *(iii)* there may be advantages of positive stiffness of actuators (*in vivo* or in technics) with respect to control.

To date, eccentric force potentiation remains a matter of debate (Siebert & Rode, 2014; Campbell & Campbell, 2011; Edman, 2012). Only a limited number of existing ideas can potentially explain strongly increased forces during and after prolonged

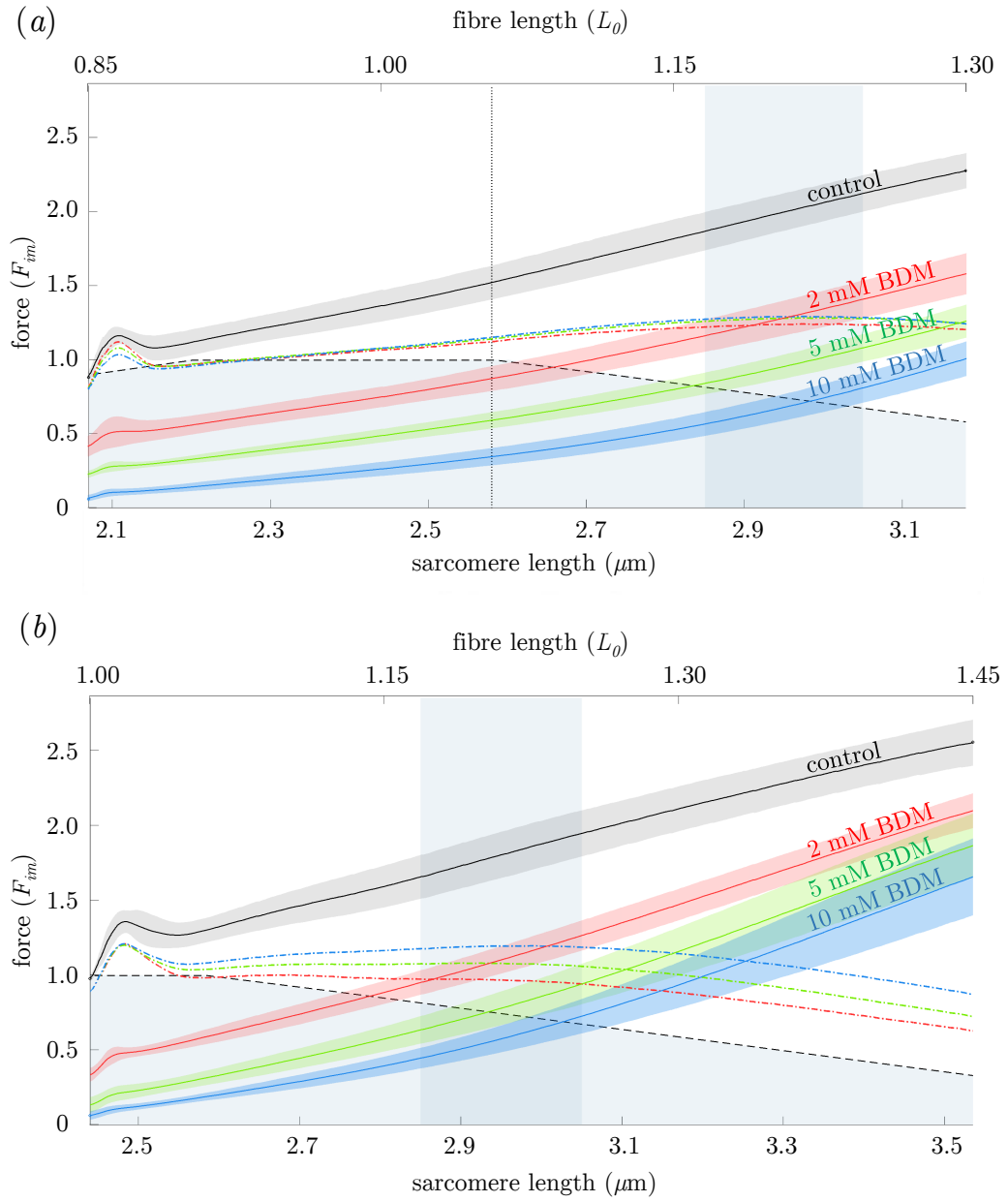

Figure 4.3: Force–length traces of eccentric isokinetic contractions at different BDM concentrations. Mean (solid line) and s.d. (shaded regions around solid lines) of control contractions (without BDM, black solid line) and contractions with increasing concentrations of BDM (2, 5, 10 mM, coloured solid lines) with stretch velocity of 11% v_{max} and initial fibre lengths of 0.85 L_0 (a) and 1.0 L_0 (b), respectively. Eccentric experiments comprised 14 valid experiments for each concentration of BDM. Coloured dashed lines represent scaled isometric cross-bridge forces underlying the ramp contractions (method A, see § 2f), which can be compared with the isometric FLR. Shaded rectangular areas indicate rightward-shifted plateau-region of FLR during eccentric contractions. Comparison of hierarchical statistical models (refer to Table 4.2) revealed increasing progressive nonlinearity with increasing BDM concentration.

stretching. Some have speculated that the classic cross-bridge dynamics (Huxley, 1957a) may be modified during eccentric contractions (Walcott & Herzog, 2008) that could not be validated in experiments so far (Mehta & Herzog, 2008). Alternatively, titin — a non-cross-bridge, cytoskeletal protein — might contribute to the enhanced force response during active stretch contractions, especially in the range of the descending limb of the FLR (Leonard & Herzog, 2010; Nishikawa *et al.*, 2012; Rode *et al.*, 2009; Edman, 2012; Heidlauf *et al.*, 2016). Combining a linear non-cross-bridge contribution with the idea that the isometrically determined FLR is not valid in eccentric contractions, Till *et al.* (2010) offered a model with constant, linear slope of force in eccentric contractions on the FLR's ascending limb (Figure 4.1*a*). They assumed that the myosin filament is compressed at short sarcomere lengths corresponding to the steep part of the ascending limb of the FLR, and that it retains its length in eccentric contractions. Additional assumptions were required to extend the resulting linear behaviour to other regions of the FLR. However, there are several strong arguments against myosin compression (refer to **Chapter 5**). To approach the physiological mechanisms, it is important to separate cross-bridge and non-cross-bridge contributions to total muscle force.

The calculated normalised and isometric force (method A; Figure 4.3, coloured dashed lines) shows distinct deviations from the typical FLR (Figure 4.3, black dashed line). Its plateau region is rightward-shifted by approximately 15% L_0 for starting lengths of 0.85 and 1.0 L_0; the plateau value is slightly increased. An arbitrarily higher f_v value of 1.3 applied during normalisation would decrease the maximal isometric force of the coloured dashed lines in Figure 4.3 to a mean 1.0 F_{im}; however, the differences between the coloured dashed lines remain. Consequently, the sum of classical FLR and non-cross-bridge forces deviates from the experimental total force response that is characterised by linearity. With the assumptions of method A, there are multiple and non-exclusive possible causes for this linearity. These include the alteration of the cross-bridge cycle during stretch, non-percentagewise effects of BDM on cross-bridge

forces during stretch, or even altered myofilament overlap. While the compliance of the myofilaments (Figure 4.1*a*, actin and myosin filaments) is low (less than 1% in active muscle at maximum isometric force) and their compliance accounts for about 70% of total active sarcomere compliance (Huxley *et al.*, 1994; Wakabayashi *et al.*, 1994), the Z-discs (Figure 4.1*a*) may still play an important role in explaining a rightward-shift of the plateau of the calculated normalised, isometric force (Figure 4.3, coloured dashed lines). In our contractions, forces exceeded the maximal isometric forces by up to 150% (Figure 4.3, black solid lines). Vertebrate muscle Z-discs transmit the forces between sarcomeres via a varying number of α-actinin-layers (Luther, 2009). Z-discs in fast-twitch fibred muscles transmit these forces via a lower number of α-actinins. This may result in increased serial compliance — narrow Z-discs in fast muscles are more prone to distortions and axial shifts of the myofilaments compared with Z-discs of slow muscles, which might be more rigid and able to maintain their structure (Burgoyne *et al.*, 2015).

If these α-actinins are subjected to a very high force, they may show increased compliance or even popping of some domains. In this case, the Z-disc is in series to titin and the myofilaments, which would lead to a rightward-shift of the plateau region (Rode & Siebert, 2009) of the FLR. Moreover, when accounting for this serial elasticity in calculations, the deviations between the FLR and the calculated, normalised isometric force would even increase (Rode & Siebert, 2009). However, this remains highly speculative because to the best of our knowledge, the behaviour of the Z-discs in longitudinal direction under high forces has not yet been investigated.

The calculated non-cross-bridge force (method B; Figure 4.4, blue dashed lines) is higher than its experimental counterpart (Figure 4.4, blue solid lines), although this counterpart contains about 6% active cross-bridges. Hence, under the assumptions of method B, BDM suppresses the non-cross-bridge force. Evidence is accumulating that the non-cross-bridge force production during active stretching is associated with titin and titin–actin binding (Leonard & Herzog, 2010; Rode *et al.*, 2009; Monroy *et al.*, 2017; Shalabi *et al.*, 2017; Powers *et al.*, 2014). To date, a conclusive understanding of the

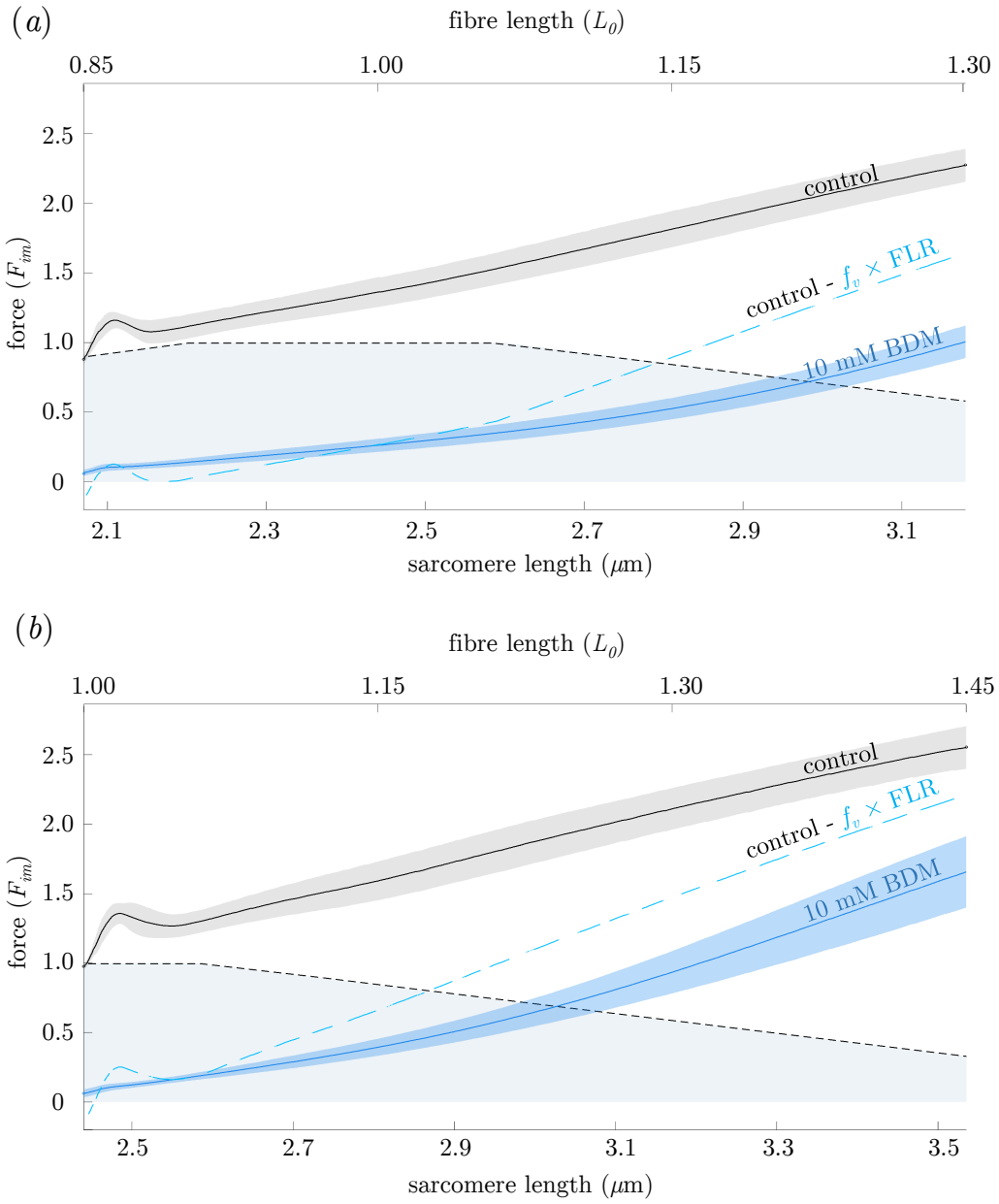

Figure 4.4: Comparison of theoretical and experimental non-cross-bridge force traces during eccentric contractions. Blue solid lines indicate depressed force responses (around 94% cross-bridges abolished) due to 10 mM BDM application (mean (solid lines) ± s.d. (shaded regions around solid lines) of 14 valid experiments) for eccentric ramps with stretch velocity of 11% v_{max} and initial fibre lengths of 0.85 L_0 (a) and 1.0 L_0 (b), respectively. The blue dashed lines are expected to have non-cross-bridge forces (method B, see section 4.2.4) assuming a valid isometric FLR (black dashed lines) during eccentric contraction.

mechanism(s) of actin–titin binding is still lacking (Shalabi *et al.*, 2017). Likewise, systematic studies of the effects of BDM on non-contractile proteins (e.g. titin or troponin) are missing. Hence, there is room for speculation. Recently, troponin C-depleted active myofibrils were reported to produce forces exceeding the passive force by only a small amount relative to active fibres (Powers *et al.*, 2014). Troponin C depletion means that no myosin binding sites are available on actin. This supports the myosin binding site-dependent (Rode *et al.*, 2009) or force-dependent (Nishikawa *et al.*, 2012) titin–actin binding. There are contradictory reports as to whether and how BDM influences the ability of non-cross-bridge force production in eccentric contractions (Rassier & Herzog, 2004; Powers *et al.*, 2014; Colombini *et al.*, 2016). In our experiments, deviations of coloured dashed lines from theoretical sarcomere FLR increased with increasing BDM concentration (especially in Figure 4.3 *b*), suggesting an effect of BDM on non-cross-bridge forces. Concluding, these considerations remain speculative and require further study.

While skinned EDL fibres can operate robustly at 12 °C (Bottinelli *et al.*, 1996; Ranatunga, 1982, 1984), they produce only about half the isometric force as at physiological temperature (Stephenson & Williams, 1985; Zhao & Kawai, 1994). Moreover, peak isometric force, time to peak force, and maximal shortening velocity decrease linearly with temperature. Thus, under physiological conditions, the cross-bridge contributions in ramps will be roughly twice as high. A reduced number of available binding sites might cause the decrease in isometric forces (Stephenson & Williams, 1981). Depending on the so far unclear mechanism of titin–actin binding (Shalabi *et al.*, 2017), such a reduction in available binding sites might hamper the ability of fibres to produce non-cross-bridge force in eccentric contractions (Nishikawa *et al.*, 2012; Rode *et al.*, 2009). Further studies are required to clarify whether non-cross-bridge contributions to force also scale with temperature.

The observed linear elastic behaviour (according to Hooke´s law) of muscle during large stretches regardless of the (even negative) slope of the underlying FLR might

also stimulate interest in biologists and roboticists investigating locomotion. Because of the important uses of compliance in locomotion (Alexander, 1990), the concept of series elastic actuators mimicking muscles has been introduced (Pratt & Williamson, 1995) and applied in the last decades (Hutter *et al.*, 2013) in robotics. What might have seemed to be a simplistic approach, namely to represent muscle behaviour by means of motors in series with springs, may actually represent observed muscle behaviour during stretch very well. For example, if the resting length of the motor spring is set to a fixed length and locked in a robotic leg before touchdown, the response of the spring to the subsequent stretch in the loading phase mimics that of a fully activated muscle in our experiments. This finding adds not only to the credibility of robotic models employing series elastic actuators as tools to understand biological motion, for example, when investigating and demonstrating simple control strategies like, for example, switching of resting lengths (Lakatos *et al.*, 2014, 2016), but also to the interpretation of neuro-muscle-mechanical models investigating control in locomotion using classic muscle models (Geyer & Herr, 2010).

4.5 Conclusion

The results support the idea of a cumulative mechanism that combines nonlinear cross-bridge and non-cross-bridge effects to result in a linear force response during muscle lengthening contractions. This linear muscle behaviour potentially facilitates control in biological locomotion. Our approach does not clearly separate non-cross-bridge and cross-bridge contributions because BDM seems to affect the non-cross-bridge and cross-bridge force. Accordingly, alternative inhibitors should be considered for further studies attempting to separate cross-bridge and non-cross-bridge contributions (Ostap, 2002; Cheung *et al.*, 2002).

Chapter 5

Myosin filament sliding through the Z–disc relates striated muscle fibre structure to function[3]

5.1 Introduction

As motors of life, muscles convert chemical energy into mechanical energy and heat. Muscles transport substances within the body, stabilise the skeleton and enable locomotion. The first property characterising the mechanical function of striated muscles to be described (Blix, 1891) was the active isometric force–length relationship. This property shows the maximal forces the striated muscle fibre can produce by electrical stimulation at different constant lengths. The classic FLR (Figure 5.1, straight lines) (Gordon *et al.*, 1966) with its strikingly linear segments has been described not only up to the fibre level but also for the whole muscle (Rode & Siebert, 2009; Winters *et al.*, 2011). Despite the fact that this relationship represents basic textbook knowledge for life science students, to date a convincing structural model explaining the shape of the

[3]Rode C., Siebert T., Tomalka A., Blickhan R. *Proc Biol Sci.* 2016 Mar 16;283(1826).

entire FLR does not exist.

According to the sliding filament (Huxley & Hanson, 1954; Huxley & Niedergerke, 1954) and cross-bridge (Huxley, 1957a) theories, actin and myosin filaments slide relative to each other in response to forces generated by temporary cross-bridges formed by myosin heads — projecting from the myosin filaments — and actin filaments.

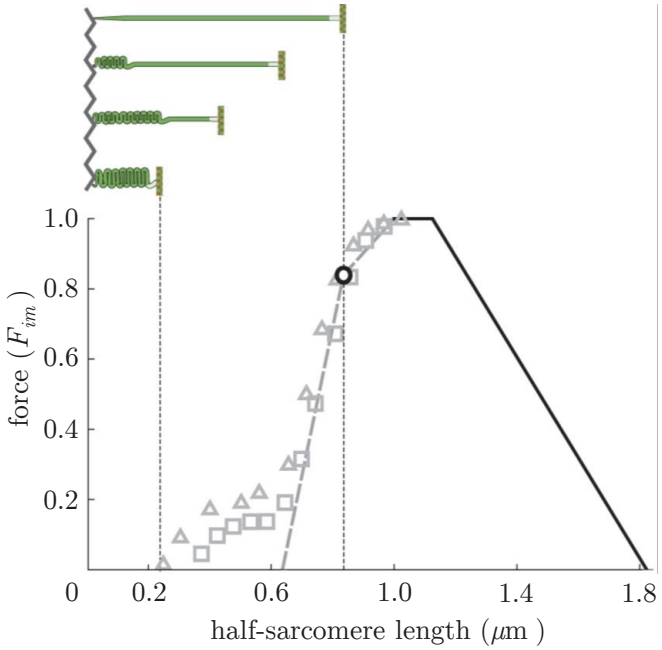

Figure 5.1: Isometric force over half-sarcomere length. Force is given as a fraction of maximum isometric force (data by Gordon *et al.* (1966) approximated as straight lines; data by Ramsey & Street (1940) shown for two specimen as squares and triangles, respectively). The descending limb and the plateau (black lines) of this curve are directly predicted by the sliding filament (Huxley & Hanson, 1954; Huxley & Niedergerke, 1954) and cross-bridge theories (Huxley, 1957a). The slope change on the ascending limb (black circle) is related to the fibre length where myosin filaments reach the Z-disc. Explanation of the grey data is subject to scientific discussion (see text). The schematic half-sarcomere (top) — bounded by Z-disc (zigzag line) and M-line (vertical line) — illustrates required myosin filament (horizontal bar) compression or folding following the typical assumption that myosin filaments cannot penetrate the Z-disc.

This yields straightforward geometric explanations for the plateau region and for the region of decreasing isometric force based on filament lengths (Figure 5.1, black lines) (Gordon *et al.*, 1966). The slope change (Figure 5.1, black circle) in the range of

increasing isometric force (ascending limb) is typically related to myosin filaments hitting the Z-disc, a thin-meshed filament structure (Knapppeis & Carlsen, 1962) defining the sarcomere boundary. It is, however, not clear which mechanism(s) are responsible for the decrease in force in the shallow and the steep slope regions of the ascending limb of the FLR (Gordon *et al.*, 1966; MacIntosh *et al.*, 2006; Allen & Moss, 1987; Scott *et al.*, 1996; Trombitas & Tigyi-Sebes, 1985).

More specifically, until now the ascending limb's steep slope is typically explained with myosin filament folding or compression (Figure 5.1, top left scheme), and a possibly decreasing number of cross-bridges (Gordon *et al.*, 1966; MacIntosh *et al.*, 2006; Trombitas & Tigyi-Sebes, 1985). An alternative recent explanation considers two-dimensional force production of cross-bridges (Williams *et al.*, 2013). Ignoring that myosin filaments reach the Z-disc at the point of slope change on the ascending limb (Figure 5.1, circle), their model predicts that the increasing filament lattice spacing leads to a considerable reduction in longitudinal force, explaining the slope of the steep part of the ascending limb. However, several studies suggest a minor impact of lattice spacing compatible with the whole working range of the fibre on longitudinal force (Millman, 1998; Gulati & Babu, 1985). In conflict with the ideas of an internal counteracting compression spring or lattice spacing being responsible for the steep slope of the ascending limb, Ramsey & Street (1940) reported a pronounced FLR foot region for short fibre lengths (Figure 5.1, symbols) produced in experiments with prolonged stimulus duration. Several phenomena were observed during and after fibre contractions within this range. Tension developed very slowly at short fibre lengths and was lower after re-elongation of the fibres. Moreover, unlike their regular behaviour, fibres did not restore their resting length after cessation of activation. These observations cannot be explained by myosin filament compression, lattice spacing or by a decreasing number of available cross-bridges, and hence seemingly contradict the classic sliding filament and cross-bridge theories of muscle contraction at these lengths.

Here we develop a model consolidating structural and micromechanical data that can explain the entire FLR and resolve the apparent conflicts between experimental evidence and classic theories of contraction. The few required model parameters are taken from the literature or set by structural arguments. The model suggests mechanical causes for the tetragonal arrangement (Knapppeis & Carlsen, 1962; Luther, 2000) of actin filaments at the Z-disc (in contrast with their hexagonal arrangement in the typical actin–myosin filament overlap), for the so far unknown function of the second myosin head (Huxley, 2000), and for the ability of myosin heads to form cross-bridges with actin filaments of opposite polarity (Toyoshima *et al.*, 1989; Reedy *et al.*, 1989).

5.2 Myosin filament sliding through the Z-disc

The core of the model developed here is the idea that myosin filaments slide through the meshed Z-disc (Figure 5.2 (Hagopian, 1970)) instead of being compressed or folded at short sarcomere lengths as typically assumed. This leads to several new types of actin–myosin filament overlap (Figure 5.3 *b–e)* affecting force production.

In the following, we first introduce structural and geometrical arguments supporting the suggested mechanism and subsequently explain our model and its predictions (see Appendix B for mathematical details of the model). The sliding of myosin filaments through the Z-disc requires a highly organised and sensibly adjusted geometry. First, the actin filament arrangement near the meshed Z-disc should be able to accommodate twice the number of myosin filaments within one half-sarcomere. The cross-section of the typical actin–myosin overlap region reveals a hexagonal arrangement of actin filaments with a myosin filament centred in each actin hexagon (Figure 5.3 *a*, cross-section **) (Knapppeis & Carlsen, 1962; Huxley, 1957b). Rearranging the actin filaments to a new regular lattice to accommodate twice the number of myosin filaments would require a tetragonal arrangement of actin filaments. Indeed, actin filament arrangement is tetragonal (square-cut) on either side of the meshed Z-disc (Figure 5.3 *a*, cross-section*)

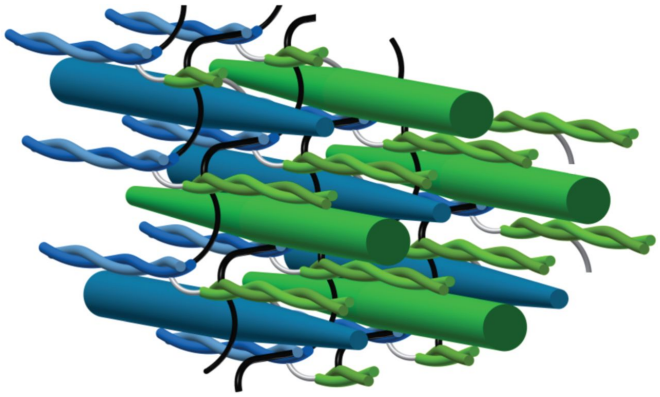

Figure 5.2: Myofilament arrangement after myosin filament sliding through the Z-disc. α-actinin molecules (black and grey) cross-link the tetragonal actin filament (helices) grids of opposite half-sarcomeres (green and blue, respectively) to form the Z-disc structure. Actin grids of opposite polarity are assumed to align as a consequence of myosin filament (thick rods) sliding through the Z-disc. Myosin filaments fill the previously empty spots within the chequered actin filament grid of the adjacent half-sarcomere. For further details on the sliding process, the Z-disc structure and the alignment of the actin grids, see text (see also Figure 5.3; and electronic supplementary material online under: http://rspb.royalsocietypublishing.org/content/royprsb/suppl/2016/02/29/rspb.2015.3030.DC1/rspb20153030supp1.pdf (Figure S1 and text S1)).

(Knapppeis & Carlsen, 1962; Luther, 2000). Moreover, myosin filaments should be guided to form a regular pattern embedded in the tetragonal actin grid before reaching the Z-disc to enable orderly sliding through the Z-disc. Titin may be involved in fulfilling this task. Titin anchors myosin filaments to the Z-disc, and two titin molecules connect to each actin filament within the Z-disc (Zou *et al.*, 2006). Because the ratio of actin to myosin filaments is 2 : 1 in regular overlap (Figure 5.3 *a*, cross-section**), the ratio of titin proteins to myosin filaments is 4 : 1. A simple possible symmetry (accounting for the two titin molecules per actin filament) in the myofilament arrangement is when each myosin filament connects via four titin proteins to four actin filaments forming the vertices of a square, resulting in a centred chequered arrangement of myosin filaments within the tetragonal actin grid. This arrangement would facilitate highly organised myosin filament sliding through the Z-disc, with the myosin filaments possibly entering the empty squares within the actin filament grid of the adjacent half-sarcomere (Figure 5.2).

Although a comparably dense structure (Zou *et al.*, 2006), the Z-disc adapts in diameter when the muscle changes in length (e.g. Huxley (1953)) and is essentially porous (Luther, 2000). Actin filament ends of opposite polarity are cross-linked by α-actinin (35 nm long molecules), forming a flexible basket weave pattern in activated muscle (Luther, 2000; Goldstein *et al.*, 1988). This structure offers a sufficient number of channels required for myosin filaments passing the Z-disc (Figure 5.2; electronic supplementary material, Figure S1). However, preceding the proposed sliding, actin filament grids of opposite polarity from neighbouring sarcomeres are not aligned at the Z-disc but are shifted by half a grid cell (approx. 20 nm; electronic supplementary material, Figure S1). Subtleties within the Z-disc structure (Luther, 2000) break the symmetry of the basket weave pattern, which may help to align the neighbouring actin filament grids during the sliding process (see electronic supplementary material, Figure S1 and text S1). This may result in a myofilament configuration after sliding through the Z-disc similar to that shown in Figure 5.2.

Tapered myosin filament ends (Luther & Squire, 1981) facilitate entering the meshed Z-disc and help to take advantage of subtle asymmetries mentioned above. Moreover, with shortening, the width of a sarcomere increases due to the preservation of volume in muscle (Swammerdam, 1737). Similarly, the Z-disc may expand laterally by unfolding its spatial zigzag structure facilitated by lower forces pulling on the actin filaments (Figure 5.1), making room for the increasingly thicker myosin filaments sliding through the Z-disc. Despite the increased number of filaments in the developing overlaps (Figure 5.3 *b–e*), the lateral distance between actin and myosin filaments would be at least 90% of their distance at optimal length in the regular overlap arrangement (see electronic supplementary material under: http://rspb.royalsocietypublishing.org/content/royprsb/suppl/2016/02/29/rspb.2015.3030.DC1/rspb20153030supp1.pdf, text S2).

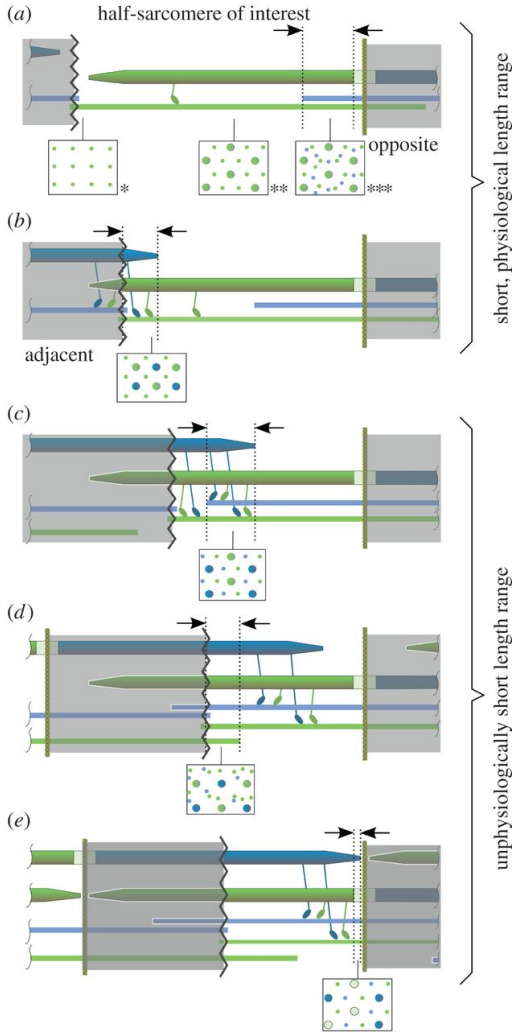

Figure 5.3: Schematic of proposed myosin (thick) and actin (thin) filament sliding. (*a*) Known (Knapppeis & Carlsen, 1962; Huxley, 1957b; Trombitas & Tigyi-Sebes, 1985) (cross-sections *, **, ***) and (*b–e*) hypothesised filament arrangements and cross-sections evolving during half-sarcomere shortening. (*a*) Starting from the plateau of the FLR, actin filaments from the opposite half-sarcomere passing the M-line enter the regular actin–myosin overlap, leading to actin–actin–myosin overlap. (*b*) Then myosin filaments from the adjacent half-sarcomere slide through the Z-disc, and a myosin–myosin–actin overlap zone evolves. (*c*) At even shorter length, the myosin–myosin–actin overlap zone meets the forthcoming actin–actin–myosin overlap zone, leading to actin–actin–myosin–myosin overlap. (*d*) Subsequently, actin filaments from the adjacent sarcomere enter the half-sarcomere of interest, leading to actin–actin–actin–myosin–myosin overlap. (*e*) Finally, the tips of myosin filaments from the adjacent half-sarcomere enter the myosin bare zone of the sarcomere of interest and eventually meet the M-line, where contraction is assumed to stop. Myosin heads projecting from the myosin filaments adjust to the polarity of the actin filament (Toyoshima *et al.*, 1989; Reedy *et al.*, 1989). Same-colour myosin and actin filament represent relative filament orientation in regular overlap. During a shortening contraction, myosin heads interacting with actin of the same colour act concentrically, while myosin heads interacting with actin of a different colour act eccentrically.

5.3 The model and its predictions

In our half-sarcomere model, active isometric force is proportional to the effective actin–myosin overlap length where force can be generated by cross-bridges. This effective length refers to the standard hexagonal arrangement of actin filaments surrounding each myosin filament (Figure 5.3 *a*, cross-section **). Different overlaps (indicated by arrows in Figure 5.3) contribute with different strength to force production. In the actin–actin–myosin overlap (5.3 *a*; the number of repetitions of the filaments' names in the description of overlaps refers to the number of filaments in relation to regular overlap, i.e. actin–actin–myosin overlap contains twice the number of actin filaments and the identical number of myosin filaments like the regular overlap region), actin is abundant and seems to impede force production (Trombitas & Tigyi-Sebes, 1985). This result is extrapolated to the newly developing overlap in Figure 5.3 *d*, where actin filaments are also abundant. Because actin polarity determines the direction of action of the cross-bridges (Toyoshima *et al.*, 1989; Reedy *et al.*, 1989), half of the cross-bridges in the remaining overlaps (Figure 5.3 *b,c,e*) would tend to shorten the sarcomere while the other half, the swivelled cross-bridges (Reedy *et al.*, 1989), would tend to lengthen the sarcomere (Figure 5.4). Assuming that the swivelled cross-bridges produce the same force as their regular counterparts, the resulting isometric force in these overlaps equals zero, and the model generates an FLR (Figure 5.5, *prediction I*) remarkably similar to the classic FLR (grey dotted lines).

However, the cross-bridge is much softer in pushing than in pulling (Kaya & Higuchi, 2010) (Figure 5.4). From experimental data (Kaya & Higuchi, 2010; Brunello *et al.*, 2014; Finer *et al.*, 1994), we estimate (see electronic supplementary material under: http://rspb.royalsocietypublishing.org/content/royprsb/suppl/2016/02/29/rspb.2015.3030.DC1/rspb20153030supp1.pdf, text S3) that the pushing force of a swivelled cross-bridge in an isometric contraction is approximately half the pulling force of a regular cross-bridge. Considering further the number of myosin filaments

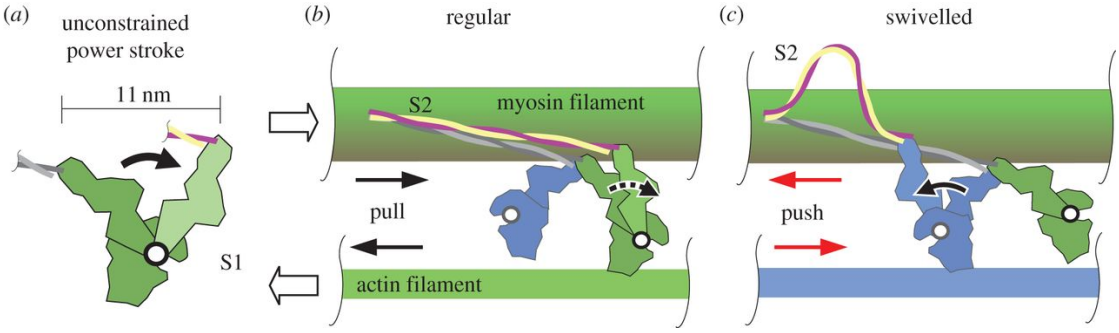

Figure 5.4: Illustration of proposed cross-bridge action. (*a*) The full, unconstrained power stroke of the myosin S1 region covers 11 nm (Swammerdam, 1737). (*b*) The two myosin heads of one myosin molecule are shown in green and blue, respectively. Stiff myofilaments (actin and myosin) and no relative myofilament movement are assumed in an isometric (constant length) contraction. During the regular cross-bridge power stroke of the green myosin head, its S1 region performs a substep of the unconstrained power stroke and deforms itself because the S2 region is stiff when pulled (Kaya & Higuchi, 2010; Brunello *et al.*, 2014). The cross-bridge force tends to shorten the sarcomere (relative filament movement for fibre shortening indicated by unfilled arrows). (*c*) The swivelled cross-bridge (blue) is formed because of flipped polarity of actin filaments (blue) compared with that in regular overlap. In contrast with the regular cross-bridge, the swivelled cross-bridge pushes the myofilaments, tending to elongate the sarcomere (red arrows). This leads to compression and buckling of the S2 region as a consequence of the power stroke because of low S2 compressive strength (Kaya & Higuchi, 2010).

interacting with each actin filament for each overlap, the model predicts an FLR (Figure 5.5, *prediction II*) that corresponds well with the classic experimental FLR, an — in the foot region below the length of classic zero force — with the data of Ramsey & Street (1940) (Figure 5.5, symbols).

5.4 Discussion

Our simple muscle model effortlessly explains the stunning linearity of the segments of the classic force–length relationship of striated muscle (Figure 5.5, *Prediction I*). It is based on the idea that myosin filaments slide through the Z-disc (Hagopian, 1970) (Figure 5.2) instead of being compressed or folded at the Z-disc as commonly assumed. By this elegant mechanism, the muscle can maintain its highly organised structure at short lengths (Figure 5.5, range B) occurring regularly during daily activities (Burkholder &

Lieber, 2001). Considering decreased swivelled relative to regular cross-bridge forces, the model predicts as yet puzzling force production at lengths shorter than the length of classic zero force (Ramsey & Street, 1940) (Figure 5.5, *Prediction II*, ranges C–E). It seems noteworthy that the good agreement of the model predictions and data were achieved without fitting of parameters; instead, parameters were obtained from the literature or set by structural arguments (cf. Appendix B). Decreased relative swivelled cross-bridge force decreases the FLR's ascending limb's slope in our model (Figure 5.5).

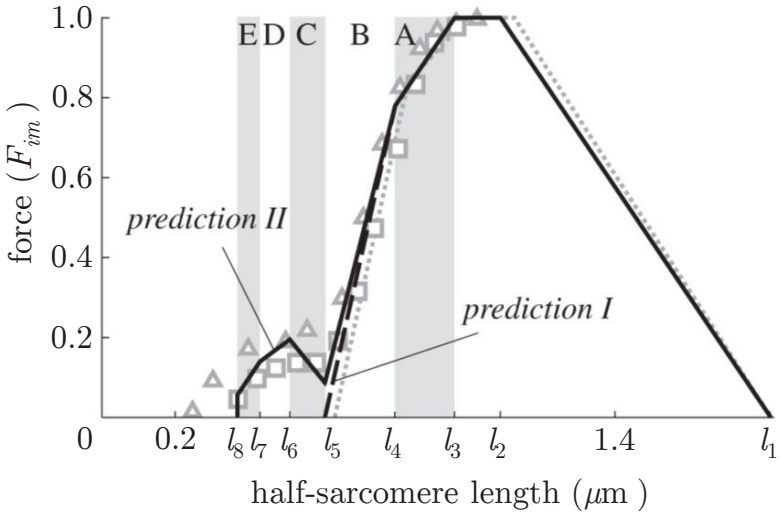

Figure 5.5: Comparison of model-predicted force–length relationship (black lines) and data (grey). *Prediction I* assumes that regular and swivelled cross-bridges produce equal forces. *Prediction II* assumes that swivelled cross-bridges produce half the force of regular cross-bridges (see Figure 5.4; electronic supplementary material, text S3). Overlap regions with abundant actin are assumed to produce no force (Trombitas & Tigyi-Sebes, 1985). Parameters used for the geometric model are myosin filament length 1.6 μm (Craig, 1977), bare region length of the myosin filaments 0.125 μm (lower range of reported values) (ter Keurs *et al.*, 1984), Z-disc width 0 μm, and actin filament length 1.025 μm (calculated from fully extended sarcomere length l_1 3.65 μm, (Gordon *et al.*, 1966)). Ranges A–E correspond to Figure 5.3 *a*–*e*, half-sarcomere lengths l_1–l_8 correspond to equation (A2).

This effect may be compensated by increasing filament lattice spacing tending to increase the slope in this range (Williams *et al.*, 2013). Although direct micrographic evidence is scarce (Hagopian, 1970), a range of micromechanical, biophysical and structural evidence supports the theory.

5.4.1 Flexural stiffness of myofilaments

The suggested mechanism relies on sufficient flexural stiffness of the myofilaments. The myosin filaments should not buckle when passing the Z-disc (Figure 5.2) or when transmitting compressive force due to eccentric cross-bridges (Figure 5.3 *b*–*e*). Conservative estimates of critical buckling force of myosin filaments based on experimental data (see electronic supplementary material, text S4) yield values of 0.90 – 1.33 nN, about three to four times the maximum isometric force in a myosin filament (Rode *et al.*, 2009). Moreover, muscle force decreases with contraction speed (Hill, 1938). Hence myosin filament buckling seems rather unlikely; vice versa, myosin filament stiffness seems to be a crucial filament property, suggesting that myosin filaments cannot be folded or even compressed at the meshed Z-disc.

In comparison, actin filaments are much more flexible (approx. 70-fold) than myosin filaments (Miller *et al.*, 2010). Still, actin filaments are sufficiently stiff to pass the sarcomere's M-line, and — after unphysiological detachment from the Z-disc — they can be pushed like rods to the opposing Z-disc by cross-bridges acting at their ends (Trombitas & Tigyi-Sebes, 1985). Their flexural stiffness may become relevant within range C (Figure 5.5) when swivelled cross-bridges would compress actin filaments (Figure 5.3 *c*, green myosin head on blue actin filament).

5.4.2 Prediction of maximum contraction velocity

Otherwise constant maximum contraction velocity of sarcomeres in regions of zero passive force is known to decrease linearly for half-sarcomere lengths shorter than length l_4 (Edman, 1979) (Figure 5.6, symbols). Swivelled cross-bridges (Figure 5.4 *c*) formed when myosin filaments slide through the Z-disc into the adjacent half-sarcomere during half-sarcomere shortening slow down the contraction. Accounting for the force – velocity relation of muscle (Hill, 1938; Till *et al.*, 2008), our model even quantitatively predicts the reported behaviour of maximum contraction velocity in frog muscle (Figure 5.6, *prediction III*; see electronic supplementary material under:

http://rspb.royalsocietypublishing.org/content/royprsb/suppl/2016/02/29/rspb.2015.3030.DC1/rspb20153030supp1.pdf, text S5), which supports the concept of myosin filament sliding through the Z-disc.

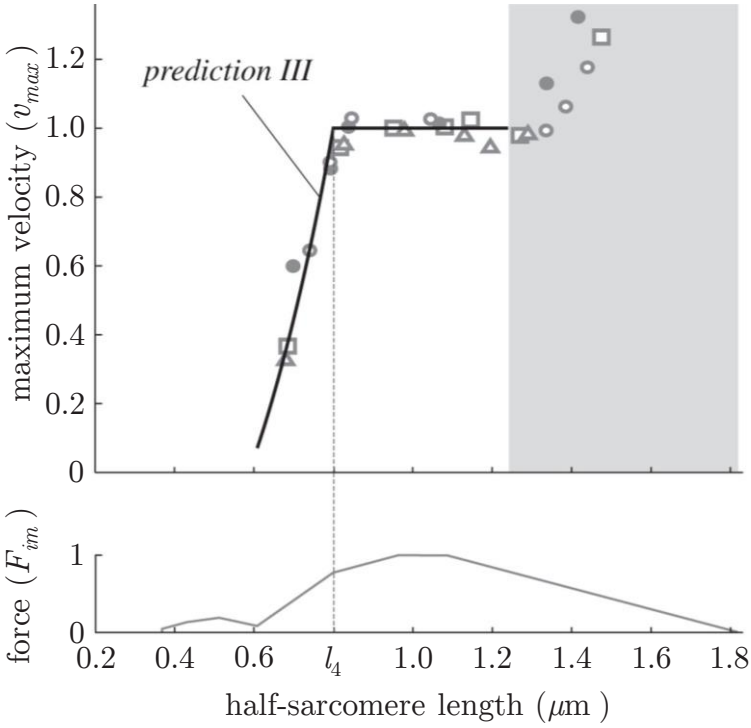

Figure 5.6: Comparison of model-predicted maximum half-sarcomere contraction velocity (black line) and data (symbols (Edman, 1979)). The model and the data show a similar decrease of maximum contraction velocity for half-sarcomere lengths smaller than l_4. For orientation, the force–length relationship is depicted below. The maximum half-sarcomere contraction velocity is normalised to v_{max}, its value in the plateau range of the force–length relationship. The increase in maximum contraction velocity in the grey shaded area stems from passive forces (Edman, 1979) not considered in our model.

5.4.3 'Strange' behaviour of muscle fibres

In early kinetic experiments on muscle fibres, Ramsey & Street (1940) reported puzzling behaviour of muscle fibres at very short fibre lengths (Figure 5.5, ranges C–E) and postulated that fibres enter a so-called 'delta state'. The described slow development of force when entering range C coincides with the development of the new myosin–myosin–actin–actin overlap (Figure 5.3 *c*). Considering the flexural stiffness of the myofilaments (see above), it is unclear how this presumed overlap should seamlessly develop from the two different adjacent overlaps with triangular myosin filament lattice on one side (actin–actin–myosin overlap; Figure 5.3 *a*, cross-section ***) and tetragonal myosin filament lattice on the other side (myosin–myosin–actin overlap; Figure 5.3 *b*). Myofilaments might interlock due to increased friction as a result of disordered filament sliding. This could be a contributing factor to the explanation of why fibres did not restore their resting length after cessation of activation (Ramsey & Street, 1940). If such a fibre is re-elongated, locked half-sarcomeres may, one by one, pop to a long length where passive half-sarcomere structures would take up the stretching force. In a subsequent end-held isometric contraction, the fibre might exert less force than expected (as observed by Ramsey & Street (1940)) because of overstretched half-sarcomeres and compensating motions of half-sarcomeres accompanying force equilibration. Accordingly, if the whole fibres would be passively overstretched after entering the 'delta state', all stuck half-sarcomeres would elongate and they would restore their resting length, as seen in experiments (Ramsey & Street, 1940).

Myosin-binding protein C, a thick filament protein that presumably bridges actin and myosin filaments (Luther *et al.*, 2011), may also contribute to the described phenomenon of locked half-sarcomeres. Intriguingly, in frog myosin filaments this large protein occurs in 43 nm intervals from approximately 250 to 500 nm (measured from the M-line) along the myosin filament (Luther *et al.*, 2011). Hence, according to our model, the first layer of myosin-binding protein C would reach the Z-disc in range C (Figure 5.5).

It is feasible that over time myosin-binding protein C gets pulled through the Z-disc in activated muscle and then prevents passive re-elongation of the muscle to resting length when activation ceases (e.g. due to friction).

Although performed in part at unphysiological lengths, the measurements by Ramsey & Street (1940) potentially contain important clues to the functioning of the contractile machinery of the muscle fibre in the physiological range. Because some doubt remains with respect to reproducibility and hence relevance of the findings by Ramsey & Street (1940) obtained with frog muscle fibres for the general functioning of vertebrate muscle fibres, we repeated parts of their experiments with fibres of the rat M. extensor digitorum longus (Figure 5.7). We likewise found considerable force development of the fibres for long duration of activation at lengths shorter (0.53 μm half-sarcomere length) than classical zero force (0.63 μm half-sarcomere length; Figure 5.1 (Gordon *et al.*, 1966)). Also, fibres did not restore their resting lengths and produced less force when re-elongated, but full force after being passively overextended. Moreover, Schoenberg & Podolsky (1972) also measured forces at half-sarcomere lengths of 0.5 – 0.6 μm. There is increasing evidence that these results are not artefacts but properties of vertebrate fibres; myosin filament sliding through the Z-disc is an appealing possibility that reconciles them with current theories of contraction.

5.4.4 Swivelled cross-bridges and evolution

More than half a billion years ago, striated muscles presumably appeared in our prebilaterian ancestors (Seipel & Schmid, 2005). Prior to the existence of exo- and endoskeletal structures, muscles probably adhered to gelatinous material such as is present, for instance, in sponge and jellyfish (Seipel & Schmid, 2005). Therefore, the muscle had to be equipped with a safety mechanism preventing extreme shortening and muscle malfunction, as described above. The swivelled cross-bridges damping muscle contraction at short lengths represent such a safety mechanism.

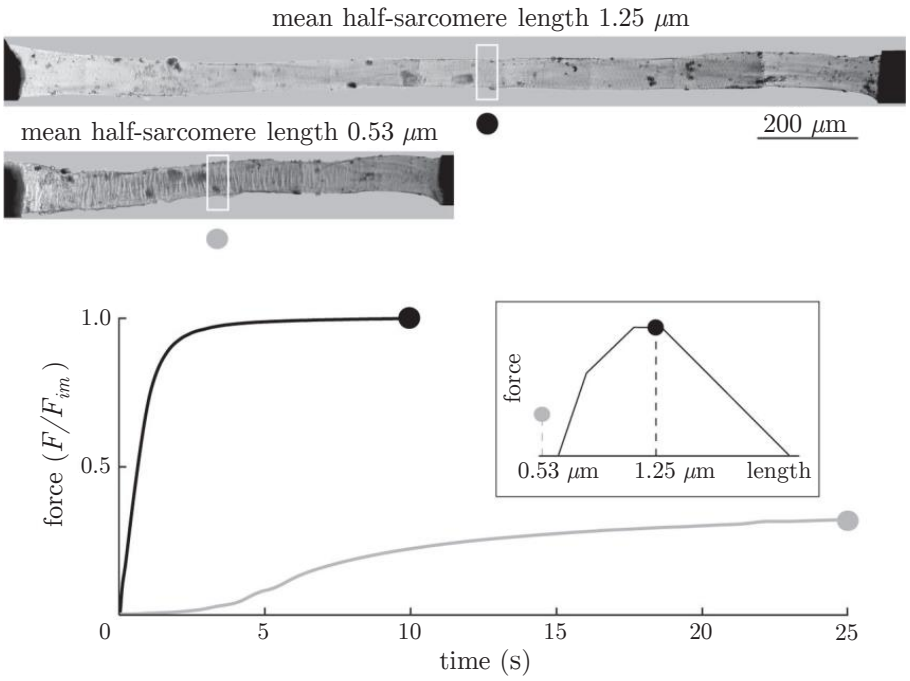

Figure 5.7: Isometric measurements with a segment of a single muscle fibre of rat M. extensor digitorum longus show considerable force at lengths below classic zero force for extended activation. Force – time traces generated by the muscle fibre at optimum (1.25 μm, black line) and short (0.53 μm, grey line) half-sarcomere lengths. Preparation and fixation of fibres followed the protocol of Goldmann & Simmons (1984) (cf. section 2.2 for details). The permeabilised fibre was maximally (pCa 4.5) activated for 10 s and 25 s at 1.25 μm and 0.53 μm, respectively, at 12 °C. Force was measured using a fibre test apparatus (Aurora Scientific, 1400A). Mean sarcomere length was measured microscopically (Nikon Ti-*S*, 500 ×) within the white boxed part of the fibre (top graphs) with a high-speed video system for sarcomere length measurement (Aurora Scientific, 901B). Calcium activation started at time $t = 0$ s. At very short, unphysiological half-sarcomere length (0.53 μm), the muscle fibre segment is initially slack (it sags). After pulling in the slack, the fibre segment becomes taut and force develops slowly. Force reached about 30% of F_{im} at the end of activation. In the inset, the measured steady-state lengths and forces can be compared with the rat's theoretical force – length relationship (obtained with the same parameters as in Figure 5.6 but with longer rat actin length of 1.13 μm (ter Keurs *et al.*, 1984)).

On a related note, this phenomenon may explain the so far unknown function of the second parallel myosin head attached to each myosin molecule (Huxley, 2000), which may generate the swivelled cross-bridges. However, this function comes at a metabolic cost. In species with skeletons, evolution may have adjusted the region of operation of the muscle by tuning origin and insertion such that it avoids damping its own contraction.

For example, floating species such as fish can function more in the plateau region of the FLR (Burkholder & Lieber, 2001) than non-floating species. In floating species, postural stability is provided by the aquatic environment. By contrast, species acting with their musculoskeletal system against gravity seem to make use of this 'old' muscle function by selected muscles operating in the range of the steep part of the ascending limb of the FLR (Burkholder & Lieber, 2001), potentially to increase stability and to facilitate docile behaviour towards perturbations.

5.5 Conclusion

The assumption of myosin filament folding or even compression (which would need to exceed 60% for extreme cases of muscle shortening; Figure 5.1) commonly used in textbooks cannot explain *(i)* how force can be produced at lengths shorter than the length of classic zero force; *(ii)* why the muscle does not restore its resting length after contractions with extended activation duration; and *(iii)* how the stiff myosin filaments can be folded or compressed at a meshed Z-disc. Accepting the idea that myosin filaments slide through the Z-disc and incorporating this mechanism into a comparably simple model with comprehensible, few parameters reconcile these data with classic theories of contraction.

In addition, the model enables new perspectives on the relation between striated fibre structure and its mechanical function. The transformation from hexagonal to tetragonal actin filament lattice near the Z-disc enables the development of an orderly myofilament structure at short fibre lengths. The Z-disc becomes an integral part of the contractile mechanism. For example, eccentric exercise (Lieber & Fridén, 2002) or muscle diseases like Duchenne muscular dystrophy or Sjögren's syndrome are accompanied by a loss of structural integrity of the Z-disc. This may result in disordered myosin sliding through the Z-disc, contributing to the observed muscle weakness. A more comprehensible understanding of muscle structure and function seems within reach.

Chapter 6

Changes in three–dimensional muscle structure of rabbit *gastrocnemius, flexor digitorum longus*, and *tibialis anterior* during growth[4]

6.1 Introduction

The architecture of the muscle-tendon complex is the main determinant for muscle function (Gans & Gaunt, 1991; Lieber & Ward, 2011; Stark & Schilling, 2010). Furthermore, it has been shown that there is an effect of the extra-cellular matrix on muscle performance by e.g. transmitting lateral forces to the muscles or providing stability (Gillies & Lieber, 2012; Kjaer & Kjær, 2004; Maas & Sandercock, 2010).

[4]Siebert T., Tomalka A., Stutzig N., Leichsenring K., Böl M. *JMBBM* 2017 Oct;74:507-519.

The most important architectural parameters are the length of the muscle fascicle (the bundle of muscle fibres), its pennation angle, the physiological cross-sectional area (PCSA), and the connective tissue properties, including the characteristics of the tendons and aponeuroses. These parameters must adapt during growth to deal with increasing body mass and size. However, little is known about the changes in the geometry of a typically developing muscle (Bénard *et al.*, 2011; Blazevich & Sharp, 2005; Böl *et al.*, 2016).

Typical changes in muscle morphology found during growth include increases in muscle length, muscle thickness, muscle mass, CSA, and tendon length (Bénard *et al.*, 2011; Binzoni *et al.*, 2001; De Koning *et al.*, 1987; Heslinga & Huijing, 1990; Woittiez *et al.*, 1989). Most studies report an increase in pennation angle over time (Binzoni *et al.*, 2001; Morse *et al.*, 2008; Stickland, 1983). There are muscle-specific differences in the development of fascicle lengths. An increase in fascicle length was reported for the human *M. gastrocnemius medialis* (GM) and *lateralis* (GL), as well as for the *M. extensor digitorum longus* (EDL) in rabbits and rats (Bénard *et al.*, 2011; Böl *et al.*, 2016; Lodder *et al.*, 1994; Mohagheghi *et al.*, 2008). In contrast, the fascicle lengths of rat GM and rabbit *M. plantaris* (PLA) remain almost constant during growth (Bénard *et al.*, 2011; Böl *et al.*, 2016). However, in most muscle growth studies, the determination of the fascicle length and pennation angle is limited to local areas within the muscle, which may hamper transfer to structural changes of the complete muscle (Bolsterlee *et al.*, 2015; Schenk *et al.*, 2013). So far, no data are available about changes in the complete three-dimensional (3D) muscle fascicle architecture during growth. Knowledge is also sparse in regard to the changing dimensions of the aponeurosis, which is an important load-transferring interface in muscle mechanics (Böl *et al.*, 2015; Epstein *et al.*, 2006). The few studies available indicate that aponeurosis length increases with growth (Bénard *et al.*, 2011; Heslinga & Huijing, 1990). However, the aponeurosis is a flat, three-dimensional structure, functioning as the attachment surface of muscle fibres. Consequently, investigating the changes in its width, length, and area is required to

better understand basic growth mechanisms such as hypertrophy or remodelling of the muscle structure (Heslinga & Huijing, 1990). Only one study (Böl *et al.*, 2016) has examined changes in aponeurosis shape during growth. In this study, spindle-like muscles (*M. soleus* (SOL), EDL, and PLA) in rabbits were investigated. Such muscles feature two pronounced tendon-aponeurosis structures on their proximal and distal ends. In contrast, nonspindle-like muscles feature, for example, large bony proximal attachment areas of muscle fibres (and no or smaller proximal aponeurosis). Thus, growth in width and proximal aponeurosis might be restricted by growth of the bony attachment areas. However, knowledge is lacking about the aponeurosis growth of non-spindle-like muscles (e.g. *M. tibialis anterior*) or more complex bipennate muscles (e.g. *M. gastrocnemius*).

Knowledge about the structural changes in muscle morphology as well as functional outcomes (i.e. metrics such as strength, power, work, endurance) is of great interest in medicine, biomechanics, and modelling. In neuromuscular disorders such as cerebral palsy, muscle growth is hampered and joint mobility is thus limited. Young patients often undergo surgical muscle lengthening to improve their gait mechanics (Arnold *et al.*, 2006). Improving the treatment of these muscles requires detailed insight into how their geometry develops during the growth phase and how it differs from that of typically developing muscle (Bénard *et al.*, 2011).

There is also a need for morphometric input data for muscle models at a particular age. Finite-element muscle modelling is used to understand the influence of muscle architecture on the 3D muscle deformation, force development, and force transmission from muscle fibres to aponeuroses to tendons (Böl *et al.*, 2011b,a; Ehret *et al.*, 2011; Heidlauf *et al.*, 2016; Röhrle *et al.*, 2016). Realistic 3D muscle models are a prerequisite to understand the interaction of muscles with surrounding tissue and external forces (Reinhardt *et al.*, 2016; Siebert *et al.*, 2014b; Yucesoy *et al.*, 2003). As muscle morphology changes during growth, age-dependent morphometric data will be required to adapt muscle models to a particular age.

The aims of the present study are to determine growth-related changes of the shank musculature (GL, GM, *M. flexor digitorum longus* (FDL), and *M. tibialis anterior* (TA)) in rabbits. The muscles were chosen for this study because they deviate from the typical spindle-like muscle shape. Focus is centred on *(i)* the geometries of the aponeurosis, muscle belly, and tendon, as well as *(ii)* the 3D muscle fascicle architecture. Due to functional and structural variations in between the observed muscles (Bensley, 1948; Siebert *et al.*, 2015) we hypothesise that differences in the growth rates of the geometrical parameters exist.

6.2 Methods

The experimental setup, handling and preparation techniques of skeletal bone – muscle complexes have been described earlier (Schenk *et al.*, 2013; Siebert *et al.*, 2015) (cf. section 2.3 for details).

Two methods were used to collect age-dependent experimental data regarding geometrical measurements of the GL, GM, FDL, and TA. Female rabbits ($n = 60$) aged between 18 and 108 days were obtained from a slaughterhouse. At the age of 108 days, skeletal growth is almost complete whereas body mass increases for much longer (Masoud *et al.*, 1986). Thus, growth data reported in this study represent early states of rabbit ontogeny. After transport to the lab, each animal was weighed prior to isolating both hind legs. To analyse the muscle, tendon, and aponeurosis structure, both hind legs of 55 animals were used in method 1, resulting in 110 preparations per muscle type. The 3D muscle architecture was determined from the left legs of the remaining 5 animals using method 2 (Table 6.1).

Rabbit number	Animal mass [kg]	Age [days]	Knee joint angle [°]	Ankle joint angle [°]	Muscle	Number of fascicles [n]	Pennation angle [°] mean ± SD
R1	0.41	21	86	94	GL	129	13.4 ± 3.3
					GM	78	25.3 ± 3.9
					FDL	42	13.3 ± 7.8
					TA	41	11.7 ± 1.9
R2	1.03	37	80	83	GL	167	12.2 ± 5.4
					GM	122	16.6 ± 4.3
					FDL	127	20.6 ± 5.9
					TA	41	13.7 ± 1.3
R3	1.5	50	84	98	GL	195	12.3 ± 2.5
					GM	158	20.4 ± 5.1
					FDL	131	19.6 ± 7.3
					TA	68	8.0 ± 4.0
R4	2.35	70	93	96	GL	652	17.5 ± 4.1
					GM	364	24.6 ± 3.4
					FDL	224	15 ± 8.1
					TA	61	11.3 ± 3.2
R5	3.65	100	95	107	GL	1005	24.3 ± 6.5
					GM	554	26.4 ± 5.7
					FDL	274	15.1 ± 7.5
					TA	70	15.1 ± 2.1

Table 6.1: Pennation angle calculated from 3D fascicle traces of five rabbits of different ages (R1 to R5).

6.2.1 Analysis of muscle, tendon, and aponeurosis structure during growth (method 1)

To ensure high reproducibility, the same assessor performed the measurements for all animals. The skin was removed from the legs, and the initial measurements of the muscles were documented for ankle and knee joint angles of 90.2° ± 2.2° (mean values ± standard deviation) and 90.1° ± 3.1°, respectively. These joint angles were chosen to enable comparison of morphological data with those from Lieber & Blevins (1989). Each muscle was removed from the bone and fixed on a pad at a length corresponding to these angles (Figure 6.1). The tendon lengths (l_t) and muscle belly dimensions (length l_m, width w_m, thickness t_m) were then determined using a sliding caliper.

The muscle fascicle length (l_{fasc}) was measured on the muscle surface as the distance from the origin of the most distal muscle fascicles (on the distal end of the proximal aponeurosis) to their insertion on the distal tendon. Muscle mass (m_{muscle}) was determined using an analytical balance.

The aponeurosis has to be separated from the muscle tissue for detailed measurement, which requires further processing. To this end, the muscles were fixed in alcoholic Bouin solution (Böl *et al.*, 2015; Gorb & Fischer, 2000) for 72 h to minimise shrinking artifacts. The specimens were then stored at room temperature in 10% caustic soda solution to dissolve the muscle tissue, including the intramuscular connective tissue (the endomysium, perimysium, and epimysium) (Böl *et al.*, 2016). To ensure that only fascicles and connective tissues were dissolved, the muscle was frequently removed from the solution and visually verified. Depending on the muscle size after 5–7 days, all fibre bundles were gradually removed. In cases where the connective tissues were not fully decomposed, the specimen was stored again in caustic soda solution for a short period. Digital photographs of the aponeurosis including a scale were then taken, and characteristic measurements were obtained, such as the aponeurosis length (l_{APO}: along the line of action between muscle origin and insertion) and width (w_{APO}: perpendicular to the line of action), as shown in Figure 6.1. Furthermore, the areas (A_{APO}) of proximal and distal aponeuroses were determined from the digital photographs. The physiological CSA (PCSA) of the muscle was calculated by the equation (Lieber & Blevins, 1989):

$$PCSA = \frac{m_{muscle} \cdot cos(\alpha)}{l_{fasc} \cdot \rho}, \tag{6.1}$$

where ρ is the density of skeletal muscle and equal to 1.054 g/cm^3 (Méndez & Keys, 1960), while α represents the mean pennation angle of the muscle. To compare aponeurosis areas with the CSA, the average of the distal and proximal aponeurosis areas (A_{APO_mean}) was divided by the corresponding CSA for each muscle to obtain the aponeurosis-CSA ratio (r_{ACSA}). For muscles with smaller proximal aponeurosis or

without a proximal aponeurosis, such as the FDL and TA, the distal aponeurosis areas were divided by the CSA to calculate r_{ACSA}.

6.2.2 Determination of 3D muscle fascicle architecture (method 2)

The fascicle orientation was manually digitised based on earlier studies of 3D muscle architecture (Böl *et al.*, 2013; Schenk *et al.*, 2013; Siebert *et al.*, 2015; Stark *et al.*, 2013). These techniques have been described in great detail in **Chapter 2**, section 2.3 *'Determination of 3D muscle structure'*.

Briefly, similar to method 1, five hind legs of different age (21, 37, 50, 70, 100 days) were fixed in Bouin solution for 72 h at the given knee and ankle joint angles (Table 6.1). In addition to recording the fascicle bundle positions, the origins, the insertions (GL, GM), and the deviating points (TA: loop of the ligamentum cruciatum cruris; FDL: dorsal border of the medial malleolus) of the muscles (see supplementary material online under: http://dx.doi.org/10.1016/j.jmbbm.2017.07.045, Dataset A5) as well as specific bony structures (e.g., tibia, calcaneus, malleolus lateralis) were recorded for each animal. Accordingly, orthogonal lever arms between the rotational axis of the ankle joint and the line of action of specific muscles (Figure 6.2) were calculated. These geometrical data are provided to enable prospective integration of the muscles analysed in musculo-skeletal models. To investigate functional adaptations of the muscle-tendon complex, the tendon-muscle fascicle length ratio (tendon length divided by fascicle length; $[r_{TFL} = l_{SEC}/l_{fasc}]$) of the series elastic component length l_{SEC} (including the tendon and the aponeurosis) and the muscle fascicle length (Mörl *et al.*, 2016) was calculated. Note that the lengths of the distal and proximal tendons and of the aponeurosis (mean of distal and proximal aponeuroses) are pooled together since they are typically related to the SEC (Epstein & Herzog, 1998) and they produce similar nonlinear stress-strain relations (Scott & Loeb, 1995).

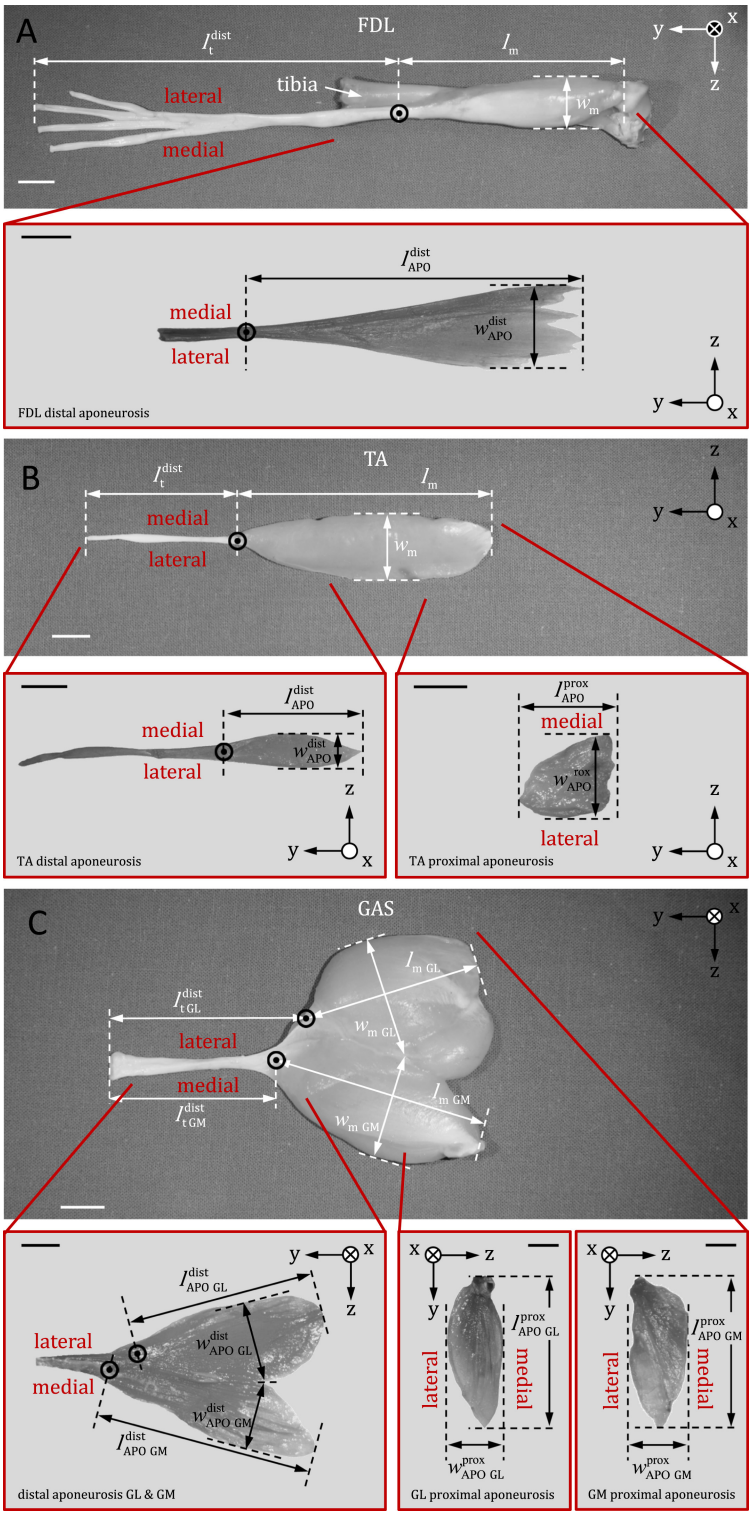

Figure 6.1: Isolated muscle-tendon complexes of the rabbit left hind limb. (A) *M. flexor digitorum longus* (FDL), (B) *M. tibialis anterior* (TA), and (C) *M. gastrocnemius* (GAS) consisting of *M. gastrocnemius lateralis* (GL) and *M. gastrocnemius medialis* (GM). Views of the corresponding isolated proximal and distal aponeurosis are shown in the subfigures below. As in Figure 6.6, the x-, y-, and z-axes correspond to the anteroposterior, proximodistal, and mediolateral directions, respectively. Horizontal black and white bars: 10 mm. APO: aponeurosis, l_t: tendon length, l_m and w_m: muscle belly length and width, l_{APO} and w_{APO}: aponeurosis length and width.

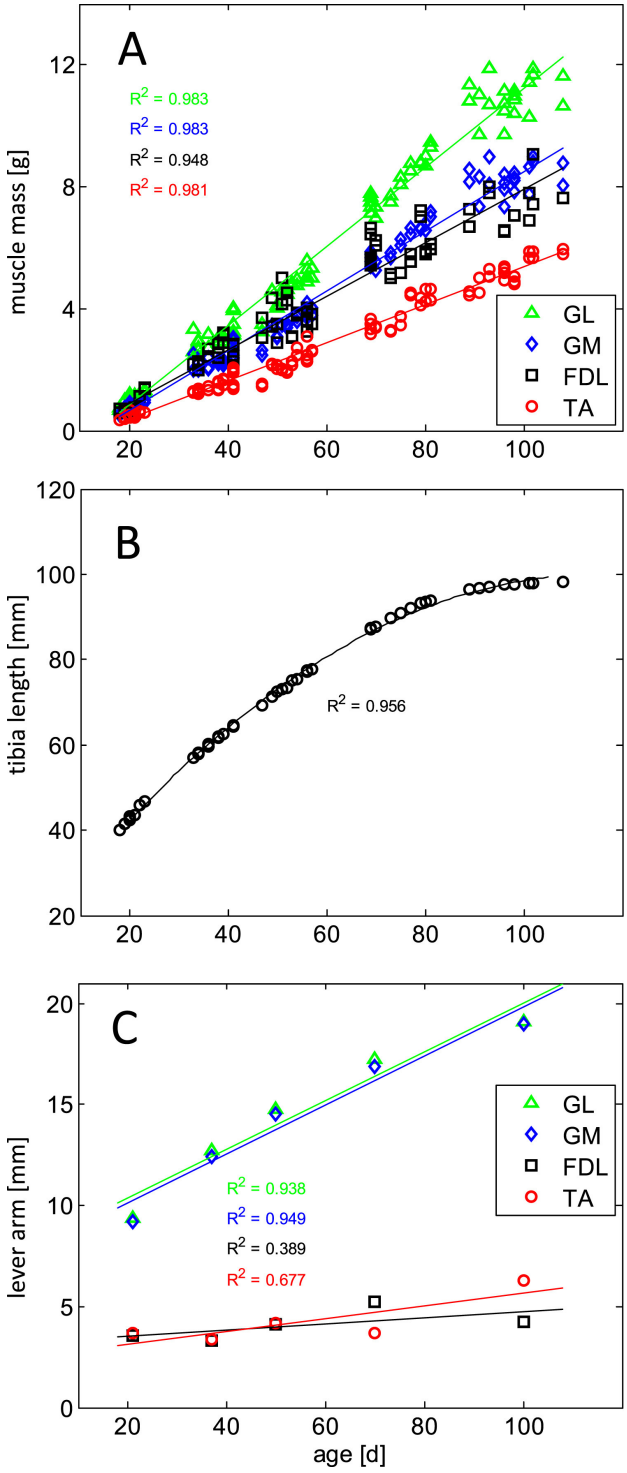

Figure 6.2: Age-related changes in the (A) muscle mass, (B) tibia length, and (C) muscle lever arm. The coefficient of determination R^2 is shown in the same colour as the regression line in the figure. Note that tibia growth shows a nonlinear characteristic similar to results from Böl *et al.* (2016) and Masoud *et al.* (1986) and was thus approximated with a parabolic function.

6.2.3 Data analyses

For better comparison of the measured parameters, several data were normalised to the initial value at the beginning of the observation period (marked by the index i); i.e., at an animal age of 18 days. To investigate the relationship between parameters and animal age, linear regression analyses were applied and evaluated using scatter plots. The coefficients of determination (R^2) and slopes of the regression lines were calculated using custom-made Matlab scripts (MATLAB R2014a, The MathWorks, Inc., Natick, MA, USA).

To test for significant differences in the slopes of the linear regressions (growth rates of geometrical parameters) across muscles (GL, GM, FDL, TA) a one-way ANOVA was conducted (Zar, 2010). A Tukey post-hoc test was performed for pair wise comparisons between the muscles similar to Lammers & German (2002). The level of significance was set at $P < 0.05$.

6.3 Results

In general, we found muscle specific differences in the normalised growth rates of muscle belly, aponeurosis, and CSA (Table 6.2) reflecting functional and structural diversity in between the observed muscles. However, for muscles featuring the same function during locomotion and exhibiting very similar structure, like GL and GM, no significant differences in the development of muscle belly mass, fascicle length, as well as length and width of the distal aponeurosis (Table 6.2) occurred. Consequently, hypothesis can be mostly confirmed.

6.3.1 Morphometric variables and muscle-tendon complex

Animal mass increased almost linearly from 0.40 ± 0.95 to 3.53 ± 0.15 kg with age ($R^2 > 0.98$) within the observed time period 18–108 days. This linear behaviour is mirrored in the increase in muscle mass of GL, GM, FDL, and TA (Figure 6.2;

Parameter	GL Mean slope	GM Mean slope	FDL Mean slope	TA Mean slope	Significant differences
Belly mass [%/*day*]	21.7	22.0	12.3	22.9	2,3,4,6
Belly width [%/*day*]	2.2	2.0	1.3	1.3	1,2,3,4,5
Belly thickness [%/*day*]	1.6	0.9	1.4	1.7	1,4,5,6
Belly length [%/*day*]	0.9	1.3	1.6	1.6	1,2,3,4,5
Distal tendon length [%/*day*]	2.0	1.4	1.1	0.8	1,2,3,4,5,6
Length APO_{prox} [%/*day*]	1.2	1.6	–	1.9	1,3,5
Width APO_{prox} [%/*day*]	0.7	1.7	–	1.2	1,3,5
Length APO_{dist} [%/*day*]	1.7	1.6	1.8	1.1	3,5,6
Width APO_{dist} [%/*day*]	2.2	2.2	2.0	1.4	3,5,6
Area APO_{prox} [%/*day*]	7.7	6.2	–	8.6	1,3,5
Area APO_{dist} [%/*day*]	7.0	6.6	11.4	9.0	1,2,3,4,5,6
CSA [%/*day*]	13.7	12.2	5.9	4.8	1,2,3,4,5,6
Fascicle length [%/*day*]	0.3	0.4	0.3	1.2	3,5,6
Tendon–muscle Fascicle length ratio r_{TFL} [%/*day*]	1.2	0.9	0.7	-0.2	1,2,3,5,6

Table 6.2: Differences across muscles (GL, GM, FDL, and TA) in the mean slope of the normalised growth rates of the geometrical parameters. Data were normalised to the initial value at the beginning of the observation period (age of 18 days). Significant differences in slope among muscles were determined by one-way ANOVA with Tukey post-hoc tests. Significant differences ($P < 0.05$) are marked as follows. 1: between GL and GM, 2: between GL and FDL, 3: between GL and TA, 4: between GM and FDL, 5: between GM and TA, 6: between FDL and TA. APO: aponeurosis.

$R^2 > 0.94$), with GL exhibiting the highest slope. Normalisation of the growth curves to the initial muscle mass at 18 days resulted in very similar growth rates ($\approx 21\%$/day) for GL, GM, and TA. In contrast, FDL showed a significantly lower growth rate of 12.3%/day (Table 6.2).

For all muscles, muscle belly growth was accompanied by increases in the belly length, width, and thickness. Figure 6.3 illustrates the normalised data with respect to their initial values. Different growth rates of the muscle belly length, width, and thickness have been observed for GL and GM. For both muscles, the highest growth rates (GL: 2.2%/day; GM: 2.0%/day) were measured for the muscle width (Figure 6.3 A, B open circles). Growth rates for length and thickness were 0.9%/day and 1.6%/day for GL and 1.3%/day and 0.9%/day for GM, respectively. In contrast, FDL and TA showed more uniform growth rates of $1.4 \pm 0.1\%$/day and $1.5 \pm 0.2\%$/day (mean values and standard deviation of growth in belly length, width, and thickness), respectively. All muscles exhibited significant differences in distal tendon growth rates (Table 6.2). The distal tendon length was almost doubled for all muscles (increase factors: GL: 2.7, GM: 2.3, FDL: 2.0, TA: 1.7) during the observed growth period. FDL exhibited the longest distal tendon, which increased from about 70–140 mm (Figure 6.4). GL, GM, and TA showed similar distal tendon lengths.

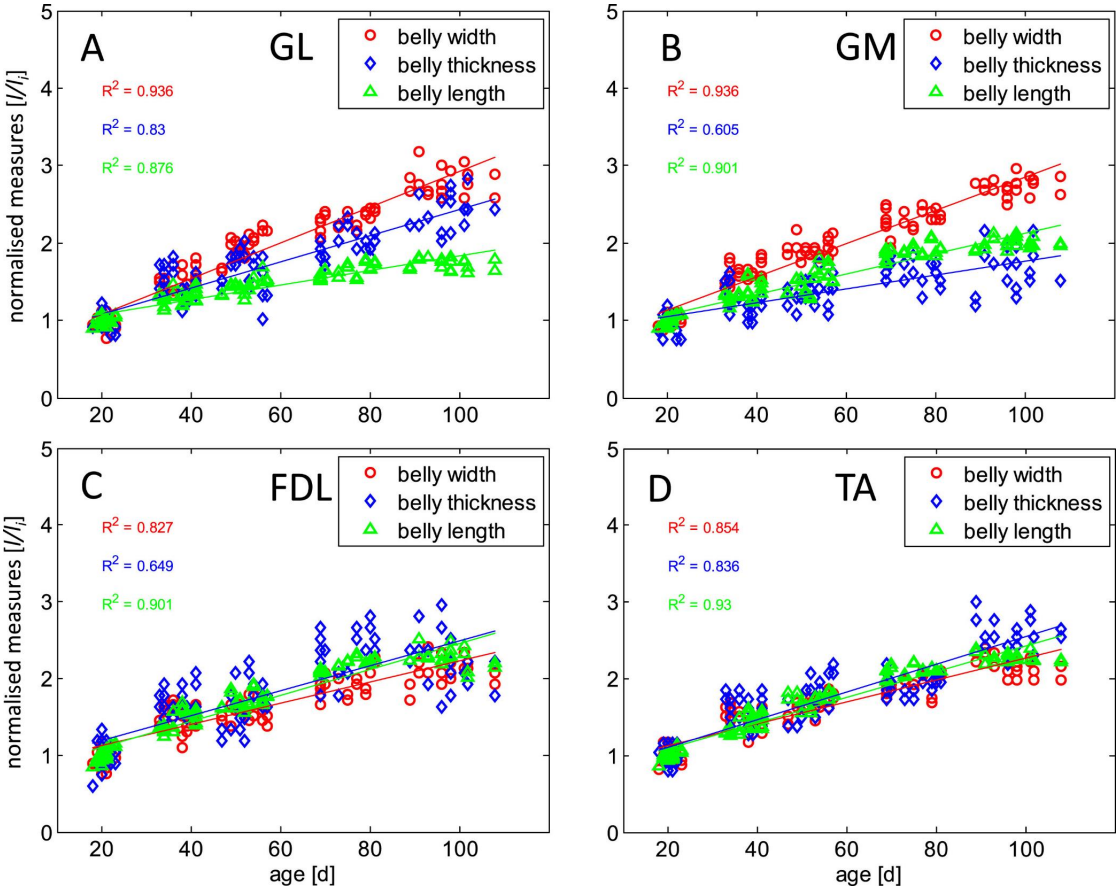

Figure 6.3: The effect of age on the muscle belly dimensions of rabbit (A) GL, (B) GM, (C) FDL, and (D) TA. Muscle belly lengths, widths, and thicknesses were normalised with respect to the initial values.

6.3.2 Aponeurosis geometry and CSA

When focusing on the aponeurosis dimensions (length and width) of the GL and GM, the distal and proximal aponeurosis were almost identical (Figure 6.5 A, C). This results in similar distal and proximal aponeurosis areas for GL (Figure 6.5 B) and GM (Figure 6.5 D). Furthermore, the growth rates normalised to the initial areas of distal and proximal aponeurosis were similar for the specific muscles (GL: 7.0%/day and 7.7%/day; GM: 6.6%/day and 6.2%/day, respectively). FDL and TA show deviations in

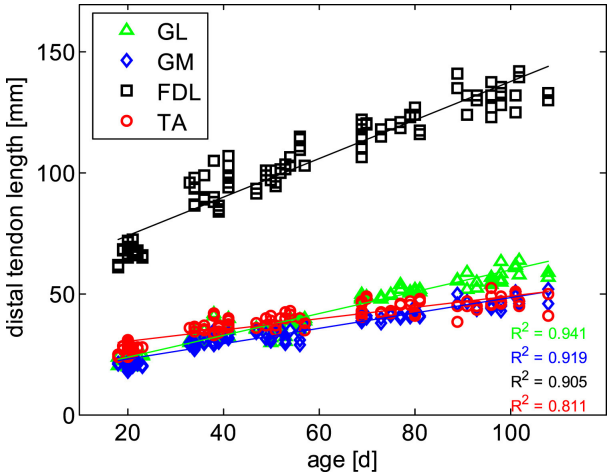

Figure 6.4: The effect of age on the distal tendon lengths of rabbit GL, GM, FDL, and TA. FDL and TA had no tendons, and GL and GM exhibited comparatively short proximal tendons (not shown). Lengths of proximal tendons of GL and GM increased from 1.2 to 4.3 mm and from 1.6 to 4.5 mm, respectively.

aponeurosis growth characteristics (Figure 6.5 E–H), as both muscles have muscle fibres originating from the tibia bone. More specifically, FDL has no proximal aponeurosis, and all muscle fibres originate from the lateral condyle of the tibia and the head of the fibula (extending to the posterior surface of the interosseous ligament and associated portions of the tibia and fibula) (Bensley, 1948). The normalised growth ratio of its distal aponeurosis is 11.4%/day. TA has a proximal aponeurosis that is much smaller than its distal one, as a proportion of muscle fibres originate from the lateral condyle of the tibia and corresponding surface of the tibial tuberosity (Bensley, 1948). However, both the distal and proximal aponeuroses exhibit similar normalised growth rates of 9.0%/day and 8.6%/day, respectively.

In general, the physiological CSAs (Figure 6.5 B, D, F, H, open triangles) are smaller than those of the distal and proximal aponeurosis areas (open circles and triangles, respectively). The aponeurosis-CSA ratio r_{ACSA} was 1.20 and 1.44 for GL and GM, respectively, and the values were about twice as high for FDL (2.24) and TA (2.04). Comparing the normalised CSA growth rates yielded significant differences between the muscles. However, growth rates for GL (13.7%/day) and GM (12.2%/day) were almost

double the value for FDL (5.9%/day). The smallest increase in CSA was observed for TA (4.8%/day).

6.3.3 Muscle fascicle characteristics

Changes in muscle fascicle length with age were determined with two methods. The results from manual digitisation of fascicles (method 2) are first presented. The 3D muscle fascicle architecture (Figure 6.6; GL: brown, GM: yellow, FDL: red, TA: green) was digitised for 5 animals with increasing age from 21 to 100 days, which corresponds to increasing body mass from 0.41 to 3.65 kg (Table 6.1). For each muscle, it was possible to digitise a specific number of fascicles (Table 6.1) that increased with increasing body mass and thus with increasing muscle mass (Figure 6.2). For example, for the youngest (21 days) and oldest GL (100 days), 129 and 1005 fascicles were tracked, respectively.

The mean pennation angles and fascicle lengths were determined from the 3D fascicle traces. The pennation angles of TA ($11.0 \pm 2.1°$) and FDL ($16.7 \pm 3.2°$) remained almost unchanged during the observed time period (Table 6.1). In contrast, the pennation angle of GL increased from the youngest ($13.4 \pm 3.3°$) to the oldest ($24.3 \pm 6.5°$) animal (Table 6.1). Large interindividual variability in the pennation angles was found for GM (the highest and lowest pennation angles were 26.4° and 16.6°, respectively). Fascicle lengths determined with method 2 are illustrated in Figure 6.7 (black filled symbols). There were almost no changes in fascicle lengths with increasing age for GL, GM, and FDL (Figure 6.7 A–C, $R^2 < 0.2$). For all three muscles, the fascicle lengths were in the range of 10–15 mm. If there were any change in length with age, then it might be visible in the first phase of the observation period between 20 and 40 days (Figure 6.7), black dashed line).

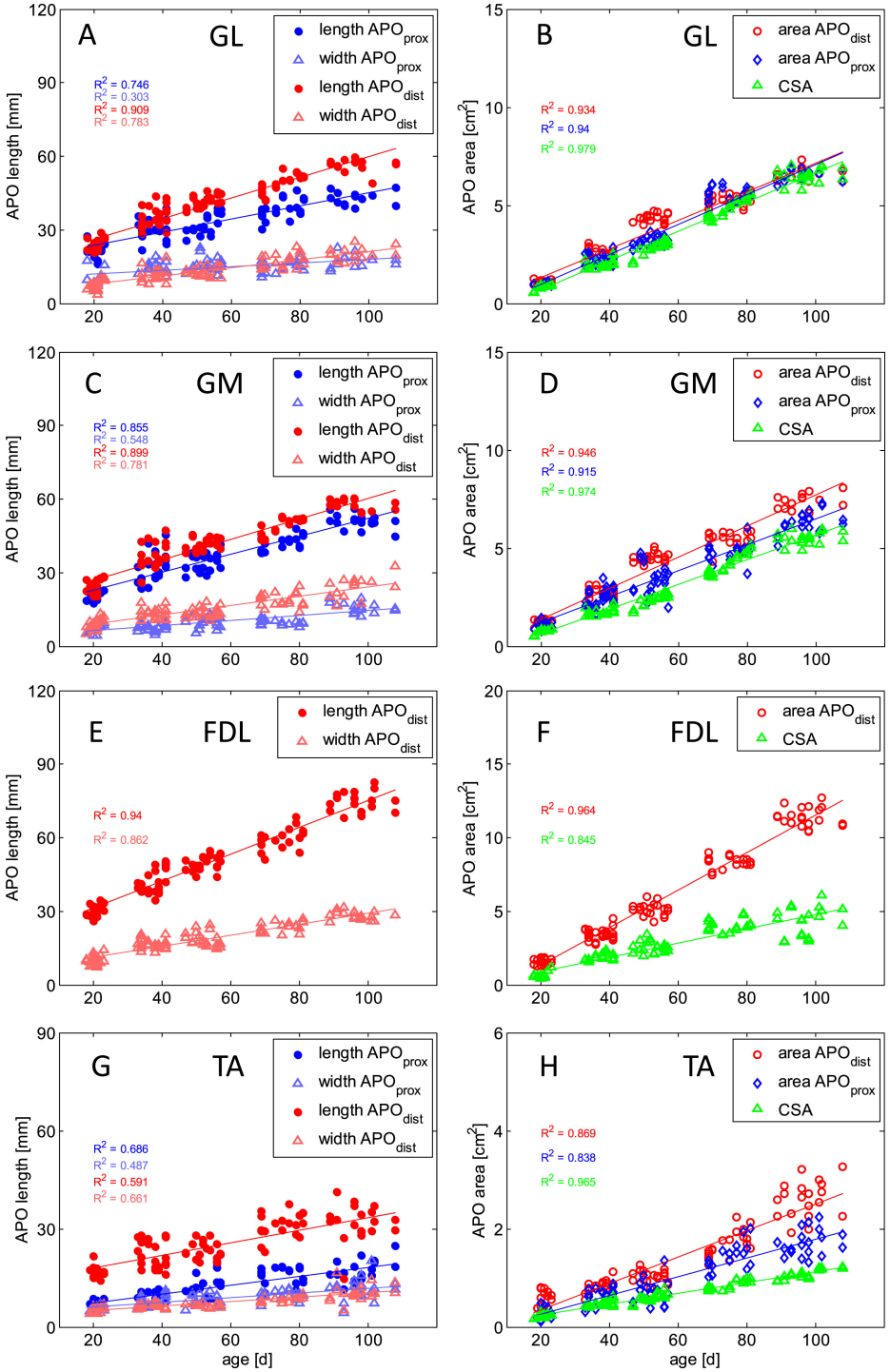

Figure 6.5: Aponeurosis growth and increase in physiological CSA of rabbit GL (A, B), GM (C, D), FDL (E, F), and TA (G, H). The lengths and widths of the proximal and distal aponeurosis are illustrated in (A, C, E, G), whereas the proximal and distal aponeurosis (APO) areas and the physiological cross-sectional areas (CSAs) are shown in (B, D, F, H). FDL exhibited no proximal aponeurosis, but a second smaller distal aponeurosis (not shown) was found.

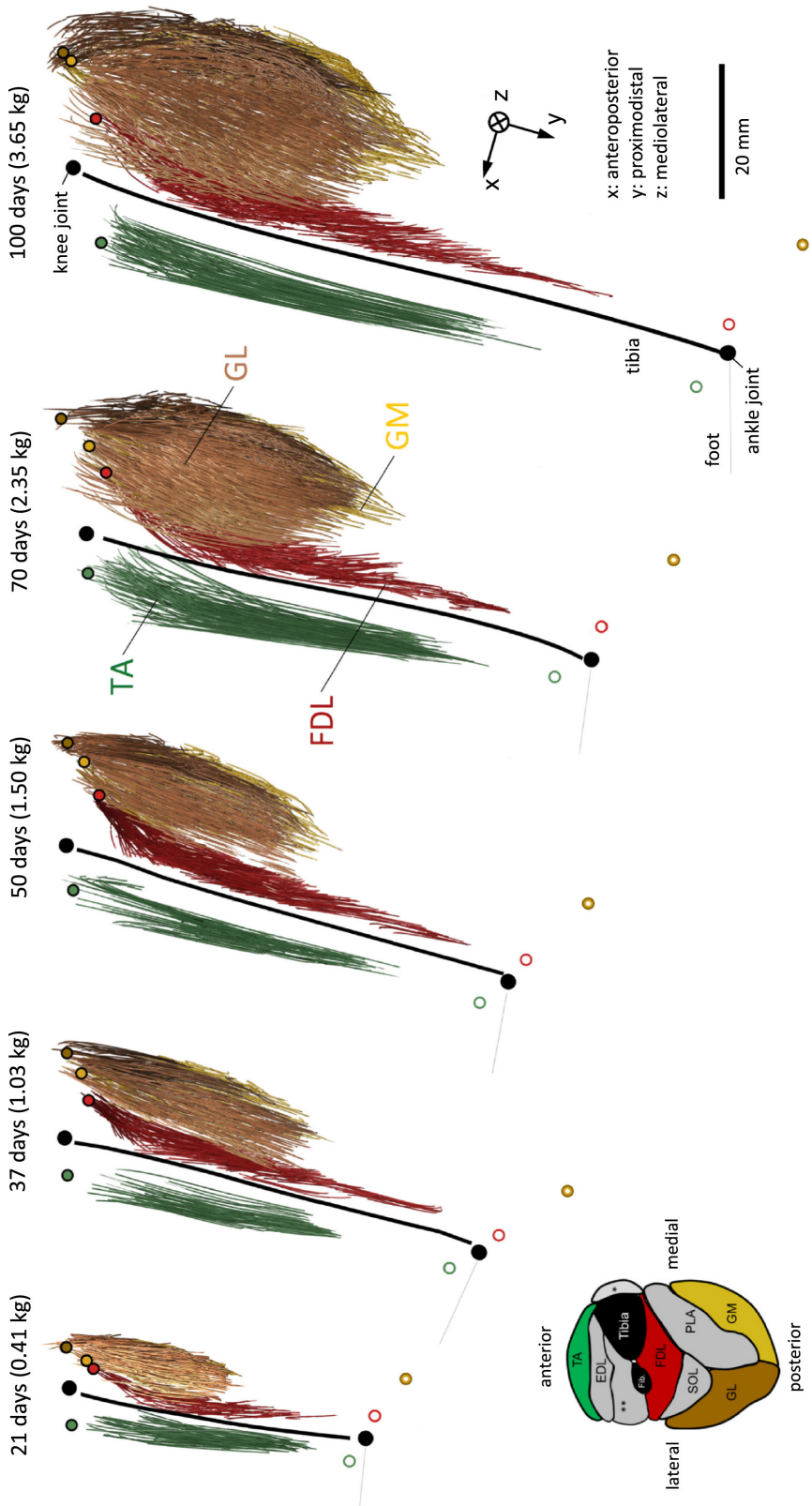

Figure 6.6: 3D muscle fascicle architectures of GL, GM, FDL, and TA from the left hind limb for particular ages (from left to right): Rabbit 1 (R1, 21 days), Rabbit 2 (R2, 37 days), Rabbit 3 (R3, 50 days), Rabbit 4 (R4, 70 days), and Rabbit 5 (R5, 100 days). Muscle fascicles of GL, GM, FDL, and TA are coloured brown, yellow, red, and green, respectively. Muscle origins (filled circles), insertions of GL and GM as well as deviating points of FDL and TA (open circles) are given in the same colour as the corresponding muscles. For better orientation, the transversal cross-section of the left hind limb is given in the lower left corner. Grey muscles were not examined in this study. **peronaei muscles, *M. extensor hallucis longus. The corresponding 3D data of the muscle fascicles, origins and insertions, respectively, are provided in the online version of this study at: http://dx.doi.org/10.1016/j.jmbbm.2017.07.045 (Data A1–A5).

In contrast, there was a clear increase in TA fascicle length from about 20 to over 40 mm (Figure 6.7 D, $R^2 = 0.833$). The fascicle lengths determined with method 1 (Figure 6.7, red open symbols) were in good agreement with those obtained using method 2. Comparing the growth rates normalised to the initial values, GL, GM, and FDL exhibited low rates of about 0.3%/day, whereas TA had a much higher rate of 1.2%/day.

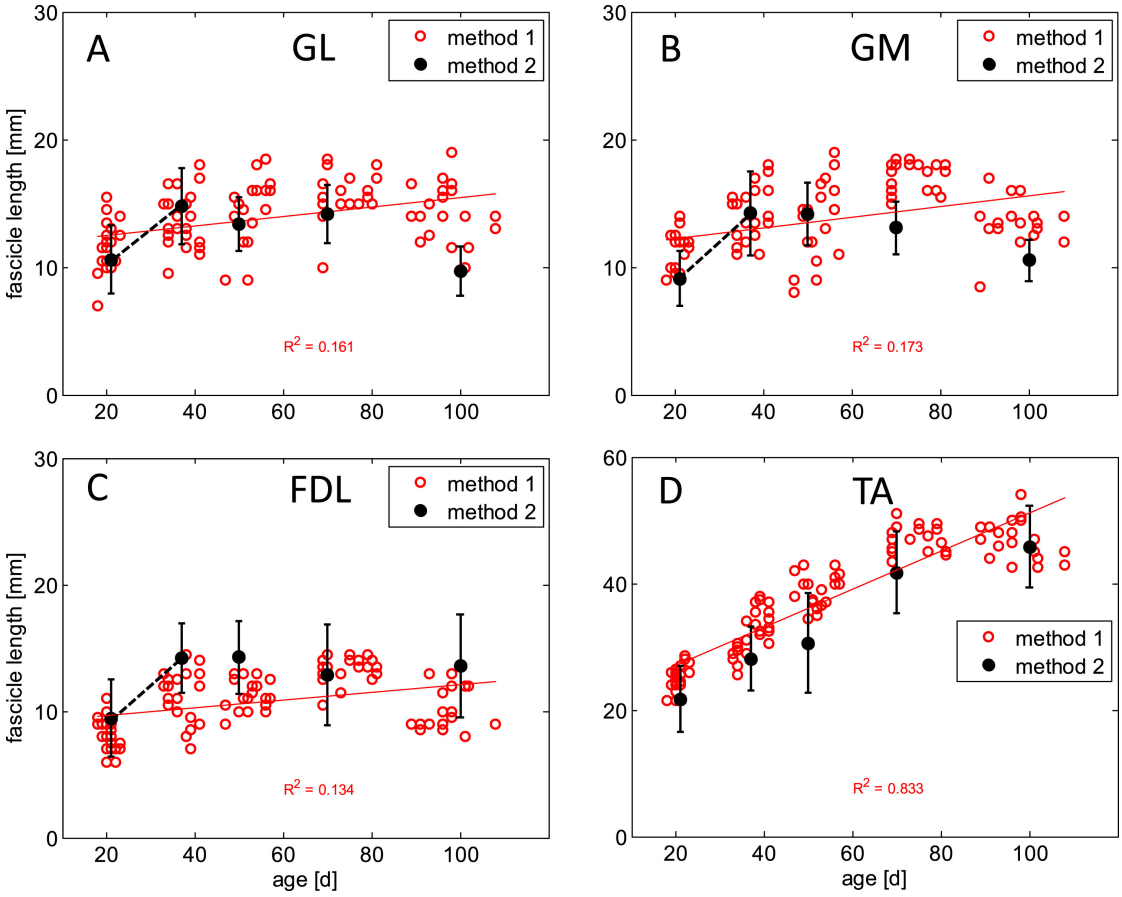

Figure 6.7: Effects of age on fascicle growth for GL (A), GM (B), FDL (C), and TA (D) determined with method 1 (open circles) and method 2 (closed circles). For GL, GM, and FDL, an increase in fascicle length might be visible between 20 and 40 days (black dotted line).

6.3.4 Changes in tendon-muscle fascicle length ratio

For all muscles observed, none of the tendon-muscle fascicle length ratios (r_{TFL}) were constant during growth, as shown in Figure 6.8. The ratios increased for GL, GM,

and FDL. Due to its long distal tendons inserted in the ungula phalanges of the four developed digits (Figure 6.1), FDL has the highest r_{TFL} value, which increases from about 8 to about 13 (Figure 6.8, open squares). GL (open triangles) and GM (open diamonds) exhibited similar increases from about 4–8. TA (open circles) had the lowest ratio, which decreased slightly from 2 to 1.5.

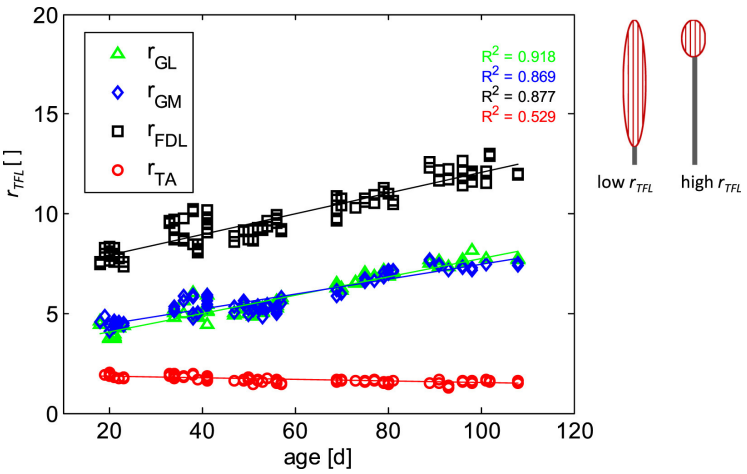

Figure 6.8: Changes in the tendon–muscle fascicle length ratio (r_{TFL}) during growth. High or low r_{TFL} mean long SECs and short muscle fibres or short SECs and long muscle fibres, respectively (see schematic on the left side).

6.4 Discussion

We observed the changes in the 3D muscle architecture and aponeurosis dimensions of rabbit GL, GM, FDL, and TA during growth. In general, an almost linear increase over time was found in most of the geometrical parameters. GL and GM showed very similar growth characteristics and thus might be represented by the same model in simulation studies addressing muscle development during growth. TA obviously exhibited deviating growth characteristics with a prominent increase in muscle fascicle length at the cost of a reduced increase in aponeurosis area and CSA. In contrast to the pronounced increase in muscle belly width of GL and GM, FDL and TA exhibited more uniform muscle belly growth in length, width, and thickness.

6.4.1 Comparison with literature

Body mass increased almost linearly during the observation period. This result is in agreement with other growth studies on humans (age: 5–12 years (Bénard *et al.*, 2011)), rabbits (age: 14–126 days (Masoud *et al.*, 1986)), and rats (age: 19–79 days (Bhaskar *et al.*, 1950; Hansson *et al.*, 1972)). Age-dependent morphometric measurements of the muscle-tendon complex during normal growth are rare, and there are only a small number of studies examining rabbits (Böl *et al.*, 2016; Crawford, 1950, 1954). The majority of research was performed on other species. To enable comparison with humans and rats as well as with deviating observation periods, growth data were normalised to the ages (t_{fg}) when skeletal growth is almost complete (rat t_{fg}: about 100 days ; rabbit t_{fg}: about 120 days (Masoud *et al.*, 1986); human t_{fg}: about 17 years (Gindhart, 1973)). Accordingly, data in this study comprise a growth period of 0.15 t_{fg} (18 days) to 0.9 t_{fg} (108 days).

Few studies have examined the same muscles analysed in the present study or provided geometric data to make subsequent comparisons. Increases in muscle belly and aponeurosis length of GM and TA were expected based on previous work (Crawford, 1954; Heslinga & Huijing, 1990; Woittiez *et al.*, 1986). Crawford (1954) observed changes in the TA muscle length of rabbits during growth. They marked the muscles of five young rabbits (35 days, $0.29t_{fg}$) in the longitudinal direction using thin steel wires at fixed intervals. They measured segmental length changes after about 119 days ($0.99t_{fg}$). The experiments showed that longitudinal growth occurred fairly evenly throughout the length of the muscle belly. They found very large interindividual differences in muscle growth, and the distance between the most distal and most proximal markers increased by about 35% and 80% for two different animals. For a conformable time period (35–108 days), a higher and more consistent increase in the whole muscle belly length (87%) was found in the present study.

The GM muscle belly length of children increased from 5 years (0.28 t_{fg}) to 12 years (0.71 t_{fg}) by 47% (Bénard *et al.*, 2011), which is in agreement with the increase of 53% for rabbit GM in the present study within the same normalised observation period.

Almost equal growth also appeared for the aponeurosis length of human GM (55% (Bénard *et al.*, 2011)) and rabbit GM (65%) within this time period (0.28–0.71 t_{fg}). Heslinga & Huijing (1990) measured the aponeurosis length of rat GM at ages of 70 days (0.7 t_{fg}) and 98 days (0.98 t_{fg}). The reported increase in aponeurosis length (19%) was also similar to that of rabbit GM (24%) within the observed time period.

Larger differences occurred for the GM fascicle length of different species. Bénard *et al.* (2011) found an increase in human GM fascicle length of 5% per year. In contrast, almost no changes were observed in the GM fascicle length during growth in the present study (Figure 6.7), which is in agreement with observations of rat GM (Heslinga & Huijing, 1990). Thus, an increase in GM muscle mass (Figure 6.2) resulted in an exclusive increase in CSA (see Eq. 6.1) of 12.2%/day. Slightly lower CSA growth rates were reported for rabbit EDL (9.5%/day) and SOL (7.7%/day) (Böl *et al.*, 2016). As the GM fascicle length (Figure 6.7) and pennation angle (mean $\alpha = 22.7° \pm 3.6°$, Table 6.1) did not change considerably for the age range studied, it is concluded that growth-related increases in muscle belly length are mainly explained by an increase in aponeurosis length, which is related to muscle fibre hypertrophy (Bénard *et al.*, 2011). Heslinga & Huijing (1990) provide a detailed discussion of the influence of increased aponeurosis length and CSA with unchanged muscle fascicle length.

Almost similar aponeurosis areas were found for GL and GM, which feature two explicitly pronounced tendon-aponeurosis structures on their proximal and distal ends (Figure 6.5). This has also been reported for rabbit SOL, EDL, and PLA (Böl *et al.*, 2016). It is reasonable for the areas and growth ratios of distal and proximal aponeuroses to be similar because at both muscle ends, the same generated forces are transferred over the aponeurosis to the tendon. Furthermore, the number of muscle fibres connected to each aponeurosis should be the same.

Böl *et al.* (2016) performed the only study available on changes in aponeurosis area during growth. For rabbits between 18 and 108 days old, they measured the aponeurosis length, width, and area of the SOL, EDL, and PLA. In general, they reported a higher

growth rate of the aponeurosis length compared to its width, which is in agreement with our observations on GL, GM, FDL, and TA, as shown in Figure 6.5. However, when normalising the distal aponeurosis growth rates to the initial values, the aponeurosis growth was higher in the width (this study: 1.9 ± 0.3%/day; Böl *et al.* (2016): 2.6 ± 0.7%/day) than in the length (this study: 1.5 ± 0.3%/day; Böl *et al.* (2016): 1.7 ± 0.2%/day). This might result from the muscle hypertrophy associated with a pronounced increase in muscle belly width, which is obvious for GL and GM in Figure 6.3 A and B. Even though the muscle belly growth is more uniform in FDL and TA (Figure 6.3 C, D), the distal aponeurosis growth in the width (FDL: 2.0%/day; TA: 1.4%/day) is slightly higher than that of the length (FDL: 1.8%/day; TA: 1.1%/day). In contrast, normalised proximal aponeurosis growth is higher in length (1.6 ± 0.3%/day) than in width (1.2 ± 0.4%/day), cf. Table 6.2, indicating that there are factors other than the increase in muscle belly width affecting aponeurosis growth.

The physiological CSAs of GL, GM, FDL, and TA were smaller than their corresponding aponeurosis areas, as shown in Figure 6.4. This was also found for rabbit SOL, EDL, and PLA (Böl *et al.*, 2016). Heslinga & Huijing (1990) explain this based on a two-dimensional approach. In principle, the appearance of a pennation angle between a muscle fibre and an aponeurosis segment requires a longer aponeurosis segment length compared to the muscle fibre diameter due to mechanical considerations. The muscle hypertrophy induced by an increase in fibre diameter may lead to an increase in pennation angle without adaption of the length of the aponeurosis segment (Heslinga & Huijing, 1990). Another mechanism may be the increase in aponeurosis segment length due to an increased muscle fibre diameter without changes in the pennation angle. For all the muscles observed, we found an obvious increase in aponeurosis length, as shown in Figure 6.5.

The pennation angle of GM, FDL, and TA hardly changed from the youngest to the oldest animal (Table 6.1). This implies that the increase in fibre and fascicle diameters during muscle hypertrophy can only be accommodated by a simultaneous

and proportional increase in the aponeurosis length. Moreover, an additional increase in the GL pennation angle during growth (Table 6.1) may further compensate for excessive hypertrophy. In fact, GL exhibits higher CSA compared to GM (Figure 6.5), although both muscles have similar aponeurosis areas. Thus, the lower aponeurosis-CSA ratio r_{ACSA} of GL (1.2) compared to GM (1.44) might be explained by the increasing pennation angle of GL and higher growth rate in GL muscle mass, as shown in Figure 6.2.

The lowest increase in CSA (4.8%/day) was found for TA. GL exhibited a growth rate that was almost three times higher (13.7%/day). This difference can be explained by the pronounced growth in the TA fascicle length (Figure 6.7) compared to the almost equal fascicle lengths of GL as well as the higher increase in GL muscle mass (Figure 6.2). The CSA growth rates observed for SOL (7.7%/day) and EDL (9.5%) by Böl *et al.* (2016) are in between the values determined for TA and GL (Table 6.2).

In contrast to the limited number of age-dependent experimental analyses, studies on rabbit muscles at particular ages are more common (Böl *et al.*, 2013; Hiepe *et al.*, 2014; Lieber & Blevins, 1989; Schenk *et al.*, 2013; Siebert *et al.*, 2015). These studies analysed muscle geometry as well as active and passive muscle properties from primarily adult specimens. However, it is possible to compare these results with the geometric data determined at discrete points. For example, Lieber & Blevins (1989) examined the muscle fibre architecture of 29 muscles of six rabbits with a mean mass of $2.5 \pm 0.2\,\mathrm{kg}$ (which roughly corresponds to an age of 73 days with respect to the present study). In accordance with our study, muscles were fixed at knee and ankle joint angles of 90° for architectural determination. Their results regarding muscle belly dimensions, fascicle lengths, and pennation angles of GL, GM, FDL, and TA were compared with our results from analysing the 3D muscle architecture of a 70-day-old rabbit ($\mathrm{m} = 2.35\,\mathrm{kg}$), as shown in Table 6.3. In general, our data are consistent with the results from Lieber & Blevins (1989). Deviations in the pennation angle (10° and 8° for GM and TA, respectively) might partially reflect variations in ankle and knee joint angles or might be induced by differences in the observation method. Lieber & Blevins (1989) measured geometrical

parameters in local regions of the muscle surface, whereas mean values from the complete 3D fascicle architecture of the muscles were determined within the present study.

Parameter	Muscle	This Study	Lieber & Blevins (1989)
Animal mass [kg]		2.35	2.5 ± 0.2
Muscle belly length [mm]	GL	52.7	57.5 ± 2.9
	GM	58.6	61.2 ± 2.9
	FDL	48.0	51.2 ± 2.1
	TA	55.6	56.9 ± 4.5
Fascicle length [mm]	GL	14.2 ± 2.3	16.1 ± 0.8
	GM	13.1 ± 2.0	14.7 ± 0.7
	FDL	12.9 ± 3.9	12.4 ± 0.5
	TA	31.7 ± 6.5	38.1 ± 3.0
Pennation angle [°]	GL	17.5 ± 4.1	15.5 ± 3.0
	GM	24.6 ± 3.4	13.8 ± 1.7
	FDL	15.0 ± 3.2	14.5 ± 3.0
	TA	11.3 ± 3.2	3.0 ± 1.0

Table 6.3: Comparison of the present results with muscle architectural parameters of rabbits with a given animal mass of 2.5 ± 0.2 kg provided by Lieber & Blevins (1989).

However, fascicle lengths were determined at a fixed ankle joint angle of 90°, similar to Lieber & Blevins (1989). Changing the ankle angle might influence the results due to increase of the muscle lever arms. Based on geometrical calculation of the muscle-tendon complex lengths for ankle joint angles of 80° and 100°, using the measured muscle lever arms (see Figure 6.2), we found an additional increase and decrease in GL and GM fascicle lengths of +1 mm and −1 mm during the growth period, which would have a small influence on the results, as shown in Figure 6.7. Due to the smaller lever arm lengths, the influence on the FDL and TA fascicle lengths was < 0.2 mm. The calculations were done under the assumption that length changes in the passive muscle-tendon complex induced by changing the ankle angle would primarily influence the fascicle length due to the higher compliance of passive muscle tissue compared to

the aponeurosis and tendons (Zuurbier *et al.*, 1994). We conclude that changes of the ankle angle of about ± 10° during fixation of the preparation are negligible for fascicle length determination.

6.4.2 Functional relevance of changing tendon–muscle fascicle length ratio

It is well known that muscles have different tendon–muscle fascicle length ratios (r_{TFL}), depending on the muscle function (Biewener, 1998; Biewener & Roberts, 2000; Mörl *et al.*, 2016). Muscles that act as springs in bouncing gates and contribute to energy conservation have long SECs and short muscle fibres, which result in high r_{TFL}. One typical example is the PLA (r_{TFL} =18.7 (Biewener, 1998)) of the wallaby, a muscle that is well adapted to spring-like energy storage and economical muscle force generation during hopping (Biewener & Baudinette, 1995; Biewener *et al.*, 2004). In contrast, muscles that primarily act as motors in concentric contractions have a comparably short SEC and long muscle fibres. One example is the pigeon pectoralis ($r_{TFL} = 0.4$), which shortens substantially during the downstroke to produce mechanical power for aerodynamic lift and thrust during flying (Biewener, 1998).

For the adult GM and GL, an intermediate r_{TFL} of 8 was observed, which is similar to that of horse M. gastrocnemius ($r_{TFL} = 8.7$ (Biewener, 1998)) and slightly lower than that of camel M. gastrocnemius ($r_{TFL} = 11$ (Alexander *et al.*, 1982)). The gastrocnemii of horses and camels have more universal functions during locomotion that involves spring- and motor-like behaviour, as well as the capability of economical force production (Biewener, 1998). Based on the intermediate r_{TFL} value, there might be a similar functional relevance of rabbit GL and GM. However, no kinematic study has examined rabbit hind-limb muscle function during locomotion. As shown in Figure 6.9, r_{TFL} is low for muscles that act as motors, like the M. biceps femoris of wallabies (Biewener & Baudinette, 1995), or for muscles that act as brakes, like M. vastus lateralis, which absorbs energy during the stance phase of walking, trotting, or galloping in rats

(Gillis & Biewener, 2001). Rabbit TA muscle exhibited a low r_{TFL} of 2, indicating a similar functional relevance. In fact, the TA acts as both a motor (by dorsiflexion of the ankle joint in the swing phase) and a brake (by energy absorption in the early stance phase) during human locomotion (Ferris *et al.*, 2005; Hamner *et al.*, 2010).

Interestingly, r_{TFL} was not a constant geometrical property of the specific muscle

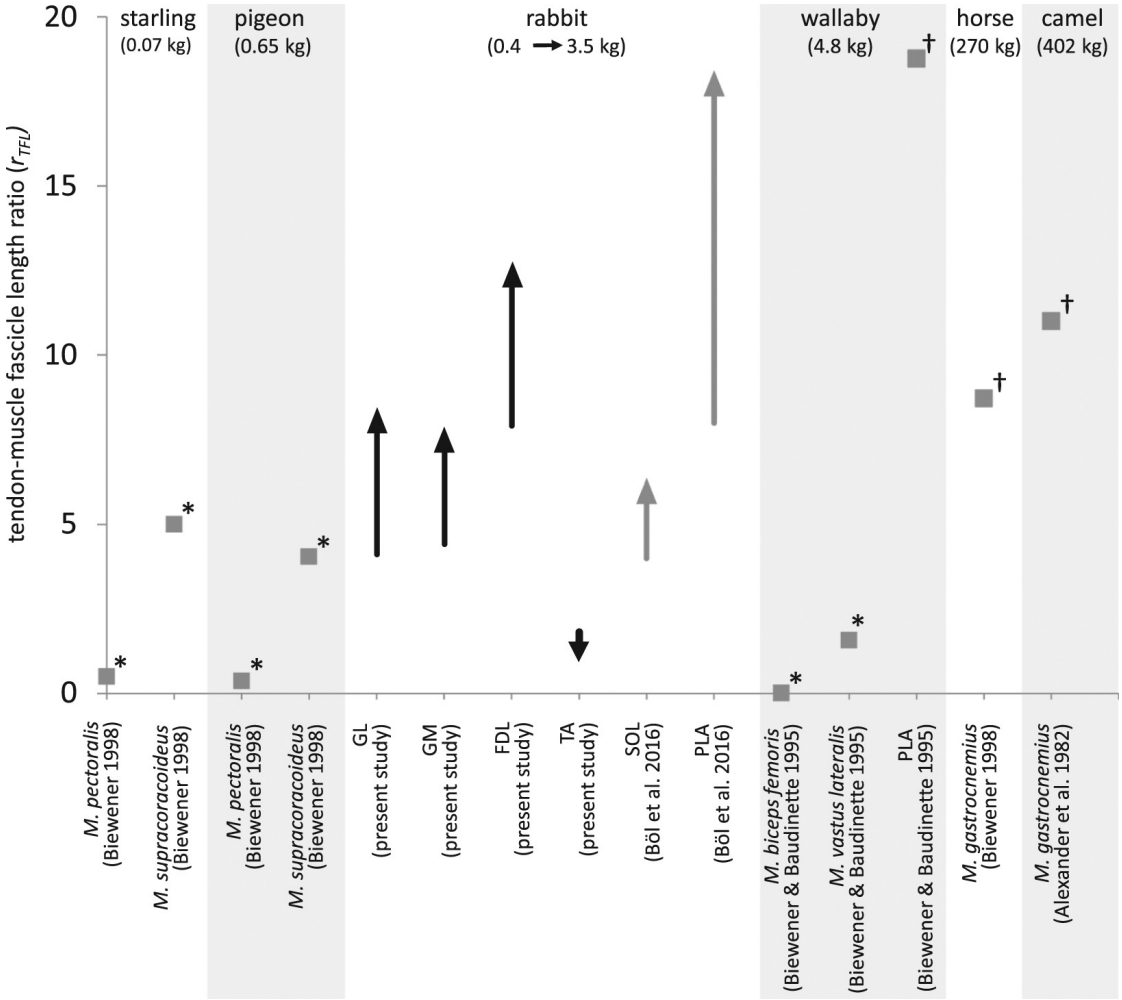

Figure 6.9: Tendon–muscle fascicle length ratios (r_{TFL}) of different adult mammalian muscles from the literature categorised by body mass. Changes in r_{TFL} with increasing body mass (from 0.4 to 3.5 kg) determined in the present study and by Böl *et al.* (2016) are shown by black and grey arrows, respectively. Muscles act as motors (*) or springs (†) during locomotion (Biewener, 1998).

but instead changes during growth, as shown in Figure 6.8. We found an increase in r_{TFL} by a factor of 2 (GL, GM, FDL) and even a slight decrease (TA). An increasing r_{TFL} was also reported for other rabbit shank muscles. During growth, r_{TFL} of the SOL and PLA increased from 4 to 6 and from 8 to 18, respectively (Böl *et al.*, 2016). The increase might indicate increasing importance of economical locomotion during growth (Böl *et al.*, 2016). The metabolic cost of transport decreases with increasing body mass in various mammalian species (Taylor *et al.*, 1970). Furthermore, an increasing r_{TFL} was reported for several shank muscles from 35 quadrupedal species ranging in body mass from 0.04 to 545 kg (Pollock & Shadwick, 1994). For instance, r_{TFL} of the PLA and GAS respectively increased 3-fold and 15-fold over the observed body mass range. These arguments indicate that increasing the capacity of strain energy storage with increasing body mass might be relevant for not only the consideration of different species but also for better understanding of the changing energetics and potentially increased economical locomotion during growth.

6.4.3 Impact on muscle modelling

From a modelling perspective, the data presented are of great interest as they support appropriate model validation and thus contribute to more meaningful model concepts. Besides the determined growth kinetics of the muscle bellies, aponeuroses, and tendons, the 3D fascicle data in particular allow for proper validation of 3D constitutive growth models. In turn, these models can be used to address functional relevance of structural changes during growth and how these changes are related to mechanical properties, which is largely unknown (Bénard *et al.*, 2011). Furthermore, with conclusive growth model approaches at hand, load transfer mechanisms such as those determined experimentally by Böl *et al.* (2015) could be analysed and predicted in the future. Hence, the extensive datasets of the present study and the one provided by Böl *et al.* (2016) are the first steps to developing and validating comprehensive growth models for the prediction of muscle development under various boundary conditions.

6.5 Conclusion

The present study has provided a comprehensive set of geometrical muscle parameters during growth for rabbit GL, GM, FDL, and TA, and it has also considered functional relevance of growth related changes in these parameters. In the observed time period (18–108 days after birth), the muscle bellies, tendons, and aponeuroses exhibited almost linear growth characteristics. However, the muscles showed specific differences in growth, which might have functional relevance. Muscles used as springs in locomotion, such as rabbit FDL, GM, GL, or PLA, have high tendon–muscle fascicle length ratios (r_{TFL}) after birth. We found that this ratio increases during growth by up to a factor of two. The observed increase in r_{TFL} results from the near lack of changes in the fascicle length in combination with large increases in the aponeurosis and tendon length during growth. Therefore, the increase in mass of spring-like muscles mainly appeared as muscle hypertrophy (the synthesis of parallel myofibrils), which resulted in an increase in the physiological CSA. However, the TA, which acts as motor and brake during locomotion, exhibited deviating morphology and growth characteristics. The growth-related increase in muscle mass resulted in a distinct increase in fascicle length. Furthermore, the tendon–muscle fascicle length ratio was low after birth and decreased during growth.

Future studies should focus on morphometric changes in muscle structure during growth, as well as altered functional demands during aging. Furthermore, deeper knowledge about age-related changes in active and passive muscle properties is required to improve the understanding of muscle growth mechanisms and age-related adaptations of muscle–tendon complexes.

Chapter 7

General Conclusion

The first goal of this thesis was the experimental determination of biomechanical and architectural muscle properties from distinct muscle types (*striated skeletal* and *smooth* musculature), and subsequently, the (re-) evaluation and interpretation of the results based on the presented research. The second goal was to embed the findings in a greater research context and to discuss their physiological and structural impact. Hence, by giving potential explanatory approaches to so far unresolved questions in terms of muscle dynamics and morphology, a more coherent picture of the muscle's structural and functional complexity can be derived by this thesis.

Since the introduction of the sliding filament theory in 1954 by Huxley & Niedergerke (1954) and Huxley & Hanson (1954), the muscular behaviour and its structural and functional complexity has been seriously re-evaluated by recent molecular and biomechanical findings (Rassier, 2017; Li *et al.*, 2016; Rivas-Pardo *et al.*, 2016; Houdusse & Sweeney, 2016; Lindstedt & Hoppeler, 2016; Zou *et al.*, 2006). Here, novel mechanisms — complementing classic theories — are proposed in order to explain the dependence of muscle force on the history of contraction as well as altered contraction dynamics at short muscle lengths. Thus, on the one hand, classic theories can be validated indirectly, on the other hand, new experimental findings (titin,

Z-disc structure) can be integrated by appropriate model expansions (in perspective). Therefore, this chapter is intended to provide general conclusions and interpretations based on the research outcomes underlying this thesis presented in the **Chapters 3–6**.

7.1 History-effects relate smooth muscle tissue to function

The stomach functions consist of storing and partially dissolving the food, secreting acid and enzymes, splitting it into separate parts and guiding the liquefied nutrients towards the small intestine (Horowitz *et al.*, 1994; Pal *et al.*, 2007). By covering these multiple tasks, the stomach represents the most extensible section of the digestive tract. Large dimensional changes during ingestion and gastric emptying of the stomach are associated with large changes in smooth muscle length. These length changes induce RFE and RFD. It could be demonstrated, that experimentally observed history-effects of smooth muscle tissue have an impact on the force-generating capacity of the stomach and subsequently support gastric emptying. Hence, a protective and supportive function of RFE prior to gastric emptying to avoid excessive distension of the stomach might represent specific adaptations to gastric functionality. Moreover, RFE might counteract rapid expansion of gastric tissue due to acceleration of gastric contents in impact situations, e.g. during jumping or running. This potentially explains the functional relevance of significantly enhanced forces during and after active lengthening as investigated in this work (**Chapter 3**). This outstanding muscle behaviour is not accounted for in existing smooth muscle models (Zhao *et al.*, 2008, 2010; Cheng *et al.*, 2010; Jia *et al.*, 2015) so far and strongly supports the idea of a holistic reflection of distinct stomach structure and function.

7.1.1 Functional and morphological differences of gastric tissue

For the first time a comprehensive set of stomach smooth muscle parameters from a distinct region of the proximal stomach (the fundus; cf. Figure 2.1), including

classic biomechanical muscle properties and history-dependent effects, is provided by this work. However, hollow organs as the stomach show species-, location-, orientation- and layer-specific differences due to their geometric and structural complexity (Jia *et al.*, 2015; Korossis *et al.*, 2009). As a result of different functions of distinguishable stomach regions as e.g. fundus and antrum (cf. Figure 2.1), location-dependent differences in morphological and biomechanical properties of smooth gastric tissue are expected, although, attracting very little attention so far. Distinctive differences in muscle properties of tissue from different regions of hollow organs, as well as in dependence of tissue strip orientation (e.g. longitudinal vs. transversal) have been reported in previous studies (Barnes *et al.*, 2015; Jia *et al.*, 2015; Korossis *et al.*, 2009; Liao *et al.*, 2005; Zhao *et al.*, 2005, 2008). Higher v_{max}-values of the distal part of the stomach smooth muscle (the antrum) (Armitage & Dean, 1966; Pal *et al.*, 2004; Zhao *et al.*, 2005) compared to the proximal part of the gastric muscle (the fundus) might promote specific antrum functions, like emptying the stomach by peristaltic contractions. However, no information about the history-dependence of antrum smooth muscle was available so far. Differences in passive muscle properties and muscle structure have been observed by Zhao *et al.* (2008) for three regions of the stomach (fundus, antrum, corpus). In general, longitudinal gastric strips were stiffer than transversal strips, whereas the strips from the corpus were the stiffest among the three regions in both directions, likely due to the thicker mucosa layer (Jia *et al.*, 2015; Zhao *et al.*, 2008). Hence, the parametrisation and validation of potentially existing active, location-dependent differences in structural and biomechanical properties seems to be a very important issue in further research to better understand whole stomach (dys-) function.

7.1.2 Relevance to smooth muscle modelling

The development of computer-based, three-dimensional stomach models might be a promising research approach to address the issue of history-dependence of force

production in smooth muscle tissue. The big advantage of computer simulations is that many different 'what-if' simulations can be done very easily by changing input parameters. These computational models potentially provide a detailed insight in the functionality and motility of hollow organs (e.g. bladder: Seydewitz *et al.* (2017) and arteries: Böl *et al.* (2012); Böl & Schmitz (2013); Schmitz & Böl (2011)), and might be used to assess specific treatments (Cheng *et al.*, 2007, 2010). In future, validated models should be capable of predicting varying functional effects of pathological tissue alterations (e.g. due to certain diseases such as cancer), and facilitate a better understanding of how gastrointestinal tissue adapts to mechanical changes (as e.g. obstruction). Building a computational whole internal organ model might assist in the training, the preparation and the planning of complex surgery of the gastrointestinal tract (e.g. by using a virtual endoscopic navigation system (Gastelum *et al.*, 2016)), due to the visualisation and navigation through anatomical structures (Hochberger *et al.*, 2002). Moreover, models potentially enable the simulation of dynamic behaviour accompanied by gastric deformation (peristalsis), and help to understand certain physical responses and pathophysiological abnormalities as e.g. vomiting (emesis) and pylorospasm (restricted food delivery from the stomach to the small intestine due to an increased muscle tone of the pylorus) (Horn, 2008).

Concluding, the development of detailed multi-scale models will allow *1.)* for the general expansion of the physiological understanding of overall stomach functioning. *2.)* A quantitative understanding of the mechanisms involved in force development — including history-dependent effects in smooth muscle tissue — allowing the consistent and realistic prediction of muscle forces throughout the entire muscle working range.

7.2 Contractile dynamics of skeletal muscle function

7.2.1 Muscles act like linear springs

Experimental observations on striated skeletal muscle tissue — presented in **Chapter 4** — demonstrated, that single muscle fibres from the *musculus extensor digitorum longus* of the rat behave like linear springs during long, eccentric contractions (nearly over the entire FLR; Figure 7.1). This is a surprising result because the underlying nonlinear force – length relationship (resulting from the actomyosin overlap) is composed of linear segments that decrease in slope with fibre length. Moreover, it could be demonstrated that both cross-bridges and non-cross-bridges contribute nonlinearly to the resulting linear total muscle force response. This muscle behaviour is not accounted for in existing models so far, and might significantly reduce the control effort. Additionally, this distinct manner might offer high impact shock absorption during eccentric movements such as landing after jumps or downhill running. Moreover, it justifies investigating biological locomotion with technical devices employing serial elastic actuators and simple control strategies.

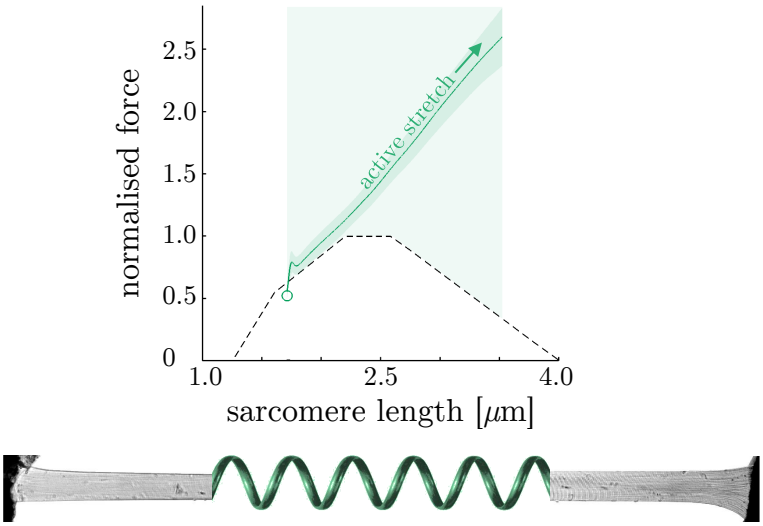

Figure 7.1: Muscle = linear spring.

To account for this striking behaviour, titin — the largest sarcomeric protein (3–4 Megadalton) (Bang *et al.*, 2001) — may play a crucial role in contributing to the enhanced force response during active stretch contractions (Linke, 2017; Shalabi *et al.*, 2017), especially in the range of the descending limb of the FLR (Rassier *et al.*, 2003; Herzog *et al.*, 2016). Titin in skeletal muscles is known to become stiffer upon muscle activation in the presence of Ca^{2+} (Labeit *et al.*, 2003). More important, however, seems to be the property of skeletal titin to significantly reduce its persistence length upon activation and thus to produce increased forces during subsequent stretching. In accordance with this mechanism, the study demonstrated in **Chapter 4** shows high force increases — despite the inhibition of cross-bridges — in extensive, eccentric contractions. Moreover, the experimentally observed slight increase in slope with initial length agrees with current models attributing the non-cross-bridge force to titin (Rode *et al.*, 2009; Nishikawa *et al.*, 2012; Schappacher-Tilp *et al.*, 2015).

One possibility of the reduction in titin's free molecular spring length in skeletal muscles is its property to bind on actin upon activation (Kellermayer & Granzier, 1996). This might be due to an interaction of titin's PEVK region with actin (Bianco *et al.*, 2007; Powers *et al.*, 2014). Another possibility would be to actively shorten and retain titin's distal immunoglobulin domain — experimentally oberserved by DuVall *et al.* (2017). This current study supports the role of a significant reduction of the activation-dependent titin spring during stretch contractions as a possible explanatory approach for RFE. Even though, these experimental findings contradict a potential titin-actin interaction (Heidlauf *et al.*, 2017, 2016; Herzog *et al.*, 2016; Monroy *et al.*, 2017; Powers *et al.*, 2014; Leonard & Herzog, 2010), and require careful further examination. However, current research outcomes (reduction of the distal titin region) can be incorporated into future muscle models — aiming at a better understanding of skeletal muscle fibre structure and function.

Consequently, there are particular uncertainties in terms of underlying mechanisms of enhanced forces during and after active stretch contractions (RFE) such as possible

binding sites (titin provides binding sites for at least 30 muscle proteins (Linke, 2017)) — and the regulation thereof (DuVall *et al.*, 2017; Rassier, 2017; Herzog *et al.*, 2016; Leonard & Herzog, 2010; Leonard *et al.*, 2010). Therefore, as intensely discussed in **Chapters 3** (section 3.4.2) and **4** (section 4.4), respectively, there is still a scientific controversy regarding history-dependent effects. The characterisation of the activation dynamics of the semi-active titin spring could account for a possible explanation of underlying binding mechanisms. Thus, a potential study for further investigating the role of Ca^{2+} in RFE would be to actively stretch functionally intact single skinned muscle fibres in the absence of Ca^{2+}. For this purpose, tropomyosin [1] could be removed from the actin filament, while the fibres will be activated in an ATP-rich solution without Ca^{2+}. Hence, this approach could clarify whether Ca^{2+} plays a crucial role in the binding of titin and actin, and whether titin binds to the myosin binding sites on the actin filaments. Therefore, *1.)* a regular or slightly reduced RFE (lack of Ca^{2+}-based stiffening of titin (Labeit *et al.*, 2003)) — on the one hand — would confirm a titin-actin interaction. *2.)* An absent RFE — on the other hand — could mean: *(i)* that titin binds to tropomyosin (Raynaud *et al.*, 2004), *(ii)* that Ca^{2+}-based stiffening of titin completely explains RFE, or *(iii)* that a Ca^{2+}-titin interaction e.g. leads to a conformational change of titin, which in turn enables the binding of titin to actin.

7.2.2 'Stunning' behaviour at short muscle lengths

In addition to the open questions about active force production in eccentric and concentric contractions on the smooth as well as on the skeletal muscle fibre level ('history-dependence'; cf. **Chapters 3** and **4**), kinetic and microstructural findings at short skeletal muscle fibre lengths (e.g. 'delta state', (Ramsey & Street, 1940); refer to **Chapter 5**) represent another, yet unresolved issue. Both, the myosin filament stiffness (cf. section 5.4) and the force production at short fibre lengths ($< l_4$; cf. Figure 5.5)

[1] A regulatory protein that spirally runs tightly around the actin filament as a helically twisted double-strand, while blocking the binding sites between actin and myosin at low Ca^{2+}-concentrations and enabling actomyosin interaction at high Ca^{2+}-concentrations (Tortora & Nielsen, 2013).

are contrary to the classic assumption of myosin filament compression at these lengths. More specifically, in addition to experimental findings on mammalian muscles from rats (cf. **Chapter 5**), there is some evidence in non-mammals for myosin filament sliding through the Z-disc (chameleon tongue: Herrel *et al.* (2001); blowfly larva: Osborne (1967); barnacle: Hoyle *et al.* (1963)).

Based on the idea of this sliding, the structurally consistent model of sarcomere contraction — proposed in **Chapter 5** — effortlessly explains the stunning linearity of the segments of the classic FLR as well as the dependence of the maximum contraction velocity of striated muscles (Edman, 1979). This sliding leads to swivelled cross-bridges (Reedy *et al.*, 1989; Toyoshima *et al.*, 1989) in the adjacent half-sarcomere that dampen contraction. Moreover, these swivelled cross-bridges could potentially explain the required prolonged stimulation times to reach maximum isometric force at lengths $< l_4$ ($\sim 1.6\,\mu$m) (cf. Figure 5.7) (Gareis *et al.*, 1992; Rack & Westbury, 1969). The proposed model reconciles contradictory experimental findings with the well-accepted sliding filament and cross-bridge theories, which provide quite robust predictions of active muscle force under isometric conditions for the plateau-region and the descending limb of the FLR. The assumption of the myosin filament sliding through the Z-disc provides a better understanding of e.g. the Z-disc structure and the function of the second myosin head in skeletal muscles (Huxley, 2000). Furthermore, the model enables a structurally and functionally consistent view of the contractile machinery of the striated muscle fibre with possible implications for evolution and physical phenomena. More precisly, prior to the existence of exo- and endoskeletal structures, muscles probably adhered to gelatinous material such as is present in jellyfish and sponge (Seipel & Schmid, 2005). Therefore, these primordial muscles had to be equipped with a protective mechanism preventing extreme or uncontrolled muscle shortening and muscular dysfunctions in the first living beings with muscles, which had no skeleton yet. Moreover, it could be speculated whether the behaviour of the muscle fibres in the 'delta state' can be explained by stuck half-sarcomeres associated with the sliding of the myosin filaments

through the Z-disc. For instance, the functionality of the fibre could be restored by passive overstretching — consistent with similar behaviour in muscle cramps.

However, despite the individual experimental evidences, the hypothesis of myosin filament sliding in mammals is new and breaks with classical ideas. Thus, a direct, structurally-based proof seems to be necessary. In order to achieve this goal, ultrathin sections ($\sim 500\,\mathrm{nm}$) of maximally contracted single skinned fibres at particular muscle lengths ($< l_4$; cf. Figure 5.5) could be used to provide fluorescence microscopic evidence for myosin filament sliding through the Z-disc.

7.3 Muscle–tendon architecture in relation to function

7.3.1 Muscles — more than just motors

Muscles act as motors, shock absorbers, energy stores and struts for stabilising posture, decelerating after a jump or accelerating external loads for ballistic motions like throwing (Dickinson *et al.*, 2000; Roberts & Azizi, 2011). To cover prevailing conditions of specific tasks, the capability of a muscle is linked to the tendon-muscle fascicle length ratio r_{TFL} (refer to **Chapter 6** for details). Thus, various skeletal muscles have different ratios of muscle fibre and tendon lengths. This means, for instance, r_{TFL} is low for muscles that act as motors — mostly performing concentric contractions, while producing maximum power (Biewener, 1998). A characteristic example is the pigeon pectoralis muscle during flying ($r_{TFL} = 0.4$) (Biewener, 1998). On the other hand, r_{TFL} is high for muscles that act as springs in bouncing gates — the metabolic energy consumption of active muscle fibres is minimised, while elastic energy storage is maximised (Biewener & Baudinette, 1995). One example is represented by the musculus plantaris of the wallaby with an r_{TFL} of 18.7. In that muscle the fibres contract almost isometrically, while the overall muscle-tendon unit undergoes a stretch-shortening cycle (Biewener *et al.*, 2004). Consequently, there is an inverse relationship for muscle work relative to force and energy economy (Biewener, 2016). This means that, due to various changes in boundary conditions (body mass, size)

during growth, the muscle's architecture — including the aponeurosis, the muscle, the tendon and the physiological cross-section — need to adapt in a manner to meet changing prevailing conditions. For instance, conditions such as changing energetics, increased economical locomotion, cost of force generation, the ability to conserve elastic energy, and the operation near optimum muscle length (cf. section 6.4.2) (Biewener, 2016).

7.3.2 Relevance to practical application

To realise a target-oriented locomotion, several organ systems and multiple muscles are involved in vertebrates. Thereby, complex arrangements of muscles, tendons, bones and ligaments are used for force generation and transmission. Forces — generated by the muscles — are transmitted via tendons to the bones. Furthermore, the bones can be interconnected via different structures (ligaments and joints). To understand how these different components work together, it is important to know their structure and function. Consequently, in addition to active and passive muscle properties (as e.g. force – length and force – velocity relations), muscular contraction dynamics depend on the three-dimensional muscle structure (e.g. muscle fascicle architecture, aponeurosis dimensions and tendon lengths), also. A muscle's architecture is an important determinant of its force-generating capacity (Gans & Bock, 1965; Blazevich & Sharp, 2005), while understanding the relationship between structure and function is of great practical importance. This understanding, on the one hand, clarifies the physiological basis of force production and movement (Lieber & Frieden, 2000). On the other hand, it is important for e.g. surgeries involving tendon/muscle transfer- or lenghtening procedures (Lieber & Frieden, 2000).

Therefore, the study demonstrated in **Chapter 6** was aimed to investigate changes in three-dimensional muscle structure of rabbit *gastrocnemius lateralis, gastrocnemius medialis, flexor digitorum longus,* and *tibialis anterior* during growth. The outcomes represent new findings regarding changes in three-dimensional muscle architecture and aponeurosis shape during growth, and they provide information for muscle force

generation, functional relevance, and adaptation with respect to animal age.

In orthopedics, especially in neurological disorders after stroke or in patients with spastic motility disorders, tendon-/muscle lenghtening operations play an essential role in correcting malpositions to restore impaired movement (Hong *et al.*, 2017; Shah *et al.*, 2017; Lieber & Frieden, 2000). Some examples are, the transfer of the musculus flexor carpi radialis — as the motor for finger extension — after radial nerve palsy (Chuinard *et al.*, 1978), or the transposition of the anterior tibial tendon in patients with idiopathic clubfoot (Dobbs *et al.*, 2000; Halanski *et al.*, 2016). To ensure successful treatment outcomes, it is essential to choose a donor muscle with architectural features similar to the original muscle to perform the original muscle's function (Lieber & Frieden, 2000). Moreover, it should also be considered that the direction of the muscle's tensile force is altered as a result of a muscle/tendon transfer procedure. Hence, a detailed knowledge of the muscle's architecture provides both, a scientific rationale as well as an explanation of the mechanical basis for orthopaedic disorders. Hence, realistic input data based on experimental observations are necessary for the elucidation of specific muscle architectures. The research outcomes might give a first hint of information useful for selection of musculo-tendinous structures used in surgeries for treatment of e.g. disorders affecting the limbs (e.g. inhibition of extension or flexing contracture). Furthermore, specific anatomical landmarks provided by accurate 3D architectural data facilitate e.g. the placement of electrodes for electromyography or the allocation of muscle biopsies. Hence, this permits to operate in an efficient manner that allows for an optimal treatment outcome (Shah *et al.*, 2017; Lieber & Frieden, 2000). Moreover, the experimentally observed findings — demonstrated within this work — help to improve the understanding of muscle growth processes, are useful as input data for muscle growth modelling, and subsequently, might improve surgical treatment techniques.

7.3.3 Future challenges in muscle modelling

Muscle models — designed to facilitate realistic predictions of muscle force production during dynamic contractions over the entire working range of the muscle — are used to answer a variety of questions in biology, medicine, biomechanics and physiology. However, it should be noted that it is not straightforward to develop realistic models of muscular contraction dynamics for detailed simulations, as this requires a detailed understanding of underlying principles. Hence, despite the increasing importance of muscle models, there are currently significant open questions about *(i)* how individual fibre forces are integrated to whole muscle forces (Biewener, 2016), and *(ii)* how three-dimensional muscle structures are affected by deformations with respect to active force generation of muscle packages (Reinhardt *et al.*, 2016; Siebert *et al.*, 2014a). The elucidation of these unresolved issues is essential for assessing the dynamics of movement in relation to the muscle design. Therefore, it seems to be important to examine *in vivo* 3D muscle architectures during contraction (preferably under dynamic conditions) with proper techniques (such as diffusion tensor imaging (DTI) and high-resolution anatomical MRI scans (Schenk *et al.*, 2013; Bolsterlee *et al.*, 2015; Siebert *et al.*, 2015)). Additionally, to validate a comprehensive 3D multi-muscle model, intermuscular pressure and multiple force measurements from individual muscles of certain muscle groups (agonistic, synergistic) should be obtained simultaneously (Röhrle *et al.*, 2012; Böl *et al.*, 2013, 2015; Siebert *et al.*, 2016, 2017; Herzog, 2017). This will likely help to quantify distinctive muscle forces in individual movements reliably and accurately.

7.4 Prospects

Based on the studies presented in the **Chapters 3–6**, this thesis enables a substantial contribution to a much more detailed understanding of overall muscle behaviour and force generation. The relevance of further clarification of the mechanical understanding of muscular contraction dynamics results from the extensive application possibilities of computer-based muscle models in the wide field of applied natural sciences and technology (such as medicine, biology, physiology, biomechanics, muscle diagnosis and orthopedics). Therefore, a precise prediction of muscular forces is needed to gain detailed knowledge of: *(i)* the structure and functioning of the muscle, *(ii)* neuromuscular relationships in locomotor systems, *(iii)* the optimisation of medical diagnostic and/or treatment methods, but also *(iv)* to address unresolved issues related to mechanical/metabolic movement principles or physiological processes. Hence, the development of numerical methods for the simulation of biological materials, hollow organs or whole skeletal muscles are of great importance. For instance, the verifcation and validation of an overall muscle fibre model might enable a structurally consistent, quantitative description of the synthesis of force-generating mechanisms on the muscle fibre level. Due to novel research approaches together with computer simulations, possible binding mechanisms (such as titin to actin or titin to tropomyosin) can be tested.

The predictive power of complex 3D muscle models is only as good as the physical accuracy comprising each of its components, generally the properties of certain muscle structures, boundary conditions, and/or underlying geometries (Röhrle *et al.*, 2017). Such predictions also depend on the correct characterisation of their smallest unit — the (half-) sarcomere. Errors in their description inevitably lead to deviations of the muscular force and thus to issues and misinterpretations of all model-based research, e.g. in the elucidation of neuromechanical relationships, investigations of the control and stability of locomotion, or in the estimation of metabolic cost. Consequently, the prediction

of realistic muscle forces in dynamic contractions allows a better understanding of e.g. overall muscular force production, functional morphology, mechanical principles of locomotion, prosthetics and robotics or provides a detailed insight into the functionality and motility of hollow organs.

Hence, this work enables potential explanatory approaches to so far unresolved questions in terms of muscular contraction dynamics and mechanisms on the molecular and cellular level. These novel insights facilitate a coherent view of the impact of contraction dynamics and 3D muscle architecture on total force production and gastrointestinal motility.

Bibliography

Abbott, B.C., & Aubert, X.M. 1952. The force exerted by active striated muscle during and after change of length. *Journal of Physiology*, **117**, 77–86.

Alexander, R. McN., Maloiy, G. M. O., Ker, R. F., Jayes, A. S., & Warui, C. N. 1982. The role of tendon elasticity in the locomotion of the camel (Camelus dromedarius). *Journal of Zoology*, **198**(3), 293–313.

Alexander, R.M. 1990. Three Uses for Spring in Legged Locomotion. *The international journal of robotics research*, **2**, 53–61.

Allen, J.D., & Moss, R.L. 1987. Factors influencing the ascending limb of the sarcomere length-tension relationship in rabbit skinned muscle fibresS. *Journal of Physiology*, **390**, 119–136.

Armitage, A K, & Dean, A C. 1966. The effects of pressure and pharmacologically active substances on gastric peristalsis in a transmurally stimulated rat stomach-duodenum preparation. *The Journal of physiology*, **182**(1), 42–56.

Arner, A, & Malmqvist, U. 1998. Cross-bridge cycling in smooth muscle: a short review. *Acta Physiol Scand.*, **164**(4), 363–372.

Arner, A., Malmqvist, U., & Uvelius, B. 1984. Structural and mechanical adaptations in rat aorta in response to sustained changes in arterial pressure. *Acta Physiol Scand*, **122**(2), 119–26.

Arnold, Allison S., Liu, May Q., Schwartz, Michael H., Õunpuu, Sylvia, Dias, Luciano S., & Delp, Scott L. 2006. Do the hamstrings operate at increased muscle-tendon lengths and velocities after surgical lengthening? *Journal of Biomechanics*, **39**(8), 1498–1506.

Azizi, E. 2014. Locomotor function shapes the passive mechanical properties and operating lengths of muscle. *Proceedings. Biological sciences / The Royal Society*, **281**(1783), 20132914.

Azizi, E., Brainerd, E., & Roberts, T. 2008. Variable gearing in pennate muscles. *Proceedings of the National Academy of Sciences*, **105**(5), 1745–1750.

Azizi, Emanuel, & Roberts, Thomas J. 2009. Biaxial strain and variable stiffness in aponeuroses. *The Journal of Physiology*, **587**(17), 4309–4318.

Azpiroz, F, & Malagelada, J R. 1984. Pressure activity patterns in the canine proximal stomach: response to distension. *American Journal of Physiology - Gastrointestinal and Liver Physiology*, **247**(3), G265—-G272.

Bagni, M.A., Cecchi, G., Colomo, F., & Garzella, P. 1992. Effects of 2,3-butanedione monoxime on the crossbridge kinetics in frog single muscle fibres. *Journal of Muscle Research and Cell Motility*, **13**(5), 516–522.

Bang, M.-L., Centner, T., Fornoff, F., Geach, A. J., Gotthardt, M., McNabb, M., Witt, C. C., Labeit, D., Gregorio, C. C., Granzier, H., & Labeit, S. 2001. The Complete Gene Sequence of Titin, Expression of an Unusual 700-kDa Titin Isoform, and Its Interaction With Obscurin Identify a Novel Z-Line to I-Band Linking System. *Circulation Research*, **89**(11), 1065–1072.

Barany, M. 1967. ATPase Activity of Myosin Correlated with Speed of Muscle Shortening. *The Journal of General Physiology*, **50**(6), 197–218.

Barnes, S C, Shepherd, D E T, Espino, D M, & Bryan, R T. 2015. Frequency dependent

viscoelastic properties of porcine bladder. *Journal of the Mechanical Behavior of Biomedical Materials*, **42**, 168–176.

Bénard, Menno R., Harlaar, Jaap, Becher, Jules G., Huijing, Peter A., & Jaspers, Richard T. 2011. Effects of growth on geometry of gastrocnemius muscle in children: A three-dimensional ultrasound analysis. *Journal of Anatomy*, **219**(3), 388–402.

Bensley, B.A. 1948. *Bensley's Practical anatomy of the rabbit: An Elementary Laboratory Text-book in Mammalian Anatomy.* 8th edn. Toronto: University of Toronto Press.

Bhaskar, S.N., Weinmann, J.P., Schour, I., & Greep, R.O. 1950. The growth pattern of the tibia in normal and ie rats. *Am J Anat*, **86**(3), 439–477.

Bianco, Pasquale, Nagy, Attila, Kengyel, András, Szatmári, Dávid, Mártonfalvi, Zsolt, Huber, Tamás, & Kellermayer, Miklós S Z. 2007. Interaction forces between F-actin and titin PEVK domain measured with optical tweezers. *Biophysical journal*, **93**(6), 2102–2109.

Biewener, A. A., McGowan, C., Card, G.M., & Baudinette, R.V. 2004. Dynamics of leg muscle function in tammar wallabies (M. eugenii) during level versus incline hopping. *Journal of Experimental Biology*, **207**(2), 211–223.

Biewener, A.A. 1998. Muscle Function in vivo: A Comparison of Muscles used for Elastic Energy Savings versus Muscles Used to Generate Mechanical Power. *American Zoologist*, **38**(4), 703–717.

Biewener, A.A. 2016. Locomotion as an emergent property of muscle contractile dynamics. *The Journal of experimental biology*, **219**, 285–294.

Biewener, A.A., & Baudinette, R.V. 1995. in Vivo Muscle Force and Elastic Energy Storage During Steady- Speed Hopping of Tammar Wallabies (Macropus Eugenii). *Journal of Experimental Biology*, **198**(Pt 9), 1829–1841.

Biewener, A.A., & Roberts, T.J. 2000. Muscle and tendon contributions to force, work, and elastic energy saving: A comparative perspective. *Exercise and Sport Sciences Reviews*, **28**, 99–107.

Binzoni, T, Bianchi, S, Hanquinet, S, Kaelin, a, Sayegh, Y, Dumont, M, & Jéquier, S. 2001. Human gastrocnemius medialis pennation angle as a function of age: from newborn to the elderly. *Journal of physiological anthropology and applied human science*, **20**(5), 293–298.

Blazevich, A.J., & Sharp, N.C.C. 2005. Understanding muscle architectural adaptation: Macro- and micro-level research. *Cells Tissues Organs*, **181**(1), 1–10.

Blix, M. 1891. Die Länge und die Spannung des Muskels. *Skandinavisches Archiv Für Physiologie*, **3**(1), 295–318.

Böl, M., & Schmitz, A. 2013. A coupled chemomechanical model for smooth muscle contraction. *Pages 63–75 of:* Holzapfel, G.A. & Kuhl, E. (ed), *Computer Models in Biomechanics, From Nano to Macro.* Springer Netherlands.

Böl, M., Weikert, R., & Weichert, C. 2011a. A coupled electromechanical model for the excitation-dependent contraction of skeletal muscle. *Journal of the Mechanical Behavior of Biomedical Materials*, **4**(7), 1299–1310.

Böl, M., Sturmat, M., Weichert, C., & Kober, C. 2011b. A new approach for the validation of skeletal muscle modelling using MRI data. *Computational Mechanics*, **47**(5), 591–601.

Böl, M., Schmitz, A., Nowak, G., & Siebert, T. 2012. A three-dimensional chemo-mechanical continuum model for smooth muscle contraction. *Journal of the Mechanical Behavior of Biomedical Materials*, **13**, 215–229.

Böl, M., Leichsenring, K., Weichert, C., Sturmat, M., Schenk, P., Blickhan, R., & Siebert, T. 2013. Three-dimensional surface geometries of the rabbit soleus

muscle during contraction: input for biomechanical modelling and its validation. *Biomechanics and modeling in mechanobiology*, **12**(6), 1205–20.

Böl, M., Leichsenring, K., Ernst, M., Wick, C., Blickhan, R., & Siebert, T. 2015. Novel microstructural findings in M. plantaris and their impact during active and passive loading at the macro level. *Journal of the Mechanical Behavior of Biomedical Materials*, **51**, 25–39.

Böl, M., Leichsenring, K., & Siebert, T. 2016. Effects of Growth on Muscle, Tendon, and Aponeurosis Tissues in Rabbit Shank Musculature. *The Anatomical Record*, **00**(October), 1–14.

Bolsterlee, B., Veeger, H.E.J., Van Der Helm, F.C.T., Gandevia, S.C., & Herbert, R.D. 2015. Comparison of measurements of medial gastrocnemius architectural parameters from ultrasound and diffusion tensor images. *Journal of Biomechanics*, **48**(6), 1133–1140.

Bond, M., & Somlyo, A. V. 1982. Dense bodies and actin polarity in vertebrate smooth muscle. *Journal of Cell Biology*, **95**(2 I), 403–413.

Bottinelli, R., Canepari, M., Pellegrino, M.A., & Reggiani, C. 1996. Force-velocity properties of human skeletal muscle fibres: myosin heavy chain isoform and temperature dependence. *The Journal of physiology*, **495(Pt 2)**, 573–586.

Brenner, B. 1983. Technique for stabilizing the striation pattern in maximally calcium-activated skinned rabbit psoas fibers. *Biophysical journal*, **41**(1), 99–102.

Brunello, E., Caremani, M., Melli, L., Linari, M., Fernandez-Martinezz, M., Narayanan, T., Irving, M., Piazzesi, G., Lombardi, V., & Reconditi, M. 2014. The contributions of filaments and cross-bridges to sarcomere compliance in skeletal muscle. *Journal of Physiology*, **17**, 3881–3899.

Burgoyne, T., Morris, E.P., & Luther, P.K. 2015. Three-Dimensional Structure of Vertebrate Muscle Z-Band: The Small-Square Lattice Z-Band in Rat Cardiac Muscle. *Journal of Molecular Biology*, **427**(22), 3527–3537.

Burkholder, T.J., & Lieber, R.L. 2001. Review Sarcomere Length Operating Range of Vertebrate Muscles During Movement. *The Journal of experimental biology*, **204**, 1529–1536.

Burton, K., Simmons, R.M., & Sleep, J. 2006. Kinetics of force recovery following length changes in active skinned single fibres from rabbit psoas muscle: analysis and modelling of the late recovery phase. *The Journal of physiology*, **573**(Pt 2), 305–328.

Butler, T.M., Siegman, M.J., & Mooers, S.U. 1983. Chemical Energy Usage During Shortening and Work Production in Mammalian Smooth-Muscle. *American Journal of Physiology*, **244**(3), C234–C242.

Campbell, S.G., & Campbell, K.S. 2011. Mechanisms of residual force enhancement in skeletal muscle: Insights from experiments and mathematical models. *Biophysical Reviews*, **3**(4), 199–207.

Cavagna, G. A., Heglund, N. C., & Taylor, C R. 1977. Mechanical work basic mechanisms in terrestrial locomotion: two for minimizing energy expenditure. *the American Journal of Physiology*, **233**(5), 243–261.

Cavagna, G.A., Dusman, B., & Margaria, R. 1968. *Positive work done by a previously stretched muscle.*

Chase, P.B., & Kushmerick, M.J. 1988. Effects of pH on contraction of rabbit fast and slow Skeletal Muscle Fibers. *Biophysical Jorunal*, **53**(6), 935–946.

Cheng, Leo K., Komuro, Rie, Austin, Travis M., Buist, Martin L., & Pullan, Andrew J. 2007. Anatomically realistic multiscale models of normal and abnormal

gastrointestinal electrical activity. *World Journal of Gastroenterology*, **13**(9), 1378–1383.

Cheng, Leo K., O'Grady, Gregory, Du, Peng, Egbuji, John U., Windsor, John A., & Pullan, Andrew J. 2010. Gastrointestinal system. *Wiley Interdisciplinary Reviews: Systems Biology and Medicine*, **2**(1), 65–79.

Cheung, A., Dantzig, J.A., Hollingworth, S., Baylor, S.M., Goldman, Y.E., Mitchison, T.J., & Straight, A.F. 2002. A small-molecule inhibitor of skeletal muscle myosin II. *Nature cell biology*, **4**(1), 83–88.

Chuinard, Robert G., Boyes, Joseph H., Stark, Herbert H., & Ashworth, Charles R. 1978. Tendon transfers for radial nerve palsy: Use of superficialis tendons for digital extension. *Journal of Hand Surgery*, **3**(6), 560–570.

Colombini, B., Nocella, M., Benelli, G., Cecchi, G., & Bagni, M.A. 2007. Crossbridge Properties During Force Enhancement By Slow Stretching in Single Intact Frog Muscle Fibres. *The Journal of physiology*, **585**(2), 607–615.

Colombini, B., Nocella, M., & Bagni, M. A. 2016. Non-crossbridge stiffness in active muscle fibres. *Journal of Experimental Biology*, **219**(2), 153–160.

Craig, R, & Megerman, J. 1977. Assembly of smooth muscle myosin into side-polar filaments. *Journal of Cell Biology*, **75**(3), 990–996.

Craig, Roger. 1977. Structure of A-segments from frog and rabbit skeletal muscle. *Journal of Molecular Biology*, **109**(1), 69–81.

Crawford, G.N.C. 1950. An experimental study of tendon growth in the rabbit. *J Bone Joint Surg (Br)*, **32-B**(2), 234–243.

Crawford, G.N.C. 1954. An experimental study of muscle growth in the rabbit. *J Bone Joint Surg (Br)*, **36-B**(2), 294–303.

De Koning, J. J., Van Der Molen, H. F., Woittiez, R. D., & Huijing, P. A. 1987. Functional characteristics of rat gastrocnemius and tibialis anterior muscles during growth. *Journal of Morphology*, **194**(1), 75–84.

de Wever, I, Eeckhout, C, Vantrappen, G, & Hellemans, J. 1978. Disruptive effect of test meals on interdigestive motor complex in dogs. *Am J Physiol Endocrinol Metab*, **235**(6), E661–E665.

Degens, H., Yu, F., Li, X., & Larsson, L. 1998. Effects of age and gender on shortening velocity and myosin isoforms in single rat muscle fibres. *Acta Physiol Scand*, **163**(1), 33–40.

Dickinson, M.H., Farley, C.T., Full, R.J., Koehl, M.A., Kram, R., & Lehman, S. 2000. How animals move: an integrative view. *Science (New York, N.Y.)*, **288**(5463), 100–106.

Dillon, P.F., Aksoy, M.O., Driska, S.T., & Murphy, R.A. 1981. Myosin phosphorylation and the cross-bridge cycle in arterial smooth muscle. *Science (New York, N.Y.)*, **211**(4481), 495–497.

Dobbs, M B, Morcuende, J A, Gurnett, C A, & Ponseti, I V. 2000. Treatment of idiopathic clubfoot: an historical review. *The Iowa orthopaedic journal*, **20**, 59–64.

DuVall, Michael M., Jinha, Azim, Schappacher-Tilp, Gudrun, Leonard, Timothy R., & Herzog, Walter. 2017. Differences in titin segmental elongation between passive and active stretch in skeletal muscle. *The Journal of Experimental Biology*, **2**(October), jeb.160762.

Ebashi, S., & Endo, M. 1968. Calcium Ion and Muscle Contraction. *Prog Biophys Mol Biol.*, **18**, 123–183.

Edman, K A. 1975. Mechanical deactivation induced by active shortening in isolated muscle fibres of the frog. *The Journal of physiology*, **246**(1), 255–75.

Edman, K. A. P. 2010. Contractile Performance of Striated Muscle. *Adv Exp Med Biol*, **682**, 7–40.

Edman, K.A.P. 1979. The velocity of unloaded shortening and its relation to sarcomere length and isometric force in vertebrate muscle fibres. *Journal of Physiology*, **291**, 143–159.

Edman, K.A.P. 2012. Residual force enhancement after stretch in striated muscle. A consequence of increased myofilament overlap? *The Journal of physiology*, **590**(Pt 6), 1339–45.

Edman, K.A.P., & Tsuchiya, T. 1996. Strain of passive elements during force enhancement by stretch in frog muscle fibres. *The Journal of Physiology*, **490**(1), 191–205.

Edman, K.A.P., Elzinga, G., & Noble, M. 1982. Residual force enhancement after stretch of contracting frog single muscle fibers. *The Journal of general physiology*, **80**(5), 769–784.

Ehret, A.E., Böl, M., & Itskov, M. 2011. A continuum constitutive model for the active behaviour of skeletal muscle. *Journal of the Mechanics and Physics of Solids*, **59**(3), 625–636.

Epstein, M, & Herzog, W. 1998. *Theoretical models of skeletal muscle: biological and mathematical considerations*. Chichester: John Wiley & Sons.

Epstein, M., Wong, M., & Herzog, W. 2006. Should tendon and aponeurosis be considered in series? *Journal of Biomechanics*, **39**(11), 2020–2025.

Essig, D A, Segal, S S, & White, T P. 1985. Skeletal muscle protein synthesis and degradation in vitro: effects of temperature. *Am J Physiol*, **249**(5 Pt 1), C464–70.

Farré, Ricard, & Tack, Jan. 2013. Food and Symptom Generation in Functional Gastrointestinal Disorders: Physiological Aspects. *The American Journal of Gastroenterology*, **108**(5), 698–706.

Fay, Fredric S, & Delise, Claudio M. 1973. of Isolated Smooth-Muscle Cells-Structural Changes. *Proceedings of the National Academy of Sciences USA*, **70**(3), 641–645.

Ferris, D.P., Czerniecki, J.M., & Hannaford, B. 2005. An ankle-foot orthosis powered by artificial pneumatic muscles. *Journal of Applied Biomechanics*, **21**(2), 189–197.

Finer, J T, Simmons, R M, & Spudich, J A. 1994. Single myosin molecule mechanics: piconewton forces and nanometre steps. *Nature*, **368**(6467), 113–119.

Ford, L.E., Huxley, A.F., & Simmons, R.M. 1977. Tension responses to sudden length change in stimulated frog muscle fibres near slack length. *The Journal of physiology*, **269**(2), 441–515.

Fryer, M.W., Owen, V.J., Lamb, G.D., & Stephenson, D.G. 1995. Effects of creatine phosphate and P(i) on Ca2+ movements and tension development in rat skinned skeletal muscle fibres. *The Journal of Physiology*, **482**(1), 123–140.

Fung, Y. C. (Yuan-cheng). 1993. *Biomechanics : mechanical properties of living tissues.* Berlin: Springer-Verlag.

Gans, C, & Bock, W. J. 1965. The functional significance of muscle architecture – a theoretical analysis. *Ergebnisse der Anatomie und Entwicklungsgeschichte*, **38**, 115–142.

Gans, Carl, & Gaunt, Abbot S. 1991. Muscle architecture in relation to function. *Journal of Biomechanics*, **24**(Suppl. 1), 53–65.

Gareis, Heather, Moshe, Solomonow, Baratta, Richard, Best, Robert, & D'Ambrosia, Robert. 1992. The isometric length-force models of nine different skeletal muscles. *Journal of Biomechanics*, **25**(8), 903–916.

Gastelum, Alfonso, Mata, Lucely, Brito-de-la Fuente, Edmundo, Delmas, Patrice, Vicente, William, Salinas-Vázquez, Martín, Ascanio, Gabriel, & Marquez, Jorge. 2016. Building a three-dimensional model of the upper gastrointestinal tract for computer simulations of swallowing. *Medical & Biological Engineering & Computing*, **54**(2-3), 525–534.

Geyer, H., & Herr, H. 2010. A Muscle-Reflex Model That Encodes Principles of Legged Mechanics Produces Human Walking Dynamics and Muscle Activities. *IEEE Transactions on Neural Systems and Rehabilitation Engineering*, **18**(3), 263–273.

Gillies, Allison R., & Lieber, Richard L. 2012. Structure and function of the skeletal muscle extracellular matrix. *Muscle nerve*, **44**(3), 318–331.

Gillis, G B, & Biewener, A A. 2001. Hindlimb muscle function in relation to speed and gait: in vivo patterns of strain and activation in a hip and knee extensor of the rat (Rattus norvegicus). *The Journal of experimental biology*, **204**(15), 2717–2731.

Gindhart, P.S. 1973. Growth standards for the tibia and radius in children aged one month through eighteen years. *American Journal of Physical Anthropology*, **39**(1), 41–48.

Goldmann, Y.E., & Simmons, R.M. 1984. Control of sarcomere length in skinned muscles fibres of Rana temporaria during mechanical transients. *Journal of Physiology*, **350**, 497–518.

Goldstein, M.A., Michael, L.H., Schroeter, J.P., & Sass, R.L. 1988. Structural states in the Z band of skeletal muscle correlate with states of active and passive tension. *The Journal of general physiology*, **92**(1), 113–9.

Gollapudi, S.K., & Lin, D.C. 2013. Prediction of the in vivo force-velocity relationship of slow human skeletal muscle from measurements in myofibers. *Annals of Biomedical Engineering*, **41**(8), 1767–1777.

Gorb, S. N., & Fischer, Martin S. 2000. Three-dimensional analysis of the arrangement and length distribution of fascicles in the triceps muscle of Galea musteloides (Rodentia, Cavimorpha). *Zoomorphology*, **120**(2), 91–97.

Gordon, A., & Siegman, M. J. 1971. Mechanical Properties of Smooth muscle. Length-tension and force-velocity relations. *American Journal*, **221**(5), 1243–1249.

Gordon, A.M., Huxley, A.F., & Julian, F.J. 1966. The variation in isometric tension with sarcomere length in vertebrate muscle fibres. *The Journal of physiology*, **184**(1), 170–192.

Gulati, J, & Babu, A. 1985. Critical dependence of calcium-activated force on width in highly compressed skinned fibers of the frog. *Biophys. J.*, **48**(5), 781–787.

Gunst, J. 1986. Effect of length history on contractile of canine tracheal smooth muscle. *Am J Physiol*, **250**(1), C146–C154.

Haeufle, D. F.B., Günther, M., Bayer, A., & Schmitt, S. 2014. Hill-type muscle model with serial damping and eccentric force-velocity relation. *Journal of Biomechanics*, **47**(6), 1531–1536.

Hagopian, M. 1970. Contraction bands at short sarcomere length in chick muscle. *J. Cell Biol.*, **47**(3), 790–796.

Halanski, Matthew A., Abrams, Sam, Lenhart, Rachel, Leiferman, Ellen, Kaiser, Teresa, Pierce, Emily, Franklin, Rachel Rebekah, Opel, Dayton, Noonan, Kenneth J., & Crenshaw, Thomas D. 2016. Tendon transfer to unossified bone in a porcine model: potential implications for early tibialis anterior tendon transfers in children with clubfeet. *Journal of Children's Orthopaedics*, **10**(6), 705–714.

Hamner, S.R., Seth, A., & Delp, S.L. 2010. Muscle contributions to propulsion and support during running. *Journal of Biomechanics*, **43**(14), 2709–2716.

Hansson, L. I., Menander-Sellman, K., Stenström, A., & Thorngren, K. G. 1972. Rate of normal longitudinal bone growth in the rat. *Calcified Tissue Research*, **10**(1), 238–251.

Heidlauf, T., & Röhrle, O. 2014. A multiscale chemo-electro-mechanical skeletal muscle model to analyze muscle contraction and force generation for different muscle fiber arrangements. *Frontiers in Physiology*, **5**(December), 1–15.

Heidlauf, T., Klotz, T., Rode, C., Altan, E., Bleiler, C., Siebert, T., & Röhrle, O. 2016. A multi-scale continuum model of skeletal muscle mechanics predicting force enhancement based on actin–titin interaction. *Biomechanics and Modeling in Mechanobiology*, **15**(6), 1423–1437.

Heidlauf, Thomas, Klotz, Thomas, Rode, Christian, Siebert, Tobias, & Röhrle, Oliver. 2017. A continuum-mechanical skeletal muscle model including actin-titin interaction predicts stable contractions on the descending limb of the force-length relation. *PLoS Comput Biol.*, **13**(10), 1–25.

Herlihy, J. T., & Murphy, R. a. 1973. Length-Tension Relationship of Smooth Muscle of the Hog Carotid Artery. *Circulation Research*, **33**(3), 275–283.

Hernanz-Schulman, Marta. 2003. Infantile Hypertrophic Pyloric Stenosis. *Radiology*, **227**(2), 319–331.

Herrel, A, Meyers, J J, Aerts, P, & Nishikawa, K C. 2001. Functional implications of supercontracting muscle in the chameleon tongue retractors. *The Journal of experimental biology*, **204**(Pt 21), 3621–7.

Herrera, Ana M, McParland, Brent E, Bienkowska, Agnes, Tait, Ross, Paré, Peter D, & Seow, Chun Y. 2005. 'Sarcomeres' of smooth muscle: functional characteristics and ultrastructural evidence. *Journal of cell science*, **118**(Pt 11), 2381–92.

Herrmann, C., Wray, J., Travers, F., & Barman, T. 1992. Effect of 2,3-butanedione

monoxime on myosin and myofibrillar ATPases. An example of an uncompetitive inhibitor. *Biochemistry*, **31**(48), 12227–12232.

Herzog, W., & Leonard, T.R. 1997. depression of cat soleus forces following isokinetic shortening. *Journal of Biom*, **30**(9), 865–872.

Herzog, W., Leonard, T.R., Joumaa, V., & Mehta, A. 2008. Mysteries of muscle contraction. *Journal of Applied Biomechanics*, **24**(1), 1–13.

Herzog, W., Schappacher, G., DuVall, M., Leonard, T.R., & Herzog, J.A. 2016. Residual Force Enhancement Following Eccentric Contractions: A New Mechanism Involving Titin. *Physiology*, **31**(4), 300–312.

Herzog, Walter. 2017. Skeletal muscle mechanics: questions, problems and possible solutions. *Journal of NeuroEngineering and Rehabilitation*, **14**(1), 17.

Heslinga, J.W., & Huijing, P.A. 1990. Effects of growth on architecture and functional characteristics of adult rat gastrocnemius muscle. *Journal of morphology*, **206**(1), 119–132.

Hessel, Anthony L., Lindstedt, Stan L., & Nishikawa, Kiisa C. 2017. Physiological mechanisms of eccentric contraction and its applications: A role for the giant titin protein. *Frontiers in Physiology*, **8**(FEB), 1–14.

Hiepe, Patrick, Herrmann, Karl Heinz, Güllmar, Daniel, Ros, Christian, Siebert, Tobias, Blickhan, Reinhard, Hahn, Klaus, & Reichenbach, Jürgen R. 2014. Fast low-angle shot diffusion tensor imaging with stimulated echo encoding in the muscle of rabbit shank. *NMR in Biomedicine*, **27**(2), 146–157.

Higuchi, H., & Takemori, S. 1989. Butanedione Monoxime Suppresses of Rabbit Skeletal Contraction and ATPase Activity adjusted. *Journal of Biochem.*, **105**(4), 638–643.

Hilber, K., & Galler, S. 1998. Improvement of the measurements on skinned muscle fibres by fixation of the fibre ends with glutaraldehyde. *Journal of Muscle Research and Cell Motility*, **19**(4), 365–372.

Hill, A.V. 1926. the viscous elastic properties of smooth muscle. *Proceedings of the Royal Society B: Biological Sciences*, **100**(701), 108–115.

Hill, A.V. 1938. The Heat of Shortening and the Dynamic Constants of Muscle. *Proceedings of the Royal Society B: Biological Sciences*, **126**(843), 136–195.

Hochberger, J., Maiss, J., & Hahn, E. G. 2002. The use of simulators for training in GI endoscopy. *Endoscopy*, **34**(9), 727–729.

Hong, Chih-Kai, Chiang, Chen-Hao, Huang, Yi-Hung, Su, Wei-Ren, & Lo, Sheng-Pin. 2017. Technique using the modified rolling hitch for split peroneus brevis tendon transfer in lateral ankle stabilization. *Foot and Ankle Surgery*, **23**(4), e35–e37.

Horn, Charles C. 2008. Why is the neurobiology of nausea and vomiting so important? *Appetite*, **50**(2-3), 430–434.

Horowitz, M., Dent, J., Fraser, R., Sun, W., & Hebbard, G. 1994. Role and integration of mechanisms controlling gastric emptying. *Digestive Diseases and Sciences*, **39**(12 Supplement), 7–13.

Houdusse, Anne, & Sweeney, H. Lee. 2016. How Myosin Generates Force on Actin Filaments. *Trends in Biochemical Sciences*, **41**(12), 989–997.

Hoyle, G., McAlear, J.H., & Severston, A. 1963. Mechanism of Supercontraction Muscle in a Striated. *The Journal of Cell Biology*, **26**, 621–640.

Hutter, M., Remy, C.D., Hoepflinger, M.A., & Siegwart, R. 2013. Efficient and versatile locomotion with highly compliant legs. *IEEE/ASME Transactions on Mechatronics*, **18**(2), 449–458.

Huxley, A.F. 1957a. Muscle structue and theories of contraction. *Progress in Biophysics and Biophysical Chemistry*, **7**, 255–318.

Huxley, A.F. 2000. Cross-bridge action: present views, prospects, and unknowns. *Journal of biomechanics*, **33**(10), 1189–95.

Huxley, A.F., & Niedergerke, R. 1954. Structural changes in muscle during contraction; interference microscopy of living muscle fibres. *Nature*, **173**(4412), 971–973.

Huxley, A.F., & Simmons, R.M. 1971. Proposed mechanism of force generation in striated muscle. *Nature*, **233**(5321), 533–538.

Huxley, H.E. 1953. X-ray analysis and the problem of muscle. *Proceedings of the Royal Society of London. Series B, Biological sciences*, **141**(902), 59–62.

Huxley, H.E. 1957b. The double array of filaments in cross-striated muscle. *The Journal of biophysical and biochemical cytology*, **3**(5), 631–48.

Huxley, H.E., & Hanson, J. 1954. Changes in the Cross-Striations of Muscle during Contraction and Stretch and their Structural Interpretation. *Nature*, **173**(4412), 973–976.

Huxley, H.E., Stewart, A., Sosa, H., & Irving, T. 1994. X-ray diffraction measurements of the extensibility of actin and myosin filaments in contracting muscle. *Biophysical journal*, **67**(6), 2411–2421.

Iwamoto, H., Sugaya, R., & Sugi, H. 1990. Force-velocity relation of frog skeletal muscle fibres shortening under continuously changing load. *J Physiol*, 185–202.

Janssen, P., Vanden Berghe, P., Verschueren, S., Lehmann, A., Depoortere, I., & Tack, J. 2011. Review article: The role of gastric motility in the control of food intake. *Alimentary Pharmacology and Therapeutics*, **33**(8), 880–894.

Jia, Z. G., Li, W., & Zhou, Z. R. 2015. Mechanical characterization of stomach tissue under uniaxial tensile action. *Journal of Biomechanics*, **48**(4), 651–658.

Joumaa, V, & Herzog, W. 2010. Force depression in single myofibrils. *Journal of applied physiology (Bethesda, Md. : 1985)*, **108**(2), 356–62.

Joumaa, V., Leonard, T.R., & Herzog, W. 2008. Residual force enhancement in myofibrils and sarcomeres. *Proceedings. Biological sciences / The Royal Society*, **275**(1641), 1411–9.

Junqueira, L. C U, Bignolas, G., & Brentani, R. R. 1979. Picrosirius staining plus polarization microscopy, a specific method for collagen detection in tissue sections. *The Histochemical Journal*, **11**(4), 447–455.

Katz, B. 1939. The relation between force and speed in muscular contraction. *The Journal of Physiology*, **96**(1), 45–64.

Kaya, Motoshi, & Higuchi, Hideo. 2010. Nonlinear elasticity and an 8-nm working stroke of single myosin molecules in myofilaments. *Science*, **329**(5992), 686–689.

Kellermayer, M., & Granzier, H.L. 1996. Calcium-dependent inhibition of in vitro thin-filament motility by native titin. *FEBS Letters*, **380**(3), 281–286.

Kim, Kyoungtae, & Keller, Thomas C S. 2002. Smitin, a novel smooth muscle titin-like protein, interacts with myosin filaments in vivo and in vitro. *Journal of Cell Biology*, **156**(1), 101–111.

Kindt, S, & Tack, J. 2006. Impaired gastric accommodation and its role in dyspepsia. *Gut*, **55**(12), 1685–1691.

Kjaer, Michael, & Kjær, Michael. 2004. Role of Extracellular Matrix in Adaptation of Tendon and Skeletal Muscle to Mechanical Loading. *Physiological reviews*, **84**(2), 649–98.

Knapppeis, G.G., & Carlsen, F. 1962. The ultrastructure of the Z disc in skeletal muscle. *J Cell Biol.*, **13**, 323–335.

Komi, P. V. 2000. Stretch-shorting cycle:a powerful model to study normal and fatigued muscle. *Journal of Biomechanics*, **33**(10), 1197–206.

Kong, Siow-Kee, & Stephens, L. 1983. Mechanical properties of pulmonary from sensitized dogs. *J Appl Physiol Respir Environ Exerc Physiol.*, **55**(6), 1669–1673.

Korossis, Sotirios, Bolland, Fiona, Southgate, Jenny, Ingham, Eileen, & Fisher, John. 2009. Regional biomechanical and histological characterisation of the passive porcine urinary bladder: Implications for augmentation and tissue engineering strategies. *Biomaterials*, **30**(2), 266–275.

Kosterina, N., Wang, R., Eriksson, A., & Gutierrez-Farewik, E.M. 2013. Force enhancement and force depression in a modified muscle model used for muscle activation prediction. *Journal of electromyography and kinesiology : official journal of the International Society of Electrophysiological Kinesiology*, **23**(4), 759–65.

Kuo, Kuo-Hsing, Herrera, Ana M, Wang, Lu, Paré, Peter D, Ford, Lincoln E, Stephens, Newman L, & Seow, Chun Y. 2003. Structure-function correlation in airway smooth muscle adapted to different lengths. *American journal of physiology. Cell physiology*, **285**(2), C384–90.

Labeit, D., Watanabe, K., Witt, C., Fujita, H., Wu, Y., Lahmers, S., Funck, T., Labeit, S., & Granzier, H.L. 2003. Calcium-dependent molecular spring elements in the giant protein titin. *Proceedings of the National Academy of Sciences of the United States of America*, **100**(23), 13716–13721.

Labeit, S., & Kolmerer, B. 1995. Titins: Giant Proteins in Charge of Muscle Ultrastructure and Elasticity. *Science*, **270**(5234), 293–296.

Lakatos, D., Rode, C., Seyfarth, A., & Albu-Schäffer, A. 2014. Design and control of compliantly actuated bipedal running robots: Concepts to exploit natural system dynamics. *IEEE-RAS International Conference on Humanoid Robots*.

Lakatos, D., Albu-Schäffer, A., Rode, C., & Loeffl, F. 2016. Dynamic Bipedal Walking by Controlling only the Equilibrium of Intrinsic Elasticities. *Pages 1282–1289 of: IEEE-RAS International Conference on Humanoid Robots*.

Lammers, Andrew R., & German, Rebecca Z. 2002. Ontogenetic allometry in the locomotor skeleton of specialized half-bounding mammals. *Journal of Zoology*, **258**(4), 485–495.

Leonard, T R, DuVall, M, & Herzog, W. 2010. Force enhancement following stretch in a single sarcomere. *American Journal of Physiology - Cell Physiology*, **299**(6), C1398–C1401.

Leonard, T.R., & Herzog, W. 2010. Regulation of muscle force in the absence of actin-myosin-based cross-bridge interaction. *American Journal of Physiology. Cell Physiology*, **299**(1), C14–20.

Li, Y., Lang, P., & Linke, W.A. 2016. Titin stiffness modifies the force-generating region of muscle sarcomeres. *Scientific Reports*, **6**(24492).

Liao, Donghua, Zhao, Jingbo, & Gregersen, Hans. 2005. Regional surface geometry of the rat stomach based on three-dimensional curvature analysis. *Physics in medicine and biology*, **50**(2), 231–246.

Lieber, R. L., & Frieden, J. 2000. Functional and Clinical Significance. *Muscle & Nerve*, **23**(11), 1647–1666.

Lieber, Richard L, & Ward, Samuel R. 2011. Skeletal muscle design to meet functional demands. *Phil. Trans. R. Soc. B*, **366**, 1466–1476.

Lieber, R.L., & Blevins, F.T. 1989. Skeletal muscle architecture of the rabbit hindlimb: Functional implications of muscle design. *Journal of Morphology*, **199**(1), 93–101.

Lieber, R.L., & Fridén, J. 2002. Mechanisms of muscle injury gleaned from animal models. *American journal of physical medicine & rehabilitation / Association of Academic Physiatrists*, **81**(11 Suppl), S70–579.

Lin, David C, & Nichols, T Richard. 2003. Parameter estimation in a crossbridge muscle model. *Journal of biomechanical engineering*, **125**(1), 132–40.

Linari, M., Caremani, M., Piperio, C., Brandt, P., & Lombardi, V. 2007. Stiffness and fraction of Myosin motors responsible for active force in permeabilized muscle fibers from rabbit psoas. *Biophysical journal*, **92**(7), 2476–2490.

Lindstedt, S. L., & Hoppeler, H. H. 2016. Expanding knowledge of contracting muscle. *Journal of Experimental Biology*, **219**(2), 134–134.

Linke, Wolfgang A. 2017. Titin Gene and Protein Functions in Passive and Active Muscle. *Annu Rev Physiol.*, 1–23.

Lodder, M A, de Haan, A, & Sargeant, A J. 1994. Effect of growth on efficiency and fatigue in extensor digitorum longus muscle of the rat. *European journal of applied physiology and occupational physiology*, **69**(5), 429–434.

Lopez, J.R., Wanek, L.A., & Taylor, S.R. 1981. Skeletal Muscle: Length-Dependent Effects of Potentiating Agents. *Science*, **214**.

Luther, P K. 2000. Three-dimensional structure of a vertebrate muscle Z-band: implications for titin and alpha-actinin binding. *Journal of structural biology*, **129**(1), 1–16.

Luther, P K, & Squire, J M. 1981. Three-dimensional structure of the vertebrate muscle A-band. II. The myosin filament superlattice. *Journal of molecular biology*, **151**(4), 703–730.

Luther, P.K. 2009. The vertebrate muscle Z-disc: Sarcomere anchor for structure and signalling. *Journal of Muscle Research and Cell Motility*, **30**(5-6), 171–185.

Luther, Pradeep K, Winkler, Hanspeter, Taylor, Kenneth, Zoghbi, Maria E, Craig, Roger, Padron, R., Squire, John M, & Liu, Jun. 2011. Direct visualization of myosin-binding protein C bridging myosin and actin filaments in intact muscle. *Proceedings of the National Academy of Sciences*, **108**(28), 11423–11428.

Maas, Huub, & Sandercock, Thomas G. 2010. Force transmission between synergistic skeletal muscles through connective tissue linkages. *Journal of Biomedicine and Biotechnology*.

MacIntosh, Brian R., Gardiner, Phillip F., & McComas, Alan J. 2006. *Skeletal muscle: form and function*. 2nd edn. Champaign, IL: Human Kinetics.

Maréchal, G, & Plaghki, L. 1979. The deficit of the isometric tetanic tension redeveloped after a release of frog muscle at a constant velocity. *The Journal of general physiology*, **73**(4), 453–67.

Martinez-Lemus, L.A., Hill, M.A., Bolz, S.S., Pohl, U., & Meininger, G.A. 2004. Acute mechanoadaptation of vascular smooth muscle cells in response to continuous arteriolar vasoconstriction: implications for functional remodeling. *The FASEB journal : official publication of the Federation of American Societies for Experimental Biology*, **18**(6), 708–710.

Masoud, Ibrahim, Shapiro, Frederic, Kent, Ralph, & Moses, Alan. 1986. A longitudinal study of the growth of the New Zealand white rabbit: Cumulative and biweekly incremental growth rates for body length, body weight, femoral length, and tibial length. *Journal of Orthopaedic Research*, **4**(2), 221–231.

McKillop, D.F., Fortune, N.S., Ranatunga, K.W., & Geeves, M.A. 1994. The influence of 2,3-butanedione 2-monoxime (BDM) on the interaction between actin and myosin

in solution and in skinned muscle fibres. *Journal of muscle research and cell motility*, **15**(3), 309–318.

Mehta, A., & Herzog, W. 2008. Cross-bridge induced force enhancement? *Journal of Biomechanics*, **41**(7), 1611–1615.

Méndez, J., & Keys, A. 1960. Density and composition of mammalian muscle. *Metabolism*, **9**, 184–188.

Menzel, R., Böl, M., & Siebert, T. 2017. Importance of contraction history on muscle force of porcine urinary bladder smooth muscle. *International Urology and Nephrology*, **49**(2), 205–214.

Millar, N.C., & Homsher, E. 1990. The effect of phosphate and calcium on force generation in glycerinated rabbit skeletal muscle fibers. A steady-state and transient kinetic study. *The Journal of biological chemistry*, **265**(33), 20234–20240.

Miller, Mark S., Tanner, Bertrand C W, Nyland, Lori R., & Vigoreaux, Jim O. 2010. Comparative biomechanics of thick filaments and thin filaments with functional consequences for muscle contraction. *Journal of Biomedicine and Biotechnology*, **2010**.

Millman, B M. 1998. The filament lattice of striated muscle. *Physiological reviews*, **78**(2), 359–391.

Minekus, J., & van Mastrigt, R. 2001. Length dependence of the contractility of pig detrusor smooth muscle fibres. *Urological Research*, **29**(2), 126–133.

Mohagheghi, A. A., Khan, T., Meadows, T. H., Giannikas, K., Baltzopoulos, V., & Maganaris, C. N. 2008. In vivo gastrocnemius muscle fascicle length in children with and without diplegic cerebral palsy. *Developmental Medicine and Child Neurology*, **50**(1), 44–50.

Monroy, J.A., Powers, K.L., Pace, C.M., Uyeno, T., & Nishikawa, K.C. 2017. Effects of activation on the elastic properties of intact soleus muscles with a deletion in titin. *The Journal of Experimental Biology*, **220**(Pt 5), 828–836.

Morgan, D. L., Mochon, S., & Julian, F. J. 1982. A quantitative model of intersarcomere dynamics during fixed-end contractions of single frog muscle fibers. *Biophysical Journal*, **39**(2), 189–196.

Morgan, D.L. 1977. Separation of active and passive components of short-range stiffness of muscle. *The American journal of physiology*, **232**(1), C45–C49.

Morgan, D.L., Whitehead, N.P., Wise, A.K., Gregory, J.E., & Proske, U. 2000. Tension changes in the cat soleus muscle following slow stretch or shortening of the contracting muscle. *The Journal of Physiology*, **522**(3), 503–513.

Moriya, M., & Miyazaki, E. 1982. The differences in contractile response to AC Field stimulation between longitudinal and circular muscles of guinea pig stomach. *Japanese Journal of Physiology*, **32**, 1–12.

Moriya, M., & Miyazaki, E. 1985. Force-Velocity Characteristics of Stomach Muscle: a Comparison Between Longitudinal and Circular Muscle Strips. *Comp Biochem Physiol A Comp Physiol.*, **81**(3), 531–537.

Mörl, F., Siebert, T., & Häufle, D. 2016. Contraction dynamics and function of the muscle-tendon complex depend on the muscle fibre-tendon length ratio: a simulation study. *Biomechanics and modeling in mechanobiology*, **15**(1), 245–258.

Morse, Christopher I, Tolfrey, Keith, Thom, Jeanette M, Vassilopoulos, Vasilios, Maganaris, Constantinos N, & Narici, Marco V. 2008. Gastrocnemius muscle specific force in boys and men. *J Appl Physiol (1985)*, **104**, 469–474.

Mulisch, M., & Welsch, U. 2010. *Mikroskopische Technik*. 18th edn. Heidelberg: Spektrum Akademischer Verlag.

Mulvany, M J, & Warshaw, D M. 1979. The active tension-length curve of vascular smooth muscle related to its cellular components. *The Journal of general physiology*, **74**(1), 85–104.

Naghshin, J., Wang, L., Pare, P.D., & Seow, C.Y. 2003. Adaptation to chronic length change in explanted airway smooth muscle. *Journal of applied physiology*, **95**(1), 448–53.

Nigg, B.M., & Herzog, W. 2007. Biomechanics of the Musculo-skeletal System. *John Wiley and Sons, Chichester*.

Nishikawa, K.C., Monroy, J.A., Uyeno, T.E., Yeo, S.H., Pai, D.K., & Lindstedt, S.L. 2012. Is titin a 'winding filament'? A new twist on muscle contraction. *Proceedings of the Royal Society B: Biological Sciences*, **279**(1730), 981–990.

Noble, M.I. 1992. Enhancement of mechanical performance of striated muscle by stretch during contraction. *Experimental physiology*, **77**(4), 539–552.

Notivol, Ricardo, Coffin, Benoit, Azpiroz, Fernando, Mearin, Fermín, Serra, Jordi, & Malagelada, Juan R. 1995. Gastric tone determines the sensitivity of the stomach to distention. *Gastroenterology*, **108**(2), 330–336.

Osborne, M.P. 1967. Supercontraction in the muscles of the blowfly larva: An ultrastructural study. *Journal of Insect Physiology*, **13**(10), 1471–1482.

Ostap, E.M. 2002. 2,3-Butanedione monoxime (BDM) as a myosin inhibitor. *Journal of Muscle Research and Cell Motility*, **23**(4), 305–308.

Pal, Anupam, Indireshkumar, Keshavamurthy, Schwizer, Werner, Abrahamsson, Bertil, Fried, Michael, & Brasseur, James G. 2004. Gastric flow and mixing studied using computer simulation. *Proceedings of the Royal Society B: Biological Sciences*, **271**(1557), 2587–94.

Pal, Anupam, Brasseur, James G., & Abrahamsson, Bertil. 2007. A stomach road or "Magenstrasse" for gastric emptying. *Journal of Biomechanics*, **40**(6), 1202–1210.

Pinheiro, J., Bates, D., DebRoy, S., Sarkar, D., & Team, R Core. 2014. nlme: Linear and Nonlinear Mixed Effects Models. R package version 3.1-131.

Pinniger, G.J., Ranatunga, K.W., & Offer, G.W. 2006. Crossbridge and non-crossbridge contributions to tension in lengthening rat muscle: force-induced reversal of the power stroke. *The Journal of Physiology*, **573**(3), 627–643.

Pollock, Colleen M, & Shadwick, Robert E. 1994. Allometry of muscle, tendon, and elastic energy storage capacity in mammals. *American Journal of Physiology*, **266**(3), R1022–R1031.

Powers, K., Schappacher-Tilp, G., Jinha, A., Leonard, T., Nishikawa, K., & Herzog, W. 2014. Titin force is enhanced in actively stretched skeletal muscle. *The Journal of experimental biology*, **217**(20), 3629–3636.

Prado, Lucas G., Makarenko, Irina, Andresen, Christian, Krüger, Martina, Opitz, Christiane A., & Linke, Wolfgang A. 2005. Isoform Diversity of Giant Proteins in Relation to Passive and Active Contractile Properties of Rabbit Skeletal Muscles. *The Journal of General Physiology*, **126**(5), 461–480.

Pratt, G.A., & Williamson, M.M. 1995. Series elastic actuators. *Pages 399–406 of: IEEE/RSJ International Conference on Intelligent Robots and Systems. 'Human Robot Interaction and Cooperative Robots'*, vol. 1.

Rack, P.M., & Westbury, D.R. 1969. The effects of length and stimulus rate on tension in the isometric cat soleus muscle. *Journal of Physiology*, **204**(2), 443–460.

Ramsey, R.W., & Street, S.F. 1940. the Isometric Length-Tension Diagram of isolated skeletal muscle fibers of the frog. *Journal of cellular physiology*, **15**(1), 11–34.

Ranatunga, K.W. 1982. Temperature-Dependence of Shortening Velocity Skeletal Muscle. *Journal of Physiology*, **329**, 465–483.

Ranatunga, K.W. 1984. The force-velocity relation of rat fast- and slow-twitch muscles examined at different temperatures. *The Journal of physiology*, **351**, 517–529.

Rassier, D., & Herzog, W. 2004. Active force inhibition and stretch-induced force enhancement in frog muscle treated with BDM. *Journal of applied physiology*, **97**(4), 1395–1400.

Rassier, D. E., Herzog, W., & Pollack, G. H. 2003. Dynamics of individual sarcomeres during and after stretch in activated single myofibrils. *Proceedings of the Royal Society B: Biological Sciences*, **270**(1525), 1735–1740.

Rassier, D.E. 2017. Sarcomere mechanics in striated muscles: from molecules to sarcomeres to cells. *American Journal of Physiology - Cell Physiology*, **313**(2), C134–C145.

Raynaud, Fabrice, Astier, Catherine, & Benyamin, Yves. 2004. Evidence for a direct but sequential binding of titin to tropomyosin and actin filaments. *Biochimica et Biophysica Acta - Proteins and Proteomics*, **1700**(2), 171–178.

Reedy, Mary C., Beall, Clifford, & Fyrberg, Eric. 1989. Formation of reverse rigor chevrons by myosin heads. *Nature*, **339**(6224), 481–483.

Reinhardt, Lars, Siebert, Tobias, Leichsenring, Kay, Blickhan, Reinhard, & Böl, Markus. 2016. Intermuscular pressure between synergistic muscles correlates with muscle force. *The Journal of experimental biology*, **219**(15), 2311–2319.

Rivas-Pardo, J.A., Eckels, E.C., Popa, I., Kosuri, P., Linke, W., & Fernández, J.M. 2016. Work Done by Titin Protein Folding Assists Muscle Contraction. *Cell Reports*, **14**(6), 1339–1347.

Roberts, T.J. 2016. Contribution of elastic tissues to the mechanics and energetics of muscle function during movement. *The Journal of Experimental Biology*, **219**(2), 266–275.

Roberts, T.J., & Azizi, E. 2011. Flexible mechanisms: the diverse roles of biological springs in vertebrate movement. *The Journal of Experimental Biology*, **214**(3), 353–361.

Rode, C., & Siebert, T. 2009. The effects of parallel and series elastic components on estimated active cat soleus muscle force. *Journal of Mechanics in Medicine and Biology*, **9**(1), 105–122.

Rode, C., Siebert, T., & Blickhan, R. 2009. Titin-induced force enhancement and force depression: a 'sticky-spring' mechanism in muscle contractions? *Journal of theoretical biology*, **259**(2), 350–360.

Röhrle, O., Davidson, J. B., & Pullan, A. J. 2012. A physiologically based, multi-scale model of skeletal muscle structure and function. *Frontiers in Physiology*, **3**(358), 1–14.

Röhrle, O., Sprenger, M., & Schmitt, S. 2016. A two-muscle, continuum-mechanical forward simulation of the upper limb. *Biomechanics and Modeling in Mechanobiology*, **16**(3), 743–762.

Röhrle, Oliver, Saini, Harnoor, & Ackland, David C. 2017. Occlusal loading during biting from an experimental and simulation point of view. *Dental Materials*, **7**(October), pii: S0109–5641(17)30756–X.

Roots, H., Offer, G. W., & Ranatunga, K. W. 2007. Comparison of the tension responses to ramp shortening and lengthening in intact mammalian muscle fibres: Crossbridge and non-crossbridge contributions. *Journal of Muscle Research and Cell Motility*, **28**(2-3), 123–139.

Rüdel, R, & Taylor, S.R. 1970. Striated Muscle Fibers: Inactivation of Contraction Induced by Shortening. *Science (New York, N.Y.)*, **167**(3919), 882–884.

Rüdel, R., & Taylor, S.R. 1971. Striated Muscle Fibers: Facilitation of contraction at short lengths by caffeine. *Science (New York, N.Y.)*, **172**(3981), 387–388.

Schaeffer, Paul J., & Lindstedt, Stan L. 2013. How animals move: Comparative lessons on animal locomotion. *Comprehensive Physiology*, **3**(1), 289–314.

Schappacher-Tilp, G., Leonard, T., Desch, G., & Herzog, W. 2015. A Novel Three-Filament Model of Force Generation in Eccentric Contraction of Skeletal Muscles. *Plos One*, **10**(3), e0117634.

Schenk, P, Siebert, T, Hiepe, P, Güllmar, D, Reichenbach, J R, Wick, C, Blickhan, R, & Böl, M. 2013. Determination of three-dimensional muscle architectures: validation of the DTI-based fiber tractography method by manual digitization. *Journal of anatomy*, **223**(1), 61–8.

Schmitz, A., & Böl, M. 2011. On a phenomenological model for active smooth muscle contraction. *Journal of Biomechanics*, **44**(11), 2090–2095.

Schoenberg, M, & Podolsky, R J. 1972. Length-force relation of calcium activated muscle fibers. *Science (New York, N.Y.)*, **176**, 52–54.

Schulze-Delrieu, K, Herman, R J, Shirazi, S S, & Brown, B P. 1998. Contractions move contents by changing the configuration of the isolated cat stomach. *The American journal of physiology*, **274**, G359–G369.

Schwizer, W, Steingotter, A, Fox, M, Zur, T, Thumshirn, M, Bosiger, P, & Fried, M. 2002. Non-invasive measurement of gastric accommodation in humans. *Gut*, **51**(Supplement 1), i59–i62.

Scott, S.H., Brown, I.E., & Loeb, G.E. 1996. Mechanics of feline soleus: I. Effect of fascicle length and velocity on force output. *J. Muscle Res. Cell Motil.*, **17**(2), 207–219.

Scott, Stephen H., & Loeb, Gerald E. 1995. Mechanical properties of aponeurosis and tendon of the cat soleus muscle during whole-muscle isometric contractions. *Journal of Morphology*, **224**(1), 73–86.

Seiberl, W., Power, G. a., Herzog, W., & Hahn, D. 2015. The stretch-shortening cycle (SSC) revisited: residual force enhancement contributes to increased performance during fast SSCs of human m. adductor pollicis. *Physiological Reports*, **3**(5), e12401–e12401.

Seipel, Katja, & Schmid, Volker. 2005. Evolution of striated muscle: Jellyfish and the origin of triploblasty. *Developmental Biology*, **282**(1), 14–26.

Seow, C Y. 2005. Myosin filament assembly in an ever-changing myofilament lattice of smooth muscle. *American journal of physiology Cell physiology*, **289**(6), C1363–8.

Seydewitz, Robert, Menzel, Robin, Siebert, Tobias, & Böl, Markus. 2017. Three-dimensional mechano-electrochemical model for smooth muscle contraction of the urinary bladder. *Journal of the Mechanical Behavior of Biomedical Materials*, **75**, 128–146.

Shah, Kalpit N., DeFroda, Steven F., Ware, James Kristopher, Koruprolu, Sarath C., & Owens, Brett D. 2017. Lateral Patellofemoral Ligament: An Anatomic Study. *Orthopaedic Journal of Sports Medicine*, **5**(12), 232596711774143.

Shalabi, N., Cornachione, A., Leite, F., Vengallatore, S., & Rassier, D.E. 2017. Residual force enhancement is regulated by titin in skeletal and cardiac myofibrils. *The Journal of Physiology*, **595**(6), 2085–2098.

Siebert, T., & Rode, C. 2014. Computational modeling of muscle biomechanics. *Pages 173–243 of:* Z.Jin (ed), *Computational Modelling of Biomechanics and Biotribology in the Musculoskeletal System. Biomaterials and Tissues.* 1st ed. Amsterdam: Woodhead Publishing / Elsevier.

Siebert, T., Rode, C., Herzog, W., Till, O., & Blickhan, R. 2008. Nonlinearities make a difference: comparison of two common Hill-type models with real muscle. *Biological cybernetics*, **98**(2), 133–43.

Siebert, T., Till, O., Stutzig, N., Günther, M., & Blickhan, R. 2014a. Muscle force depends on the amount of transversal muscle loading. *Journal of Biomechanics*, **47**(8), 1822–1828.

Siebert, T., Till, O., & Blickhan, R. 2014b. Work partitioning of transversally loaded muscle: experimentation and simulation. *Computer methods in biomechanics and biomedical engineering*, **17**(3), 217–29.

Siebert, T., Leichsenring, K., Rode, C., Wick, C., Stutzig, N., Schubert, H., Blickhan, R., & Böl, M. 2015. Three-Dimensional Muscle Architecture and Comprehensive Dynamic Properties of Rabbit Gastrocnemius, Plantaris and Soleus: Input for Simulation Studies. *Plos One*, **10**(6), e0130985.

Siebert, Tobias, Rode, Christian, Till, Olaf, Stutzig, Norman, & Blickhan, Reinhard. 2016. Force reduction induced by unidirectional transversal muscle loading is independent of local pressure. *Journal of Biomechanics*, **49**(7), 1156–1161.

Siebert, Tobias, Stutzig, Norman, & Rode, Christian. 2017. A hill-type muscle model expansion accounting for effects of varying transverse muscle load. *Journal of Biomechanics*, pii: S0021–9290(17)30583–3.

Siegman, M J, Butler, T M, Mooers, S U, & Davies, R E. 1976. Calcium-dependent resistance to stretch and stress relaxation in resting smooth muscles. *The American journal of physiology*, **231**(5 Pt. 1), 1501–1508.

Siegman, M. J., Davidheiser, S., Mooers, S. U., & Butler, T. M. 2013. Structural Limits on Force Production and Shortening of Smooth Muscle. *Journal of Muscle Research and Cell Motility*, **34**(1), 43–60.

Somlyo, A P, Devine, C E, Somlyo, A V, & Rice, R V. 1973. Filament organization in vertebrate smooth muscle. *Philosophical transactions of the Royal Society of London Series B, Biological sciences*, **265**(867), 223–229.

Soukup, T., Zachařová, G., & Smerdu, V. 2002. Fibre type composition of soleus and extensor digitorum longus muscles in normal female inbred Lewis rats. *Acta Histochemica*, **104**(4), 399–405.

Stålhand, Jonas, & Holzapfel, Gerhard A. 2016. Length adaptation of smooth muscle contractile filaments in response to sustained activation. *Journal of Theoretical Biology*, **397**, 13–21.

Stark, H., & Schilling, N. 2010. A novel method of studying fascicle architecture in relaxed and contracted muscles. *Journal of Biomechanics*, **43**(15), 2897–2903.

Stark, Heiko, Fröber, Rosemarie, & Schilling, Nadja. 2013. Intramuscular architecture of the autochthonous back muscles in humans. *Journal of Anatomy*, **222**(2), 214–222.

Stephenson, D.G. 2003. Relationship between isometric force and myofibrillar MgATPase at short sarcomere length in skeletal and cardiac muscle and its relevance to the concept of activation heat. *Clin Exp Pharmacol Physiol*, **30**(8), 570–575.

Stephenson, D.G., & Williams, D.A. 1981. calcium-activated force responses in fast-and slow-twitch skinned muscle fibres of the rat at different temperatures. *Journal of Physiology*, **317**, 281–302.

Stephenson, D.G., & Williams, D.A. 1982. Effects of sarcomere length on the force-pCa relation in fast- and slow-twitch skinned muscle fibres from the rat. *Journal of Physiology*, **333**, 637–653.

Stephenson, D.G., & Williams, D.A. 1985. Temperature-dependent calcium sensitivity changes. *J Physiol.*, **360**, 1–12.

Stickland, N.C. 1983. The arrangement of muscle fibers and tendons in two muscles used for growth studies. *Journal of anatomy*, **136**(1), 175–179.

Sugi, H., & Ohta, T. 1983. Development of the maximum isometric force at short sarcomere lengths in calcium-activated muscle myofibrils. *Experientia*, **39**, 1982–1983.

Swammerdam, J. 1737. *Biblia naturae*. Leyden: Isaak Severinus, Boudewyn and Peter van der Aa.

Tack, J, Demedts, I, Meulemans, a, Schuurkes, J, & Janssens, J. 2002. Role of nitric oxide in the gastric accommodation reflex and in meal induced satiety in humans. *Gut*, **51**(2), 219–24.

Taylor, C R, Schmidt-Nielsen, K, & Raab, J L. 1970. Scaling of energetic cost of running to body size in mammals. *The American journal of physiology*, **219**(4), 1104–1107.

Telander, R L, Morgan, K G, Kreulen, D L, Schmalz, P F, Kelly, K A, & Szurszewski, J H. 1978. Human gastric atony with tachygastria and gastric retention. *Gastroenterology*, **75**(3), 497–501.

Telley, I. A., Denoth, J., Stüssi, E., Pfitzer, G., & Stehle, R. 2006. Half-sarcomere dynamics in myofibrils during activation and relaxation studied by tracking fluorescent markers. *Biophysical journal*, **90**(2), 514–30.

ter Keurs, H.E., Luff, A.R., & Luff, S.E. 1984. Force — Sarcomere-Length Relation and Filament Length in Rat Extensor Digitorum Muscle. *Adv. Exp. Med. Biol.*, **170**, 511–525.

Thirlwell, H., Corrie, J. E. T., Reid, G. P., Trentham, D. R., & Ferenczi, M. A. 1994. Kinetics of Relaxation from Rigor of Permeabilized Fast-Twitch Skeletal Fibers

from the Rabbit Using a Novel Caged ATP and Apyrase. *Biophysical Jorunal*, **67**(December), 2436–2447.

Till, O., Siebert, T., Rode, C., & Blickhan, R. 2008. Characterization of isovelocity extension of activated muscle: a Hill-type model for eccentric contractions and a method for parameter determination. *Journal of theoretical biology*, **255**(2), 176–187.

Till, O., Siebert, T., & Blickhan, R. 2010. A mechanism accounting for independence on starting length of tension increase in ramp stretches of active skeletal muscle at short half-sarcomere lengths. *Journal of theoretical biology*, **266**(1), 117–123.

Toigo, M. 2015. *Muskelrevolution - Konzepte und Rezepte zum Muskel- und Kraftaufbau.* Berlin: Springer Spektrum.

Tortora, Gerard J., & Nielsen, Mark T. 2013. *Principles of human anatomy.* 13th edn. Hoboken, New Jersey: Wiley.

Toyoshima, Y.Y., Toyoshima, C., & Spudich, J.A. 1989. Bidirectional movement of actin filaments along tracks of myosin heads. *Nature*, **341**(6238), 154–156.

Trombitas, K, & Tigyi-Sebes, A. 1985. How actin filament polarity affects crossbridge force in doubly-overlapped insect muscle. *Journal of Muscle Research and Cell Motility*, **6**, 447–459.

van Asselt, E., Pel, J. J M, & van Mastrigt, R. 2007. Shortening induced effects on force (re)development in pig urinary smooth muscle. *Journal of Biomechanics*, **40**(7), 1534–1540.

Van Den Akker, Jeroen, Schoorl, Marieke J C, Bakker, Erik N T P, & Vanbavel, Ed. 2010. Small artery remodeling: Current concepts and questions. *Journal of Vascular Research*, **47**(3), 183–202.

van Mastrigt, R. 2002. Mechanical properties of (urinary bladder) smooth muscle. *Journal of Muscle Research and Cell Motility*, **23**(1), 53–57.

van Mastrigt, R., & Glerum, J. J. 1985. In Vitro Comparison of Isometric and Stop-Test Contractility Parameters for the Urinary Bladder. *Journal of Urology and Research*, **13**, 11–17.

Veigel, Claudia, Molloy, Justin E, Schmitz, Stephan, & Kendrick-Jones, John. 2003. Load-dependent kinetics of force production by smooth muscle myosin measured with optical tweezers. *Nature cell biology*, **5**(11), 980–986.

Villanova, N, Azpiroz, F, & Malagelada, J R. 1997. Gastrogastric reflexes regulating gastric tone and their relationship to perception. *American Journal of Physiology*, **273**(2 Pt 1), G464–9.

Wakabayashi, K., Sugimoto, Y., Tanaka, H., Ueno, Y., Takezawa, Y., & Amemiya, Y. 1994. X-ray diffraction evidence for the extensibility of actin and myosin filaments during muscle contraction. *Biophysical Journal*, **67**(6), 2422–2435.

Walcott, S., & Herzog, W. 2008. Modeling residual force enhancement with generic cross-bridge models. *Mathematical Biosciences*, **216**(2), 172–186.

Walker, S.M., & Schrodt, G.R. 1974. I segment lengths and thin filament periods in skeletal muscle fibers of the rhesus monkey and the human. *The Anatomical Record*, **178**(1), 63–81.

Wang, L., Paré, P.D., & Seow, C.Y. 2001. Plasticity in Skeletal, Cardiac, and Smooth Muscle Selected Contribution: Effect of chronic passive length change on airway smooth muscle length-tension relationship. *Journal of Applied Physiology*, **90**(2), 734–740.

Wang, L C, & Kernell, D. 2001. Fibre type regionalisation in lower hindlimb muscles of rabbit, rat and mouse: a comparative study. *Journal of anatomy*, **199**(6), 631–643.

Warshaw, D M. 1987. Force: velocity relationship in single isolated toad stomach smooth muscle cells. *The Journal of general physiology*, **89**(5), 771–89.

Warshaw, D M, McBride, W J, & Work, S S. 1987. Corkscrew-like shortening in single smooth muscle cells. *Science (New York, N.Y.)*, **236**(4807), 1457–9.

Williams, C. D., Salcedo, M. K., Irving, T. C., Regnier, M., & Daniel, T. L. 2013. The length–tension curve in muscle depends on lattice spacing. *Proceedings of the Royal Society B: Biological Sciences*, **280**(1766), 20130697.

Winters, T. M., Takahashi, M., Lieber, R. L., & Ward, S. R. 2011. Whole muscle length-tension relationships are accurately modeled as scaled sarcomeres in rabbit hindlimb muscles. *Journal of Biomechanics*, **44**(1), 109–115.

Woittiez, R. D., Heerkens, Y. F., Huijing, P. A., Rijnsburger, W. H., & Rozendal, R. H. 1986. Functional morphology of the M. Gastrocnemius medialis of the rat during growth. *Journal of Morphology*, **187**(2), 247–258.

Woittiez, R D, Heerkens, Y F, Huijing, P A, & Rozendal, R H. 1989. Growth of medial gastrocnemius muscle and Achilles tendon in Wistar rats. *Anatomischer Anzeiger*, **168**(5), 371–80.

Xu, J.Q., Harder, B.A., Uman, P., & Craig, R. 1996. Myosin filament structure in vertebrate smooth muscle. *Journal of Cell Biology*, **134**(1), 53–66.

Yucesoy, C.A., Koopman, B.H., Baan, G.C., Grootenboer, H.J., & Huijing, P.A. 2003. Extramuscular Myofascial Force Transmission: Experiments and Finite Element Modeling. *Archives of Physiology and Biochemistry*, **111**(4), 377–388.

Zajac, F.E. 1989. Muscle and tendon properties, models, scaling, and application to biomechanics and motor control. *Crit. Rev. in Biomedical Engineering*, **17**(4), 359–411.

Zar, J.H. 2010. *Biostatistical Analysis.* 5th edn. New Jersey: Prentice Hall.

Zeidan, A., Nordström, I., Dreja, K., Malmqvist, U., & Hellstrand, P. 2000. Stretch-dependent modulation of contractility and growth in smooth muscle of rat portal vein. *Circulation research*, **87**(3), 228–234.

Zhao, J., Liao, D., & Gregersen, H. 2005. Tension and stress in the rat and rabbit stomach are location- and direction-dependent. *Neurogastroenterology and Motility*, **17**(3), 388–398.

Zhao, J., Liao, D., Chen, P., Kunwald, P., & Gregersen, H. 2008. Stomach stress and strain depend on location, direction and the layered structure. *Journal of Biomechanics*, **41**(16), 3441–3447.

Zhao, J., Liao, D., Yang, J., & Gregersen, H. 2010. Biomechanical remodeling of obstructed guinea pig jejunum. *J Biomech*, **43**(7), 1322–1329.

Zhao, Y., & Kawai, M. 1994. BDM affects nucleotide binding and force generation steps of the cross-bridge cycle in rabbit psoas muscle fibers. *American Journal of Physiology - Cell Physiology*, **266**(2 Pt 1), C437–C447.

Zou, P., Pinotsis, N., Lange, S., Song, Y.-H., Popov, A., Mavridis, I., Mayans, O. M., Gautel, M., & Wilmanns, M. 2006. Palindromic assembly of the giant muscle protein titin in the sarcomeric Z-disk. *Nature*, **439**(7073), 229–233.

Zuurbier, Coert J., Everard, Andre J., van der Wees, Philip, & Huijing, Peter A. 1994. Length-force characteristics of the aponeurosis in the passive and active muscle condition and in the isolated condition. *Journal of Biomechanics*, **27**(4), 445–453.

List of Publications

Publications in peer-reviewed journals

- Tomalka A., Borsdorf M., Böl M., Siebert T. 2017. Porcine stomach smooth muscle force depends on history-effects. *Frontiers in Physiology - Gastrointestinal Sciences*, **8** (802). DOI: 10.3389/fphys.2017.00802 **(Impact Factor: 4.13)**

- Tomalka A., Rode C, Schumacher J, Siebert T. 2017. The active force–length relationship is invisible during extensive eccentric contractions in skinned skeletal muscle fibres. *Proceedings of the Royal Society B: Biological Sciences*, **284** (1854). DOI: 10.1098/rspb.2016.2497 **(Impact Factor: 4.94)**

- Siebert T., Tomalka A., Stutzig N., Leichsenring K., Böl M. 2017. Changes in three–dimensional muscle structure of rabbit *gastrocnemius, flexor digitorum longus*, and *tibialis anterior* during growth. *Journal of the Mechanical Behavior of Biomedical Materials*, **74**: 507-519. DOI: 10.1016/j.jmbbm.2017.07.045 **(Impact Factor: 3.11)**

- Rode C., Siebert T., Tomalka A., Blickhan R. 2016. Myosin filament sliding through the Z-disc relates striated muscle fibre structure to function. *Proceedings of the Royal Society B: Biological Sciences*, **283** (1826). DOI: 10.1098/rspb.2015.3030 **(Impact Factor: 4.94)**

Contributions of the Author

The first hurdle which I had to overcome was the implementation and validation of a fibre test system — including all the challenging needs (as e.g. robustly functioning of hard- and software, manufacturing of customised attachment hooks and 'T-clips' (see Appendix A), dissection and preparation of muscles, as well as composing of solutions used for biochemical activation of muscular tissue). After the successful validation of the test apparatus — launching distinct muscle fibre experiments in a wide variety — the groundwork for this work has been laid.

Nevertheless, the ideas, thoughts, experiments and findings demonstrated within this work — subsequently finding their way into international scientific journals — arised from an intense cooperation with numerous colleagues. With the exception of **Chapter 1** (*'General Introduction'*), **Chapter 2** (*'Description of Experimental Setups'*), and **Chapter 7** (*'General Conclusion'*), the colleagues contributing to the publications that emerged from the research presented in this thesis (**Chapters 3–6** [1,2,3,4]), were involed in different ways:

Prof. Dr. Tobias Siebert, Prof. Dr. Markus Böl and I conceived and designed the experiments of the study presented in **Chapter 3**. I and Mischa Borsdorf performed the experiments. I analysed the data and prepared the figures; Prof. Dr. Tobias Siebert, I and Mischa Borsdorf interpreted the results. I drafted, edited and revised the manuscript.

[1] Tomalka A., Borsdorf M., Böl M., Siebert T. *Front. Physiology* 2017 Oct 18;8:802.
[2] Tomalka A., Rode C., Schumacher J., Siebert T. *Proc Biol Sci.* 2017 May 17;284(1854).
[3] Rode C., Siebert T., Tomalka A., Blickhan R. *Proc Biol Sci.* 2016 Mar 16;283(1826).
[4] Siebert T., Tomalka A., Stutzig N., Leichsenring K., Böl M. *JMBBM* 2017 Oct;74:507-519.

The process of drafting the manuscript was accompanied by an intense consultation and collaboration with Prof. Dr. Tobias Siebert. Prof. Dr. Markus Böl helped editing the final manuscript. This work was funded by the Deutsche Forschungsgemeinschaft (DFG) under Grants SI 841/12-1 and BO 3091/18-1.

I, Dr. Christian Rode and Prof. Dr. Tobias Siebert developed the ideas of the manuscript that emerged from the research presented in **Chapter 4** within this thesis. I performed the experiments, analysed the data and prepared the figures. Dr. Jens Schumacher performed the statistical analyses. The process of data interpretation and writing the manuscript involved an intense collaboration with Dr. Christian Rode and Prof. Dr. Tobias Siebert.

Dr. Christian Rode developed the ideas, performed the research, analysed the data and drafted the manuscript for the article emerged from the research presented in **Chapter 5**. Prof. Dr. Tobias Siebert contributed to the ideas, supervised the experiments and helped draft the manuscript. I performed the experiments, contributed to their evaluation, and prepared Figure 5.7. Prof. Dr. Reinhard Blickhan contributed micromechanical considerations and helped draft the manuscript. Anvar Jakupov helped preparing Figure 5.2.

Prof. Dr. Tobias Siebert and Prof. Dr. Markus Böl conceived and designed the experiments of the study presented in **Chapter 6**. I performed the experiments in order to gather the 3D muscle fascicle architecture, analysed corresponding data, and prepared Figure 6.6. Furthermore, I performed the geometrical calculations of the muscle-tendon complex lengths for ankle joint angles of $80° - 100°$ and interpreted corresponding data. Dr. Kay Leichsenring performed measurements of the muscle and aponeurosis structures. Prof. Dr. Tobias Siebert analysed the 3D muscle properties (as aponeurosis and muscle dimensions), and, together with Dr. Norman Stutzig, he performed the statistical analyses. Prof. Dr. Tobias Siebert drafted the manuscript based on the experimental observations presented in **Chapter 6**. I, Prof. Dr. Markus Böl and Dr. Norman Stutzig assisted by drafting the first version of the manuscript.

Acknowledgement

First of all, I profoundly thank my parents, *Jörg* & *Marika*, for their unshakeable trust in me and continuous support throughout this process. Special thanks goes to my partner *Ivka* and my great daughter *Lara*. Furthermore, I am really grateful to Prof. Dr. Tobias Siebert, my Ph.D. supervisor. Despite his varied commitments as chair of the Institute of Sport and Motion Science at the University of Stuttgart, he always took the time for stimulating and beneficial discussions that contributed vastly to the ideas presented here. He has been the person who guided my theoretical interest towards the fascinating variety of muscular structures, and continuously supported me throughout this thesis. I thank Dr. Christian Rode, he assisted me during the process of drafting a manuscript, a period characterised by intense collaboration and transfer of knowledge. I would also like to thank Martin Kitsche — my brother-in-law. He has been always helping me with minor and major issues in terms of realising this work. He was reviewing and proofreading the thesis and gave valuable comments. Thanks a lot for that. Another thanks goes to Markus Osburg. He assisted me in bulding the temperature-controlled stage and he has been the first contact for all technical matters. Furthermore, my thank goes to Sven Döring and Tobias Ullsperger from the Institute of Applied Physics, Abbe Center of Photonics, Friedrich-Schiller-University Jena, for manufacturing the aluminum foil T-clips required for the muscle fibre experiments. Finally, I am thankful to all the people, including my supervisor, colleagues, friends, and many more, who supported me with valuable input for realising this work.

Appendix A

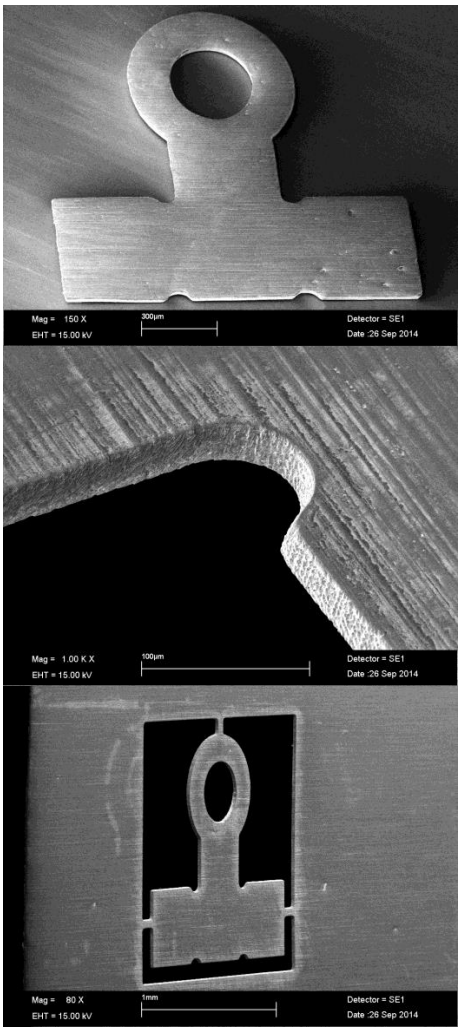

Detailed photographs of an aluminum foil T-clip, captured with an REM.

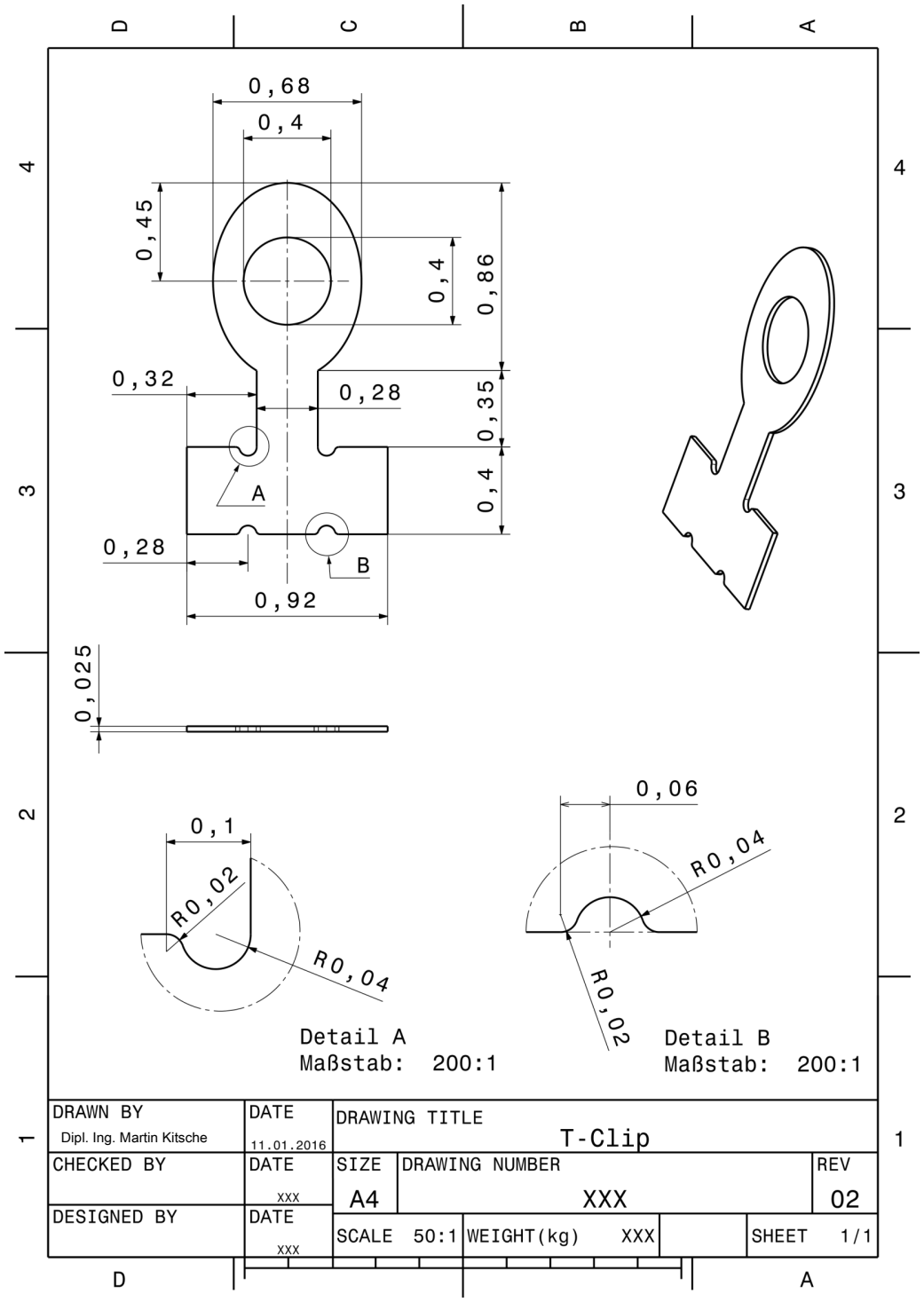

Technical CAD-drawing of an T-clip.

Appendix B

The mathematical model of sarcomere contraction

Active isometric half-sarcomere force F depends on half-sarcomere length l_{hs} and is proportional to an effective actin–myosin overlap region l_{eff}, where force can be generated by cross-bridges. Normalising this length to the maximum effective actin–myosin filament overlap length (l_{effmax}, the zone of myosin heads in a half-myosin), we obtain the isometric force as percentage of maximum isometric half-sarcomere force F_{im} at optimal fibre length:

$$\frac{F(l_{hs})}{F_{im}} = \frac{l_{eff}(l_{hs})}{l_{effmax}}. \tag{A.1}$$

The Z-disc is assumed to have zero depth. Then, starting from long lengths, half-sarcomere lengths l_1 (no actin–myosin overlap), l_2 (start of plateau), l_3 (start of shallow slope), l_4 (start of steep slope), l_5 (actin–actin–myosin overlap meets myosin–myosin–actin overlap), l_6 (actin filaments of adjacent half-sarcomere meet Z-disc), l_7 (myosin filaments of adjacent half-sarcomeres meet bare zone) and l_8 (myosin filaments of adjacent half-sarcomeres meet M-line) are given by

$$\left.\begin{aligned} l_1 &= l_a + \tfrac{l_m}{2}, \\ l_2 &= l_a + \tfrac{l_{bare}}{2}, \\ l_3 &= l_a - \tfrac{l_{bare}}{2}, \\ l_4 &= \tfrac{l_m}{2}, \\ l_5 &= \tfrac{2l_a+l_m}{6}, \\ l_6 &= \tfrac{l_a}{2}, \\ l_7 &= \tfrac{l_m+l_{bare}}{4}, \\ l_8 &= \tfrac{l_m-l_{bare}}{4}, \end{aligned}\right\} \tag{A.2}$$

with actin filament length l_a, myosin filament length l_m and the bare zone length without myosin heads at the centre of the myosin filament l_{bare}. Each different overlap region (Figure 5.3, between arrows) is scaled by an individual factor c to a corresponding length of regular overlap (i.e. three myosin filaments interact with each actin filament tending to shorten the sarcomere); the sum of the scaled lengths yields the effective overlap length

$$l_{eff}(l_{hs}) = \begin{cases} (l_1 - l_{hs}), & l_2 \leq l_{hs} \leq l_1 \\ (l_1 - l_2), & l_3 \leq l_{hs} < l_2 \\ (\frac{l_m}{2}2 + l_{hs} - l_a) + c_{aam}(l_3 - l_{hs}), & l_4 \leq l_{hs} < l_3 \\ (3l_{hs} - l_a - \frac{l_m}{2}) + c_{aam}(l_3 - l_{hs}) + c_{mma}(l_m/2 - l_{hs}), & l_5 \leq l_{hs} < l_4 \\ c_{aam}(2l_{hs} - \frac{l_m}{2} - \frac{l_{bare}}{2}) + c_{mma}(2l_{hs} - l_a) + c_{aamm}(l_a + \frac{l_m}{2} - 3l_{hs}), & l_6 \leq l_{hs} < l_5 \\ c_{aam}(2l_{hs} - \frac{l_m}{2} - \frac{l_{bare}}{2}) + c_{aamm}(\frac{l_m}{2} + l_{hs} - l_a) + c_{aaamm}(l_a - 2l_{hs}), & l_7 \leq l_{hs} < l_6 \\ c_{aamm}(3l_{hs} - l_a - \frac{l_{bare}}{2}) + c_{aaamm}(l_a - 2l_{hs}) + c_{aamm*}(2l_7 - 2l_{hs}), & l_8 \leq l_{hs} < l_7. \end{cases} \tag{A.3}$$

The index of c denotes the corresponding overlap region. For instance, c_{aamm} scales the actin–actin–myosin–myosin overlap (Figure 5.3*c*). The asterisk in the bottom row of equation (3.3) indicates its quantitative change within the bare zone of myosin of the half-sarcomere of interest where only half of myosin heads are available (Figure 5.3*e*).

Calculating *prediction I* (Figure 5.5), all c factors equal zero. For calculating *prediction II* (Figure 5.5) and *prediction III* (Figure 5.6), c factors consider the available number of actin filaments, the number of myosin filaments interacting with each actin filament and the orientation of the cross bridges. c_{aam} and c_{aaamm} were set to zero because experiments indicate that force is zero when actin filaments are abundant (Trombitas & Tigyi-Sebes, 1985). From the cross-sections in Figure 5.3*b,c,e,* we count how many myosin filaments produce regular (M_r) and swivelled cross-bridges (M_s) with each actin, respectively. Sectors M_s tending to lengthen the sarcomere produce half the force ($f = 0.5$; see electronic supplementary material, text S3) of filament sectors M_r, tending to shorten the sarcomere. Thus, we subtract the number of M_s per actin filament scaled by f from M_r per filament and divide this difference by three (the number of myosin filaments per actin tending to shorten the sarcomere in regular overlap). Finally, this number is multiplied by A (the number of available actin filaments divided by the number of actin filaments in regular overlap) to yield individual c:

$$c = A \cdot \frac{M_r - f \cdot M_r}{3}. \tag{A.4}$$

According to the mechanism of myosin sliding through the Z-disc (Figure 5.2), we expect a regular tetragonal pattern of actin filaments and myosin filaments within the myosin–myosin–actin overlap (Figures 5.2 and 5.3*b*, cross-section). Within this overlap region, two myosin filaments from the current half-sarcomere and two myosin filaments from the adjacent half-sarcomere (forming swivelled cross-bridges) act on each actin filament. Hence, $c_{mma} = 1(2 - 0.5 \cdot 2)/3 = 0.33$. In the actin–actin–myosin–myosin overlap the actin– myosin filament ratio is 2 : 1. Though formation of a regular

structure may be inhibited (see chapter 4 Discussion), for the sake of simplicity we assume the development of a hexagonal actin filament arrangement similar to the regular overlap zone. Here, on average, 1.5 myosin filaments per actin filament tend to shorten the sarcomere, and 1.5 myosin filaments per actin filament tend to extend the sarcomere. Because there are twice as many actin filaments compared with regular overlap, this results in $c_{aamm} = 2(1.5 - 0.5 \cdot 1.5)/3 = 0.5$. Accordingly, the actin–actin–myosin–myosin overlap within the bare zone of one set of myosin filaments must be scaled by $c_{aamm*} = 0.25$.

Appendix C

EINVERSTÄNDNISERKLÄRUNG

Die Co-Autoren der in dieser Dissertation verwendeten Manuskripte sind sowohl über die Nutzung, als auch über die entsprechend angegebenen Eigenanteile informiert und stimmen dem zu.

„Ich bin mit der Verwendung der Publikation/-en (nachstehend zitiert), bei denen Ich als Mitautor erscheine, im Rahmen der Dissertationsschrift des Promovenden (André Tomalka), und der damit einhergehenden Erklärung zum Eigenanteil, einverstanden."

- Tomalka A., Borsdorf M., Böl M., Siebert T. 2017. Porcine stomach smooth muscle force depends on history-effects. *Frontiers in Physiology*, 8 (802). DOI: 10.3389/fphys.2017.00802
- Tomalka A., Rode C, Schumacher J, Siebert T. 2017. The active force–length relationship is invisible during extensive eccentric contractions in skinned skeletal muscle fibres. *Proceedings of the Royal Society B: Biological Sciences*, 284 (1854). DOI: 10.1098/rspb.2016.2497
- Siebert T., Tomalka A., Stutzig N., Leichsenring K., Böl M. 2017. Changes in three–dimensional muscle structure of rabbit gastrocnemius, flexor digitorum longus, and tibialis anterior during growth. *Journal of the Mechanical Behavior of Biomedical Materials*, 74: 507-519. DOI: 10.1016/j.jmbbm.2017.07.045
- Rode C., Siebert T., Tomalka A., Blickhan R. 2016. Myosin filament sliding through the Z-disc relates striated muscle fibre structure to function. *Proceedings of the Royal Society B: Biological Sciences*, 283 (1826). DOI: 10.1098/rspb.2015.3030

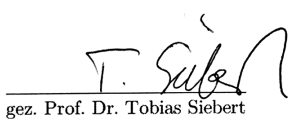

gez. Prof. Dr. Tobias Siebert

EINVERSTÄNDNISERKLÄRUNG

Die Co-Autoren der in dieser Dissertation verwendeten Manuskripte sind sowohl über die Nutzung, als auch über die entsprechend angegebenen Eigenanteile informiert und stimmen dem zu.

„Ich bin mit der Verwendung der Publikation/-en (nachstehend zitiert), bei denen Ich als Mitautor erscheine, im Rahmen der Dissertationsschrift des Promovenden (André Tomalka), und der damit einhergehenden Erklärung zum Eigenanteil, einverstanden."

- Tomalka A., Borsdorf M., Böl M., Siebert T. 2017. Porcine stomach smooth muscle force depends on history-effects. *Frontiers in Physiology*, 8 (802). DOI: 10.3389/fphys.2017.00802
- Tomalka A., Rode C, Schumacher J, Siebert T. 2017. The active force–length relationship is invisible during extensive eccentric contractions in skinned skeletal muscle fibres. *Proceedings of the Royal Society B: Biological Sciences*, 284 (1854). DOI: 10.1098/rspb.2016.2497
- Siebert T., Tomalka A., Stutzig N., Leichsenring K., Böl M. 2017. Changes in three–dimensional muscle structure of rabbit gastrocnemius, flexor digitorum longus, and tibialis anterior during growth. *Journal of the Mechanical Behavior of Biomedical Materials*, 74: 507-519. DOI: 10.1016/j.jmbbm.2017.07.045
- Rode C., Siebert T., Tomalka A., Blickhan R. 2016. Myosin filament sliding through the Z-disc relates striated muscle fibre structure to function. *Proceedings of the Royal Society B: Biological Sciences*, 283 (1826). DOI: 10.1098/rspb.2015.3030

gez. Prof. Dr. Markus Böl

TECHNISCHE UNIVERSITÄT BRAUNSCHWEIG
Institut für Festkörpermechanik
Langer Kamp 8, 38106 Braunschweig
Telefon 05 31 – 391 – 70 51
Telefax 05 31 – 391 – 70 53

EINVERSTÄNDNISERKLÄRUNG

Die Co-Autoren der in dieser Dissertation verwendeten Manuskripte sind sowohl über die Nutzung, als auch über die entsprechend angegebenen Eigenanteile informiert und stimmen dem zu.

„Ich bin mit der Verwendung der Publikation/-en (nachstehend zitiert), bei denen Ich als Mitautor erscheine, im Rahmen der Dissertationsschrift des Promovenden (André Tomalka), und der damit einhergehenden Erklärung zum Eigenanteil, einverstanden."

- Tomalka A., Borsdorf M., Böl M., Siebert T. 2017. Porcine stomach smooth muscle force depends on history-effects. *Frontiers in Physiology*, 8 (802). DOI: 10.3389/fphys.2017.00802
- Tomalka A., Rode C, Schumacher J, Siebert T. 2017. The active force–length relationship is invisible during extensive eccentric contractions in skinned skeletal muscle fibres. *Proceedings of the Royal Society B: Biological Sciences*, 284 (1854). DOI: 10.1098/rspb.2016.2497
- Siebert T., Tomalka A., Stutzig N., Leichsenring K., Böl M. 2017. Changes in three–dimensional muscle structure of rabbit gastrocnemius, flexor digitorum longus, and tibialis anterior during growth. *Journal of the Mechanical Behavior of Biomedical Materials*, 74: 507-519. DOI: 10.1016/j.jmbbm.2017.07.045
- Rode C., Siebert T., Tomalka A., Blickhan R. 2016. Myosin filament sliding through the Z-disc relates striated muscle fibre structure to function. *Proceedings of the Royal Society B: Biological Sciences*, 283 (1826). DOI: 10.1098/rspb.2015.3030

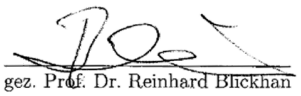

gez. Prof. Dr. Reinhard Blickhan

EINVERSTÄNDNISERKLÄRUNG

Die Co-Autoren der in dieser Dissertation verwendeten Manuskripte sind sowohl über die Nutzung, als auch über die entsprechend angegebenen Eigenanteile informiert und stimmen dem zu.

„Ich bin mit der Verwendung der Publikation/-en (nachstehend zitiert), bei denen Ich als Mitautor erscheine, im Rahmen der Dissertationsschrift des Promovenden (André Tomalka), und der damit einhergehenden Erklärung zum Eigenanteil, einverstanden."

- Tomalka A., Borsdorf M., Böl M., Siebert T. 2017. Porcine stomach smooth muscle force depends on history-effects. *Frontiers in Physiology*, 8 (802). DOI: 10.3389/fphys.2017.00802
- Tomalka A., Rode C, Schumacher J, Siebert T. 2017. The active force–length relationship is invisible during extensive eccentric contractions in skinned skeletal muscle fibres. *Proceedings of the Royal Society B: Biological Sciences*, 284 (1854). DOI: 10.1098/rspb.2016.2497
- Siebert T., Tomalka A., Stutzig N., Leichsenring K., Böl M. 2017. Changes in three–dimensional muscle structure of rabbit gastrocnemius, flexor digitorum longus, and tibialis anterior during growth. *Journal of the Mechanical Behavior of Biomedical Materials*, 74: 507-519. DOI: 10.1016/j.jmbbm.2017.07.045
- Rode C., Siebert T., Tomalka A., Blickhan R. 2016. Myosin filament sliding through the Z-disc relates striated muscle fibre structure to function. *Proceedings of the Royal Society B: Biological Sciences*, 283 (1826). DOI: 10.1098/rspb.2015.3030

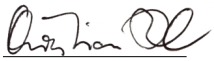

gez. Dr. Christian Rode

EINVERSTÄNDNISERKLÄRUNG

Die Co-Autoren der in dieser Dissertation verwendeten Manuskripte sind sowohl über die Nutzung, als auch über die entsprechend angegebenen Eigenanteile informiert und stimmen dem zu.

„Ich bin mit der Verwendung der Publikation/-en (nachstehend zitiert), bei denen Ich als Mitautor erscheine, im Rahmen der Dissertationsschrift des Promovenden (André Tomalka), und der damit einhergehenden Erklärung zum Eigenanteil, einverstanden."

- Tomalka A., Borsdorf M., Böl M., Siebert T. 2017. Porcine stomach smooth muscle force depends on history-effects. *Frontiers in Physiology*, 8 (802). DOI: 10.3389/fphys.2017.00802
- Tomalka A., Rode C, Schumacher J, Siebert T. 2017. The active force–length relationship is invisible during extensive eccentric contractions in skinned skeletal muscle fibres. *Proceedings of the Royal Society B: Biological Sciences*, 284 (1854). DOI: 10.1098/rspb.2016.2497
- Siebert T., Tomalka A., Stutzig N., Leichsenring K., Böl M. 2017. Changes in three–dimensional muscle structure of rabbit gastrocnemius, flexor digitorum longus, and tibialis anterior during growth. *Journal of the Mechanical Behavior of Biomedical Materials*, 74: 507-519. DOI: 10.1016/j.jmbbm.2017.07.045
- Rode C., Siebert T., Tomalka A., Blickhan R. 2016. Myosin filament sliding through the Z-disc relates striated muscle fibre structure to function. *Proceedings of the Royal Society B: Biological Sciences*, 283 (1826). DOI: 10.1098/rspb.2015.3030

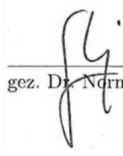

gez. Dr. Norman Stutzig

EINVERSTÄNDNISERKLÄRUNG

Die Co-Autoren der in dieser Dissertation verwendeten Manuskripte sind sowohl über die Nutzung, als auch über die entsprechend angegebenen Eigenanteile informiert und stimmen dem zu.

„Ich bin mit der Verwendung der Publikation/-en (nachstehend zitiert), bei denen Ich als Mitautor erscheine, im Rahmen der Dissertationsschrift des Promovenden (André Tomalka), und der damit einhergehenden Erklärung zum Eigenanteil, einverstanden."

- Tomalka A., Borsdorf M., Böl M., Siebert T. 2017. Porcine stomach smooth muscle force depends on history-effects. *Frontiers in Physiology*, 8 (802). DOI: 10.3389/fphys.2017.00802
- Tomalka A., Rode C, Schumacher J, Siebert T. 2017. The active force–length relationship is invisible during extensive eccentric contractions in skinned skeletal muscle fibres. *Proceedings of the Royal Society B: Biological Sciences*, 284 (1854). DOI: 10.1098/rspb.2016.2497
- Siebert T., Tomalka A., Stutzig N., Leichsenring K., Böl M. 2017. Changes in three–dimensional muscle structure of rabbit gastrocnemius, flexor digitorum longus, and tibialis anterior during growth. *Journal of the Mechanical Behavior of Biomedical Materials*, 74: 507-519. DOI: 10.1016/j.jmbbm.2017.07.045
- Rode C., Siebert T., Tomalka A., Blickhan R. 2016. Myosin filament sliding through the Z-disc relates striated muscle fibre structure to function. *Proceedings of the Royal Society B: Biological Sciences*, 283 (1826). DOI: 10.1098/rspb.2015.3030

gez. Dr. Kay Leichsenring

EINVERSTÄNDNISERKLÄRUNG

Die Co-Autoren der in dieser Dissertation verwendeten Manuskripte sind sowohl über die Nutzung, als auch über die entsprechend angegebenen Eigenanteile informiert und stimmen dem zu.

„Ich bin mit der Verwendung der Publikation/-en (nachstehend zitiert), bei denen Ich als Mitautor erscheine, im Rahmen der Dissertationsschrift des Promovenden (André Tomalka), und der damit einhergehenden Erklärung zum Eigenanteil, einverstanden."

- Tomalka A., Borsdorf M., Böl M., Siebert T. 2017. Porcine stomach smooth muscle force depends on history-effects. *Frontiers in Physiology*, 8 (802). DOI: 10.3389/fphys.2017.00802
- Tomalka A., Rode C, Schumacher J, Siebert T. 2017. The active force–length relationship is invisible during extensive eccentric contractions in skinned skeletal muscle fibres. *Proceedings of the Royal Society B: Biological Sciences*, 284 (1854). DOI: 10.1098/rspb.2016.2497
- Siebert T., Tomalka A., Stutzig N., Leichsenring K., Böl M. 2017. Changes in three–dimensional muscle structure of rabbit gastrocnemius, flexor digitorum longus, and tibialis anterior during growth. *Journal of the Mechanical Behavior of Biomedical Materials*, 74: 507-519. DOI: 10.1016/j.jmbbm.2017.07.045
- Rode C., Siebert T., Tomalka A., Blickhan R. 2016. Myosin filament sliding through the Z-disc relates striated muscle fibre structure to function. *Proceedings of the Royal Society B: Biological Sciences*, 283 (1826). DOI: 10.1098/rspb.2015.3030

gez. Dr. Jens Schumacher

Jena, 01.11.2017

EINVERSTÄNDNISERKLÄRUNG

Die Co-Autoren der in dieser Dissertation verwendeten Manuskripte sind sowohl über die Nutzung, als auch über die entsprechend angegebenen Eigenanteile informiert und stimmen dem zu.

„Ich bin mit der Verwendung der Publikation/-en (nachstehend zitiert), bei denen Ich als Mitautor erscheine, im Rahmen der Dissertationsschrift des Promovenden (André Tomalka), und der damit einhergehenden Erklärung zum Eigenanteil, einverstanden."

- Tomalka A., Borsdorf M., Böl M., Siebert T. 2017. Porcine stomach smooth muscle force depends on history-effects. *Frontiers in Physiology*, 8 (802). DOI: 10.3389/fphys.2017.00802
- Tomalka A., Rode C, Schumacher J, Siebert T. 2017. The active force–length relationship is invisible during extensive eccentric contractions in skinned skeletal muscle fibres. *Proceedings of the Royal Society B: Biological Sciences*, 284 (1854). DOI: 10.1098/rspb.2016.2497
- Siebert T., Tomalka A., Stutzig N., Leichsenring K., Böl M. 2017. Changes in three–dimensional muscle structure of rabbit gastrocnemius, flexor digitorum longus, and tibialis anterior during growth. *Journal of the Mechanical Behavior of Biomedical Materials*, 74: 507-519. DOI: 10.1016/j.jmbbm.2017.07.045
- Rode C., Siebert T., Tomalka A., Blickhan R. 2016. Myosin filament sliding through the Z-disc relates striated muscle fibre structure to function. *Proceedings of the Royal Society B: Biological Sciences*, 283 (1826). DOI: 10.1098/rspb.2015.3030

gez. Mischa Borsdorf

Declaration

I hereby declare, that this dissertation is solely my original work. I have used only the sources and materials indicated and have not received any unauthorised assistance from others. All quotations from other works as well as paraphrases or summaries of other works have been identified as such and properly acknowledged in the dissertation.

Ich erkläre, dass Ich die Arbeit selbständig erstellt und nur die angegebenen Hilfsmittel verwendet habe. Alle Stellen, die dem Wortlaut oder dem Sinn nach anderen Werken, gegebenenfalls auch elektronischen Medien, entnommen sind, sind von mir durch Angabe der Quelle als Entlehnung kenntlich gemacht.

Stuttgart, January 2018

André Tomalka,
January 16, 2018